Proton diffusion spectroscopy and modeling of brain metabolism at 14.1T

THÈSE N° 7275 (2016)

ÉCOLE POLYTECHNIQUE FÉDÉRALE DE LAUSANNE

POUR L'OBTENTION DU GRADE DE DOCTEUR ÈS SCIENCES

PAR

Masoumeh DEHGHANI MOGHADAM

EPFL

ÉCOLE POLYTECHNIQUE
FÉDÉRALE DE LAUSANNE

Suisse
2016

Abstract

Nuclear magnetic resonance (NMR) spectroscopy is intrinsically interdisciplinary, embracing physics, mathematics, neuroscience and physical biochemistry. As a field at the CIBM, NMR spectroscopy can be applied non-invasively to explore the metabolic fate of energy fuel substrates, as well as the rate at which they are consumed, using ^{13}C and ^{1}H nuclei. The work of this thesis encompasses both nuclei, and focuses on (1) improving the quantification and modeling of glucose-derived metabolites; and (2) characterizing diffusion-related parameters of the purportedly glial-specific energy substrate, acetate. Both aim to quantitatively explore cerebral energy metabolism, at ultra-high magnetic field, *in vivo*, in the healthy rat.

^{13}C NMR spectroscopy, as a tool, enables measuring the progressive incorporation of ^{13}C-glucose into brain glucose and then NMR detectable amino acids (glutamate and glutamine); this relies on the infusion of the ^{13}C-labeled energy substrate. The experimentally obtained ^{13}C labelling curves are analyzed using suitable mathematical models to provide an estimation of cerebral metabolic rates. Here, a dynamic model of time-courses of ^{13}C multiplets arising from isotopomers was considered. So beyond the two-compartment neuronal-glial model, we took into account additional data on the dynamics of ^{13}C isotopomers, available from the fine structure multiplets in ^{13}C spectra of glutamate and glutamine, measured under prolonged [1-6,^{13}C] glucose infusion. We concluded that the dynamic analyses of ^{13}C multiplet time courses of glutamate and glutamine resulted in a higher precision for estimating the absolute values of most cerebral metabolic rates.

Acetate metabolism is challenging because dynamic metabolic modeling requires prior knowledge of the transport and uptake kinetics of infused acetate. We sought this information by determining the apparent concentration and distribution volume (V_d) of cerebral acetate between the intracellular and the extracellular compartments. Experimentally, the diffusion characteristics of cerebral acetate were measured, relative to that of *N*-Acetylaspartate (NAA, known to be mainly intracellular) using diffusion-weighted ^{1}H NMR spectroscopy at 14.1T, under prolonged acetate infusion. The detection of an acetate and NAA signal at large diffusion weighting provided direct experimental evidence of intracellular cerebral acetate and NAA, although a substantial fraction of acetate was extracellular. To estimate the apparent concentration of *in vivo* brain acetate, T_1 and T_2 relaxation times of acetate were measured. The longer T_1 relaxation and shorter T_2 relaxation times of acetate compared with NAA provided evidence of its small molecular size, and possibly different chemical environment. Our experimentally determined value of V_d led to cerebral metabolic rates of acetate (CMR acetate) of the same order reported for the glial Kreb's cycle rate, an indication that estimates of CMR acetate are highly dependent on V_d.

Finally, in order to pursue metabolic mapping of cerebral acetate uptake in the rat, *in vivo*, at 14.1 T, the design and construction of a combined transmit-birdcage coil and receive-quadrature pair surface coil was considered. Its performance was compared to a single birdcage coil in the transmit/receive

mode. So far, the preliminary results of the 2-coil configuration are promising: homogenous excitation and a gain in sensitivity up to a distance of 5 mm are achievable. Improvements are ongoing for NMR spectroscopic and imaging applications at 14.1 T.

Keywords: Brain energy metabolism, ^{13}C NMR spectra, diffusion weighted spectroscopy, physical distribution volume, cerebral metabolic rate, TCA cycle, T_1 and T_2 relaxations, kinetic of transport and uptake of acetate, surface coil, birdcage coil.

Résumé

La spectroscopie de résonance magnétique nucléaire (RMN) est intrinsèquement interdisciplinaire, englobant la physique, les mathématiques, la neuroscience et la biochimie physique. Comme champ d'étude au CIBM, la spectroscopie RMN peut être utilisée de façon non invasive pour explorer le devenir métabolique des substrats énergétiques tout autant que la vitesse à laquelle ils sont consommés, en utilisant les noyaux ^{13}C and ^{1}H. Le travail de cette thèse inclut les deux noyaux, et se focalise (1) sur l'amélioration de la quantification et de la modélisation des métabolites dérivés du glucose ; et (2) sur la caractérisation des paramètres liés à la diffusion de l'acétate, substrat énergétique supposé spécifique aux cellules gliales, dans le but d'explorer quantitativement le métabolisme énergétique cérébral, à très haut champ magnétique, *in vivo*, dans le rat sain.

La spectroscopie RMN du carbone 13 permet de mesurer l'incorporation progressive de glucose-^{13}C dans le glucose cérébral, puis dans les acides aminés détectables par NMR (glutamate et glutamine) ; ceci repose sur l'infusion de substrats énergétiques marqués au ^{13}C. Les courbes expérimentales de marquage ^{13}C sont analysées avec un modèle mathématique adapté pour estimer les taux métaboliques cérébraux. Un modèle dynamique temporel des multiplets ^{13}C provenant des isotopomères a été considéré. En plus du modèle à deux compartiments neuronal-glial, des données additionnelles sur la dynamique des isotopomères, disponibles grâce aux multiplets de structure fine des spectres ^{13}C du glutamate et glutamine mesurés lors d'une infusion prolongée de [1-6,^{13}C] glucose, ont été prises en compte. Nous concluons que les analyses dynamiques des multiplets ^{13}C du glutamate et glutamine permettent une plus haute précision dans l'estimation des valeurs absolues de la plupart des taux métaboliques cérébraux.

Le métabolisme de l'acétate est complexe à étudier, car un modèle métabolique dynamique requiert des connaissances préalables sur la cinétique du transport et de l'absorption de l'acétate infusé. Cette information a été recherchée en déterminant la concentration apparente et le volume de distribution (V_d) de l'acétate cérébrale entre les compartiments intra et extracellulaires. Les caractéristiques de diffusion de l'acétate cérébral ont été mesurées expérimentalement, relativement à celles de l'acide *N*-acétylaspartique (NAA, connu pour être principalement intracellulaire) en utilisant la spectroscopie RMN ^{1}H pondérée en diffusion à 14.1T, sous infusion prolongée d'acétate. La détection de signaux d'acétate et de NAA avec une pondération large en diffusion a apporté des preuves expérimentales évidentes d'acétate et de NAA intracellulaire, bien qu'une fraction substantielle d'acétate soit extracellulaire. Pour estimer la concentration apparente d'aspartate cérébral *in vivo*, les temps de relaxation T_1 et T_2 de l'acétate ont été mesurés. Un plus long T_1 et un plus court T_2 de l'acétate apportent des preuves de sa petite taille moléculaire, et d'un possible environnement chimique différent. Nos valeurs expérimentales de V_d mènent à des taux métaboliques cérébraux d'acétate (CMR acétate) du même ordre de grandeur que ceux rapportés pour le taux du cycle de Krebs glial, indiquant que le CMR acétate est hautement dépendant de V_d.

Finalement, afin de poursuivre la cartographie métabolique de la consommation d'acétate cérébral dans le rat *in vivo* à 14.1T, la conception et la construction d'une antenne combinée birdcage en transmission et paire d'antenne de surface en quadrature en réception ont été considérées. Sa performance a été comparée à une antenne birdcage en transmission et réception. Les résultats préliminaires de la configuration à deux antennes sont prometteurs : une excitation homogène et un gain en sensitivité jusqu'à une distance de 5 mm sont atteints. Des améliorations sont en cours pour des applications de spectroscopie NMR et d'imagerie à 14.1T.

Mots clés: Métabolisme énergétique cérébral, les spectres de RMN ^{13}C, la spectroscopie pondérée en diffusion, le volume physique de distribution, le taux métabolique, le cycle de Krebs, les temps de relaxations T_1 et T_2, la cinétique du transport et de l'absorption de l'acétate, l'antenne de surface, birdcage antenne.

Contents

Outline of thesis

In its simplest form, nuclear magnetic resonance (NMR) is the absorption of electromagnetic radiation at a specific resonance frequency by an atomic nucleus, as a result of being placed in a strong external static magnetic field, and the generation of an oscillating magnetic field detected by an NMR probe. If the atomic nucleus within the sample is rich in either H or C, as it is in biological tissues, and if the living subject is administered the isotopic forms ^{1}H and ^{13}C linked to glucose, then NMR enables following the metabolic fate of this important energy substrate through major biochemical pathways in the living brain in situ.

In **Chapter 1,** I will briefly describe what nuclear magnetic resonance is, and the challenges of implementing this technique to the living brain. In this regards, I will introduce a specific part of brain energy metabolism, and the glutamate glutamine cycle. This cycle is essential to overall brain function; it provides an adequate supply of the major excitatory neurotransmitter glutamate during cerebral synaptic neurotransmission; and it involves the orchestrated metabolism between neurons and glial cells, the brain's two major cell types. From the viewpoint of NMR, I will talk about how the magnetization of ^{13}C nuclei, following the infusion of ^{13}C-labelled energy substrates, e.g. glucose, enables one to follow and quantify this glutamate-glutamine cycle in the central nervous system using ^{13}C magnetic resonance spectroscopy (MRS). Strengths and inherent weaknesses of MRS in the field of brain energy metabolism are presented, in parallel with the use of mathematical models and simulations that enable analyses and interpretations of the data. Finally, I describe how I newly extended the concept of dynamic bonded cumulative isotopomers, or simply, dynamic bonded cumomers, as a suitable approach to optimize the *in vivo* metabolic fluxes of the brain's major neuronal excitatory neuro transmitter glutamate (glu) and its glial precursor glutamine (gln) with high temporal resolution. In that particular study I implemented a two compartment neuronal-glial model and the use of existing *in vivo* NMR data.

In **Chapter 2**, the dynamic bonded cumomer approach which take into account spin-spin coupling of covalently bonded labeled carbon atoms, is experimentally applied in the rat brain *in vivo*: here, the two-compartment neuronal/glial model is extended to include the dynamics of ^{13}C isotopomers available from the fine structure multiplets in ^{13}C spectra of brain glutamate and glutamine from rats under infusion of [1, 6-^{13}C$_2$]-glucose at 14.1T. We began with glucose, as it is the principle energy substrate for both neurons and glial cells of the brain; glucose first enters into metabolism via glycolysis. Then, the glucose-derived metabolites enter into the Krebs TCA cycle. The notable improvements in the precision of the experimentally obtained metabolic parameters, as a result of implementing the bonded cumomer approach, are discussed and then compared to the conventional metabolic modeling approaches.

In **Chapter 3**, I introduce acetate, a purportedly glial-specific energy substrate of the Krebs cycle. We discuss the beauty of this substrate in simplifying modeling, while increasing the sensitivity of the glutamate/glutamine measurements. However, we also identify parameters of acetate within the brain, which have yet to be established, and which are necessary to know a priori, if we are to take full advantage of the dynamic bonded cumomer approach. These unknowns are the distribution volume of acetate, and the transport and uptake kinetics of acetate. This chapter addresses how I implemented localized, non-invasive ^{1}H NMR spectroscopy using a diffusion weighted-STEAM sequence at 14.1T to estimate the relative contributions of acetate in the intracellular and extracellular compartments of the rat brain, *in vivo*.

In **Chapter 4**, I discuss how prior knowledge of transport and uptake kinetics of acetate are dependent on the time course of the apparent acetate concentration in brain and plasma, which in turn can be sought from measuring the T_1 and T_2 relaxation times of acetate *in vivo*. This led me to experimentally perform such measurements in the rat brain *in vivo* at 14.1T during prolonged Ace infusion of the animal. In that study, which I describe in detail, we not only determined the kinetics of transport and utilization of acetate; we were able to more accurately estimate the apparent concentration of acetate.

Finally, in **Chapter 5**, we begin to come full circle on the glutamate-glutamine cycle. Metabolic mapping of acetate uptake in the brain of living animals may provide new insights into the kinetics of acetate uptake, and open the way to further dynamic metabolic modeling of brain metabolite time courses obtained during labeled acetate infusions. This approach depends critically on the coil characteristics of the NMR probe. Towards this objective, I describe a transmit-high pass birdcage coil and a receive-quadrature pair surface coil that I constructed and tested for experiments performed at 14.1T, and which takes advantage of a uniform excitation from a whole birdcage coil combined with the improved detection sensitivity of the surface coil. This chapter concludes with a working evaluation of the probe, both on the bench and at 14.1T, as well as a discussion of the issues faced by the design of a separate coil for transmit and receive.

Chapter 1. An introduction to nuclear magnetic resonance

Nuclear magnetic resonance spectroscopy (MRS) has become a dominant analytical method by which the physical, chemical, and biological properties of living matter can be quantified. MRS performed at high magnetic fields has enabled studying brain metabolism *in vivo* in laboratory animals.

During the course of my PhD thesis, I've come to appreciate the fact that the process towards reaching an experimental result is just as important as the result itself. For this reason, Chapter 1 provides a general background for each of the subsequent chapters, all of which touch upon some aspect of nuclear magnetic resonance spectroscopy. I will begin the story with a quantum mechanical treatment to describe the intrinsic properties of atomic nuclei, in general, and how they might interact with an electromagnetic field. Then, a semi-classical approach will be used to describe spin magnetization of atomic nuclei under an applied external magnetic field. Thereafter, I will discuss how the interaction between atomic nuclei and magnetic fields are used to generate spectra, and what a typical spectrum contains in the way of information. Afterwards, I will place the MRS measurements within a broader context with regards to software and hardware. Finally, two aspects of MRS will be presented: (1) diffusion-weighted spectroscopy; and (2) ^{13}C spectroscopy; and I will describe how they are valuable approaches to better understanding, respectively, the diffusion characteristics of a selected molecule in question; and metabolic interactions between neurons and glial cells.

1.1. The Physics of NMR

In its simplest form, nuclear magnetic resonance (NMR) is the absorption and emission of electromagnetic radiation at a specific resonance frequency by an atomic nucleus, as a result of being placed in a strong external static magnetic field and an oscillating magnetic field. If the atomic nucleus within the sample is rich in H or C, as it is in biological tissues, and if the living subject is administered the isotopic forms ^{13}C or ^{1}H linked to substrate, then NMR enables following the metabolic fate of energy substrate through major biochemical pathways in the living brain in situ.

1.1.1. Nuclear spin

NMR relies on the intrinsic property of nuclei, spin angular momentum. Spin angular momentum is characterized by a nuclear spin angular momentum quantum number, I. For example, values of I are equal to zero when nuclei possess an even mass number (A) and an even atomic number (Z), (e.g. ^{16}O); likewise, nuclei with an even A and an odd Z have integer I (e.g. $I = 1$ for ^{2}H); and finally nuclei with an odd A and an odd or even Z possess half integer I (e.g. ^{13}C or ^{15}N).

I is directly related to the nuclear spin angular momentum vector $\vec{L}$ (Pauli, 1924), whose magnitude is given by:

$$L = (\frac{h}{2\pi})\sqrt{I\,(I+1)}$$
<div align="right">Eq. 1.1</div>

Where h is the Planck's constant. $\vec{L}$ has certain quantized projections with respect to a given direction and is specified by a quantum number m, which can take on discrete values of $2I+1$. The projection of $\vec{L}$ in the conventional z-direction is:

$$L_z = (\frac{h}{2\pi})m \quad , \quad m = I, I-1, I-2, \dots -I$$
<div align="right">Eq. 1.2</div>

For protons, neutrons and electrons, the spin quantum number I equals ½, and so spin angular momentums L_z, can have two values $(\frac{h}{4\pi})$ or $(-\frac{h}{4\pi})$.

Although the classical model of charged particles is incorrect, imagine the nucleus as a small particle with electrical charge e and mass m that is spinning around its own axis and thus representing an electric current. Due to this current, the atomic nucleus behaves as a small electromagnet. The magnetic moment $\vec{\mu}$ is related to the angular momentum of the nucleus as:

$$\vec{\mu} = \left(\frac{e}{2m}\right)\vec{L} = \gamma\vec{L}$$
<div align="right">Eq. 1.3</div>

Where γ is characteristic of each isotope and is called the gyromagnetic ratio of a nuclear spin. The sensitivity of a nucleus in NMR depends on γ (high γ, high sensitivity). Nuclei with a zero spin number are invisible by NMR and nuclei with $I > 1/2$ have an electrical quadrupole moment interfering with their $\vec{\mu}$. Consequently nuclei with spin $1/2$ are more frequently considered in NMR studies, with their two distinctive states for orientation of spin angular momentum.

1.1.2. The resonance phenomenon

When a magnetic field $\vec{B}_0$ is applied (Fig 1.1), spins become field aligned or field opposed and the atomic energy levels are split into a few levels and the spectral lines are also split (Zeeman effect). Due to the interaction of the nuclear magnetic moment $\vec{\mu}$ with the magnetic field $\vec{B}_0$, the splitting occurs and the energy of the nuclei slightly shifts by an amount of:

$$E = -\vec{\mu}.\vec{B}_0$$
<div align="right">Eq. 1.4</div>

This energy shift depends on the relative orientation of the $\vec{\mu}$ and $\vec{B}_0$ (Fig 1.1). The angle θ between $\vec{\mu}$ and $\vec{B}_0$ is given by:

$$cos\theta = \frac{m}{\sqrt{I(I+1)}}$$
<div align="right">Eq. 1.5</div>

For nuclei with spin ½ two energy levels exist according to a parallel (m = 1/2) or antiparallel (m = −1/2) orientation of the magnetic moment $\vec{\mu}$ with respect to the $\vec{B}_0$, and spins are distributed on the surface of two cones which make an angle of $\theta = 54.74^0$ with respect to the axis of $\vec{B}_0$ direction (Fig 1.1).

The energy of the spin ½ placed in a magnetic field $\vec{B}_0$ in the z direction (by convention) can be calculated using Eq. 1.2 and Eq. 1.3:

$$E = -\mu_z B_o = -\gamma\left(\frac{h}{2\pi}\right)mB_0$$
<div align="right">Eq. 1.6</div>
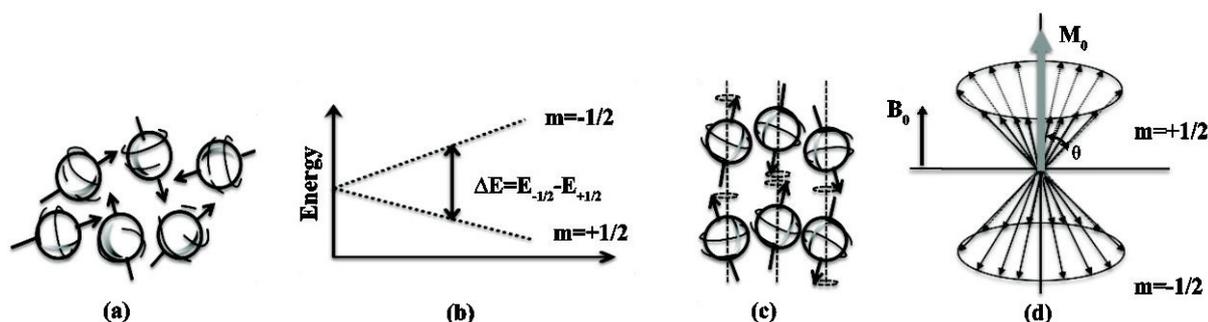
Fig 1.1 Semi-classical representation of spin magnetization in an external field: (a) Nuclear spin typical of nuclei with spin number ½. In the absence of an external magnetic field, the spins are randomly oriented and precessing around their individual magnetic moment $\vec{\mu}$, (b) in the presence of an external magnetic field $\vec{B}_0$, the interaction between $\vec{\mu}$ and $\vec{B}_0$ results in the splitting of the nuclei energy, (c) nuclei line up parallel to $\vec{B}_0$, either spin aligned or spin opposed, and (d) form two precessing cones about their $\vec{\mu}$ and $\vec{B}_0$ axes.

The magnetic moment of nucleus precesses around $\vec{B}_0$ with the Larmor frequency v_0. Larmor frequency is proportional to the energy difference between the two energy levels of the spin ½.

$$v_0 = \frac{\Delta E}{h} = -\left(\frac{\gamma}{2\pi}\right)B_0 \qquad \text{Eq. 1.7}$$

v_0 depends on the gyromagnetic ratio and the strength of the static magnetic field. At a magnetic field of 14.1 T used in thesis project, the Larmor frequency of carbon nuclei and proton is 150 and 600 MHz, respectively.

1.1.3. Spin population and equilibrium magnetization

An NMR sample contains many identical molecules and their spins align independently of each other, parallel (m = 1/2) or antiparallel (m = −1/2) relative to the axis of the external field $\vec{B}_0$. Within $\vec{B}_0$, there is slight tendency for more spins to align parallel with $\vec{B}_0$ axis.

The ratio of antiparallel spins to the parallel ones is given by the Boltzmann distribution:

$$\left(\frac{n_{m=-1/2}}{n_{m=+1/2}}\right) = e^{-\frac{\Delta E}{KT}} = e^{-\frac{hv}{KT}} \qquad \text{Eq. 1.8}$$

where K is the Boltzmann constant (1.38×10^{-23} m^2 kg s^{-2} K^{-1}) and T is the absolute temperature (in Kelvin) of the sample. The amplitude of the received signal in NMR is proportional to the difference in population of spins in the two energy levels. Both energy levels are nearly equally populated at room or body temperatures. For example, the ratio of spin populations between the two spin states of proton (the hydrogen nucleus) in a magnetic field of 14T at 37°C is close to 1, $n_{m=-\frac{1}{2}}/n_{m=+\frac{1}{2}} = 0.99991$.

This is the main reason for the inherently low sensitivity of NMR when compared to other spectroscopy methods. The magnetic moments of the individual spins ($\vec{\mu}_i$) sum up to a macroscopic magnetization $\vec{M}_0$ that can be estimated according to Curie's law:

$$\vec{M}_0 = \sum_{i=1}^{N} \vec{\mu}_i = N.v_0{}^2.\left(\frac{h}{2\pi}\right)^2.\vec{B}_0.\frac{I.(I+1)}{3KT} \qquad \text{Eq. 1.9}$$

where N is the total number of spins in the sample. In thermal equilibrium, only magnetization along the z-axis of the static magnetic field exists because the x and y components sum up to zero (Fig 1.1).

1.1.4. Motion of magnetization under external magnetic fields

When nuclei are placed in a magnetic field $\vec{B}_0$, the torque ($\vec{\tau}$), produced by the interaction of $\vec{B}_0$ and $\vec{\mu}$, changes the angular momentum of $\vec{L}$ as a function of time and causes precession of the nuclear spins. The torque on the bulk magnetization is given by:

$$\vec{\tau} = \frac{dL}{dt} = \vec{M}(t) \times \vec{B}_0 \qquad \text{Eq. 1.10}$$

According to equation (Eq. 1.3), the temporal changes of bulk magnetization is described by:

$$\frac{d\vec{M}(t)}{dt} = \gamma\left(\vec{M}(t) \times \vec{B}_0\right) = \hat{\imath}\gamma M_y(t)B_o - \hat{\jmath}\gamma M_x(t)B_o \qquad \text{Eq. 1.11}$$

Where $\hat{\imath}$ and $\hat{\jmath}$ are the unit vectors along the x and y.

$$\frac{dM_x(t)}{dt} = \gamma M_y(t)B_o, \qquad \frac{dM_y(t)}{dt} = -\gamma M_x(t)B_o, \qquad and \quad \frac{dM_z(t)}{dt} = 0 \qquad \text{Eq. 1.12}$$

The above Bloch equations (Bloch et al., 1946) describe the time dependence of the magnetization components under the effect of a static magnetic field without considering any relaxation effect. Therefore the z component of $\vec{M}$ is independent of time and the x and y component of $\vec{M}$ are oscillating as a function of time.

The observable NMR signals are the time dependent transverse magnetization. As mentioned in part 1.1.3), at equilibrium the x and y components of $\vec{M}$ sum to zero due to the random distribution of the transverse component of the underlying nuclear spins. The solution is to apply a torque on $\vec{M}$ by a radio frequency (RF) field $\vec{B}_{rf}$ and flip the z component of the magnetization $\vec{M}$ to the transverse plane. The requirement for this condition is that the radio frequency field $\vec{B}_{rf}$ should be perpendicular to field $\vec{B}_0$ and oscillating at the frequency that matches the Larmor frequency of the considered nuclei in $\vec{B}_0$ field. This results in a rotation of $\vec{M}_0$ towards the transverse plane and a simultaneous precession at the Larmor frequency about $\vec{B}_0$, called excitation. When $\vec{B}_{rf}$ is turned off, the generated transverse component of $\vec{M}_0$ is precessing about the $\vec{B}_0$ while decaying back to the initial state (z -axis) under interaction with $\vec{B}_0$ field. The decay of the transverse component of $\vec{M}_0$ in the xy plane is called the free induction decay (FID), forms the observable NMR signal detected by the receiver (Fig 1.2).

In the laboratory frame, an RF field can be generated by a linearly polarized magnetic field applied in the xy plane rotating about z-axis at a carrier frequency of ω_{rf}:

$$\vec{B}_{rf}(t) = 2B_1 \cos(\omega_{rf}t + \varphi)\,\hat{\imath} \qquad \text{Eq. 1.13}$$

The RF field is defined by the amplitude B_1 and the phase φ. $\vec{B}_{rf}(t)$ can be decomposed in two circularly polarized fields rotating in opposite directions about the z-axis as following:

$$\vec{B}_{rf}(t) = B_1\{\cos(\omega_{rf}t + \varphi)\,\hat{\imath} + \sin(\omega_{rf}t + \varphi)\,\hat{\jmath}\} \qquad \text{Eq. 1.14}$$
$$+ B_1\{\cos(\omega_{rf}t + \varphi)\,\hat{\imath} - \sin(\omega_{rf}t + \varphi)\,\hat{\jmath}\}$$

where $\hat{\imath}$ and $\hat{\jmath}$ are unit vectors in the x and y directions, respectively. Only the field rotating in the same direction as the magnetic moment $\vec{M}_0$ interacts significantly with the magnetic moment. The field rotating in the opposite direction of $\vec{\omega}_o$ has a small influence on the order of $(B_1/2B_0)^2$ which can be ignored (Bloch and Siegert, 1940). Thus the RF field simplifies to:
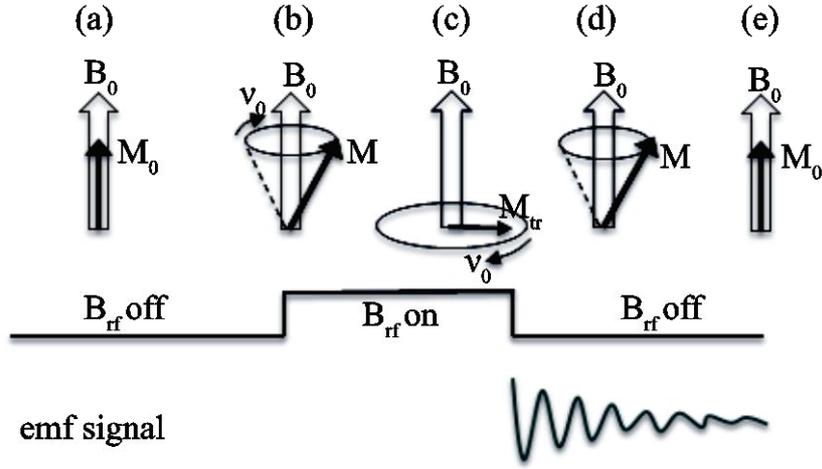
Fig 1.2 (a) Macroscopic sum of magnetic moments $\vec{M}$ is aligned in direction $\vec{B}_0$, (b) magnetization $\vec{M}$ is tilted towards transverse plane using RF field $\vec{B}_{rf}$ which is orthogonal to $\vec{B}_0$, (c) generated transverse magnetization is rotating about $\vec{B}_0$, (d) when $\vec{B}_{rf}$ is turned off, FID is detected by the receiver while transverse magnetization is decaying due of relaxation effects, and (e) all magnetization $\vec{M}$ is turned back to the initial thermal equilibrium in direction of $\vec{B}_0$.

$$\vec{B}_{rf}(t) = B_1\{\cos(\omega_{rf}t + \varphi)\,\hat{\imath} - \sin(\omega_{rf}t + \varphi)\,\hat{\jmath}\} \qquad \text{Eq. 1.15}$$
$$= B_{1x}(t)\hat{\imath} + B_{1y}(t)\hat{\jmath}$$

The Bloch equation (Eq. 1.11) can be extended to cover simultaneously the effect of $\vec{B}_{rf}$ and $\vec{B}_0$ on time variation of the magnetic moment.

$$\frac{d\vec{M}(t)}{dt} = \gamma\big(\vec{M}(t) \times (\vec{B}_0 + \vec{B}_{rf}(t))\big) \qquad \text{Eq. 1.16}$$

Because two external fields $\vec{B}_0$ and $\vec{B}_{rf}$ act simultaneously on $\vec{M}$, the motion of $\vec{M}$ in a Cartesian frame fixed respect to the laboratory, i.e. laboratory frame, becomes very complicated (Fig 1.3.a). To simplify the rotation of $\vec{M}$ under the effect of several external magnetic fields, the concept of rotating frame is introduced. In a rotating frame, a new set of axis x', y', and z' are rotating about the static magnetic field $\vec{B}_0$ with the frequency that matches the frequency of RF field (ω_{rf}). The z′-axis of the rotating frame is collinear with the z-axis of the laboratory frame. To summarize, the coordinates of $\vec{M}$ in the rotating frame ($\vec{M}'$) are given by:

$$M'_x = M_x \cos \omega_{rf}t + M_y \sin \omega_{rf}t \qquad \text{Eq. 1.17}$$

$$M'_y = M_y \cos \omega_{rf}t - M_x \sin \omega_{rf}t \qquad \text{Eq. 1.18}$$

$$M'_z = M_z \qquad \text{Eq. 1.19}$$

There are three interesting features in describing NMR in a rotating frame. First, the effect of the main field $\vec{B}_0$ has disappeared; second, the $\vec{B}_{rf}$ field is no longer rotating but appears static; and third, $\vec{M}'$ has begun a new precession around $\vec{B}_{rf}$.

The Bloch equations can be written in the rotating frame, which is related to their form in the laboratory frame in Eq. 1.12 according to the following relationship:

a. Laboratory frame   b. Rotational frame
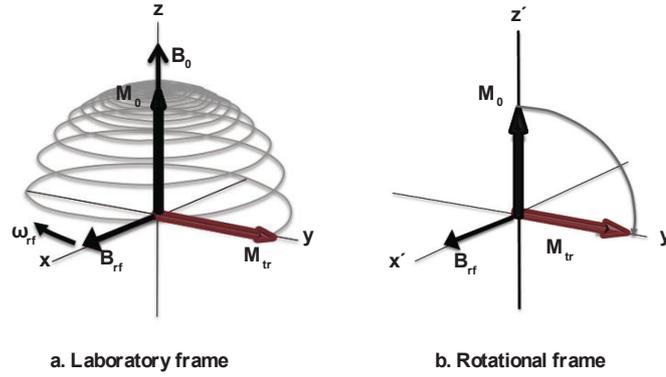
Fig 1.3 Vector model representation of an excitation experiment using radiofrequency field $\vec{B}_{rf}$. $\vec{B}_{rf}$ is perpendicular to $\vec{B}_0$ field and oscillating at the frequency $\vec{\omega}_{rf}$ equal to the Larmor frequency $\vec{\omega}_0$ of the bulk magnetization $\vec{M}_0$. (a) Laboratory frame: the magnetization along the z-axis is flipped in spiral path to the y-axis by a $\vec{B}_{rf}$ field along the x-axis. (b) Rotating frame: rotation of new frame matches the Larmor frequency $\vec{\omega}_0$, the magnetization appears stationary relative to z-axis and is rotating about $\vec{B}_{rf}$.

$$\left(\frac{d\vec{M}(t)}{dt}\right)' = \left(\frac{d\vec{M}(t)}{dt}\right)_{lab} + \vec{M}(t) \times \vec{\omega}_{rf} \qquad \text{Eq. 1.20}$$

$$\left(\frac{d\vec{M}(t)}{dt}\right)' = \vec{M}(t) \times \left(\gamma\vec{B}_0 + \vec{\omega}_{rf}\right) \qquad \text{Eq. 1.21}$$

where $\vec{\omega}_{rf}$ is the angular frequency of the rotating frame. When $\vec{\omega}_{rf}$ matches the larmor frequency $\vec{\omega}_0 = -\gamma\vec{B}_0$, the magnetization is stationary in the rotating frame in the absence of $\vec{B}_{rf}(t)$.

In the presence of RF field $\vec{B}_{rf}(t)$, the Bloch equation Eq. 1.21 will be extended as following:

$$\left(\frac{d\vec{M}(t)}{dt}\right)' = \vec{M}(t) \times \gamma\left(\vec{B}_{rf}(t) + \vec{B}_0 + \frac{\vec{\omega}_{rf}}{\gamma}\right) \qquad \text{Eq. 1.22}$$

$$\left(\frac{d\vec{M}(t)}{dt}\right)' = \vec{M}(t) \times \gamma\left(\vec{B}_{eff}(t)\right) \qquad \text{Eq. 1.23}$$

$$B_{eff}(t) = \left|\vec{B}_{eff}(t)\right| = \sqrt{\vec{B}_{rf}(t)^2 + \left(\frac{\vec{\omega}_{rf} - \vec{\omega}_0}{\gamma}\right)^2} \qquad \text{Eq. 1.24}$$

$$\Delta B_0 = -\frac{(\omega_0 - \omega_{rf})}{\gamma} = -\frac{\Omega}{\gamma} \qquad \text{Eq. 1.25}$$

where Ω is known as the offset and ΔB_0 is the reduced static field that is equivalent to the z-component of the effective field.

In case of on-resonance condition, i.e. $\vec{\omega}_{rf} = \vec{\omega}_0$, the effective magnetic field $\vec{B}_{eff}$ is reduced to $\vec{B}_{rf}$ and the magnetization simply rotates about $\vec{B}_{rf}$ at precession velocity $\vec{\omega}_{rf}$. In case of an off-resonance situation, $\vec{B}_{eff}$ is tilted from the transverse plane and the magnetization will precess about $\vec{B}_{eff}$, leading to a more complex rotation compared with on-resonance situation. The angle α through which the effective field is tilted relative to the z-axis is defined by:

$$tan\alpha = \frac{B_{rf}}{\Delta B_0} = -\frac{\gamma B_{rf}}{\Omega} = \frac{\omega_{rf}}{\Omega}$$

<div align="right">Eq. 1.26</div>

Bloch equations for individual components of $\vec{M}'$ in direction of x', y', and z' can be written as:

$$\frac{\partial}{\partial t}\begin{pmatrix} M'_x \\ M'_y \\ M'_z \end{pmatrix} = \gamma \begin{pmatrix} M'_x \\ M'_y \\ M'_z \end{pmatrix} \times \begin{pmatrix} B'_{rfx} \\ B'_{rfy} \\ B_0 + \frac{\omega_{rf}}{\gamma} \end{pmatrix}$$

<div align="right">Eq. 1.27</div>

1.1.5. Relaxation of nuclear magnetization

Relaxation is the process of returning a perturbed spin population from a non-equilibrium state to an equilibrium state. After perturbation applied by B_{rf}, the transverse components (i.e. M_x and M_y) and the longitudinal component (i.e. M_z) relax with different time constant.

The decay constant for the recovery of the longitudinal component of the magnetization toward its thermal equilibrium state value is called longitudinal relaxation (Fig 1.4.a) and characterized by T_1.

<div align="right">Eq. 1.28</div>

$$M_z(t) = M_{z,0}(1 - e^{-\frac{t}{T_1}})$$

Since longitudinal relaxation involves transferring energy from spins to the surrounding lattice, T_1 is also referred as spin-lattice relaxation. T_1 values are relatively long (around seconds) due to the lack of means to transfer energy of NMR transitions into the thermal energy. Few requirements should be met to transfer energy from spin to lattice or vice versa. First, motion in the lattice causes a fluctuating magnetic field at the site of the nuclear spin, second, the local fluctuating field should have a component at the Larmor frequency of the nucleus and third, only the transverse component of the local field can cause T_1-relaxation. The most common source of the local fluctuating magnetic field for spin ½ nuclei is direct dipolar interaction. In the liquid state, the rapid orientation of the dipolar interaction due to molecular motions provides fluctuating fields and thus T_1 is temperature-dependent.
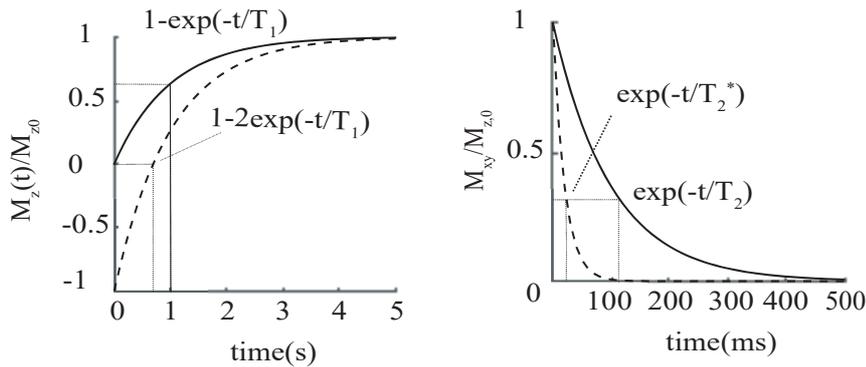
Fig 1.4 Illustration of relaxation times for spin 1/2 with T_1=1 s, T_2=100 ms and T_2^*=20 ms. (a) Recovery of longitudinal magnetization M_z towards its thermal equilibrium $M_{z,0}$ via T_1 relaxation. After a 90° excitation pulse (solid line) M_z recover to 63% of $M_{z,0}$ after one time constant T_1. After a 180° excitation pulse (dashed line), magnetization is nulled at t = ln(2)T_1, (b) Decaying transverse magnetization M_{xy} after a 90° excitation pulse. The M_{xy} drops to 37% of its initial magnitude after one time of T_2. The T_2^* relaxation of M_{xy} is faster than T_2 duration.

The relationship between T_1 and the molecular motion can be expressed generally as:

$$\frac{1}{T_1} \propto \gamma^2 \overline{H^2} \frac{\tau_c}{1 + (2\pi\nu_0\tau_c)^2}$$

Eq. 1.29

Where $\overline{H^2}$ is the mean square average of the local magnetic fields and the τ_c is the correlation time, i.e. a measure of the rate of a molecular motion.

The spin-lattice relaxation time determines what recycle delay between consecutive pulses trains should be considered. In spectroscopy, the magnetization must be allowed to relax back mostly to equilibrium before the next pulse is applied and this time period is determined by T_1.

Relaxation of transverse component at its most fundamental level corresponds to de-coherence of the transverse nuclear spin magnetization (Fig 1.4.b) and is characterized by T_2^*.

$$M_{xy}(t) = M_{xy,0}\, e^{-\frac{t}{T_2^*}}$$

Eq. 1.30

Random fluctuation of the local magnetic field experienced by spins leads to random variation in the instantaneous NMR precession frequency of different spins. Consequently the initial phase coherence of the individual nuclear spins in the macroscopic magnetization is lost, and results in net transverse magnetization decay.

The transverse relaxation includes the relaxation due to the static magnetic field inhomogeneities, $T_{\Delta B_z}$, and the inherent relaxation due to spin-spin interactions, T_2. To summarize:

$$\frac{1}{T_2^*} = \frac{1}{T_{\Delta B_z}} + \frac{1}{T_2}$$

Eq. 1.31

The random local fluctuating magnetic fields leading to spin-lattice relaxation T_1 are also necessary for spin-spin relaxation T_2. The T_2 relaxations can be defined generally as follow:

$$\frac{1}{T_2} \propto \gamma^2 \overline{H^2}(\tau_c + \frac{\tau_c}{1 + (2\pi\nu_0\tau_c)^2})$$

Eq. 1.32

The frequency term in equations Eq. 1.29 and Eq. 1.32 expresses the possible dependency of T_1 and T_2 to the magnetic field $\vec{B}_0$. T_1 and T_2 relaxation times are very long compared to the period of precession of the nuclei, typically on the range of second for T_1 and millisecond for T_2 and a few tens of nanosecond for the precession period.

The T_1 and T_2^* relaxation processes can be taken into account in the equation of motion of the magnetization and yields the Bloch equations (without diffusion term) in the laboratory frame:

$$\frac{\partial}{\partial t}\begin{pmatrix} M_x \\ M_y \\ M_z \end{pmatrix} = \gamma \begin{pmatrix} M_x \\ M_y \\ M_z \end{pmatrix} \times \begin{pmatrix} B_{rfx} \\ B_{rfy} \\ B_0 \end{pmatrix} - \begin{pmatrix} \dfrac{M_x}{T_2^*} \\ \dfrac{M_y}{T_2^*} \\ \dfrac{(M_z(t) - M_{z,0}(t))}{T_1} \end{pmatrix}$$

Eq. 1.33

And in the rotating frame:

$$\frac{\partial}{\partial t}\begin{pmatrix} M_x' \\ M_y' \\ M_z' \end{pmatrix} = \gamma \begin{pmatrix} M_x' \\ M_y' \\ M_z' \end{pmatrix} \times \begin{pmatrix} B_{rfx}' \\ B_{rfy}' \\ B_0 + \dfrac{\omega_{rf}}{\gamma} \end{pmatrix} - \begin{pmatrix} \dfrac{M_x'}{T_2} \\ \dfrac{M_y'}{T_2} \\ \dfrac{M_z'(t) - M_{z,0}(t)}{T_1} \end{pmatrix}$$

Eq. 1.34

1.1.6. Signal detection

Signal detection in NMR is based on the physics phenomenon of induction, first described by Faraday in 1831, which states that a time-varying magnetic flux within a conductive loop or coil will cause a voltage to be induced across the wire of the coil.

When applying an RF pulse with magnetic field amplitude of $\vec{B}_1$ and a frequency of ω_0, the bulk magnetization of spins aligned longitudinally with $\vec{B}_0$ is rotated towards the transverse plane. The generated transverse magnetization M_{xy} is precessing about the $\vec{B}_0$ at a Larmor frequency ω_0 and induces an oscillating electromotive force (emf) in the receive coil, typically positioned in the transverse plane (see part 1.1.10).

As mentioned in section 1.2.5, the T_2^* relaxation of the magnetization leads to a loss of the transverse component, and thereby decreases the induced electromotive force (emf) as a function of time. The characteristic decay of the magnetization transverse component is called free induction decay or FID. Thus, the NMR signal contains a sets of sine and cosine waves components measured as a function of time and decaying at a rate of T_2^*.

$$S_{NMR}(t) \propto M_{xy}(t) = M_0.e^{i\varphi}e^{\frac{-t}{T_2^*}}$$
<div align="right">Eq. 1.35</div>

Where φ is the phase of the magnetization in the xy plane at $t = 0$, and M_0 is the equilibrium magnetization. This time varying signal is recorded in the time domain using an analogue to digital converter. Fourier transformation of the FID yields the frequency domain signal, which we know as the spectrum:

$$F(\omega) = \int_0^t S_{NMR}(t')e^{-i\omega t}\, dt'$$
<div align="right">Eq. 1.36</div>

$$F(\omega) = (A(\omega) + i\, D(\omega))e^{i\varphi}$$
<div align="right">Eq. 1.37</div>

$$A(\omega) + i\, D(\omega) = \frac{M_0\, T_2^*}{1 + (\omega_0 - \omega)^2 T_2^{*2}} + i\, \frac{M_0(\omega_0 - \omega)T_2^*}{1 + (\omega_0 - \omega)^2 T_2^{*2}}$$
<div align="right">Eq. 1.38</div>

$A(\omega)$ and $D(\omega)$ are referred as the absorption and dispersion mode of the spectra. Absorption and dispersion modes contain the same frequency data but with different combination of phase and amplitude. When the magnetization is properly flipped onto the axes orthogonal to the $\vec{B}_0$ and $\vec{B}_1$ fields ($\varphi = 0$), the real and imaginary parts of the spectrum are a representation of the absorption and dispersion mode, respectively. The data is generally displayed in the absorption mode, which has a Lorentzian shape in case of $\varphi = 0$. The width at half maximum height of the absorption line shape is given by $1/\pi T_2^*$. So, a faster decay of the FID yields a broader line in the way that the area under the line remains constant. As a consequence, the area under the line approximates the relative number of spins contributing to the signal.

In some situations, the position of the nuclei generating the signal might induce a phase shift at time zero and leads to a situation in which the real part of the spectrum does not show a pure absorption line shape. The solution for this is to multiply the FID or Fourier transform of FID by $e^{i\varphi_0}$ where $\varphi_0 = -\varphi$. Such a correction is referred to as a frequency independent or zero order phase correction. If the phase shift is frequency-dependent, lines at different offsets in the spectrum will have different phase errors, with the error increasing as the offset increases. In this respect, it is necessary to perform a linear, first order phase correction given by $(\omega_0 - \omega).\varphi_1$. Thus, total phase correction will be as:

$$\varphi_{corr} = \varphi_0 + (\omega_0 - \omega).\varphi_1$$
<div align="right">Eq. 1.39</div>

1.1.7. Chemical shift

As noted by Cavanaugh and Dailey, 1961 the difference between the observed and predicted resonance frequencies (called the chemical shift) is attributed to the local environment of individual nuclei. By local environment, the effect of nearby nuclei within the same molecule and absorption of energy at different resonance frequencies are taken into account (Dickinson, 1950; Proctor and Yu, 1950). Moreover, the response of electrons (of atoms) to an external magnetic field can produce a small magnetic field at the nuclei, which opposes the external magnetic field. In other words, the presence of electrons surrounding nuclei can constitute an electric shield, called diamagnetic shielding. Consequently, the effective magnetic field experienced by the nuclei is:

$$B = B_0(1 - \sigma)$$
Eq. 1.40

where the σ is referred as shielding (screening) factor. To display the acquired NMR spectrum, in a manner that is independent of the static magnetic field used for the measurement, the concept of chemical shift (δ_{cs}) is used for localizing the spectral peak(s):

$$\delta_{cs} = \frac{(f_s - f_{ref})}{f_{ref}} \times 10^6$$
Eq. 1.41

where f_s and f_{ref} are the frequencies of the sample(s) and reference (ref) in the laboratory frame. Chemical shift is expressed in units of ppm (parts per million). Typically, the reference used in proton spectroscopy is TMS (tetramethyl-sialne [$(CH_3)_4$ Si)]) and its singlet peak is assigned a chemical shift of 0.0 ppm. Contrary to NMR liquid sample spectra, *in vivo* spectra are acquired without a TMS reference and the chemical shift without this reference is defined as:

$$\delta_{cs} = \frac{f_s}{f_{transmitter}} \times 10^6 + offset$$
Eq. 1.42

where f_s is the frequency of sample in the rotating frame and $f_{transmitter}$ is the frequency of the transmitter in the laboratory frame. The offset value is determined by measuring the frequency of the *in vivo* standard and $f_{transmitter}$. In cerebral proton spectroscopy, the *in vivo* standard is typically the CH_3 peak of N-acetyl aspartate (NAA) with a chemical shift value of 2.01 ppm. All spectral frequencies (in Hz) can be converted to ppm based on the determined experimental offset.

1.1.8. Scalar coupling

Scalar J-coupling is a magnetic interaction between individual nuclear spins transmitted by the bonding electrons through which the nuclear spins are indirectly coupled. J-coupling contains information about the electronic structure of the molecule, the connectivity of molecules, as well as bond distance and angles. J-coupling interactions are responsible for the appearance of fine structure of multiplets in spectra of simple molecules. J-coupling interaction has no direct analogy in classical physics, but could be explained in quantum-mechanical description as follows.

We consider a system with two spins S and I in a magnetic field of $\vec{B}_0$ in direction z. For every nuclei with spin value of ½ in a magnetic field of $\vec{B}_0$ (assume z-axis), there are two possible states parallel or antiparallel with magnetic field ($m = \pm 1$), which correspond to wave functions of $|\alpha\rangle$ and $|\beta\rangle$. The wave function of the two non-interacting spin system are simply the Zeeman products of the wave function of individual spins as follow:

$$I: |\alpha\alpha\rangle \quad II: |\alpha\beta\rangle \quad III: |\beta\alpha\rangle \quad IV: |\beta\beta\rangle$$
Eq. 1.43

Therefore the energy level of the two-spin system in the magnetic field $\vec{B}_0$ can be found by solving the

Schrödinger equation:

$$\widehat{H}\psi = E\psi$$

where ψ is the wave function of the two-spin system. The generalized spin Hamiltonian of a system of two interacting spins will be:

$$\widehat{H} = -\gamma_I B_0 \hat{I}_z - \gamma_2 B_0 \hat{S}_z + J\,\hat{I}.\hat{S}$$

The J in third term describes the scalar coupling of spins S and I in the system.
The wave functions of a scalar-coupled two-spins system are as linear combination of the wave function of the two non-interacting spin system.

$$\psi_i = C_{i1}\,|\alpha\alpha\rangle + C_{i2}\,|\alpha\beta\rangle + C_{i3}\,|\beta\alpha\rangle + C_{i4}|\beta\beta\rangle \quad i = 1,2,3,4$$

Then the matrix representation of the spin Hamiltonian in Eq. 1.45 is given by:

$$\widehat{H} = \begin{bmatrix} -\dfrac{\nu_I}{2} - \dfrac{\nu_S}{2} + \dfrac{J}{4} & 0 & 0 & 0 \\[2mm] 0 & -\dfrac{\nu_I}{2} + \dfrac{\nu_S}{2} - \dfrac{J}{4} & \dfrac{J}{2} & 0 \\[2mm] 0 & \dfrac{J}{2} & +\dfrac{\nu_I}{2} + \dfrac{\nu_S}{2} - \dfrac{J}{4} & 0 \\[2mm] 0 & 0 & 0 & +\dfrac{\nu_I}{2} + \dfrac{\nu_S}{2} + \dfrac{J}{4} \end{bmatrix}$$

The off diagonal elements of the matrix describe the mixing of the spin states $|\alpha\beta\rangle$ and $|\beta\alpha\rangle$ originated from the J-coupling between spins. The energy levels of the scalar-coupled two-spin system are the Eigen values of the matrix in Eq. 1.44.

$$\begin{bmatrix} E_1 \\ E_2 \\ E_3 \\ E_4 \end{bmatrix} = \begin{bmatrix} -\dfrac{\nu_I}{2} - \dfrac{\nu_S}{2} + \dfrac{J}{4} \\[2mm] -\dfrac{1}{2}(\nu_I - \nu_S)\sqrt{1+Q} - \dfrac{J}{4} \\[2mm] +\dfrac{1}{2}(\nu_I - \nu_S)\sqrt{1+Q} - \dfrac{J}{4} \\[2mm] +\dfrac{\nu_I}{2} + \dfrac{\nu}{2} + \dfrac{J}{4} \end{bmatrix}$$

where Q describes the deviation of the scalar-coupled two-spin system from the system of two non-interacting spins and is defined as:

$$Q = \left[\dfrac{J}{\nu_I - \nu_S}\right]$$

The energy values and wave functions of two-spin system for two extreme cases of weakly interacting ($Q \ll 1$) and very strong scalar-coupled ($Q \gg 1$) spins are simplified to:

$$Q \ll 1 \qquad \begin{bmatrix} E_1 \\ E_2 \\ E_3 \\ E_4 \end{bmatrix} = \begin{bmatrix} -\dfrac{\nu_I}{2} - \dfrac{\nu_S}{2} + \dfrac{J}{4} \\[1mm] -\dfrac{\nu_I}{2} + \dfrac{\nu_S}{2} - \dfrac{J}{4} \\[1mm] +\dfrac{\nu_I}{2} - \dfrac{\nu_S}{2} - \dfrac{J}{4} \\[1mm] +\dfrac{\nu_I}{2} + \dfrac{\nu_S}{2} + \dfrac{J}{4} \end{bmatrix}, \qquad \begin{bmatrix} \psi_1 \\ \psi_2 \\ \psi_3 \\ \psi_4 \end{bmatrix} = \begin{bmatrix} |\alpha\alpha\rangle \\ |\alpha\beta\rangle \\ |\beta\alpha\rangle \\ |\beta\beta\rangle \end{bmatrix}$$
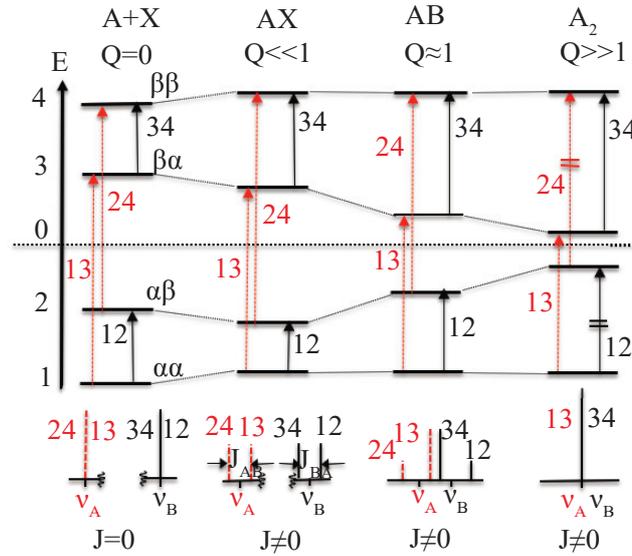
Fig 1.5 Allowed transitions and corresponding spectral lines in two spins system for the scalar coupled $A + X$, AX, AB, A_2. In case of $Q \gg 1$, the intensity for two transitions of 1-2 and 2-4 is zero (Intensity$_{1-3,3-4} \propto \frac{\hbar^2}{4}(1 + f)$, Intensity$_{1-2,2-4} \propto \frac{\hbar^2}{4}(1 - f)$, $f = \sqrt{\frac{Q}{1+Q}}$).

$$Q \gg 1 \quad \begin{bmatrix} E_1 \\ E_2 \\ E_3 \\ E_4 \end{bmatrix} = \begin{bmatrix} -\dfrac{\nu_I}{2} - \dfrac{\nu_S}{2} + \dfrac{J}{4} \\[2mm] -\dfrac{3}{4}J \\[2mm] +\dfrac{1}{4}J \\[2mm] +\dfrac{\nu_I}{2} + \dfrac{\nu_S}{2} + \dfrac{J}{4} \end{bmatrix} \quad \begin{bmatrix} \psi_1 \\ \psi_2 \\ \psi_3 \\ \psi_4 \end{bmatrix} = \begin{bmatrix} |\alpha\alpha\rangle \\[2mm] \dfrac{1}{\sqrt{2}}(|\alpha\beta\rangle - |\beta\alpha\rangle) \\[2mm] \dfrac{1}{\sqrt{2}}(|\alpha\beta\rangle + |\beta\alpha\rangle) \\[2mm] |\beta\beta\rangle \end{bmatrix} \quad \text{Eq. 1.51}$$

After applying perturbation using RF pulses in an NMR experiment, the condition for allowed transitions of spin S and I is $m = \pm 1$ (see Eq. 1.2). Then the intensity of the observed NMR signal is proportional to the probability of transition between two allowed states. Based on time-dependent perturbation theory, the intensity could be written as follows:

$$Intensity \propto P_{transition} = (\langle \Psi_{initial} | \hat{H}' | \Psi_{final} \rangle) \qquad \text{Eq. 1.52}$$

Where $\hat{H}'$ is the perturbation applied by RF pulse (Becker, 2000). Resonances of two non-coupled spins $(A + X)$ will appear as two singlets in the NMR spectrum.

Weak scalar coupling (AX) will lead to the splitting of the line into doublet which are separated by the value of the scalar coupling constant J and have same intensities. If the scalar-coupling constant is comparable with the difference in resonance frequency of the two peaks, the intensity of the inner components in the multiplets is higher than the outer ones (*roof effect*). Finally in case of homo-nuclear spins A_2 with strong scalar couplings only one line appears in the resulting spectrum. This explains why we do not see scalar spin-spin couplings between chemically equivalent nuclei, such as three protons in CH_3 group.

Allowed transitions and corresponding spectra lines for I) non-interacting two-spin system, $Q = 0$ $(A + X$ spin system), II) vry weak scalar coupling two-spin system, $Q \ll 1$ (AX spin system), III)

intermediate scalar coupling two-spin system, $Q \approx 1$ (AB spin system) and strong scalar coupling two-spin system, $Q \gg 1$ (A_2 spin system) are shown in Fig 1.5

1.1.9. Static and gradient fields

Three types of electromagnetic fields contribute to the NMR signal: (1) the static magnetic field B_0; (2) the radio frequency (RF) magnetic field B_1; and (3) the time-varying spatial gradient magnetic field, G. The heart of any NMR system is its magnet, which is designed to provide a strong, uniform, and steady field. The most popular type of the magnet at fields higher than $0.2\ T$ currently relies on current passing without resistance through superconducting closed wires (Geballe and Hulm, 1980).

Most superconducting NMR magnets are designed in a solenoidal configuration enclosed by a cryostat for cooling. The maximum attainable magnetic field is restricted by the penetration of the magnetic field into the wire (e.g. Niobium-titanium coils could sustain a field as high as $20T$ at $4.2\ K$, McFarland and Rosen, 1986). The characteristics of the MR system ($14.1T$) used in this thesis are listed in Table 1.1 Gradient coils are implemented in the NMR systems to spatially encode the position of the resonating nuclei by varying B_0 field. Since the Larmor frequency of spins depends on the magnetic field experienced by a spin, the spatial variation of the magnetic field causes a variation in the Larmor frequency of spins as a function of their positions. The idea of encoding the position of the spins using a gradient field was proposed for the first time by Lauterbur, 1973 and simultaneously by Mansfield and Grannell, 1973.

Three orthogonal coils along the axes of x, y, and z are required to generate a linear variation of the magnetic field. Assuming B_0 in direction of z-axis, the set of gradient coils for the z-axis are Helmholtz pairs, and while for the x and y axes, paired saddle coils are used (Fig 1.6). Passing current through wire coils configured on a cylindrical surface produces field gradients, and gradient strength is measured in $T\ m^{-1}$ or $G\ cm^{-1}$.

Efficiency of a gradient coil is based on the homogeneity of the generated linear gradient over a large volume with the ability to switch the gradient amplitude rapidly with minimum amount of stored magnetic energy (Hidalgo-Tobon, 2010). Rapid gradient switching can lead to generation of knocking sounds, i.e. gradient noise, heard during a NMR scan because of the produced Lorentz forces on the coil. To reduce the auditory dangers of high noise levels, different solutions such as active acoustic screening (Mansfield et al., 1995) have been proposed.

The minimum interaction of the gradient coil field with other conducting material is important because this interaction is a source for the generation of eddy currents (Carlson et al., 1992). Large, rapid switching of magnetic field gradients with minimal eddy current are necessary for the implementation of high-speed techniques in imaging and spectroscopy. For example, gradient coils are important element for diffusion-weighted measurements in NMR, where the diffusion sensitivity is determined by the square of the gradient field.

Table 1.1 Characteristics of the 14.1T NMR system located in Centre d'Imagerie BioMédicale (CIBM), EPFL,Lausanne.

B_0 (T)	Length× Diameter (mm)	Bore size(mm)	Weight (ton)	Wire
14.1	2030×1820	260	~13	Nb-Sn
Temp(K)	Stored Energy (MJ)	I(A)	L(H)	N$_2$/He(L)
<2.5	~62	250	990	400/1900

| (a) Helmholtz coils | (b) Saddle coils, y-axis | (c) Saddle coils, y-axis |
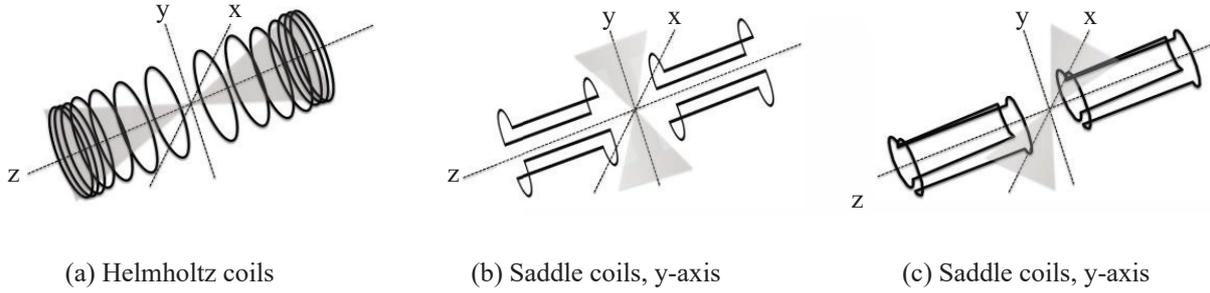
Fig 1.6 Three sets of orthogonal coils along the axes of x, y, and z generate a linear variation of the magnetic field. Gradient fields are zero in the iso-center and increase towards the outside in every direction (shown by shaded area). (a) z gradients generated by the Helmholtz coils, (b) and (c) x - and y-gradients are generated both by Saddle coils. x- and y- gradients are identical but rotated by 90° about the z axis.

1.1.10. Radio frequency NMR probe

Radiofrequency (RF) coils are critical for transmitting and receiving the RF signal in an NMR system. To observe the magnetization of spins ½ aligned with the static magnetic field along the z-axis, a second rotating field is required to flip the aligned magnetization towards the transverse plane. As explained in part 1.1.4, the frequency of the rotating field should be matched with Larmor frequency of the spins of interest in the magnetic field $\vec{B}_0$. After being tilted towards the transvers plane, the nuclear magnetization undergoes a precession motion about the static magnetic field $\vec{B}_0$. If a conducting loop is placed in the vertical plane, radiofrequency magnetic field originated from this precession will induce a voltage (electromotive force) in the loop according to Faraday's law. The coils used for transmitting and receiving the RF signal are called transmit and receive coils, respectively. Typically, the static magnetic field used in NMR is in the range of 1 to 23 T, which causes a Larmor frequency in the range of radio frequency waves for typical spins used in NMR, such as protons. Thus, NMR devices such as coils or amplifiers should operate in the appropriate radio frequency range.

In general, the transmit system consists of a transmit coil and a RF power amplifier; the receive system consists of a receive coil and low noise preamplifier for intensifying the tiny induced voltage in the coil (Fig 1.7).

For a given polarized RF field of a transmit coil, $\vec{B}_{rf}$, the flipped angle of a nuclear magnetization with gyromagnetic ratio γ is given by:

$$\theta = \gamma \left(\frac{B_{rf}}{2}\right) \tau \qquad \text{Eq. 1.53}$$

where τ is the duration of the RF pulse during transmit. $B_{rf}/2$ is denoted as B_1 in the rotating frame (see 1.1.4). Since the B_1 value is on order of 10^{-4} T, radio frequency pulses should be applied approximately for 100 μs to tilt the proton magnetization by 90° respect to its initial direction. The RF power delivered to the probe by the transmitter (RF power amplifier) is on the order of 10 to 1000 watts depending on the nuclei under study and the probe geometry. The electromotive force (*emf*) induced in the receive coil following the application of an excitation pulse of 90° to the sample is:

$$emf = \omega_0 \frac{B_1}{I} M_0 V_s \qquad \text{Eq. 1.54}$$

where I is the current produced in the coil; V_s is the sample volume; and emf is measured in volts. The signal-to-noise ratio (SNR) is a widely accepted standard for the measurement of quality of an NMR system. Hoult and Richards, 1976 developed the following expression for SNR of induced signal in the coil:

$$SNR = \frac{EMF}{Noise} = \frac{\omega_0 \frac{B_1}{I} M_0 V_s}{\sqrt{4k_B \, T \, r_{coil} \, \Delta f}} \qquad \text{Eq. 1.55}$$

where k_B is Boltzmann constant, T the temperature of the probe, and Δf is the bandwidth of the receive coil. Every RF coil is made of RLC (resistors, inductors and capacitors) circuit with the total impedance $Z_{tot}(\omega)$ at a given frequency of ω:

$$Z_{tot}(\omega) = r + i(XL(\omega) - XC(\omega)) \qquad \text{Eq. 1.56}$$

where r is the total resistance representing the losses in the probe and the $XL(\omega)$ and $XC(\omega)$ are the impedance of inductors and capacitors, respectively. The impedance of capacitors and inductors are defined as follow:

$$XL(\omega) = L\omega \ , \ XC(\omega) = \frac{1}{C\omega} \qquad \text{Eq. 1.57}$$

To have optimum energy transfer between the probe and the spectrometer system, the coils should be impedance matched to the impedance of the spectrometer, which generally is purely resistive with an impedance of 50 Ω. Considering a parallel RLC configuration for the coil as in Fig 1.8.a and neglecting the small resistance of the capacitor, the total impedance of the circuit is given by:

$$Z_{tot}(\omega) = 1/\left(\frac{1}{r + iL\,\omega} + iC\omega\right) \qquad \text{Eq. 1.58}$$

Dependency of the real and imaginary part of the impedance to ω is depicted in Fig 1.8.b. Considering $r^2C/2L$ term as very small value and so negligible, the value of real ($Z_{tot}(\omega)$) will be maximum at the resonance frequency of the coil which fulfills the following condition:

$$\omega_0{}^2 = \frac{1}{LC} \qquad \text{Eq. 1.59}$$

Thus the total maximum impedance is estimated as:

$$Z_{tmax}(\omega_0) = QL\omega_0 \qquad \text{Eq. 1.60}$$

where Q is referred as the quality factor and determines the sensitivity of the probe.
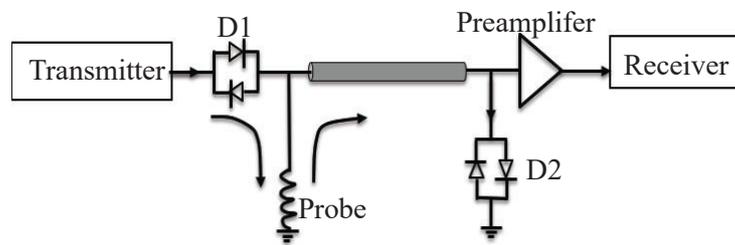
Fig 1.7 Transmit-receive switching networks: Transmit: diode D_1 is closed and power from transmitter are transferred to the RF probe. To protect the preamplifier from high power penetrated from transmitter cross diode D_2 is placed before preamplifier. Receive: Cross diode D_1 is opened and the generated voltage in RF probe passes through $\lambda/4$ to the preamplifier and is intensified before reaching to the receiver.

| (a) | (b) |
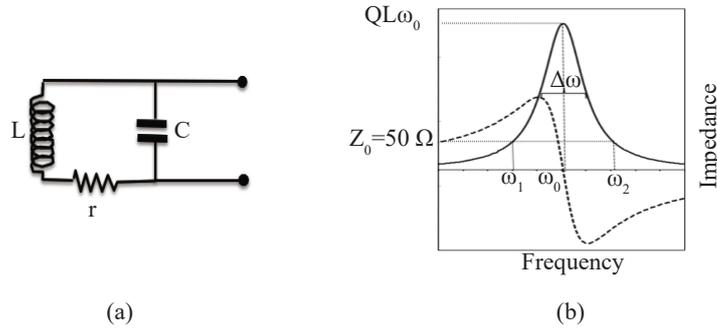
Fig 1.8 (a) Parallel RLC configuration, and (b) its impedance frequency dependence. There are two frequencies ω_1 and ω_2 corresponding with real impedance of 50 Ω. The inductance impedance ($L\omega_0$) and Q factor determine the maximum amplitude of real impedance of RLC circuit. The Q factor is given by the ratio of width at half maximum of real impedance ($\Delta\omega$) to frequency of RLC circuit, ω_0.

The Q-factor is defined as 2π times ratio of the energy stored in the coil by the energy dissipated per cycle of oscillation. So we have:

$$Q = 2\pi \left(\frac{\frac{1}{2} L I^2}{\frac{1}{2} r I^2 \big/ f_0} \right) = \frac{L\omega_0}{r} \qquad \text{Eq. 1.61}$$

The voltage induced by the emf is increased by a factor Q:

$$V = Q \cdot EMF \qquad \text{Eq. 1.62}$$

In order to match the parallel circuit to the real impedance Z_0 (here 50 Ω), there are two frequencies ω_1 and ω_2 in Fig 1.8.b which give a real impedance Z_0. ω_1 is lower than ω_0 and has positive inductive impedance and ω_2 is higher than ω_0 and has negative inductive impedance. Commonly, ω_1 is preferred as spectrometer frequency. The positive inductive impedance could be compensated by a capacitor that is available as non-magnetic component with high Q factor.

To obtain the best sensitivity for the probe, minimizing the electric field and electromagnetic interaction around the probe are essential parameters that should be concerned in the probe design. The capacitive coupling of coil with the sample causes some dielectric losses which could be minimized by equilibrating the probe potential respective to the sample. Radiating losses happen when the dimension of the probe reach about one tenth of wavelength in given magnetic field. In this case, the probe acts as antenna and irradiates energy. For example at a magnetic field of 14.1 T the wavelength for proton is 50 cm and probe length should be less than 5 cm to avoid antenna effect. The solution for avoiding antenna effect is to split the wire of the probe by inserting capacitors. This segmentation also has the advantages of disturbing the electric field all around the coil and minimizing the dielectric losses.

The capacitive or inductive coupling of the coaxial cable shield, used for connecting the probe to transmitters or preamplifiers, to the electromagnetic field generated by the probe causes circulating currents on the cable in same direction towards and from the probe and appearance of the common mode on the cable. The common mode causes additional losses, changing the tuning and matching of the probe and picking up extra noise from the surrounding and radiating energy. Usually the cable currents due to common mode are stopped through inserting baluns in specific points of the cable length.

RF coils can be classified into three main groups: transmit and receive coils, transmit only coils, and receive only coils. When a coil is used as transmitter and receiver, a transmit-receive (TR) switch is required to allow for dual functioning of the probe. The TR switch is usually made of cross diodes and $\lambda/4$ line (Lowe and Tarr, 1968). The TR switch connects the coil to the RF power amplifier and isolates the preamplifier from high power during transmit. It also blocks RF power amplifier coming to the coil and passes the induced current in the coil to the preamplifier during receive (Fig 1.7).

1.1.10.1. Surface coil

The surface coil was probably introduced by Suryan, 1951 and later by Singer, 1959 for observing NMR in flowing blood. After observation of *ex vivo* phosphorous metabolites of muscle tissue by Hoult et al., 1974, it was found out that NMR has great prospect in noninvasive study of living systems. Ackerman et al., 1980 designed a surface coil for localization of signal and monitoring the metabolic state of skeletal muscle and brain within intact rats using high resolution ^{31}P NMR. A surface coil is essentially a loop of conducting material such as copper. The loop may form in various shapes depending to the sample under study. The magnetic field generated by the current flowing in the loop at a position of $\vec{r}$ (Fig 1.9) can be estimated based on Biot-Savart's law:

$$\vec{B}(r) = \frac{\mu_0}{4\pi} \oint I \frac{d\vec{l} \times \vec{r}}{|\vec{r}^3|} \qquad \text{Eq. 1.63}$$

where μ_0 is the permeability constant of vacuum, $d\vec{l}$ the small element along the loop and I is the whole current flowing in the loop. The corresponding magnetic field is linearly polarized and can be considered as two rotating magnetic fields with equal amplitude. The magnetic field along the coil axis can be simplified to:

$$B_y = \frac{\mu_0 I}{2} \frac{R^2}{(R^2 + y^2)^{3/2}} = 2B_1^+ \qquad \text{Eq. 1.64}$$

The specific localization of the surface coil can be optimized from the dependency of the magnetic field B_y to the distance from the coil in equation Eq. 1.64. Thus a surface coil has high sensitivity in regions close to the coil that results in its high performance as receive probe. The magnetic field generated by a surface coil is not homogenous over the volume of interest in a sample, decreasing nonlinear with r. Dependencies of the magnetic field to size of the loop and distance from the loop are depicted in Fig 1.9.b. A smaller coil generates bigger magnetic field close to its surface that falls down sharply with distance compared with a larger coil.

Surface coils used as transmit-receive probe suffer from poor homogeneity in excitation. One usually prefers to use the surface coil as receive-only if possible, as more efficient pulse-sequence options are available with the uniform excitation field of a transmit volume coil. However, in some situations, there is no space for a suitable volume coil, or perhaps it is preferable to restrict the transmit region to the receive region as for high-power ^{1}H decoupling (de Graaf et al., 2011). For these cases, the (transmit/receive) T/R surface coil is appropriate.

1.1.10.2. Birdcage coil

The concept of the birdcage resonator, introduced by Hayes et al., 1985, appeared as great improvement in probe design for high frequency. A birdcage coil is a circular ladder network composed of elementary cell circuits. All elementary cell circuits are made of capacitors and inductors distributed with equal distance in a cylindrical configuration. After application of an RF current in such a network, the waves are propagating along the network and at some particular frequency the waves are combined and form

stationary states. The ideal homogenous magnetic field generated from cosine current distribution can be obtained for one particular stationary state. Because of the great performance of the birdcage coils in generating a homogenous magnetic field, the design of a transmit birdcage coil at 14.1 T was considered in this thesis. In the following part, the general principles and configuration of the birdcage coils is explained and more details about the particular performance of the designed birdcage coil at 14.1T are addressed in Chapter 5 of this thesis.

In an ideal birdcage coil, $2N$ vertical legs (called rungs) are arranged on a cylinder with diameter d and length l (Fig 1.10). The relative position of every rung is defined by θ_n that depends to the number of rungs:

$$\theta_n = \frac{n\pi}{N} \qquad n = 0,1,\dots,2N-1$$

<div align="right">Eq. 1.65</div>

The current directed in nth rung of the birdcage with a total of 2N rungs is expected to follow a cosine distribution in an ideal case:

$$I_n = I(2N)\cos(\theta_n/N + \varphi)$$

<div align="right">Eq. 1.66</div>

$$\varphi = \frac{\pi}{2N}$$

<div align="right">Eq. 1.67</div>

where the φ depends on the driving mode of the birdcage. The driving mode determines the polarization of the magnetic field generated in the xy plane of the birdcage coil.

As the number of rungs increases, the current distribution become closer to an ideal cosine distribution and so increases the homogeneity of the generated magnetic field. Therefore, designing a birdcage coil with a maximum number of rungs is an advantage but at the expense of small drops in magnetic field amplitude at the center. In an ideal case of a birdcage coil, the position and current distribution in rungs are assumed to be perfect. In practice, tuning and matching the birdcage coil at the right frequency for a given loading provided maintaining the symmetry of the coil is very challenging.

Birdcage coil can be driven in the quadrature mode that produces a circularly polarized magnetic field. This results in a sensitivity gain by a factor of √2 and halves the transmitter RF power required to rotate the nuclear magnetization. The price to be paid is an increased complexity in tuning the resonator and a great dependency of the RF magnetic field homogeneity to the coil design.
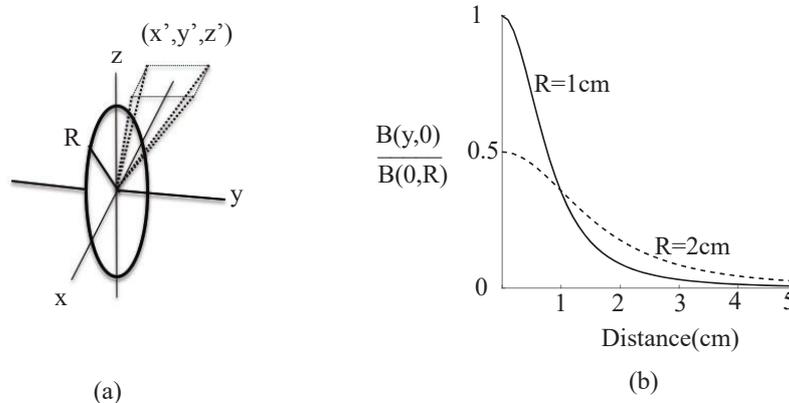
Fig 1.9 (a) Geometry of a simple surface coil and (b) the axial magnetic field (y-axis) as a function of distance from the center of the loop for two coils with different radius.
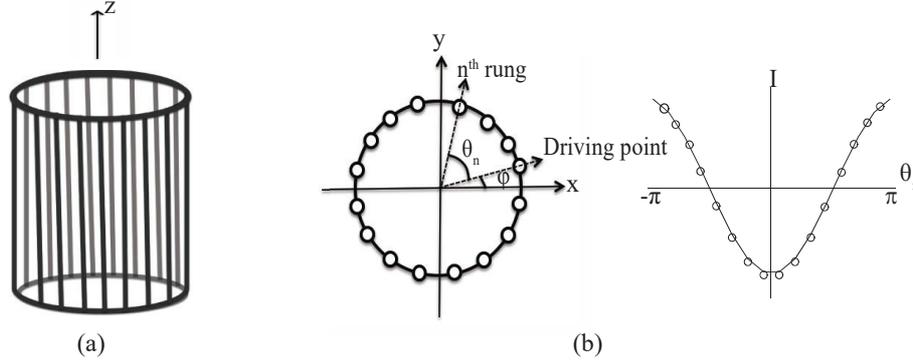
Fig 1.10 (a) Spatial representation of a birdcage coil (capacitances not shown), (b) the cosine distribution of current flowing in vertical legs (rungs) as a function of the azimuthal angle.

For a birdcage coil with diameter of d and length of l oriented in the direction z (Fig 1.10), the x and z component of the magnetic field at the center of the coil are cancelled out and its y component is given by:

$$B_y = \frac{2\mu_0 I}{\pi d} \frac{l}{\sqrt{l^2 + d^2}} \left(1 + \frac{d^2}{l^2 + d^2}\right) \zeta = 2 B_1^+ \qquad \text{Eq. 1.68}$$

$$\zeta = \frac{\sum_{n=0}^{\frac{N}{2}-1} cos^2\left[\frac{\pi}{2N}(2n+1)\right]}{\sum_{n=0}^{\frac{N}{2}-1} cos\left[\frac{\pi}{2N}(2n+1)\right]} \qquad \text{Eq. 1.69}$$

The amplitude of the magnetic field depends on the number of rungs (see factor ζ in Eq. 1.69). For a coil with given number of rungs, the amplitude in center of the coil is maximum when the ratio of length to diameter is equal to $\sqrt{2}$.

Birdcage coils are available in different configuration; high pass, low pass and hybrid. Their physical shape and elementary cell circuits network is shown in Fig 1.11.

The high pass birdcage coil has usually been chosen for high magnetic field because of its ability to achieve circular polarization at high resonance frequencies using small capacitors and inductors. The resonance frequency of a high pass birdcage coil with a total inductance of L and capacitance of C is given by:

$$\omega_k^2 = \frac{1}{4LC \, sin^2(k\pi/2N)} \qquad k \in \mathbb{N} \qquad \text{Eq. 1.70}$$

where k represents the mode of the resonance.

(a) Low pass   (b) High pass   (c) Hybrid
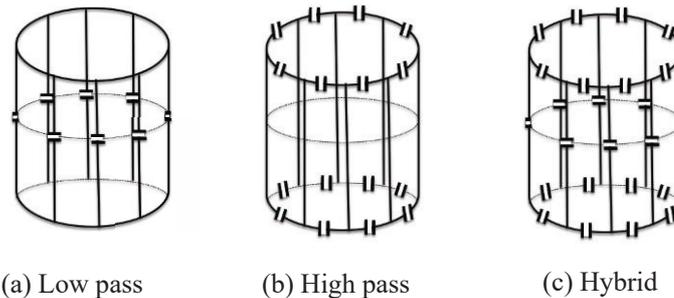
Fig 1.11 The spatial representation of different configuration of birdcage coils corresponding to (a) low pass, (b) high pass, and (c) hybrid birdcage.

The mode of $k = 0$, corresponds to the response of two coupled end-ring, called Maxwell resonant mode. The $k = 1$ is the homogenous mode of the interest from the NMR point of view. Other modes $k > 1$ results in non-homogenous magnetic fields (Leifer, 1997).

1.1.10.3. Phased array coil

An array coil consists of an assembly of small loops electromagnetically decoupled from each other for simultaneous data acquisition. The advantage of this setup is the increased sensitivity of several smaller coils, each of which covers only a certain region of the whole field of view, compared with one large resonator which detects all signal and noise from the whole sample. The use of phased arrays in magnetic resonance imaging has become widespread; both in applications where high sensitivity over a large field-of-view is required (Wright and Wald, 1997) and in cases where parallel imaging techniques can be used to speed up data acquisition by utilizing the inherent spatial information of the coils (Ohliger and Sodickson, 2006).

The phased array technique is well established on clinical MR systems at magnetic field strengths of $1.5–3\ T$ and minimal space limitations. Recent developments increased the number of receivers (and elements in the coil array) on clinical scanners up to 128 channel (Hardy et al., 2008). On the other hand, the design of phased array coils for high-field NMR in animal research application has received relatively little attention despite the possibilities of substantial SNR increase. The use of array coil at high magnetic field requires solving two major problems, the small size of the coil and the inductive coupling between the coils.

Coupling between the coils can degrade the performance of the array coil and it can be very difficult to match the impedance of each element simultaneously to the input impedance of the receiver circuitry. When this match is non-optimal, it could result in the measurement of an image with a poor SNR. In Fig 1.12, a system of two coupled coils was depicted where every coil is represented by inductance $L_{1,2}$, resistance, $R_{1,2}$ and capacitance $C_{1,2}$. V_1 indicates the signal induced in coil 1 and V_{out} indicates the output voltage. When the AC current, I_1, flows in coil 1, mutual inductances between two coils M_{12} will induce current I_2 in the coil 2. The output voltage from coil 1 is determined by:

$$V_{out} = V_1 + \left(R_1 + i\left(\omega L_1 - \frac{1}{\omega C_1} \right) \right) I_1 + i\omega M_{12} I_2 \qquad \text{Eq. 1.71}$$

The second term in Eq. 1.71 represents the contribution of noise from coil 1 and third term is related to the noise resulting from mutual coupling between two coils. Noise from coil 1(second term) could be minimized by tuning and matching the coil to the operating frequency ω and reducing the resistance of circuit. Third term could be suppressed either by nulling the current I_2 or removing the mutual inductance M_{12}.

A common way to remove the mutual inductance between two adjacent coils is the overlapping method (Fig 1.13.a). The optimum distance between two coils for minimizing the mutual inductance depends on the geometry of the coils. Capacitive decoupling may be employed to cancel the mutual inductance. The principle behind the capacitive decoupling is that the non-zero mutual inductance is modeled as an inductance. The inductance can be canceled by the addition of a capacitor.
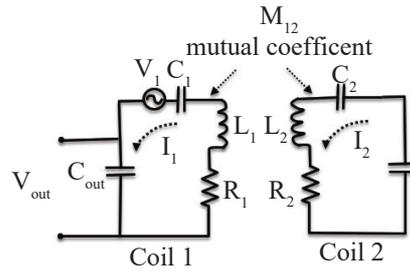
Fig 1.12 A system of two coils coupled through non-zero mutual inductance.

The other approach for removing the last term in Eq. 1.71 ($I_2 = 0$) is preamplifier decoupling. In this method, a low impedance preamplifier is integrated in the circuit of every coil (Fig 1.13.b). The requirement for preamplifier decoupling is a particular type of impedance transformation network in which low impedance of preamp is transformed to high impedance, at the frequency ω in the input of coil.

Consequently, high impedance in the input point of coil results in opening the coil circuit ($I = 0$) and forces the magnetic coupling between the coils to zero. In preamplifier decoupling approach every coil is behaving independently and the NMR signal is fed into the receiver mainly via the electric field and also used as most common approach for reducing the coupling between the nonadjacent coils in array. More detail about the decoupling methods is explained by Lian and Roemer, 1998.

(a) Overlapping method   (a)Preamplfier method
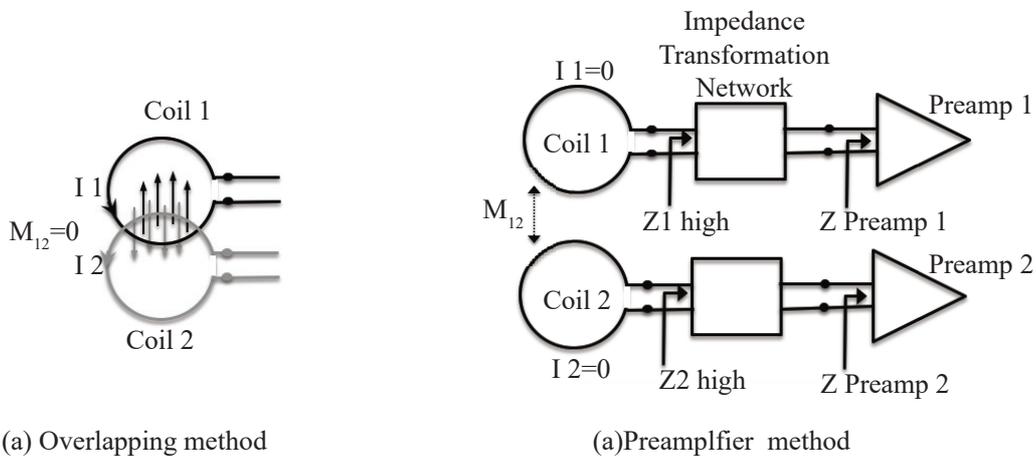
Fig 1.13 Current flowing in every loop generates a magnetic flux passing through other neighboring loops, resulting in perturbation of the magnetic field in every loop by mutual inductances, M_{12}. (a) Overlapping method for decoupling of array elements: net change of magnetic flux is minimized with an optimum overlapping distance between neighboring loops and the M_{12} is reduced accordingly to ignorable level. (b) Preamplifier decoupling: low impedance preamplifier is integrated to every coil through an impedance transformation network. The low impedance of the preamplifier transforms to high impedance at the input of every coil and stops the net current flowing to the coil. The absence of currents in the coils forces the magnetic coupling between the coil elements to zero.

1.2. Magnetic resonance techniques

Nowadays one of the most established NMR approach to explore chemical components in the living organs in clinics is the ^{1}H NMR spectroscopy, benefiting from high magnetic ratio and high natural abundance of protons. Moreover, the SNR of spectroscopic data is increased at high magnetic fields, and may translate to increased metabolite measurement precision. This gain, as well as increased spectral dispersion, becomes important for low concentration metabolites, in situ; as well as for spectra displaying overlapping spectral lines and for compounds that give rise to complex J-coupled spectral patterns. It should be mentioned that a precise quantification of metabolites requires compensating eddy currents (see 1.1.9), optimizing first and second order shimming (see 1.1.1.2.4) and performing efficient water and outer volume suppression (see 1.1.1.2.5).

To identify the anatomical location of voxel of interest for acquiring localized MRS data *in vivo*, magnetic resonance imaging (MRI) technique is required. Selecting a slice plane and spatially encoding each voxel in MRI involves the use of magnetic field gradients. In the following we go through the techniques used for the spatial encoding in MRI. Later mechanism used for localization of detected spectra, shimming, outer and water suppression are explained. At the end, common used NMR sequences and quantification of spectra are discussed briefly.

1.2.1.   Spatial encoding

Applying an RF pulse produces a signal consisting at a single frequency; Fourier-transforming this signal gives a spectrum with a single peak. To spatially encode the resonance frequency of spins, a field gradient linearly varies the homogenous magnetic field $\vec{B}_0$ across a sample resulting in linear changes of the resonance frequencies at different locations (see part 1.1.9).

To understand the principle of spatial encoding, we consider transverse magnetization of spins that are precessing around the main magnetic field $\vec{B}_0$ and induce current in the receive coil. In the general case of spatially varying $\vec{B}_0$, the total signal is given by:

$$S(t) = \iiint \rho(\mathrm{x,y,z,t}) \, e^{i(\omega_0(x,y,z,t)t + \varphi_0(x,y,z,t))} dx \, dy \, dz \qquad \text{Eq. 1.72}$$

Where $\rho(\mathrm{x,y,z,t})$ is the spin density of the sample. The task of spatial encoding is to change linearly the frequency $\omega_0(\mathrm{x,y,z,t})$ and/or phase $\varphi_0(\mathrm{x,y,z,t})$ of spins over the sample volume by gradient fields. There are three different types of spatial encoding processes in MRI, slice selective excitation, phase encoding and frequency encoding.

1.2.1.1. Slice selective excitation

Slice selective excitation of spins placed in $\vec{B}_0$ is achieved by applying a slice selection gradient (G_{ss}) in a given direction (assumed to be the z -axis), resulting in a nuclear spin resonance frequency deviated linearly from the nominal ω_0 with the position of the considered nucleus along the z direction (Fig 1.14).

$$\omega = \omega_0 + \gamma G_{ss} \, z \qquad\qquad\qquad \text{Eq. 1.73}$$

Where G_{ss} is the amplitude of the gradient. An RF pulse is applied simultaneously with the gradient field G_{ss} to excite spins in the selected plane. RF pulse bandwidth (BW) depends on the shape of the pulse and its duration. Adjusting the bandwidth of the selective pulse and the amplitude of the G_{ss} varies the thickness of the slice. The thickness of the selected slice is given by:
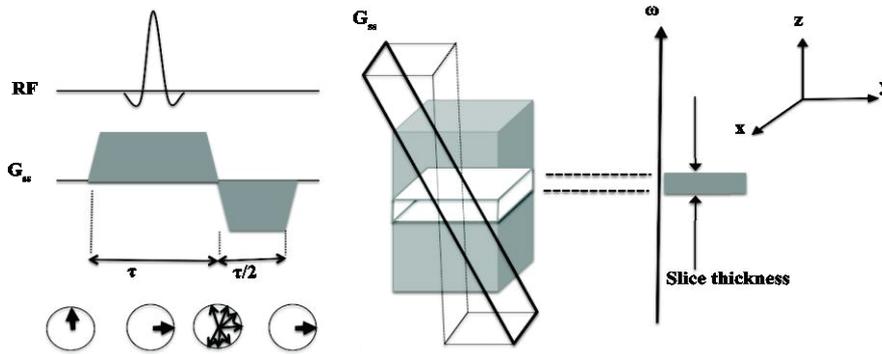
Fig 1.14 Slice selection: a gradient magnetic field, G_{ss} is applied along z-axis, and changes linearly the magnetic field $\vec{B}_0$ relative to the position on the z axis. Applying simultaneously an RF pulse with G_{ss} results in the excitation of a single slice of the sample. At the end of the slice selective gradient, the spins are dephased due of their different precession. A second gradient is typically applied along the same axis with opposite polarity and half of the area to compensate this dephasing.

$$Thickness = \frac{BW}{\gamma . G_{ss}}$$ Eq. 1.74

1.2.1.2. Phase encoding

After the excitation pulse, the distribution of transverse magnetizations in the sample is in a 2-D plane. Applying a second linear gradient field (assumed in y-axis), perpendicular to the G_{ss} will change linearly the phase of the magnetization in the selected slice (Fig 1.15). After applying this second gradient for a time τ, the phase of a magnetization in a point (x, y) is determined by:

$$\varphi(x,y) = (\omega(x,y) - \omega_0)\tau = \gamma\, G_{pe} y\, \tau$$ Eq. 1.75

where G_{pe} is the amplitude of the gradient. When the G_{pe} is switched off, the precession frequency returns to a constant value, while the phase remains proportional to the y position in the slice. However the phase information is not unique (e.g. application of $G_{pe,1}$ cause same phase for the first and third slices in Fig 1.15). Therefore to encode spatially the sample along the y-axis, the experiment must be repeated with different amplitude of G_{pe}.
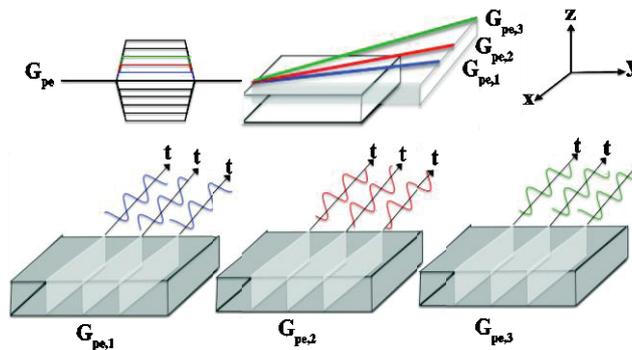
Fig 1.15 (a) Phase encoding. A magnetic field gradient $\bar{G}_{pe}$ is applied along the y-axis and changes linearly the y component of the magnetic field $\bar{B}_0$ relative to the position on the y-axis. (b) The nuclei in the sample experience different magnetic field depending to their position on the y axis. This results in precessing all protons in the same frequency with different phases.

1.2.1.3. Frequency encoding

After every step of phase encoding, a constant gradient in direction of x is applied to the sample, the frequency of precession changes linearly with the location as follow:

$$\omega(x,y) = \gamma G_{ro}\, x \qquad\qquad\qquad \text{Eq. 1.76}$$

If the signal is read out while this gradient is on, voxels at different locations will have different frequencies (Fig 1.16). The phase and the frequency encoding steps encode every location in the excited slice with a distinct pair of phase and frequency of the magnetization precession. At time t after frequency encoding, the induced signal from the transverse magnetization of voxel (x, y) in the excited slice is given by:

$$S(t) = \iiint M_{xy}(x,y,t) e^{i(\gamma G_{ro}xt + \gamma G_{pe}y\tau)} dx\, dy \qquad\qquad \text{Eq. 1.77}$$

The signal measured during each iteration produces a row in spatial frequency space, referred as k space:

$$S(k_x(t), k_y) = \iiint M_{xy}(x,y,t) e^{-i(k_x x + k_y y)} dx\, dy \qquad\qquad \text{Eq. 1.78}$$

$$k_x = -\gamma G_{ro}t \;,\; k_y = -\gamma G_{pe}\tau \qquad\qquad\qquad \text{Eq. 1.79}$$

Thus acquiring signal for different values of G_{pe} will complete the whole rows of the matrix in k space. The image of transverse magnetization in every selected slice can be recovered by applying the inverse discrete Fourier transforms. The size of the image (field of view, FOV) along the frequency encoding and the phase encoding direction is determined as follow:

$$FOV_{ro} = \frac{2\pi}{\gamma G_{ro}.r_s} \qquad FOV_{pe} = \frac{1}{\gamma \Delta G_{pe}} \qquad\qquad \text{Eq. 1.80}$$

Where r_s is the sampling rate during acquisition, ΔG_{pe} is the amplitude of phase encoding gradient step. The image resolution $(\Delta x, \Delta y)$ in direction read out, ro, and phase encoding, pe, is determined as:

$$\Delta x_{ro} = \frac{2\pi}{n_s.\gamma.G_{ro}.r_s} \quad \Delta y_{pe} = \frac{1}{2N.\gamma.\Delta G_{pe}} \qquad\qquad \text{Eq. 1.81}$$

Where $2N$ is the number of phase encoding step and n_s is the number of points acquired at a sampling rate r_s.
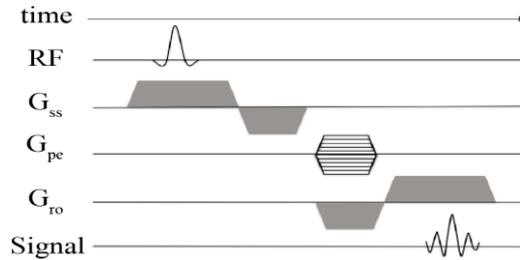
Fig 1.16 Frequency encoding: After applying G_{ss} to select slice along the z-axis and G_{pe} to encode the phases along the y-axis, a magnetic field gradient G_{ro} is applied along the x axis to change the precession frequency of the nuclei depending to their position on the x axis. A dephasing frequency gradient (negative polarity) is applied at the same time as the phase encoding gradient, so as to cause the spins to be in phase with maximum signal at the center of the acquisition period.

1.2.2.   Gradient echo (GE)

The use of gradient echo (GE) sequence is a technique for generating echo as shown in Fig 1.17. When the first gradient is applied, the spins will rapidly dephase in the transverse plane. After applying the second gradient with same amplitude and shape, but with reversed polarity and double duration, the spins will rephase and produce a gradient echo. Part of the dephased spins caused by field inhomogeneities will not be rephased. GE is generated using magnetic fields in two directions, the slice selection direction and the readout direction. Spoiled gradients are applied in the slice selection direction at the end of the sequence in order to dephase any remaining spins, resulting in reducing TR. The optimum flipped angle in GE, called Ernst angle, depends on the T_1 value of a tissue being imaged and is given by:

$$\alpha_{Ernst} = \arccos(e^{\frac{-TR}{T_1}})$$ Eq. 1.82

where TR is the repetition time of the sequence. The flip angle in GE is commonly in a range of about 10° to 80° degrees, typically lower than 90°. Thus the buildup time for longitudinal magnetization in GE is significantly reduced for the subsequent pulses, allowing faster image acquisition in GE.

An important feature of GE is that signal decays with T_2^* which is more rapid than the T_2 decay process underlying GE sequence (leading to shorter TE). Therefore GE is more susceptible to static field inhomogeneities.
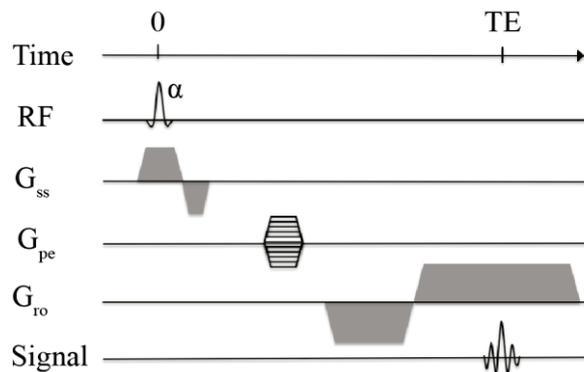
Fig 1.17 Gradient echo sequence: Magnetizations in a sample slice are tilted by a small angle α, by applying an RF pulse during slice selection gradient G_{ss}. It is followed by a phase encoding gradient G_{pe}. In read out direction (ro), two gradients with opposite polarity are applied forming an echo at time of TE where the second gradient lope of G_{ro} has compensated the first dephasing gradient completely. The signal decays with relaxation time T_2^* as a function of TE.

1.2.3.   Spin echo (SE)

The microscopic magnetic moments of the total transverse magnetization, generated by an initial excitation pulse, will lose their phase coherence with time resulting in decay of NMR signal. The source of signal decay through spin dephasing could have reversible and irreversible components. Reversible dephasing is due to the main magnetic field inhomogeneity, local magnetic susceptibility and chemical shift. Irreversible dephasing relates to random processes such as spin-spin interactions or diffusion through magnetic field gradient. Reversible dephasing could be recovered by using a technique called spin echo, SE (Hahn, 1950). In SE, a slice selective 90° pulse is followed by a 180° refocusing pulse (Fig 1.18.a). Immediately after the 90° RF excitation pulse, all the spins are in phase. During the time TE/2, some spins precess faster and some slower than average, resulting in dephasing spins. Application

of an 180° pulse after a time TE/2 flips the spins in the transverse plane and reverses the spin phases. As the spins continue to precess at their respective frequency, they are rephased and after a time TE/2 equal to the original dephasing time, an echo forms.

SE technique in MRI has been used for T_1, T_2 and proton density (PD) weighting in a sample. Because of the need for a relatively long TR value, SE is generally considered a slow pulse sequence. SE is less sensitive to constant magnetic field inhomogeneities and therefore removes the T_2^* contribution in the signal decaying, (see part 1.1.5).
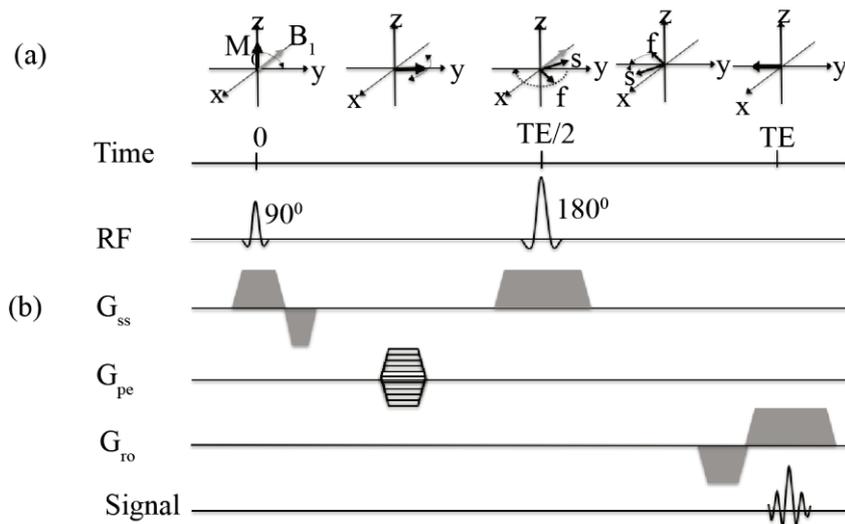
Fig 1.18 Spin echo sequence. (a) Vector presentation: Magnetizations are flipped to the xy plane by 90° pulse and dephasing due to the T_2 relaxation and inhomogeneous effect. Reversible dephasing can be recovered by applying an 180° inversion pulse at half of the echo time (TE/2), (b) Spatial encoding for a spin echo sequence: magnetization from a sample slice is first flipped to the xy plane through application of a 90° RF pulse during slice selection gradient G_{SS}. A phase encoding gradient is applied during the delay between the 90° and 180° RF pulses. To improve the localization of signal, the slice selection gradient G_{ss} is applied again during inversion pulse 180°. Frequency encoding gradient is applied during the signal acquisition to encode the readout direction. In order to sample the entire k space, the sequence is repeated with different amplitude of phase encoding gradient G_{pe}.

1.2.4. Magnetic field homogeneity and shimming

Homogeneity of the stationary magnetic field is a critical parameter in NMR applications such as spectroscopy to distinguish different peaks of metabolites separated in some cases less than 0.1 ppm. In reality, the static magnetic field inside an NMR spectrometer is far from homogenous field. Sources of inhomogeneity are potentially magnet design, the materials in the probe, as well as ferromagnetic materials around the magnet. Distortions in the homogeneity of the stationary magnetic field result in a distribution of the Larmor frequency of spins over the sample space, resulting in low quality and poor resolution spectra.

To create an optimal homogenous stationary magnetic field over the sample, a set of coils with adjustable currents (shim coils) are placed within the magnet, surrounding the field of view. The shim coils create various functional forms of field gradients ($Z°,Z,Z^2,X,XZ, XZ^2,Y, XY, X^2Y^2$, etc) with

desired strength and direction in order to cancel the residual inhomogeneity of the main field as completely as possible, a process called magnet shimming. The optimum shim current settings are found by minimizing the line width of a spectrum, or equivalently maximizing the area under the FID, or maximizing the total signal.

Different techniques have been developed for providing a map of B_0 inhomogeneities in the shimming procedure. In this thesis, FASTMAP (fast, automatic shimming technique by mapping along projections) has been used for shimming. The details about mechanism of FASTMAP is explained by Gruetter, 1993.

1.2.5.   Water and outer volume suppression

Detection of metabolites in regions such as brain using NMR spectroscopy is complicated because of presence of intense water signal and overlapping of the broad baseline of water signal with other metabolites. Additionally, some unwanted signals from outside of the volume of interest (e.g. lipids in the outer surface of skull) present in very high concentration that disturb the spectral shape. Therefore, water and outer volume suppression are critical for spectroscopy in order to reliably observe small metabolite signals, specific to the region of interest.

The most common approach for water suppression is to pre-saturate the water signal using chemical shift-selective (CHESS) pulses (Haase et al., 1985) prior to the localization pulse sequence. The water signal is excited by applying an RF pulse with a very narrow selective bandwidth. The flipped spins of water are subsequently dephased in the transverse plane by applying a strong magnetic field gradient (crusher gradient). Good water suppression can be achieved using more than one pulse and optimizing the selectivity of RF pulse on water resonance.

To suppress the unwanted signal from neighboring tissue (outer volume suppression, OVS), a series of slice selective RF-pulse followed by crushers are applied. In practice, eight slices are successively exited with adiabatic pulses to get rid of the outer volume signal.

The technique used in this thesis for water in ^{1}H spectroscopy is variable power RF pulses with optimized relaxation delays (VAPOR), along with six hyperbolic secant pulses for OVS (Tkác et al., 1999). VAPOR sequence employs seven asymmetric sinc pulses of variable power and optimizing timing to suppress water.

1.2.6.   STEAM sequence

Most single voxel localization techniques use three orthogonal slice-selective pulses to select a signal from the region where they intersect. An optimal sequence designed for voxel localization is stimulated echo acquisition mode (STEAM) generated by applying three 90^0 RF pulses:

$$90° - TE/2 - 90° - TM - 90° - TE/2 - echo \qquad \text{Eq. 1.83}$$

A distinctive advantage of STEAM is the mixing time (TM) that does not contribute to the entire echo time (TE). This period can be used to apply strong crusher gradients and additional water suppression (WS) without affecting TE. However, the stimulated echo has only 50% of the signal intensity of a spin echo. This is because the second 90° pulses only rotates half of the excited spins from transverse plane to the longitudinal axis and the other half is dephased by the crusher gradient in TM (see Fig 1.19).

In chapter 3 of this thesis, the STEAM sequence was chosen to study the kinetic parameters of acetate transport and utilization in the living rat brain during prolonged acetate infusion. Another interesting feature is coupling the STEAM sequence with diffusion gradients. The TM can be considerably extended without experiencing T_2 relaxation and used for the study of molecular diffusion motion

during longer periods (see part 1.3). Therefore, diffusion-weighted STEAM sequence was used in this thesis to assess the diffusion characteristics of acetate in the rat brain *in vivo*.
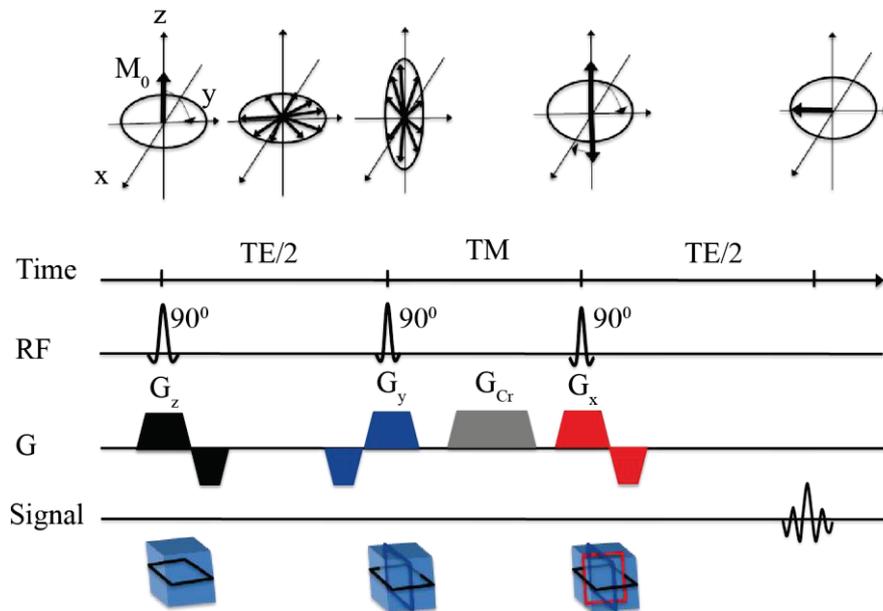
Fig 1.19 The typical STEAM sequence. Following a selective 90° RF pulse, magnetization is flipped into the transverse plane xy. During the first TE/2, spins start to dephase due to the local field inhomogeneity. A second selective 90° RF pulse is applied on the y direction, resulting in the rotation of the spin distribution form the xy plane to the xz plane. A crusher gradient (G_{Cr}) is applied during the mixing time (TM). As a consequence, the transverse spins (in xy plane) are strongly dephased through G_{Cr}, while the vertical components of the magnetization is stored along the z-axis. Application of a third selective 90° RF pulse returns the stored vertical magnetization to the transverse plane and refocuses it as a stimulated echo. Every selective RF pulse results in selecting a slice of sample in a given direction that is shown with different colors. The final signal from the stimulated echo is obtained on the VOI placed at the intersection of all three-selected slices.

1.2.7.   Quantification of spectra

In any MRS study, an accurate and reliable quantification of metabolite concentrations is essential and challenging. Several post-processing tools have been developed for this purpose such as JMRUI(Stefan et al., 2009), TARQUIN(Reynolds et al., 2006), and TDFDfit (Slotboom et al., 1998), among which the LCModel (Stephen Provencher, 2015) is one of the most popular. In this thesis, the LCModel was used to quantify the ^{1}H and ^{13}C spectra. LCModel is a software tool for the analysis and quantification of *in vivo* and *in vitro* MRS data. It estimates the spectrum under evaluation as a linear combination of a set of model spectra for each metabolite of interest. This model spectrum forms a basis set within LCModel, measured *in vitro* using phantom containing the considered metabolites or simulated based on the quantum mechanical description. The basis sets should be generated under the same conditions as used for data acquisition, namely same pulse sequence and acquisition parameters. LCModel uses a nearly model-free regularization method, which attempts to choose the best compromise by finding the

smoothest line shape and baseline consistent with the data. Phase correction and baseline artifacts removal are automatically performed. Estimated standard deviations (Cramer-Rao lower bounds) are expressed in percent of the estimated concentrations. The SNR is defined as the ratio of the maximum peak in the spectrum corrected for the baseline over the analysis window to twice the RMS (root mean square) residuals.

1.3. Diffusion weighted ^{1}H spectroscopy

MR is well known for its potential to measure the diffusion properties of solutes and solvent in physics, chemistry, biology and medicine. Because of its non-invasive nature, MR is also uniquely suited to assess the diffusion characteristics of molecules in intact biological tissue.

The Chapter 3 of this thesis is dedicated to the *in vivo* measurement of metabolites diffusion in the brain using diffusion weighted MR spectroscopy (DW-MRS). Thereby, a brief outline of the physiochemical concept of diffusion is explained here. It is followed by the basis of the MR measurement of diffusion and pulse sequence used for diffusion-weighted spectroscopy.

1.3.1. Elemental concepts of the diffusion process

Diffusion is the random translational (brownian) motion of molecules or ions that is driven by the internal thermal energy. Under macroscopic system in equilibrium, in the absence of any chemical potential gradient, the molecule/ion will change its position as a function of time randomly in all direction due to Brownian motion, in a process called self-diffusion.

The following description was inspired by the book of Crank, 1979. The self-diffusion coefficient D (in unit of length^2/time) is an important parameter of the diffusion mobility and is proportionality constant between the diffusion flux (J) and the gradient in the concentration of the diffusing species (∇c). Looked at in another way, the flux of particles J at position $\vec{r}$ is directly proportional to the local concentration gradient, ∇c $(\vec{r}, t)$, given by Fick's law:

$$J(\vec{r}, t) = -D \, \nabla c(\vec{r}, t) \qquad \text{Eq. 1.84}$$

Moreover, the temporal evolution of the local concentration is equal to spatial changes of local flux $J(\vec{r}, t)$.

$$\frac{\partial c(\vec{r}, t)}{\partial t} = -\nabla . J(\vec{r}, t) \qquad \text{Eq. 1.85}$$

$$\frac{\partial c(\vec{r}, t)}{\partial t} = D\nabla^2 c(\vec{r}, t) \qquad \text{Eq. 1.86}$$

Particle displacements due to diffusion in a homogenous infinite space in three dimensions are normally distributed. As a consequence, the probability of displacement of a particle from its initial position $\vec{r}_o$ to $\vec{r}$ at time t is given by:

$$P(\vec{r}_0 | \vec{r}, t) = \frac{1}{(4\pi D t)^{3/2}} exp^{[-(\vec{r}-\vec{r}_0)^2/4Dt]} \qquad \text{Eq. 1.87}$$

Since diffusion is a random process, there is equal probability for displacement in all directions. Thus, the expected value for the net molecular displacement, $<\vec{r} - \vec{r}_o>$, is averaged to zero. The average square displacement in three dimensions is calculated as follows:

$$< (\vec{r} - \vec{r}_0)^2 > = \int P(\vec{r}_0 | \vec{r}, t) \, (\vec{r} - \vec{r}_0)^2 \, dr \qquad \text{Eq. 1.88}$$

$$< (\vec{r} - \vec{r}_0)^2 > = 6Dt \qquad \text{Eq. 1.89}$$

Which yields the well-known Einstein-Smoluchowski relation:

$$D = \mu \, k_B \, T$$ Eq. 1.90

where μ is the mobility of a particle that could be defined as the ratio of the particle drift velocity to an applied force. k_B is the Boltzmann constant and T is the temperature.

Following Stokes law, the force required to move a spherical particle of radius R through a continuous medium of viscosity η with a velocity V is:

$$F = 6\pi\eta R \, V$$ Eq. 1.91

The Stokes-Einstein equation describes the proportional increase of diffusion with temperature and its proportional decrease with the fraction coefficient ($f = F/V$), as follows:

$$D = \frac{k_B \, T}{6\pi\eta R}$$ Eq. 1.92

The fraction coefficient f should be modified for non-spherical particles. Consequently, the diffusion coefficient provides information on the shape and interaction of the diffusing molecule. Because diffusion is a temperature dependent process as can be seen from equation Eq. 1.92, the temperature should be kept constant or tightly controlled throughout the diffusion measurements.

We next consider the basis of the MR measurement of diffusion and the pulse sequences used for diffusion-weighted spectroscopy.

1.3.2. Diffusion MRS technique

Diffusion MRS techniques rely on attenuation of MR signal resulting from the dephasing of transverse nuclear magnetizations. Signal attenuation in NMR is due to the combined effect of the translational motion of the molecules carrying the magnetization and the application of spatially gradient pulses. The pulsed field gradient (PFG) method was first introduced by Stejskal and Tanner, 1965 who incorporated a pair of diffusion-sensitizing linear magnetic field gradients into the Hahn spin-echo sequence, referred as pulsed field gradient spin echo (PFG SE). In Fig 1.20, a schematic picture of PFGSE is displayed. The magnetization is flipped to the transverse plane with a 90° RF pulse and then dispersed using a magnetic field gradient pulse with an amplitude g and duration δ, called diffusion gradient. After a period of $\Delta/2$, 180° RF pulse flips the dispersed magnetization. At time Δ, a second diffusion gradient with same amplitude and duration as the first one is applied to refocus the signal.

When transverse magnetization at position $\vec{r}_o$ is exposed to the first diffusion pulse gradient, they will acquire a phase given by:

$$\varphi_1(\vec{r}_o) = \gamma \, \delta \, \vec{g}.\vec{r}_0$$ Eq. 1.93

If spins maintain their position throughout the experiment, they will acquire an equal but opposite phase from the second diffusion gradient placed after the 180^0 pulse. Consequently, the two opposite phases cancel out each other and stationary spins will refocus completely into the spin echo. On the other hand, if spins change their position during the experiment, e.g. spins moved to the position $\vec{r}$, they will acquire a different phase during the second diffusion gradient. The change in phase of a nuclear magnetization during the diffusion experiment is given by:

$$\Delta\varphi(\vec{r} - \vec{r}_0) = \gamma.\delta \, \vec{g}.(\vec{r} - \vec{r}_0)$$ Eq. 1.94

where $\vec{r}_0$ is the initial position of the magnetization and $\vec{r}$ its final one, at the application of the second diffusion gradient. Thus the refocusing will be incomplete, resulting in a decrease in the intensity of the spin echo.

There are several approaches to describe the theory of signal attenuation in NMR diffusion experiment. Here, a brief classical derivation of the attenuation of the spin echo due to translational diffusion will be given in the context of the macroscopic nuclear magnetization $\vec{M}$ and the Bloch equation. Bloch equations with presence of diffusion in the laboratory frame is given by:

$$\frac{\partial \vec{M}(\vec{r},t)}{\partial t} = \gamma\, \vec{M} \times \vec{B} - \frac{M_x + M_y}{T_2} - \frac{M_z - M_0}{T_1} + D\, \nabla^2 (M_x + M_y + M_z) \qquad \text{Eq. 1.95}$$

Considering the z-axis along the statistic magnetic field $\vec{B}_0$, the total local field at position $\vec{r}$ is given by:

$$\vec{B} = \vec{B}_0 + \vec{g}.\vec{r} \qquad \text{Eq. 1.96}$$

The transverse magnetization can be expressed using the complex formalism as follows:

$$\left(M_x + iM_y\right) = \psi(r,t)e^{-i\,(\omega_0 + 1/T_2)t} \qquad \text{Eq. 1.97}$$

where the function ψ is independent of the transverse relaxation T_2 and describes the behavior of the spin in a coordinate system rotating with angular velocity ω_0 about the z-axis and in the same sense as $\vec{M}$ precesses. Thus we can rewrite the part of Eq. 1.95 that does not depend on the relaxation in terms of ψ:

$$\frac{\partial \psi(\vec{r},t)}{\partial t} = -i\gamma\, \vec{g}.\vec{r}\, \psi(\vec{r},t) + D\, \nabla^2 \psi(\vec{r},t) \qquad \text{Eq. 1.98}$$

Imposing the boundary condition $\psi = S$ immediately following the 90° pulse, the solution of equation (Eq. 1.98) between the 90° and 180° pulses in the absence of the diffusion is given by:

$$\psi(\vec{r},t) = S\, e^{-i\,\gamma \int_0^t \vec{g}(t').\vec{r}\, dt'} \qquad \text{Eq. 1.99}$$

The accumulated phase before applying the 180° pulse is:

$$\varphi(\tau) = \gamma \int_0^\tau \vec{g}(t').\vec{r}\, dt' \qquad \text{Eq. 1.100}$$

The effect of the 180° pulse is to set back the accumulated phase of ψ to zero at the time of the echo, namely 2τ; Thus, we could write the following expression for the behavior of ψ from the 90° pulse to the echo time in the absence of diffusion:

$$\psi(r,t) = S\, e^{-i\,\gamma \int_0^t \vec{g}(t').\vec{r}\, dt'}\, e^{-i \int_0^t (\xi-1)\varphi(\tau)\, dt'} \qquad \text{Eq. 1.101}$$
$$\begin{cases} \xi = +1 & 0 < t < \tau \\ \xi = -1 & t > \tau \end{cases}$$

In presence of diffusion, we can work with the same solution modified by considering S as a function of t :

$$\frac{dS}{dt} = -\gamma^2 D \left[\int_0^t [g(t') + (\xi - 1)\, \varphi(\tau)/r]dt'\right]^2 S \qquad \text{Eq. 1.102}$$

Then we integrate the equation Eq. 1.102 between t = 0 and $t = 2\tau$ and impose the boundary conditions following the 90° pulse ($t = o$) and at the pick of echo ($t = 2\tau$).

$$t = 0 \quad \psi(\vec{r},0) = S(0) \quad \text{And} \quad t = 2\tau \quad \psi\,(\vec{r},2\tau) = S(2\tau) \qquad \text{Eq. 1.103}$$

We obtain:

$$S(2\tau) = S(0)\, e^{-\gamma^2 D \int_0^{2\tau}\left[\int_0^t [g(t')+(\xi-1)\,\varphi(\tau)/r]dt'\right]^2 dt} \qquad \text{Eq. 1.104}$$

For the case of a rectangular gradient pulse in the spin echo sequence displayed in Fig 1.20, the amplitude is calculated as follows:

$$S(2\tau) = S(0)e^{-\gamma^2 \, \delta^2 g^2 \left(\Delta - \frac{1}{3}\delta\right).D} \qquad \text{Eq. 1.105}$$

where the g and δ is the amplitude and duration of the diffusion gradients, respectively . Δ is the time interval between the two diffusion gradients, which start from the middle of the first diffusion gradient and continue until the middle of the second diffusion gradient. The term $\Delta - \frac{1}{3}\delta$ in equation Eq. 1.105 is usually referred to as the diffusion time, t_{diff}. Equation 1.106 is often presented in the following form:

$$S(b) = S(0)e^{-b.D} \qquad \text{Eq. 1.106}$$

$$b = \gamma^2 \, \delta^2 g^2 \left(\Delta - \frac{1}{3}\delta\right) \qquad \text{Eq. 1.107}$$

Where b is the so-called b-factor that is used to indicate the strength of the diffusion weighting and typically given in the unit of s.mm^{-2}.

Up to this point only the isotropic diffusion has been considered and this implies a scalar diffusion coefficient, D. In case of anisotropic diffusion, the diffusion tensor is defined as follow:

$$\vec{D} = \begin{pmatrix} D_{xx} & D_{xy} & D_{xz} \\ D_{yx} & D_{yy} & D_{yz} \\ D_{zx} & D_{zy} & D_{zz} \end{pmatrix} \qquad \text{Eq. 1.108}$$

The diagonal elements represent the diffusion along the x, y, and z axis in the laboratory frame and off diagonal elements represent the correlation between the diffusion in the perpendicular directions. In case of isotropic diffusion, the off diagonal element are zero and $D = D_{xx} = D_{yy} = D_{zz}$.

For the uncharged particles such as water, the diffusion tensor is symmetric and the attenuated signal from Eq. 1.106 could be rewritten as:

$$S(b) = S(0) \, e^{-\sum_{i=1}^{3}\sum_{j=1}^{3} b_{ij} \, D_{ij}ij} \qquad \text{Eq. 1.109}$$

Where b_{ij} is a component of the b matrix and D_{ij} is a component of the diffusion tensor D. To describe quantitatively the anisotropic diffusion, at least seven experiments with diffusion gradient in various directions need to be performed to characterize the different components of the tensor D and $S(0)$. Knowledge of the complete diffusion tensor opens insight into the orientation dependence of diffusion. However, for many applications, knowledge of the average diffusion is sufficient and given by:

$$D_{ave} = \frac{Tr(D)}{3} = \frac{D_{xx} + D_{yy} + D_{zz}}{3} \qquad \text{Eq. 1.110}$$

D_{ave} can be obtained by three separate measurement of diffusion coefficients in three directions x, y, and z.

The majority of the DW-MRS studies have been aiming at quantifying the apparent diffusion coefficient of a given metabolite by using a step-wise increase in the diffusion gradient amplitude at fixed times. Apparent diffusion coefficient can be calculated from such a series of spectra by fitting the peak integrals to equation Eq. 1.106.

Since a strong diffusion gradient pulses are required for the metabolite diffusion studies *in vivo*, diffusion gradients pairs should be well balanced and induce minimal eddy currents(Hrabe et al., 2007). Macroscopic motion in the presence of a linear magnetic field variation causes a change in the phase of the MR signal, resulting in signal loss. Consequently, macroscopic motion-signal losses cause an overestimation of the diffusion coefficient. Posse et al., 1993 proposed some motion correction strategies to avoid signal losses in ^{1}H-MRS studies of metabolite diffusion. Motion correction strategies

such as storing each FID separately, individual phase correction and signal averaging are undertaken in most diffusion spectroscopy studies.

The measurement of self-diffusion by PFG SE is limited by the loss of phase coherence due to the transverse relaxation. One solution for this is to store the spatially encoded magnetization along the longitudinal axis as done in the STEAM sequence (See part 1.2.6). More details about the diffusion weighted STEAM (DW-STEAM) sequence and experimental considerations are explained in Chapter 3.
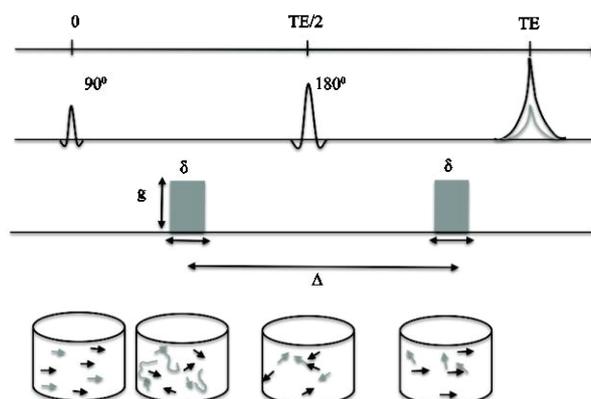
Fig 1.20 Principle of pulse field gradient sequence (PFG SE). Static spins, (black arrows) are dephased by the first diffusion gradient (duration of δ and amplitude of g) according to their respective position. 180° pulse and second diffusion gradient rephase those static spins and generate an echo at time TE (black line). Moving spins (gray arrows) do not have the same position when the second diffusion gradient is applied. Therefore, all spins are not perfectly in phase at time TE, resulting in smaller echo (gray line).

1.4. Metabolic modeling using ^{13}C NMR spectroscopy

^{13}C NMR spectroscopy is a powerful tool, providing information on the dynamics of brain biochemical pathways and metabolic interactions underlying the cerebral activation process. The high chemical specificity of ^{13}C NMR allows us to follow incorporation of labeled carbon into different molecules and even into specific carbon positions within the same molecule. Thus, ^{13}C NMR spectroscopy allows us to assess quantitatively the transport step of substrates into the organ of interest, the metabolic fluxes and cellular compartmentation of pathways from the primary cell culture to the intact rodent or human organs such as brain and heart. In the following section, a brief overview of the experimental design for a ^{13}C metabolic modeling study will be presented. Since part of this thesis is on mathematical modeling of rat brain metabolism using ^{13}C labeled glucose as a substrate (Chapter 2), the emphasis was laid on brain metabolic modeling and ^{13}C-labeled glucose as a metabolic substrate.

1.4.1.   Choice of labeled substrate and infusion protocol

^{13}C NMR spectroscopy detects resonances from ^{13}C, the only stable isotope of carbon having a magnetic moment. However the natural abundance of ^{13}C is only approximately 1.1% of the total carbon and its gyromagnetic ratio is approximately one-fourth of the ^{1}H one. These two limitations make the ^{13}C NMR spectroscopy a relative insensitive technique. The combination of ^{13}C NMR spectroscopy detection and

infusion of substrates enriched in ^{13}C in specific carbon positions improve noticeably the sensitivity of the ^{13}C NMR approach and its potential. Tracking the labeled carbon from the substrate in the different metabolic products opens the possibility to assess the activity of different metabolic pathways *in vivo* and *in vitro* in the brain. The labeled substrate chosen for ^{13}C study should have minimum side effects on the biochemical system under study. The choice of the substrate (e.g. glucose, acetate, pyruvate) will allow feeding specific cell types such as neurons and/or astrocytes or specific cellular processes, resulting in cell specific labeling patterns of metabolites such as glutamate, glutamine, aspartate and etc.

Adequate brain physiology depends largely on the proper supply of enough oxygen and plasma glucose. It is generally accepted that brain metabolism is not affected by plasma glucose concentration as long as it remains above a certain threshold (Duckrow and Bryan, 1987). Consequently ^{13}C-labeled glucose has been the preferred substrate for ^{13}C metabolic studies in the brain. Most *in vivo* ^{13}C-studies in the brain have been performed using [1-^{13}C] glucose or [1-6-^{13}C] glucose.

The metabolism of ^{13}C-labeled substrates can be followed in real time, in situ and noninvasively. Moreover, when two or more carbon atoms of the same molecule are labeled, multiple labeling of metabolites gives rise to homo-nuclear spin coupling (see part 1.1.8) and to the appearance of multiplets. Analysis of these homo-nuclear spin-coupling patterns provides a particular gain in the brain metabolic modeling (see Chapter 2.).

In *in vivo* studies, the infusion protocol for labeled glucose is optimized to reach a high isotopic enrichment in the metabolic products, resulting in sufficient sensitivity for ^{13}C NMR detection. One common infusion protocol for metabolic studies is the hyperglycemic clamp, which increases the glucose concentration from normal levels to a hyperglycemia level using a bolus of enriched glucose. The bolus of labeled glucose results in given enrichment of plasma glucose within a few minutes. The bolus is followed by a continuous infusion of enriched glucose to keep the concentration and ^{13}C enrichment of glucose in plasma and brain at steady state (e.g. see Henry et al., 2003b)).

Knowledge of the time course of glucose concentration and enrichment in the plasma and brain is essential for the quantitative analysis of the measured ^{13}C labeling time course of the metabolites such as glutamate, glutamine and etc.

1.4.2. Detection and quantification of ^{13}C labeled metabolites

Methods for detection of ^{13}C label incorporation into the brain metabolites during infusion of ^{13}C-labeled glucose fall into two groups: direct detection at ^{13}C frequency, and indirect detection at ^{1}H frequency. The choice of the detection method depends among others on the type of information required for metabolic modeling, the size of the volume of interest and the sensitivity of the RF transducers.

Indirect detection of ^{13}C relies on the detection of ^{13}C through the attached hydrogen nuclei. Thus, indirect detection ^{1}H-[^{13}C] offers a higher sensitivity making use of the fourfold higher gyromagnetic ratio of protons compared with the carbon nucleus. However, the smaller chemical shift range of ^{1}H spectra increases the spectral overlapping between the resonances of interest. Consequently, the number of labeled carbon positions that are measured for every metabolite through indirect detection is reduced and therefore available biochemical information for metabolic modeling become limited.

Direct ^{13}C-detection offers the large spectral dispersion of ^{13}C spectra and consequently less spectral overlapping compared with ^{1}H spectrum. Direct ^{13}C-detection allows resolved and simultaneous detection of labeled metabolites at different carbon positions. Another advantage of direct detection relies on the appearance of multiplets in ^{13}C spectra originating from multiple labeling of the metabolite

at different positions within the same molecule. The time courses of these multiplets provide additional information for the determination of cerebral metabolic fluxes (see Chapter 2). However, the low SNR of ^{13}C spectra limits this method to the detection of metabolites with high concentration and enrichment during prolonged ^{13}C-labeled substrate infusion such as glutamate and glutamine. To enhance the NMR signal for resonances with sufficient long T$_2$, polarization transfer techniques are used in direct ^{13}C detection. The polarization transfer technique is described using the concept of product operators in quantum mechanical descriptions (Keeler, 2011 and Soerensen et al., 1983). The polarization transfer technique increases the NMR signal by a factor of four ($\frac{\gamma_{1H}}{\gamma_{13C}}$) and also enables the localization of signal within the region of interest using the initial ^{1}H magnetization. ^{1}H spectra have a narrow chemical shift range and localization using ^{1}H magnetization results in a substantial reduction of artifacts due to the chemical shift displacement especially at high magnetic field.

In the metabolic modeling presented in this thesis, localized ^{13}C NMR spectra were obtained using the distortionless enhancement by polarization transfer (DEPT) sequence combined with ^{1}H localization (Doddrell et al., 1982, Henry et al., 2003b), resulting in simultaneous detection of singly and multiply labeled isotopomers of the metabolites *in vivo* with excellent sensitivity and spectral resolution.

1.4.3. Metabolic pathways in brain metabolism of glucose

Universal biochemical pathways in mammals are the means by which energy is extracted to maintain the cell function. To interpret the ^{13}C NMR data acquired in the brain, an a priori knowledge of the involved metabolic pathways and related analysis with a metabolic model are required.

There are two major cell types in the brain, neurons and glial cells. Neurons transmit information as electrical impulses and communicate with each other by release of neurotransmitter. Glial cells surround the neurons and provide the neurons with key substrates while maintaining a stable extracellular environment.

Although the main fuel for brain function under physiological conditions is glucose, alternative fuels such as acetate, lactate or ketone bodies may be used under certain conditions such as fasting or starving. The substrates used by the brain cross the blood-brain-barrier and enter brain cells through specific transporter proteins. Glucose is taken up and metabolized by both neurons and glial cells, while acetate is preferentially transported and metabolized mainly by astrocytes (see Chapter 2 and Chapter 4).

After crossing the blood-brain barrier, a glucose molecule breaks down into two pyruvate (Pyr) molecules through glycolysis. Pyr can be metabolized to lactate (Lac) as a reversible reaction. The lactate dehydrogenase (LDH) enzyme atalyzes the interconversion of Pyr and Lac with concomitant conversion of NADH and NAD$^+$. Oxidative conversion of Pyr, called pyruvate dehydrogenase (PDH) reaction, results in the formation of acetyl-CoA (AcCoA). Direct synthesis of AcCoA can also happen via the link of acetate (Ace) and a Coenzyme-A group, which that is less common than the PDH route. AcCoA enters the tricarboxylic acid (TCA) cycle under irreversible condensation with oxaloacetate (OAA) to generate citrate. Subsequently, isocitrate is converted irreversibly to alpha-ketoglutrate (αKG) and CO$_2$. αKG is degraded to succinate, a symmetric molecule. Oxidation of succinate generates fumarate that is then converted to malate by the fumarase enzyme. The TCA cycle is completed with the oxidation of malate to oxaloacetate (OAA). In addition to the PDH route, OAA can be generated through anaplerotic in astrocytes, which creates an OAA molecule from pyruvate through pyruvate carboxylase (PC) activity. The anaplerosis route generates new carbon skeletons through OAA synthesis and can consequently replenish the TCA cycle for net effluxes, in particular through the exchange between the TCA cycle and amino acids (Fig 1.21).

The TCA cycle intermediates OAA and $\alpha - KG$ are in fast exchange with the amino acids glutamate (Glu) and Aspartate (Asp), respectively. The excitatory neurotransmitter Glu can be converted to the inhibitory neurotransmitter GABA using the L-glutamic acid decarboxylase (GAD) and pyrodixal phosphate as a cofactor. GABA is converted back to Glu by a metabolic pathway called the GABA shunt.

The release, reuptake and recycling of the excitatory neurotransmitter Glu are critical for mammalian brain function. One of the proposed and well-established pathways for clearance and repletion of Glu is the glutamate/glutamine (Glu/Gln) cycle. In this pathway, Glu is taken up by astrocytes and condensation of glutamate and ammonia by glutamine synthetase (GS) forms Gln (Cooper and Plum, 1987; Meister, 1985). Gln is released to the extracellular fluid, where it is taken up by neurons and split by the intramitochondrial phosphate-activated glutaminase enzyme (PAG) into glutamate and ammonia (Kvamme et al., 1985). Since GS is mostly located in astrocytes and PAG mostly presents in neurons, it is suggested that most of the Glu is placed in neurons and most of the Gln is located in glial cells.
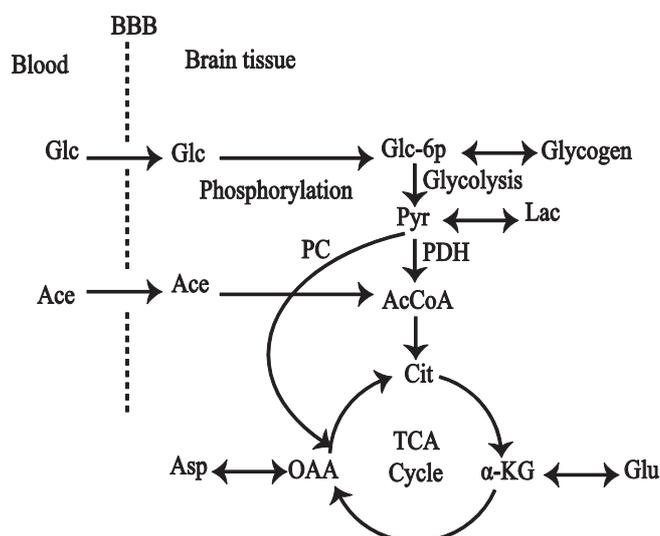
Fig 1.21 Schematic view of the main biochemical steps in the brain energy metabolism for Glc and Ace as substrate. After transporting across the blood brain barrier (BBB), Glc is phosphorylated and enters the glycolysis to produce pyruvate. Pyruvate enters the TCA cycle either through the pyruvate dehydrogenase pathway (PDH) or through the anaplerotic pyruvate carboxylase pathway (PC) in the glial cells. Ace is transported specifically in the glial cells and enters the TCA cycle at the level of acetyl-CoA.

1.4.4. Metabolic models based on the chemical specificity and temporal dynamic of data

Following infusion of labeled substrate such as [1-6-^{13}C$_2$] Glc, the ^{13}C label flows through metabolic pathways in the brain resulting in ^{13}C labeling of different brain metabolites. However the concentrations of TCA cycle intermediates such as OAA and αKG are smaller than the MRS detection threshold, typically in the millimolar (mM) range. Fortunately, the amino acids Glu, Gln and Asp exist at high concentrations and their labeling turnover curves correspond to the labeling of TCA cycle

intermediates that are in exchange with and therefore the kinetics of their labeling is driven by the TCA cycle activity.

Multiple labeling of amino acids at different carbon positions can occur, through further cycling of ^{13}C in the TCA cycle. The different ^{13}C labeling patterns of a given molecule are called isotopomers. The presence of ^{13}C-^{13}C J coupling within isotopomers results in splitting the singlet resonance of the corresponding carbon position, forming the fine structure of multiplets. For example, ^{13}C from [1-6-^{13}C$_2$]Glc substrate enters into the first turn of the TCA cycle labels Glu at position C4 and generates a singlet resonance of GluC4 in ^{13}C spectra. Recycling ^{13}C in the second turn of the TCA cycle labels Glu at position C3 and C2. Consequently, there is a possibility for a Glu molecule to be multiple-labeled at few different carbon positions. In case of Glu, multiple labeling of Glu at position C4 and C3 forms a doublet of Glu (GluC4 D43) in ^{13}C spectra. In the same way, there is a possibility for all isotopomers of Glu, Gln and Asp to be multiple-labeled at several carbon positions according to their labeling pathways. The analysis of the measured ^{13}C turnover curves of isotopomers and their ^{13}C multiplets using metabolic models ultimately yields quantitatively estimation of metabolic rates based on mass and isotopic balance equations (see part 1.4.6).

There are two different metabolic models based on the temporal dynamics of the input data, isotopic steady state model and isotopic dynamic model. In isotopic steady state model, the final ^{13}C enrichment of metabolites at isotopic steady state allows the estimation of ratio of metabolic fluxes. The drawback of this modeling approach is that it does not provide absolute flux values. The isotopic steady state model is preferred when the detection sensitivity is not good enough to quantify the time course of labeled isotopomers with low ^{13}C enrichment level.

The isotopic dynamic modeling is based on the information from temporal enrichment curves of metabolites before reaching isotopic steady state. Contrary to isotopic steady state model, the isotopic dynamic modeling can yield absolute values of metabolic rates.

Based on the chemical specificity of the input data, metabolic model can be of two types: a positional model and/or an isotopomer model. The positional models are built based on the data obtained from the total amount of ^{13}C accumulated at each carbon position, regardless of the labeling situation of neighboring carbons. For example, in the case of a metabolite with four carbon positions, the total ^{13}C accumulated at position C3, will be the sum of singlet (S), doublets (D23, D34) and doublet of doublet (Q234) labeling of the metabolite, considering ^{13}C-^{13}C coupling with other ^{13}C isotopes within the same molecule. Isotopomers models take advantage of the additional dynamic ^{13}C labeling information available from ^{13}C-^{13}C multiplets. However, the dynamic measurement of labeling turnover curves of the metabolite multiplets is difficult *in vivo* due to a broader linewidth and limited sensitivity as compared to high resolution NMR. High magnetic field MRS systems allowed the dynamic detection of ^{13}C multiplets in the rat brain *in vivo* during [1-6,^{13}C$_2$] Glc or [U-^{13}C] Glc infusion (Henry et al., 2003a; Xu and Shen, 2006). All possible ^{13}C multiplets of the created isotopomers are not detectable *in vivo* with MRS tools. In this regard, a simplified model, called bonded cumomer model was introduced by Shestov et al., 2012. The bonded cumomer model considers all possible isotopmers and their multiplets that are detectable in ^{13}C spectra *in vivo* with enough precision. Consequently the number of equations will be reduced compared with the full isotopomers model, while retaining all the NMR measurable isotopomers information. In this thesis, a metabolic modeling study was performed in the rat brain during intravenous infusion of [1-6,^{13}C$_2$] Glc. Thanks to the higher sensitivity obtained at the high magnetic field of 14.1T, we were able to quantify ^{13}C turnover curves of total enrichment of Glu and Gln at positions C4, C3, C2 and their detectable multiplets (in total 17 turnover curves). Introducing additional dynamic ^{13}C information obtained from the dynamic labeling of ^{13}C multiplets in the bonded

cumomer model improved the precision and independency of the majority of the determined metabolic rates, as compared to the positional model (see Chapter 2).

1.4.5. Compartment modeling

To understand the neuronal and glial oxidative reactions and neurotransmission process in the brain, compartmental modeling is used for the analysis of ^{13}C NMR data obtained during infusion of labeled substrates. The compartments in ^{13}C NMR metabolic modeling are usually defined as cellular entities (neurons, astrocytes, etc.) between which the set of labeled pools are distributed and interconnected by biochemical fluxes. The configuration of compartments is based on the proposed hypothesis on the biochemical and physiological details of the metabolic system, as reported by previous biochemical studies of brain tissue. The number of compartments varies from one single compartment to multiple compartments (two or three compartments) in the different reported *in vivo* ^{13}C NMR studies (Duarte and Gruetter, 2013; Gruetter et al., 2001; Henry et al., 2006a; Patel et al., 2005; Rodrigues et al., 2013). The choice of the model depends on several parameters, including the known biochemical pathways for the chosen ^{13}C labeled substrate, level of details of the experimental ^{13}C NMR data (e.g. number of measured carbon positions and temporal resolution) and metabolic fluxes that are adjusted as free parameters or fixed based on previous studies. The number of measured ^{13}C turnover curves for the different metabolites and the number of free parameters in the model have an effect on the accuracy and stability of the model and derived metabolic fluxes. The number of free parameters should be kept as low as possible to avoid multiple solutions for estimating the metabolic rates, while still having a complete description of the measurements with the model output curves.

Two-compartment modeling combined with dynamic ^{13}C MRS has proven to be a powerful tool to probe oxidative metabolism as well as the glutamate-glutamine cycle between the neuronal and glial cell (associated to glutamatergic neurotransmission) in rodent studies and humans (Gruetter et al., 2001a; Henry et al., 2006b). The two-compartment model consists of two main metabolic compartments corresponding to the neuronal and glial cells. Each compartment has its respective TCA cycle and both compartments are linked by the Glu-Gln cycle. In Chapter 2 of this thesis, a two-compartment model was used for the analysis of ^{13}C labeling turnover curves of Glu and Gln.

1.4.6. Mass and isotopic balance equations

Once the model is defined, differential equations expressing the flow of mass and ^{13}C labeling among metabolic pools will be generated and solved using numerical tools. Any active metabolic pool in a compartment has carbon chain flowing into and out of it, adding or removing mass. The relationship between the inflow and outflow can be described by a mass balance equation. Considering three metabolic pools S, P, F as in Fig 1.22, there is a net influx V_{in} from S to P and net out flux V_{out} from P to F. Metabolic fluxes V_{in} and V_{out} are defined as the amount of metabolite molecules in one pool converted to another metabolite in the next pool and is usually given in $\frac{mM}{s}$ or $\frac{\mu mol}{g.s}$. Metabolic fluxes are proportional with the conversion speed of a molecule from a metabolic pool into a molecule in another metabolic pool, called reaction rate k (s^{-1}). Thus metabolic fluxes are written mathematically as:

$$V_{in} = k_{S-P}[S] \qquad\qquad \text{Eq. 1.111}$$

$$V_{out} = k_{P-F}[P] \qquad\qquad \text{Eq. 1.112}$$

where $[S]$ and $[P]$ are the concentrations of the substrate S and product P (in mM or $\frac{\mu mol}{g}$).

The temporal changes of the pool size of product P correspond to the amount of substrate converted to product P minus the amount of product P converted to F. Thus, the mass balance equation is written as:

$$\frac{d[P(t)]}{dt} = V_{in} - V_{out}$$
Eq. 1.113

In most cases in ^{13}C NMR studies, there is a metabolic steady state condition for metabolites pool size, expressed as a constant concentration for all metabolites. Thus, the mass balance equation simplifies to:

$$V_{in} = V_{out}$$
Eq. 1.114

Introducing a label in the substrate such as ^{13}C allows to follow the temporal evolution of ^{13}C labeling of pool P and provides information about the dynamic behavior of P. Mathematically, the dynamic ^{13}C labeling of product P, called isotope-balance equation, can be described by:

$$\frac{d[P^*(t)]}{dt} = V_{in}\frac{[S^*(t)]}{[S]} - V_{out}\frac{[P^*(t)]}{[P]}$$
Eq. 1.115

where the superscript star (*) indicates the ^{13}C labeling of the corresponding metabolite and the ratio of labeled concentration to unlabeled concentration of metabolite, $\frac{[P^*(t)]}{[P]}$, is typically referred to as the fractional enrichment ($o \le FE \le 1$) of the metabolite.

If a step function is considered for the labeling of the substrate (such as labeling Glc in plasma),^{13}C label in substrate will increase abruptly from the basal level to an optimum final level. Consequently the fractional enrichment of the substrate can be assumed constant over time.

$$\begin{cases} FE_S = 0 & t < 0 \\ FE_S = Const & t > 0 \end{cases}$$
Eq. 1.116

As a consequence, the temporal enrichment of the product at metabolic steady state condition ($V_{in} = V_{out}$) is determined as:

$$FE_P(t) = FE_S\left(1 - e^{-\frac{V_{in}}{[p]}t}\right)$$
Eq. 1.117

Eq. 1.117 demonstrates that the fraction enrichment of product P builds up as an exponential function to reach the fractional enrichment of the substrate at a rate of $\frac{V_{in}}{[p]}$ (see Fig 1.22). Thus the labeling turnover curve of a large metabolite pool is slower than for a small metabolite pool. In case of a substrate with a time dependent FE, solving the isotope balance equation is more complex and typically needs a numerical approach.

The mass balance and isotope balance equations could be generalized to multiple inflow and outflow pathways into a single pool.

$$\frac{d[P(t)]}{dt} = \sum_{j=1}^{n} V_{in}^j - \sum_{j=1}^{m} V_{out}^j$$
Eq. 1.118

$$\frac{d[P^*(t)]}{dt} = \sum_{j=1}^{n} V_{in}^j FE_S^j(t) - \sum_{j=1}^{m} V_{out}^j FE_p(t)$$
Eq. 1.119

Where n and m indicate the number of inflow and outflow pathways, respectively. Based on the mass balance and isotope balance equations, differential equations can be generated for all metabolic pools,

thereby making up the metabolic model (see appendix of Chapter 2). These differential equations will be implemented in software such as Matlab and solved using the numerical calculations.
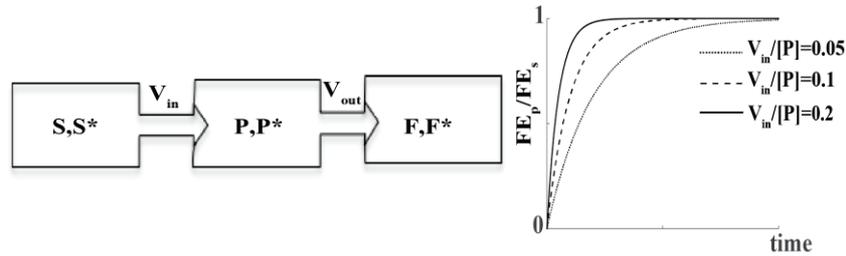

Fig 1.22 Inflow of label from pool S to P, V_{in}, and outflow of label from P to F, V_{out}. The time evolution of the fractional enrichment of pool P follows an exponential function with a rate of $\frac{V_{in}}{[p]}$ in case of metabolic steady state condition ($V_{in} = V_{out}$), assuming a step function increase in the fractional enrichment of substrate pool S at time t = 0.

1.4.7. Fitting procedure, evaluation of fit reliability

Systems of equations describing the labeling of the observable metabolites are generated based on the mass and isotope balance equations. These equations are implemented in the given model and solved using numerical approaches to find the optimum value of metabolic fluxes that describe the experimental data. The metabolic fluxes in the model are the free parameters of the regression process. To find the value of free parameters, the model output functions are fitted to the experimental data. The most common way to measure the proximity of the data to the simulation is the least square criterion. Least square fitting finds the optimal model curves to a given set of data by minimizing χ^2 which given by:

$$\chi^2 = \sum_{i=1}^{n} [f(a_{1\dots m}, t_i) - y(t_i)]^2 \qquad \text{Eq. 1.120}$$

Where $y(t_i)$ is the i th experimental observation at time t_i and $f(a_{1\dots m}, t_i)$ is the simulated function calculated at time t_i. For a straight line, which has two free parameters (slope and intercept), least square fitting yields analytically to the value of these two free parameters(Hansen et al., 2012).

For most cases in the metabolic modeling, there are no analytical solutions for the best value of the fitted parameters and they must be determined with iterative procedures. The Levenberg-Marquardt algorithm is the most common fitting iterative procedure for the analysis of data from biochemical pathway.

The reliability of the determined fluxes can be assessed using Monte Carlo simulations. Briefly, random Gaussian noise is added to the least square fit to generate a simulated noisy data set. The amplitude of the noise can be determined based on the difference between the measured and simulated data in fitting (when the model describes the experimental data properly). The noisy simulated data is then fitted to the same model as for the experimental and the simulated metabolic rates are extracted. The process of generating noisy data is repeated many times (100 or 500 or even more) to generate a histogram of distribution of the fitted parameters. The distribution of simulated parameters yields the standard deviation of the estimated metabolic rates, as well as information on the skewness of the distribution.

When not enough is known about the nature of the measurement errors to do a Monte Carlo simulation, there is another powerful technique, called bootstrap method(Haukoos and Lewis, 2005). Bootstrapping relies on random sampling with replacement and allows estimation of the sampling distribution of almost any statistics. Let's consider the measured data sets as D_0^m, which has n data points and the number of sets is determined by repetitions number of experiment. The bootstrap method uses the actual data sets for every data point and generates any number of synthetic data sets $D_1^s, D_2^s, ...$ also with n data points. The procedure is simply to draw N data points with replacement from the set D_0^m. In this way the generated synthetic data sets could replace Monte Carlo simulation to estimate the distribution of estimated parameters in the model. The basis behind the bootstrap method is that the actual data set, viewed as a probability distribution consisting of delta functions at the measured values, is in the most cases the best or only available estimator of the underlying probability distribution (Press, 2007).

1.5.References

1. Ackerman, J.J.H., Grove, T.H., Wong, G.G., Gadian, D.G., Radda, G.K., 1980. Mapping of metabolites in whole animals by ^{31}P NMR using surface coils. Nature 283, 167–170. doi:10.1038/283167a0

2. Becker, E.D., 2000. Chapter 6 - Structure and Analysis of Complex Spectra, in: High Resolution NMR (Third Edition). Academic Press, San Diego, pp. 139–181.

3. Bloch, F., Hansen, W.W., Packard, M., 1946. The Nuclear Induction Experiment. Phys. Rev. 70, 474–485. doi:10.1103/PhysRev.70.474

4. Bloch, F., Siegert, A., 1940. Magnetic Resonance for Nonrotating Fields. Phys. Rev. 57, 522–527. doi:10.1103/PhysRev.57.522

5. Carlson, J.W., Derby, K.A., Hawryszko, K.C., Weideman, M., 1992. Design and evaluation of shielded gradient coils. Magn. Reson. Med. 26, 191–206. doi:10.1002/mrm.1910260202

6. Cavanaugh, J.R., Dailey, B.P., 1961. Proton chemical shifts for the Alkyl derivatives. J. Chem. Phys. 34, 1099–1107. doi:10.1063/1.1731707

7. Cooper, A.J., Plum, F., 1987. Biochemistry and physiology of brain ammonia. Physiol. Rev. 67, 440–519.

8. Crank, J., 1979. The Mathematics of diffusion. Clarendon Press.

9. de Graaf, R.A., Rothman, D.L., Behar, K.L., 2011. State-of-the-Art direct 13C and indirect ^{1}H-[^{13}C] NMR spectroscopy *in vivo*. NMR Biomed. 24, 958–972. doi:10.1002/nbm.1761

10. Dickinson, W.C., 1950. Dependence of the F19 nuclear resonance position on chemical compound. Phys. Rev. 77, 736–737. doi:10.1103/PhysRev.77.736.2

11. Doddrell, D.M., Pegg, D.T., Bendall, M.R., 1982. Distortionless enhancement of NMR signals by polarization transfer. J. Magn. Reson. 48, 323–327. doi:10.1016/0022-2364(82)90286-4

12. Duarte, J.M.N., Gruetter, R., 2013. Glutamatergic and GABAergic energy metabolism measured in the rat brain by (13) C NMR spectroscopy at 14.1 T. J. Neurochem. 126, 579–590. doi:10.1111/jnc.12333

13. Duckrow, R.B., Bryan, R.M., 1987. Regional cerebral glucose utilization during hyperglycemia. J. Neurochem. 48, 989–993.

14. Geballe, T.H., Hulm, J.K., 1980. Superconductors in electric-power technology. Sci. Am. 243, 138–172. doi:10.1038/scientificamerican1180-138

15. Gruetter, R., Seaquist, E.R., Ugurbil, K., 2001. A mathematical model of compartmentalized neurotransmitter metabolism in the human brain. Am. J. Physiol. Endocrinol. Metab. 281, E100-112.

16. Haase, A., Frahm, J., Hänicke, W., Matthaei, D., 1985. ^{1}H NMR chemical shift selective (CHESS) imaging. Phys. Med. Biol. 30, 341–344.

17. Hahn, E.L., 1950. Spin Echoes. Phys. Rev. 80, 580. doi:10.1103/PhysRev.80.580

18. Hansen, P.C., Pereyra, V., Scherer, G., 2012. Least squares data fitting with applications. Johns Hopkins University Press, Baltimore, Md.

19. Hardy, C.J., Giaquinto, R.O., Piel, J.E., Rohling, K.W., Marinelli, L., Blezek, D.J., Fiveland, E.W., Darrow, R.D., Foo, T.K.F., 2008. 128-channel body MRI with a flexible high-density receiver-coil array. J. Magn. Reson. Imaging JMRI 28, 1219–1225. doi:10.1002/jmri.21463.

20. Haukoos, J., Lewis, R., 2005. Advanced statistics: bootstrapping confidence intervals for statistics with "difficult" distributions. PubMed – NCBI.

21. Hayes, C.E., Edelstein, W.A., Schenck, J.F., Mueller, O.M., Eash, M., 1985. An efficient, highly homogeneous radiofrequency coil for whole-body NMR imaging at 1.5 T. J. Magn. Reson. 63, 622–628. doi:10.1016/0022-2364(85)90257-4

22. Henry, P.-G., Adriany, G., Deelchand, D., Gruetter, R., Marjanska, M., Oz, G., Seaquist, E.R., Shestov, A., Uğurbil, K., 2006b. *In vivo* ^{13}C NMR spectroscopy and metabolic modeling in the brain: a practical perspective. Magn. Reson. Imaging 24, 527–539. doi:10.1016/j.mri.2006.01.003

23. Henry, P.-G., Lebon, V., Vaufrey, F., Brouillet, E., Hantraye, P., Bloch, G., 2002. Decreased TCA cycle rate in the rat brain after acute 3-NP treatment measured by *in vivo* ^{1}H-[^{13}C] NMR spectroscopy. J. Neurochem. 82, 857–866.

24. Henry, P.-G., Oz, G., Provencher, S., Gruetter, R., 2003a. Toward dynamic isotopomer analysis in the rat brain *in vivo*: automatic quantitation of ^{13}C NMR spectra using LCModel. NMR Biomed. 16, 400–412. doi:10.1002/nbm.840

25. Henry, P.-G., Tkác, I., Gruetter, R., 2003b. ^{1}H-localized broadband ^{13}C NMR spectroscopy of the rat brain *in vivo* at 9.4 T. Magn. Reson. Med. 50, 684–692. doi:10.1002/mrm.10601

26. Hidalgo-Tobon, S. s., 2010. Theory of gradient coil design methods for magnetic resonance imaging. Concepts Magn. Reson. Part A 36A, 223–242. doi:10.1002/cmr.a.20163

27. Hoult, D.I., Busby, S.J., Gadian, D.G., Radda, G.K., Richards, R.E., Seeley, P.J., 1974. Observation of tissue metabolites using ^{31}P nuclear magnetic resonance. Nature 252, 285–287.

28. Hoult, D.I., Richards, R.E., 1976. The signal-to-noise ratio of the nuclear magnetic resonance experiment. J. Magn. Reson. 1969 24, 71–85. doi:10.1016/0022-2364(76)90233-X.

29. Hrabe, J., Kaur, G., Guilfoyle, D., 2007. Principles and limitations of NMR diffusion measurements. J. Med. Phys. 32, 34. doi:10.4103/0971-6203.31148

30. Keeler, J., 2011. Understanding NMR Spectroscopy. John Wiley & Sons.

31. Kvamme, E., Torgner, I.A., Svenneby, G., 1985. Glutaminase from mammalian tissues. Methods Enzymol. 113, 241–256.

32. Lauterbur, P.C., 1973. Image formation by induced local interactions: examples employing nuclear magnetic resonance. Nature 242, 190–191. doi:10.1038/242190a0

33. Leifer, M.C., 1997. Resonant modes of the birdcage Coil. J. Magn. Reson. 124, 51–60. doi:10.1006/jmre.1996.7488

34. Lian, J., Roemer, P., 1998. MRI RF coil. patent U.S. 5.

35. Lowe, I.J., Tarr, C.E., 1968. A fast recovery probe and receiver for pulsed nuclear magnetic resonance spectroscopy. J. Phys. 1, 320–322. doi:10.1088/0022-3735/1/3/312

36. Mansfield, P., Chapman, B.L., Bowtell, R., Glover, P., Coxon, R., Harvey, P.R., 1995. Active acoustic screening: reduction of noise in gradient coils by Lorentz force balancing. Magn. Reson. Med. 33, 276–281.

37. Mansfield, P., Grannell, P.K., 1973. NMR "diffraction" in solids? J Phys C 6 22, L422–L426.

38. McFarland, E.W., Rosen, B.R., 1986. NMR instrumentation and hardware available at present and in the future. Cardiovasc. Intervent. Radiol. 8, 238–250.

39. Meister, A., 1985. Glutamine synthetase from mammalian tissues. Methods Enzymol. 113, 185–199.

40. Ohliger, M.A., Sodickson, D.K., 2006. An introduction to coil array design for parallel MRI. NMR Biomed. 19, 300–315. doi:10.1002/nbm.1046

41. Patel, A.B., de Graaf, R.A., Mason, G.F., Rothman, D.L., Shulman, R.G., Behar, K.L., 2005. The contribution of GABA to glutamate/glutamine cycling and energy metabolism in the rat cortex *in vivo*. Proc. Natl. Acad. Sci. U. S. A. 102, 5588–5593. doi:10.1073/pnas.0501703102.

42. Posse, S., Cuenod, C.A., Le Bihan, D., 1993. Human brain: proton diffusion MR spectroscopy. Radiology 188, 719–725. doi:10.1148/radiology.188.3.8351339.

43. Press, W.H., 2007. Numerical Recipes 3rd Edition: The Art of scientific computing. Cambridge university press.

44. Proctor, W.G., Yu, F.C., 1950. The dependence of a nuclear magnetic resonance frequency upon chemical compound. Phys. Rev. 77, 717–717. doi:10.1103/PhysRev.77.717

45. Reynolds, G., Wilson, M., Peet, A., Arvanitis, T.N., 2006. An algorithm for the automated quantitation of metabolites in *in vitro* NMR signals. Magn. Reson. Med. 56, 1211–1219. doi:10.1002/mrm.21081

46. Rodrigues, T.B., Valette, J., Bouzier-Sore, A.-K., 2013. (13)C NMR spectroscopy applications to brain energy metabolism. Front. Neuroenergetics 5, 9. doi:10.3389/fnene.2013.00009

47. Shestov, A.A., Valette, J., Deelchand, D.K., Uğurbil, K., Henry, P.-G., 2012. Metabolic modeling of dynamic brain ^{13}C NMR multiplet data: concepts and simulations with a two-compartment neuronal-glial model. Neurochem. Res. 37, 2388–2401. doi:10.1007/s11064-012-0782-5

48. Singer, J.R., 1959. Blood flow rates by nuclear magnetic resonance measurements. Science 130, 1652–1653. doi:10.1126/science.130.3389.1652

49. Slotboom, J., Boesch, C., Kreis, R., 1998. Versatile frequency domain fitting using time domain models and prior knowledge. Magn. Reson. Med. 39, 899–911. doi:10.1002/mrm.1910390607

50. Soerensen, O.W., Eich, G.W., Levitt, M.H., Bodenhausen, G., Ernst, R.R., 1983. Product operator formalism for the description of NMR pulse experiments. Prog. Nucl. Magn. Reson. Spectrosc. 16, 163–92.

51. Stefan, D., Cesare, F.D., Andrasescu, A., Popa, E., Lazariev, A., Vescovo, E., Strbak, O., Williams, S., Starcuk, Z., Cabanas, M., Ormondt, D. van, Graveron-Demilly, D., 2009.

Quantitation of magnetic resonance spectroscopy signals: the jMRUI software package. Meas. Sci. Technol. 20, 104035. doi:10.1088/0957-0233/20/10/104035

52. Stejskal, E.O., Tanner, J.E., 1965. Spin Diffusion measurements: spin echoes in the presence of a Time-dependent field gradient. J. Chem. Phys. 42, 288–292. doi:10.1063/1.1695690

53. Stephen Provencher, 2015. LCModel & LCMgui User's Manual. URL http://s-provencher.com/pub/LCModel/manual/manual.pdf.

54. Suryan, G., 1951. , in: Proc. Indian Acad. Sci A33. p. 107.

55. Tkác, I., Starcuk, Z., Choi, I.Y., Gruetter, R., 1999. *In vivo* ^{1}H NMR spectroscopy of rat brain at 1 ms echo time. Magn. Reson. Med. 41, 649–656.

56. Wright, S.M., Wald, L.L., 1997. Theory and application of array coils in MR spectroscopy. NMR Biomed. 10, 394–410.

57. Xu, S., Shen, J., 2006. *In vivo* dynamic turnover of cerebral ^{13}C isotopomers from [U-^{13}C]glucose. J. Magn. Reson. San Diego Calif 1997 182, 221–228. doi:10.1016/j.jmr.2006.07.003.

Chapter 2. Refined analysis of brain energy metabolism using *in vivo* dynamic enrichment of ^{13}C multiplets

^{13}C NMR spectroscopy in combination with the infusion of ^{13}C-labeled precursors is a unique approach to study *in vivo* brain energy metabolism. Incorporating the maximum information available from *in vivo* localized ^{13}C spectra is of importance to get broader knowledge on cerebral metabolic pathways. Metabolic rates can be quantitatively determined from the rate of ^{13}C incorporation into amino acid neurotransmitters such as glutamate and glutamine using suitable mathematical models. The time course of multiplets arising from ^{13}C-^{13}C coupling between adjacent carbon atoms was expected to provide additional information for metabolic modeling leading to potential improvements in the estimation of metabolic parameters.

The aim of the present study was to extend two-compartment neuronal/glial modeling to include dynamics of ^{13}C isotopomers available from fine structure multiplets in ^{13}C spectra of glutamate and glutamine measured *in vivo* in rat brain at 14T, termed bonded cumomer approach. Incorporating the labeling time courses of ^{13}C multiplets of glutamate and glutamine resulted in improved precision of the estimated fluxes in the rat brain as well as reduced correlations between them.

2.1. Introduction

A powerful approach to study brain metabolism has been the combination of ^{13}C-enriched substrates and *in vivo* magnetic resonance spectroscopy (Lanz et al., 2013; Rodrigues et al., 2013; Henry et al., 2006b; Mason and Rothman, 2004; Gruetter, 2002). NMR measurements enable detection of ^{13}C label incorporation from infused ^{13}C-enriched substrate (e.g. glucose) into different carbon positions of amino acids in brain such as glutamate (Glu), glutamine (Gln), and aspartate (Asp) (de Graaf et al., 2003; Gruetter et al., 2003).

Metabolic modeling of ^{13}C labeling time courses of amino acids in brain allows quantitative measurements of metabolic fluxes *in vivo* (Oz et al., 2004; Rothman et al., 2003; Gruetter et al., 2001a). In the past decade, questions have been raised concerning the reliability of some estimated fluxes in brain (Shen et al., 2009; Shestov et al., 2007; Uffmann and Gruetter, 2007) and many efforts have been undertaken to improve their accuracy through adaptation of the metabolic models used to analyze the ^{13}C turnover curves. Monte-Carlo simulations showed that an increased number of measured time courses of ^{13}C positions of Glu and Gln as input for the metabolic modeling analysis results in improved precision and reliability of brain metabolic fluxes (Shestov et al., 2007). However, the number of

measured ^{13}C labeling time courses of metabolites relies on the NMR detection method, the chosen magnetic field strength and pulse sequence and in different studies varied from two to seven ^{13}C uptake curves (Xin et al., 2015, 2010; de Graaf et al., 2004; Choi et al., 2002; Gruetter et al., 2001a; Mason et al., 1995).

Due to the difficulty of measuring ^{13}C multiplets of Glu and Gln *in vivo* with high temporal resolution, derivation of metabolic fluxes has been performed almost exclusively using dynamic positional enrichment (e.g. Henry et al., 2006b; de Graaf et al., 2003; Gruetter et al., 2003; Duarte et al., 2011) which is the time course of total ^{13}C enrichment of each carbon position of each metabolite.

The measurement of labeling time courses of ^{13}C isotopomers noninvasively in the rat brain has been already reported by Henry et al., 2003a. A first analysis of *in vivo* measured ^{13}C dynamic labeling of isotopomers in a heart metabolic study led to improved precision of the estimated tricarboxylic acid cycle flux (Jeffrey et al., 1999). In study of brain metabolism by the same group, the ^{13}C time courses of the singlet and doublet of cerebral Glu labeled at position C4 was included in the metabolic analysis and resulted in a poorer determination of glutamate/alpha–ketoglutarate and oxaloacetate/aspartate exchange rate, called V_x (Jeffrey et al., 2013), probably reflecting the incomplete description of the Glu C4 singlet turnover by the considered metabolic model.

Recently a new ^{13}C metabolic modeling approach using the concept of bonded cumomers was proposed, taking full advantage of the available time courses of ^{13}C multiplets of Glu and Gln in the metabolic model (Shestov et al., 2012). The performance of bonded cumomers approach was evaluated based on simulated ^{13}C data by Shestov et al., 2012 who reported that the bonded cumomer approach led to better precision than the positional approach in the determination of brain metabolic fluxes using artificial ^{13}C time-courses of Glu and Gln multiplets generated with the two-compartmental description of brain energy metabolism (Gruetter et al., 2001) for different infused ^{13}C labeled substrates.

Including the individual time courses of ^{13}C multiplets in the metabolic modeling process is expected to provide more information about the number and/or precision of the metabolic fluxes of interest. Therefore, the aim of this study was to incorporate the ^{13}C dynamic labeling of observable multiplets of Glu and Gln measured with *in vivo* ^{13}C MRS in the rat brain at 14.1 T to estimate brain metabolic fluxes in the case of a neuronal-glial compartmentalized metabolic network, under infusion of [1, 6-$^{13}C_2$] glucose.

2.2. Methods

2.2.1. Animal preparation

All animal procedures were performed according to federal guidelines and approved by the local ethics committee from the canton Vaud, Switzerland. The presented ^{13}C-glucose infusion studies were performed following a previously described protocol (Duarte et al., 2011). Briefly, four male Sprague–Dawley rats (276±11 g, delivered from Charles River Laboratories, France) were fasted for 6 h prior to the NMR experiment. Animals were intubated and ventilated with 2% isoflurane during surgery. Both femoral veins were catheterized for the administration of glucose and α-chloralose for anesthesia. Two arteries were cannulated for continuous monitoring of physiology (blood pressure, heart rate) and periodic blood sampling for blood gas, plasma lactate and glucose concentration measurements as well as for further high resolution NMR analyses of substrates ^{13}C enrichment. Body temperature was maintained between 37.0 and 37.5 °C with a temperature-regulated circulating water bath. Following surgery, anesthesia was switched to intravenous α–chloralose administration (bolus of 80mg/kg and

continuous infusion rate of 28 mg/kg/h). Animals were placed in a home-built holder and the head position was fixed using ear rods and a bite-bar.

After adjustment of MRS parameters, an exponentially decaying 5 minutes bolus of 99%-enriched [1, 6-^{13}C$_2$] glucose (1.1 M in saline solution) was administered. The volume of this bolus was adapted to the basal glycemia in order to reach 70% plasma glucose fractional enrichment at the end of the 5 minutes. The bolus was followed by a continuous infusion of 70%-enriched glucose at a rate equivalent to the whole body glucose disposal rate of 33.2 mg/kg/min (Jucker et al., 2002) and adjusted based on periodically measured arterial plasma glucose concentrations in order to maintain a constant glycemia of 350 mg/dl throughout the experiment. This protocol results in a stable 70% plasma glucose fractional enrichment reached within 5 minutes (Henry et al., 2002).

At the end of experiment, rats were sacrificed and brain extracts prepared as previously described (Duarte et al., 2007) for further processing and analysis.

2.2.2.   In vivo and in vitro NMR spectroscopy

All *in vivo* and *in vitro* data have been measured by Duarte et al., 2011 and 2013 at Centre d'Imagerie BioMédicale (CIBM), Lausanne. I briefly explain the protocol taken for acquisition of MRS data in following.

In vivo spectra were acquired on a 14.1 T MRI system interfaced to a 26-cm horizontal bore magnet (Varian, Palo Alto, CA, USA; Magnex Scientific, Oxford, UK), equipped with 12 cm inner diameter actively-shielded gradient reaching 400 mT/m in 120 μs.

The coil assembly consisted of a home-built ^{1}H quadrature surface coil and an inner ^{13}C linearly polarized surface coil.

After initial setting, fast spin echo images (TR= 5 s and TE = 52 ms; eight echoes) were acquired to select a volume of interests (VOI) 320 μl in the brain. Magnetic field homogeneity was adjusted using FAST(EST)MAP (Gruetter and Tkác, 2000). Localized ^{1}H NMR spectra were acquired using the spin-echo full-intensity acquired localized spectroscopy (SPECIAL) sequence (echo time of 2.8 ms and repetition time of 4s). During the labeling experiment, ^{13}C NMR spectra were acquired *in vivo* using the semi-adiabatic distortionless enhancement by polarization transfer (DEPT) technique combined with 3D-ISIS ^{1}H localization (Henry et al., 2003b).

Water-soluble metabolites from brain extract and plasma samples were quantified by ^{1}H and ^{13}C NMR spectroscopy with a 14.1T DRX-600 spectrometer equipped with a 5-mm cryo-probe (BrukerBioSpin SA, Fällanden, Switzerland).

2.2.3.   Spectral analysis

The signal to noise ratio (SNR) of acquired ^{13}C spectra is an important factor for the accuracy and precision in quantification of individual ^{13}C multiplets of Glu and Gln labeled at positions C4, C3 and C2. To achieve higher SNR, a possibility is to increase temporal averaging of ^{13}C spectra acquired with 5.3 min time resolution. After correction for phase and frequency drifts, consecutive MRS acquisition blocks were summed two by two resulting in dynamic spectral data with 10.6 min resolution. For every time point, the 10.6 min spectra from four animals were combined to a single dataset after correction for frequency drifts. In the averaging process, the possible time shifts between different animals due to intermediate periods of shimming were taken into account. Summed ^{13}C NMR *in vivo* spectra were processed using LCModel (Stephen Provencher Inc., Oakville, ON, Canada). The basis sets for LCModel were generated using Matlab (TheMathWorks, Natick, MA, USA) by simulating each ^{13}C isotopomer with the appropriate chemical-shift and J-coupling pattern as described by Henry et al.,

(2003b). The dynamically measured ^{13}C spectra were scaled based on the Glu pool size measured with ^{1}H MRS and the fractional enrichment (FE) of GluC3, which was determined with the following formula: FE (C3) =C4 D34/ (C4 S+C4 D34) where C4 D34 indicates area of the C4 doublet resulting from double labeling of Glu at position C4 and C3, and C4 S the singlet area of Glu at position C4. Multiplets of GluC4 resonances were averaged over the last 30 min, assuming steady state enrichment for GluC4 at this later stage of infusion.

Correction factors, found by *in vitro* ^{13}C NMR spectra from brain extracts and standard solutions containing the metabolites of interest (Duarte and Gruetter, 2013), were applied to account for the relative different efficiencies in signal enhancement by polarization transfer in DEPT for the considered carbon positions of Glu and Gln.

2.2.4.   Labeling chain of metabolites by [1,6-^{13}C$_2$] Glc

Glucose labeled at positions C1 and C6, [1,6-^{13}C$_2$] Glc, has been an interesting substrate for intravenously infusion in animal in *in vivo* ^{13}C NMR study. Double ^{13}C labeled glucose offers high sensitivity detection because of double labeling of metabolites in the brain. After transport of [1,6-^{13}C$_2$] Glc, two molecules of pyruvate labeled at position C3 will be generated by the glycolysis and enter the TCA cycle. Fig 2.1 shows the different molecules and chemical reactions involved in the TCA cycle. Pyruvate enters both the glial and neuronal TCA cycle and is in exchange with cytosolic amino acids glutamate and aspartate.

Two molecule of PyrC3 enter the TCA cycle and label citrate at the position C4. In the first turn of ^{13}C in the TCA cycle, OG is labeled at position C4 and later transfers its label to Glu at the same position. Presenting symmetric succinate molecule in the following path of ^{13}C gives rise to labeling of OG at position C2 and C3 in the second turn of the TCA cycle. Through the transmitochondrial label exchange, GluC3 and GluC2 are labeled from OGC2 and OGC3, respectively.

In the third turn of the TCA cycle, the half of labeled carbons at the position C3 of OG goes to the position C2 of the same molecule, while the other half remain at the same position. In the same time, OGC2 transfer its label to the position C1 of same molecule, result in labeling the position C1 of glutamate. The resonance of Glu at position C1 is appeared at large chemical shift in ^{13}C spectra, therefore it is not simultaneously measurable with Glu at positions C4, C3 and C2 using ^{13}C MRS.

Through anaplerotic pathway in the glial compartment, PyrC3 labels the position C2 of OAA, which further labels the position C2 of OGG and glial Glu. Anaplerotic pathway also dilutes the position C3 of glial glutamate that cause forming different dynamic turnover curves for Glu and Gln following [1,6-^{13}C$_2$] Glc infusion (see Fig 2.2). Also the glial AcCoA is diluted at the entrance of the glial TCA cycle by alternative non-labeled glial substrates such as acetate or fatty acids

In the Glu/Gln cycle, the carbon position is kept, e.g. the Glu labeled at the position C4 transfers its label to the position C4 of Gln. Moreover, in the malate-aspartate shuttle the labels at a given carbon position of OAA are transferred to the same carbon position in Asp.

TCA cycle:
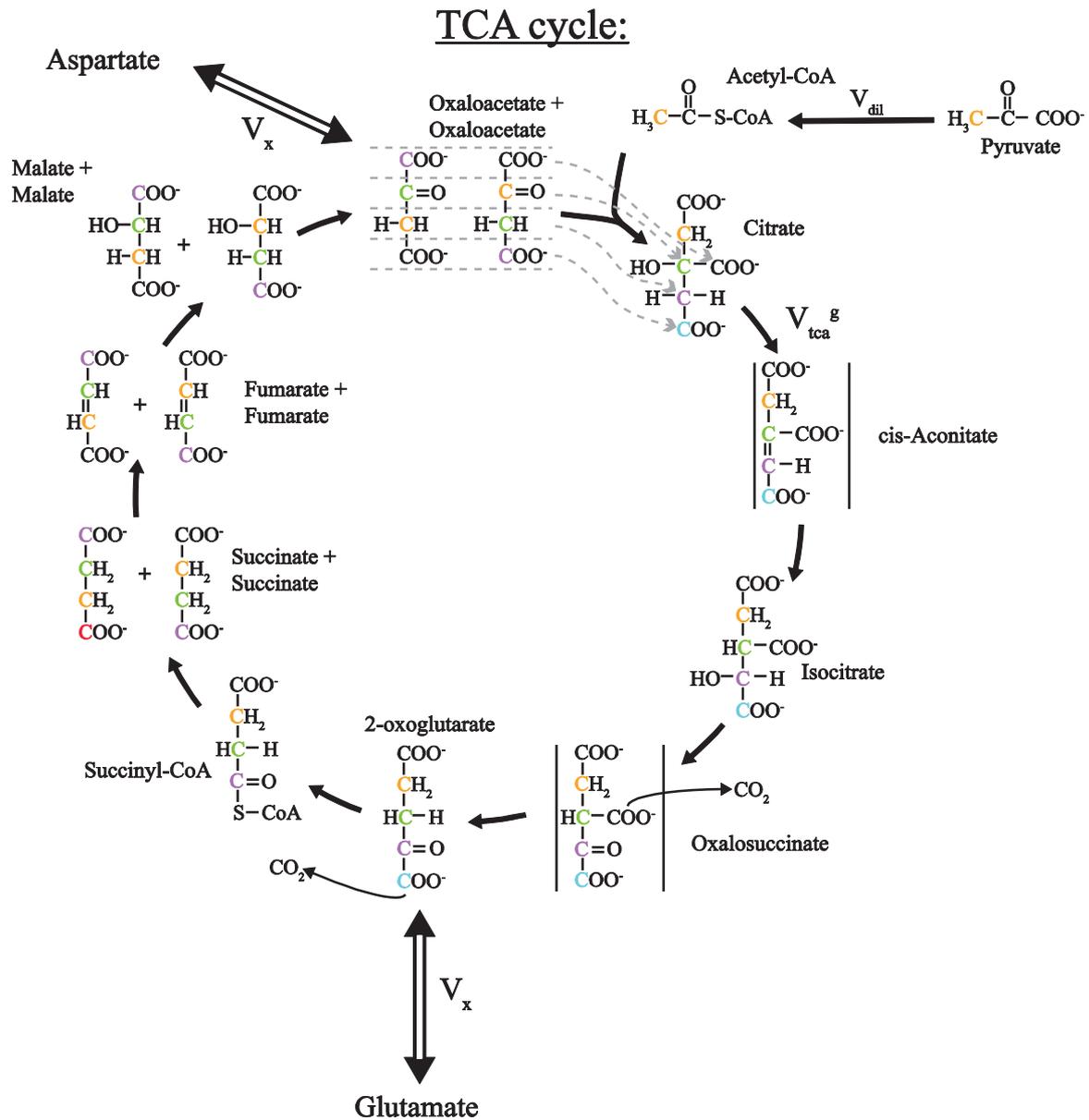
Fig 2.1 Metabolic pathway for labeled pyruvate through pyruvate dehydrogenase path. The color-coding allows following carbon labeling from one molecule to the next. The carbon positions of glutamate are identical to those of 2-oxoglutarte (modified figure by Lanz, PhD thesis, 2012).

Pyruvate carboxylation:
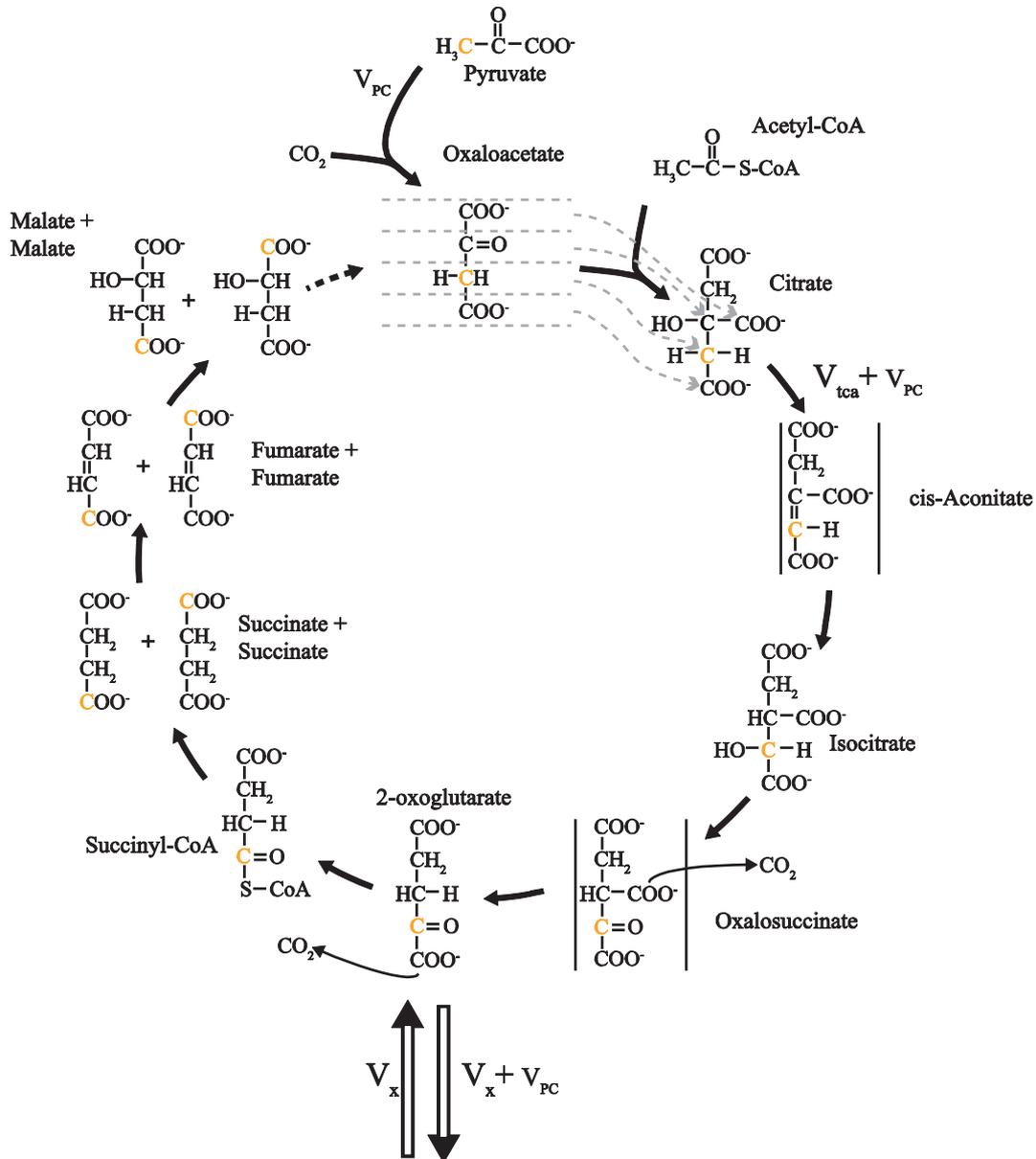
Fig 2.2 Metabolic pathway for labeled pyruvate through pyruvate carboxylation path (modified figure by Lanz, PhD thesis, 2012).

2.2.5. Metabolic modeling

The ^{13}C turnover curves of Glu and Gln were analyzed using a metabolic model built based on the bonded cumomers concept (Shestov et al., 2012) in the case of a two-compartment neuronal-glial metabolic network description (adapted from Gruetter et al., 2001) , shown in Fig 2.3. This model was adapted to include a non-zero concentration of aspartate in the glial compartment and a dilution factor at the level of glial acetyl-CoA as in previous study by Duarte et al., 2011. This model introduces and

assesses a new metabolic modeling approach that allows the analysis of individual ^{13}C multiplets time courses of *in vivo* NMR spectra from the rat brain.

The principles of bonded cumomers modeling were explained comprehensively by Shestov et al., 2012. The cumomer fraction, abbreviated word of cumulated isotopomer fraction, is sum of isotopomer fractions of a metabolite and can be calculated from the isotopomer fractions and vice versa. In other word, cumomer fraction, noted $\pi_{M\{i\}}$, is simply the sum of isotopomer fractions for all isotopomers of the molecule M labeled at least at the set of positions $\{i\} = i_1, i_2, \dots, i_n$ independently from the label at other positions. The size n of the set $\{i\}$ will be referred to as the order of the π–function. Cumomer fraction could be assigned to a virtual molecule, called cumomer. Clearly, a cumomer is not a real particle but rather a set of different isotopomer (Wiechert et al., 1999). Bonded cumomers model consider those cumomers whose indices refer to adjacent carbons because all possible metabolites isotopomers are not detectable *in vivo* by NMR. Since four different splitting patterns are possible for any carbon with two direct carbon neighbors, they can be expressed in terms of the ''bonded'' cumomer of order $n \leq 3$.

The following equation shows the transformation for all observable Glu multiplets of the position C4 in a ^{13}C spectrum, where the indexes S, D and Q refer to singlet, doublet and doublet of doublet in the GluC4 signal, to the related cumomer fractions:

$$\begin{pmatrix} GluC4\ Q \\ GluC4\ D43 \\ GluC4\ D45 \\ GluC4\ S \end{pmatrix} = \begin{pmatrix} 0 & 0 & 0 & 1 \\ 0 & 1 & 0 & -1 \\ 0 & 0 & 0 & -1 \\ 1 & -1 & -1 & 1 \end{pmatrix} \times \begin{pmatrix} \pi_{Glu\{4\}} \\ \pi_{Glu\{3,4\}} \\ \pi_{Glu\{4,5\}} \\ \pi_{Glu\{3,4,5\}} \end{pmatrix} \qquad \text{Eq. 2.1}$$

Furthermore, if the couplings with the two neighboring carbons in the carbon chain of a given metabolite are identical, such as for C3 of Glu, the above equation simplifies to the following transformation, where the index T represents the triplet signal:

$$\begin{pmatrix} GluC3\ T \\ GluC3\ D \\ GluC3\ S \end{pmatrix} = \begin{pmatrix} 0 & 0 & 0 & 1 \\ 0 & 1 & 1 & -2 \\ 1 & -1 & -1 & 1 \end{pmatrix} \times \begin{pmatrix} \pi_{Glu\{3\}} \\ \pi_{Glu\{2,3\}} \\ \pi_{Glu\{3,4\}} \\ \pi_{Glu\{2,3,4\}} \end{pmatrix} \qquad \text{Eq. 2.2}$$

In the equation above, intensities are normalized so that the total signal is the sum of all multiplet components. For example, in the case of GluC4 we have:

$$GluC4\ tot = GluC4\ Q + GluC4\ D43 + GluC4\ D45 + GluC4\ S \qquad \text{Eq. 2.3}$$

The system of differential equations that describe labeling of all observable multiplets of Glu and Gln and the principal chemical intermediates implied in the generation of these multiplets was derived. The final system describing the incorporation of ^{13}C from labeled-glucose into the multiplets of Glu and Gln consisted of a total of 133 differential equations (see appendix).

The Cramer-Rao lower bounds obtained from the LCModel spectral quantification (expressed as coefficient of variation (%SD)) were used as a confidence criterion to select the measurable individual ^{13}C multiplets of each metabolite. The threshold SD to include a multiplet in the metabolic analysis was set to 15% for every observable ^{13}C multiplet of Glu or Gln at the labeling steady state.

The two-compartment metabolic model was first fitted to the ^{13}C enrichment curves of total concentration of Glu and Gln C4, C3, and C2 (i.e. the bonded cumomer model reduced to first order cumomers, i.e. positional model) over time using the Levenberg–Marquardt algorithm for non-linear regression, coupled to a Runge–Kutta method for non-stiff systems to obtain numerical solutions of the ordinary differential equations. The different ^{13}C uptake curves used in the regression were weighted according to square root of the inverse of the variance (square Cramer-Rao lower bounds) extracted

from the LCModel quantification for every data point of Glu and Gln, to correct for overweighting of noisy data in the multiple curve regression (Cobelli et al., 2000).

The reliability of the estimated fluxes in brain was derived by Monte Carlo simulation. Artificial datasets (500 series) were generated by adding random Gaussian noise with same variance as the experimental data to each model turnover curve obtained from the best fit of the experimental data. This resulted in 500 datasets with the same characteristics as the experimental data, but different noise realizations. All numerical procedures were performed in Matlab (MathWorks, Natick, MA, USA).

In a second step, the bonded cumomer model was used for fitting the time courses of both the total ^{13}C enrichment of every carbon position and every NMR-observable ^{13}C multiplet of Glu and Gln, which was detected experimentally with sufficient precision (<15% CRLB). The precision of the obtained metabolic fluxes was assessed with an equivalent Monte Carlo simulation.

To investigate the particular changes in the correlations and probability distributions of V_{dil} and V_{nt} using both the positional model and bonded cumomer model, a sensitivity analysis was undertaken for the fluxes V_{dil} and V_{nt}. The mentioned fluxes were constrained to a range of chosen values and their effect on the ^{13}C labeling curves of Glu and Gln in the positional modeling and cumomer modeling approaches were compared. For each constrained value of V_{dil} or V_{nt}, the metabolic model was fitted to the measured total ^{13}C enrichment time courses in positional modeling and total and multiplets ^{13}C enrichment time courses in bonded cumomer modeling. In the positional model, the time courses of ^{13}C multiplets of Glu and Gln were also simulated in every step of the sensitivity analysis to illustrate the separate effect of V_{dil} and V_{nt} on the simulated ^{13}C multiplets time courses and therefore the potential of adding those curves to the metabolic modeling process.

Finally, the effect of removing the time course of total ^{13}C enrichment of Glu and Gln C4, C3, and C2 in the bonded cumomer model (referred in following as Individual multiplet model) on the precision of the obtained metabolic fluxes was investigated.

Statistical significance of differences in flux values found with the various modeling approaches was tested using two-sample unpaired t-test, corrected for multiple comparisons using Bonferroni correction when necessary.
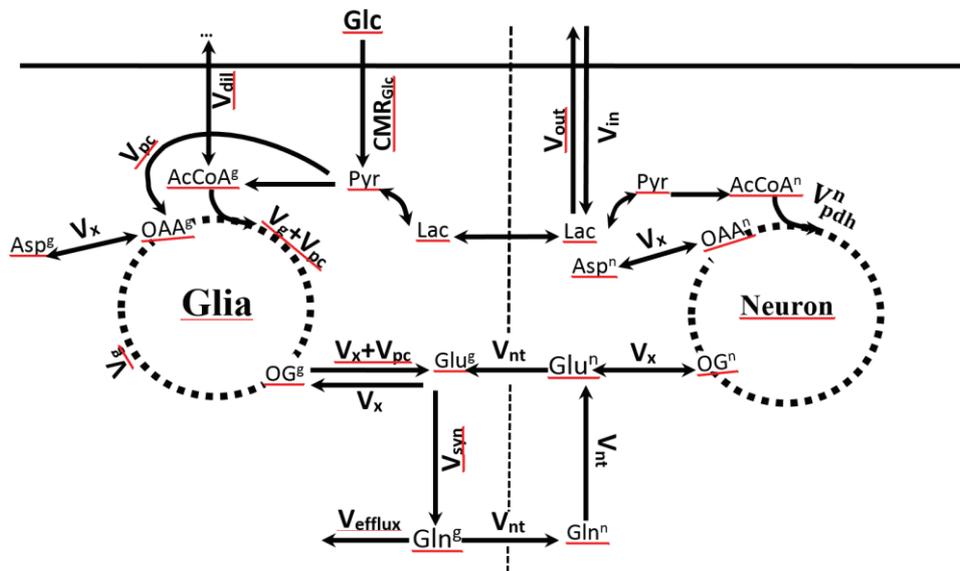
Fig 2.3 The Neuronal-glial compartmentalized metabolic network used for the different metabolic modeling approaches.
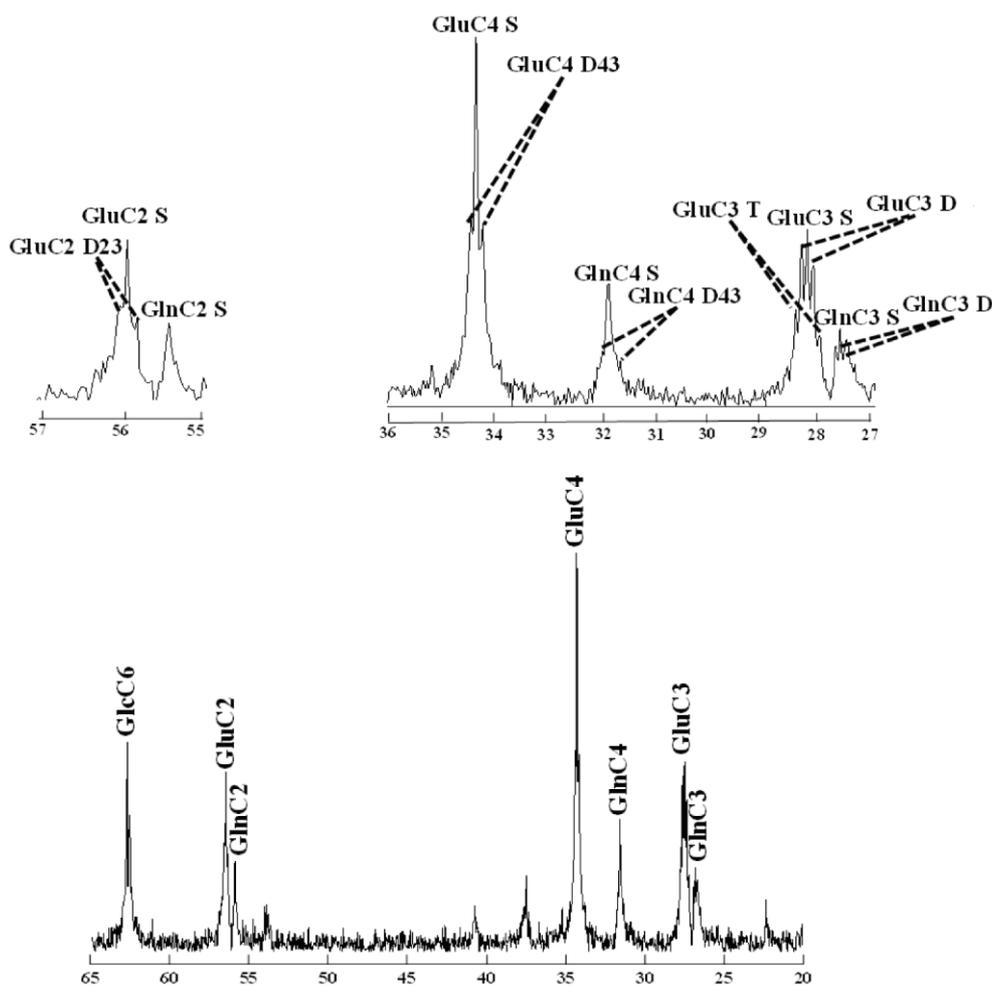
Fig 2.4 *In vivo* ^{13}C NMR spectra acquired three hours after starting [1,6-$^{13}C_2$] glucose infusion at 14.1T from a 320μL volume in the rat brain (summed spectra from four animals with averaged time of 10.6 min, no appodization applied). The fine structure of Glu and Gln at position 4, 3 and 2 is depicted in details in the enlarged spectrum in the top.

2.3. Results

To increase the signal-to-noise ratio enabling the measurement of isotopomers at low ^{13}C enrichment, temporal averaging to a time resolution of 10.6 min of the measured ^{13}C MRS data was used and ^{13}C spectra from different animals were combined prior to spectral quantification leading to spectra of higher quality and SNR (e.g. SNR of 24 after 2h [1, 6-^{13}C] Glc infusion, based on the GluC4 S peak). The high quality of the spectra was judged from the well-resolved resonances and appearance of multiplet fine structures of Glu and Gln in spatially localized ^1H-decoupled ^{13}C NMR spectra (Fig 2.4). The total metabolite concentrations measured by ^1H MRS and averaged over four animals were 8.4 ± 1.2 μmol/g for Glu, 4.3 ± 0.3 μmol/g for Gln and 2.5 ± 0.3 μmol/g for Asp.

At the beginning of the [1,6-^{13}C] glucose infusion, due to very low concentration of the singlet and triplet peak of Glu and Gln labeled at position C3, it was not possible to resolve these multiplets with enough precision in spectral fitting. These two metabolites have strong correlation from metabolic respective and underestimating the triplet peak could result in overestimating the singlet peak or vice

versa. Therefore, the sum of singlet and triplet resonances in GluC3 and GlnC3 time courses (GluC3 S+T and GlnC3 S+T) was considered as input for the cumomer model, taking advantage of the reliable spectral quantification of the summed multiplets GluC3 S+T and GlnC3 S+T, as judged from the respective Cramer-Rao lower bounds being less than 15% at steady state.

The *in vivo* time courses of total ^{13}C labeling of Glu and Gln at carbon position C4, C3 and C2 and their observable ^{13}C multiplets quantified with SD lower than 15% were considered for metabolic modeling analysis during infusion of [1,6-^{13}C] glucose (Fig 2.5). The fitted time-courses for the positional model included the total ^{13}C enrichment of Glu and Gln at positions C4, C3 and C2.

The fitted ^{13}C turnover curves for the bonded cumomers approach included the following separate components:

GluC4 total, GluC4 S, GluC4 D43, GluC3 total, GluC3 S+T, GluC3 D, GluC2 total, GluC2 S, GluC2 D23, GlnC4 total, GlnC4 S, GlnC4 D43, GlnC3 total, GlnC3 S+T, GlnC3 D, GlnC2 total, GlnC2 S (total 17 curves). The same notation as Henry at al., 2003a and Lanz et al. 2013 has been used for the different ^{13}C labeling patterns of Glu and Gln.

To determine the metabolic rates upon infusion of ^{13}C-enriched glucose, either the positional or the bonded cumomer model were fitted to the aforementioned ^{13}C time courses.

The resulting metabolic rates included neuronal TCA cycle (V_{pdh}^{n}), glial TCA cycle ($V_{TCA}^{g} = V_{g} + V_{pc}$), the malate–aspartate shuttle activity (V_{x}), apparent neuro transmission flux (V_{nt}), and glial anaplerotic pyruvate carboxylation (V_{pc}) (Table 2.1). Assuming metabolic steady-state for the metabolite pools, the Glc oxidation ($CMR_{glc(ox)}$), the inflow of labeling from extra cerebral lactate (V_{in}) and the Gln synthesis rate (V_{syn}) were calculated (Table 2.1) from the mass balance equations (See A-1). To estimate the pure effect of individual ^{13}C multiplets of metabolites as input information for metabolic modeling, brain metabolic fluxes were also estimated by considering all NMR-observable multiplets of Glu and Gln without total ^{13}C enrichment time courses (i.e. Individual multiplet model) at each carbon position (Table 2.1).

Overall, the estimated metabolic fluxes in all three approaches were precisely determined with SD lower than 20% (determined by Monte Carlo analysis), which owes to the good quality of input dynamic ^{13}C time courses with adapted time resolution and also the completeness of the used neuronal-glial metabolic model. The most significant differences in the value of estimated fluxes using the different mentioned approaches were for V_{nt} and V_{dil}, with differences of 60 % between the bonded cumomer model and positional model and 80% between the individual multiplet model and positional model.

The probability distribution of metabolic flux values, calculated by Monte Carlo simulation, was fitted with a Gamma distribution for every model (Positional model, Individual multiplet model and Bonded Cumomer model) and compared with each other (Fig 2.6). The probability density for all estimated fluxes determined by Monte Carlo simulations approached a Gaussian distribution for the three modeling approaches, as a consequence of determined flux values clearly different from zero. In general, the distributions of most metabolic fluxes in every approach were narrow, reflecting the precision of the estimated fluxes and the fact that the models are numerically identifiable.

a) Positional model

b) bonded cumomer model
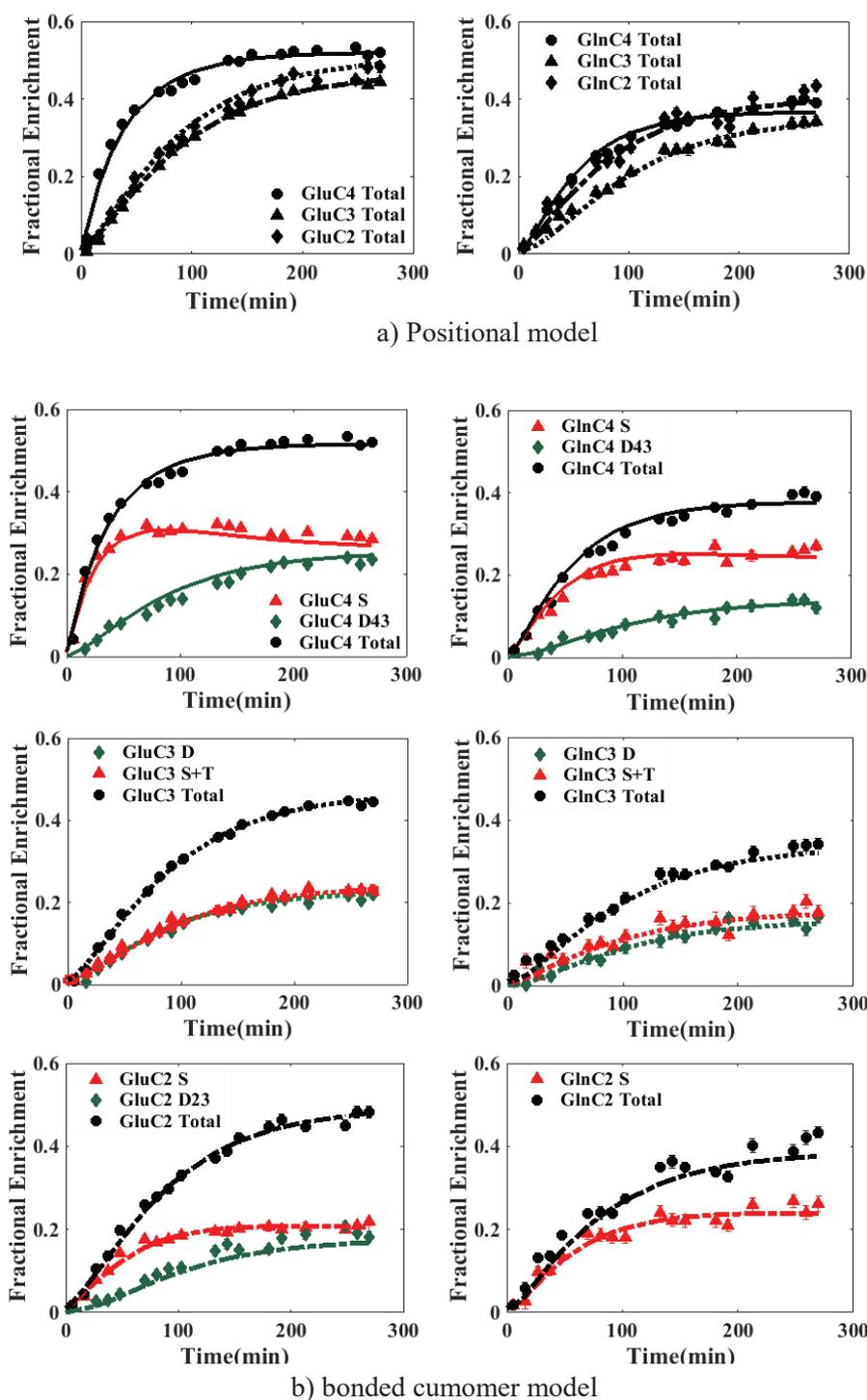
Fig 2.5 Averaged (four animals) *in vivo* time courses and model fits of Glu and Gln ^{13}C enrichment using (a) the positional model and (b) the bonded cumomer model at the carbon positions C4, C3 and C2 during [1,6-^{13}C$_2$] glucose infusion (each time point averaged over 10.6 min). Due to low concentartion of GlnC2 D23 at the beginig of [1,6-^{13}C$_2$] Glucose infusion , its timecourse was not fitted in the bonded cumomer model.

Table 2.1 The metabolic fluxes in µmol/g/min (Value ±SD) determined using the bonded cumomer model, individual multiplet model and positional model. The ±SD was determined by Monte carlo analysis over 500 simulations.

Flux (µmol/g/min)	Bonded cumomer	Individual multiplet	Positional
V_g	0. 17±0.02	0.18±0.03	0.13±0.02
V_x	0.48±0.06	0.57±0.12	0.39±0.06
V_{nt}	0.063±0.009	0.048±0.007	0.110±0.012
V_{pdh}^n	0.33±0.01	0.32±0.01	0.34±0.01
V_{out}	0.62±0.02	0.67±0.03	0.53±0.04
V_{pc}	0.040±0.002	0.037±0.003	0.041±0.003
V_{dil}	0.18±0.02	0.14±0.03	0.31±0.09
Calculated Fluxes			
V_{TCA}^g	0.21±0.02	0.22±0.03	0.17±0.02
V_{in}	0.20±0.04	0.24±0.05	0.08±0.05
V_{syn}	0.10±0.01	0.08±0.01	0.15±0.01
$CMR_{glc(ox)}$	0.29±0.02	0.29±0.03	0.28±0.02
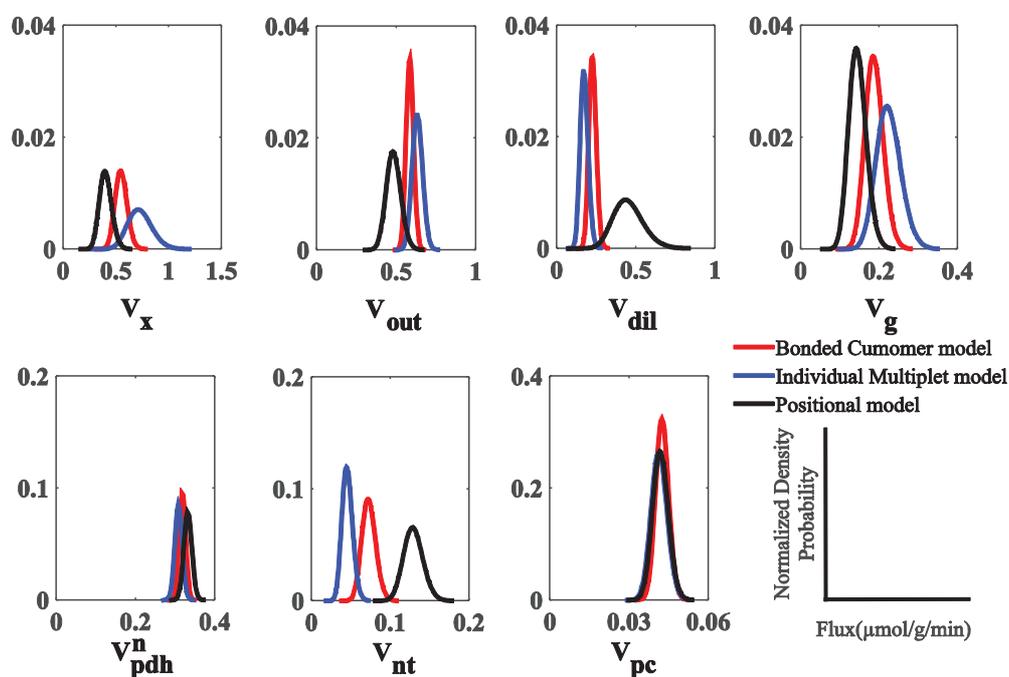
Fig 2.6 Probability distribution of the determined metabolic fluxes obtained from Monte Carlo simulations (n=500) and fitted with a Gamma distribution for visualization purposes, in the cases of the positional model, the individual multiplet model and the bonded cumomer model. The density probability is normalized to the number of simulation, n=500.

Fig 2.7 Correlation matrix between metabolic fluxes estimated from the mathematical regression of the turnover curves of Glu and Gln multiplets at position 4, 3 and 2 using a) positional model, b) bonded cumomer model and c) individual multiplet model.
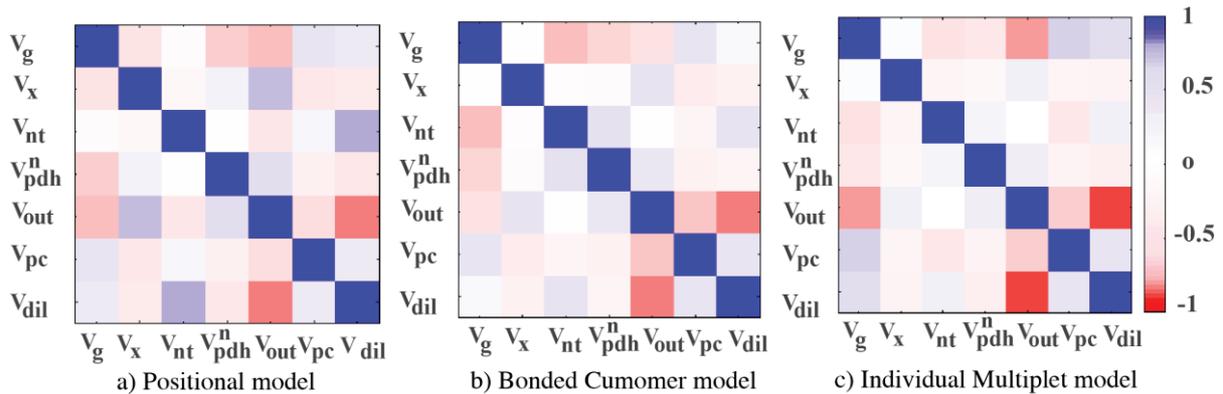
Including ^{13}C multiplets time courses of Glu and Gln in the bonded cumomer model resulted in slightly narrower distributions for most metabolic fluxes. The most significant impact was on V_{dil} distribution for which the full width at half maximum (FWHM) of the probability distribution decreased by a factor of five in the bonded cumomer model compared to the positional model. Removing total enrichment in the individual multiplet model resulted in an approximately twofold increase of the FWHM of most fluxes probability distributions, as compared to the complete bonded cumomer model.

The effect of the applied modeling approach on the correlation between metabolic fluxes (Fig 2.7) was an overall decrease of correlations between most metabolic fluxes when applying bonded cumomer modeling. V_{out} and V_{dil} showed remarkably strong correlations in every approach, more than 80%, independently of the addition of the ^{13}C multiplets turnover curves. However, introducing information about time courses of ^{13}C multiplets of Glu and Gln had significant impact on reducing correlation between V_{nt} and V_{dil} in the bonded cumomer model and individual multiplet model, reduced from 80% to 45% and 30%, respectively.

On the other hand, removing information about total ^{13}C enrichment of Glu and Gln in the individual multiplet model increased slightly the correlation between several fluxes. For example, the correlation of V_{dil} with V_g increased from 13% in bonded cumomer model to 57% in individual multiplet model.

In addition, to visualize the improvements obtained with the bonded cumomer model and better understand the particular effect of it on the particular correlation of V_{nt} and V_{dil}, sensitivity analysis was undertaken for V_{nt} and V_{dil}. In this analysis, the remaining metabolic fluxes were adapted through the non-linear regression process to get the best fit of the total ^{13}C enrichment curves with constrained V_{nt}. Generally, the time courses of GluC4 and GlnC4 isotopomers showed the highest sensitivity to V_{nt} and V_{dil}, which is illustrated in Fig 2.8. Total ^{13}C enrichment time courses of GlnC4 and GluC4 showed low sensitivity to the constrained value of V_{nt} either in the positional or bonded cumomer model.

In both situations, a combination of the remaining fluxes could compensate largely for the fixed V_{nt} constraint, except for the steady-state level of GlnC4 total enrichment. On the contrary, the underlying ^{13}C multiplet time courses simulated for the positional modeling approach showed a higher sensitivity to changes in V_{nt} in particular for GlnC4 doublet and singlet curves. This observation remained valid when including the ^{13}C multiplet curves in the fitting process (bonded cumomer model), which shows that no combination of the remaining adjusted parameters enabled to compensate for the fixed V_{nt} constraint. ^{13}C-labeling curves for doublet and singlet of GlnC4 changed in opposite direction for

increasing values of V_{nt}. As a consequence, the total ^{13}C enrichment curve of GlnC4 was not significantly altered.

Sensitivity analysis in both models showed that ^{13}C time courses of GluC4 isotopomers are not as sensitive as GlnC4 to the value of V_{dil}. From this analysis, it also appeared that the sensitivity of total GlnC4 enrichment to the value of V_{dil} was a reflection of GlnC4 singlet sensitivity, while its doublet remained unchanged. There is no significant difference in sensitivity of time courses of Glu and Gln at position C3 and C2 between bonded cumomer model and positional model (Fig 2.9 and Fig 2.10).

a) Positional model

b) Bonded Cumomer model

Fig 2.8 Sensitivity analysis for the fluxes V_{nt} and V_{dil} plotted for the ^{13}C labeling curves of GluC4 and GlnC4 for three different values of V_{nt} (0.07, 0.1 and 0.20 µmol g^{-1}min^{-1}) and three different values of V_{dil} (0.20, 0.30 and 0.60 µmol g^{-1}min^{-1}) using positional model in the top and bonded cumomer model in the bottom.

(a) Positional model

(b) Bonded Cumomer model

Fig 2.9 Sensitivity analysis for the fluxes V_{nt} and V_{dil} plotted for the ^{13}C labeling curves of GluC3 and GlnC3 for three different values of V_{nt} (0.07, 0.1 and 0.20 µmol g^{-1}min^{-1}) and three different values of V_{dil} (0.20, 0.30 and 0.60 µmol g^{-1}min^{-1}) using positional model in the top and bonded cumomer model in the bottom.

(a) Positional model

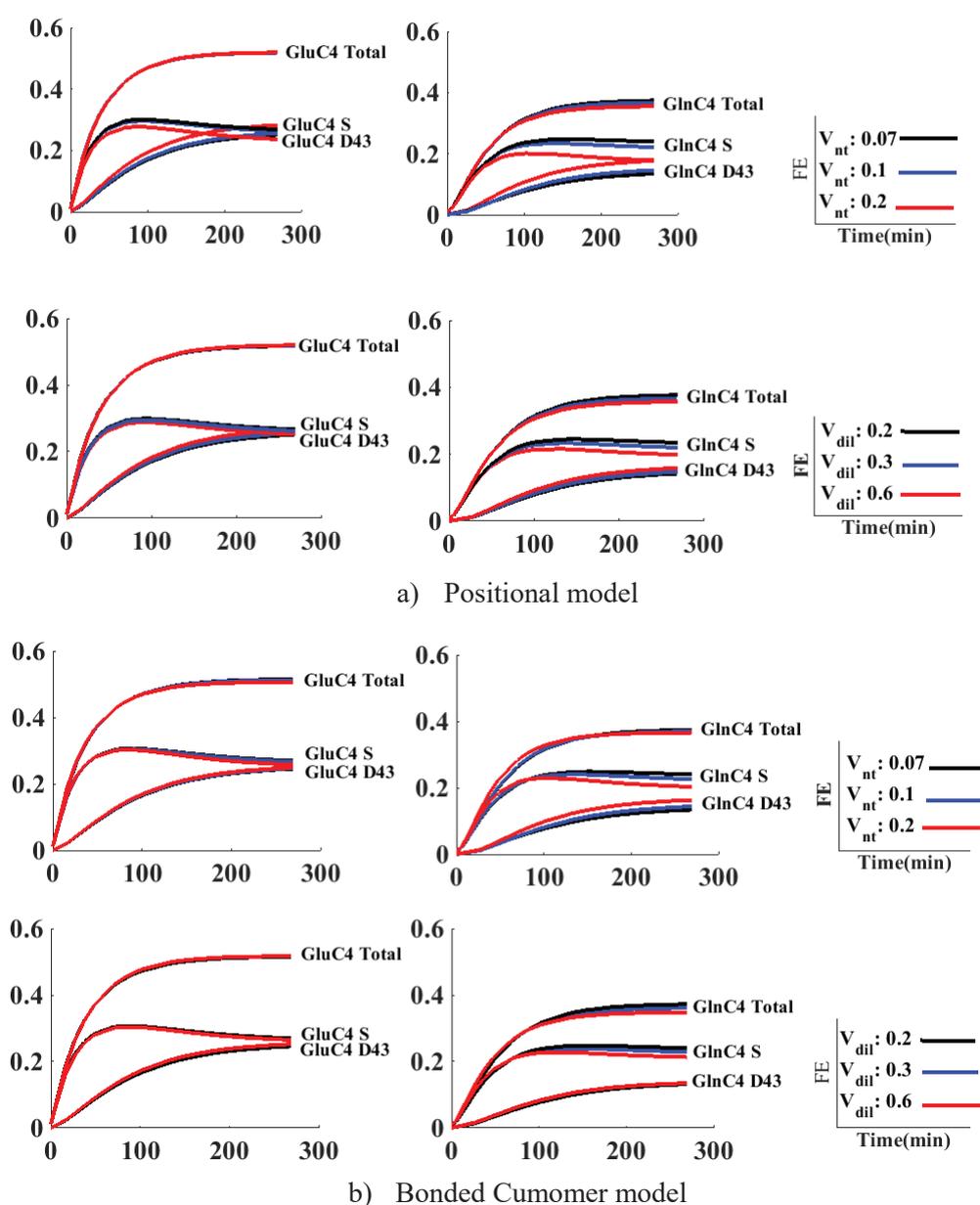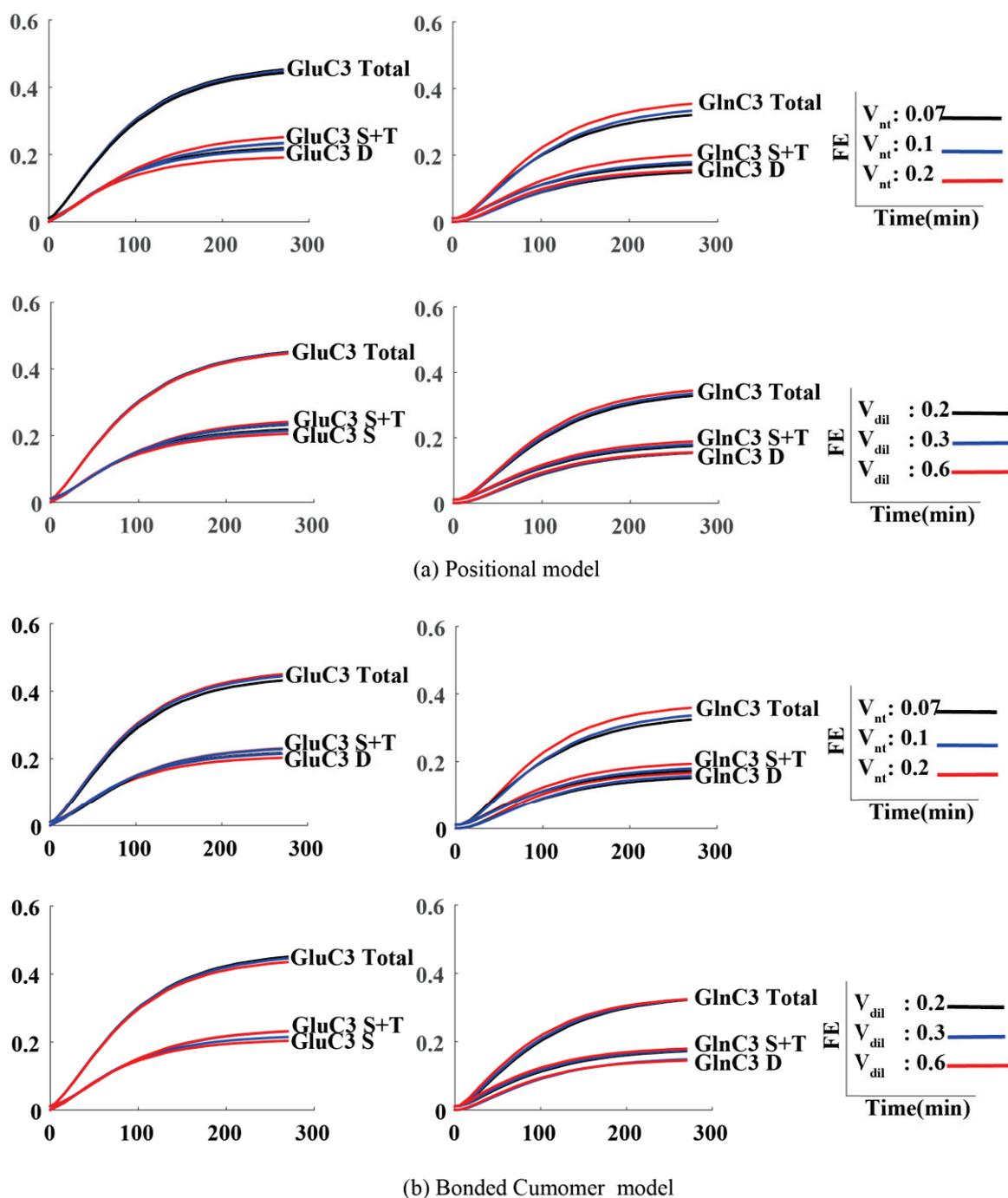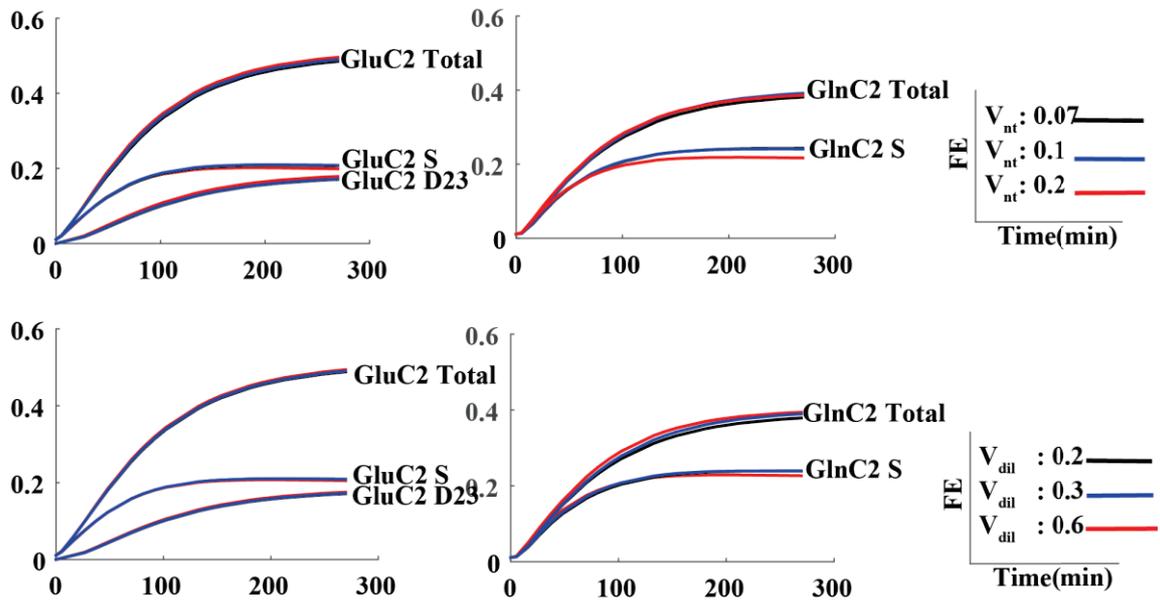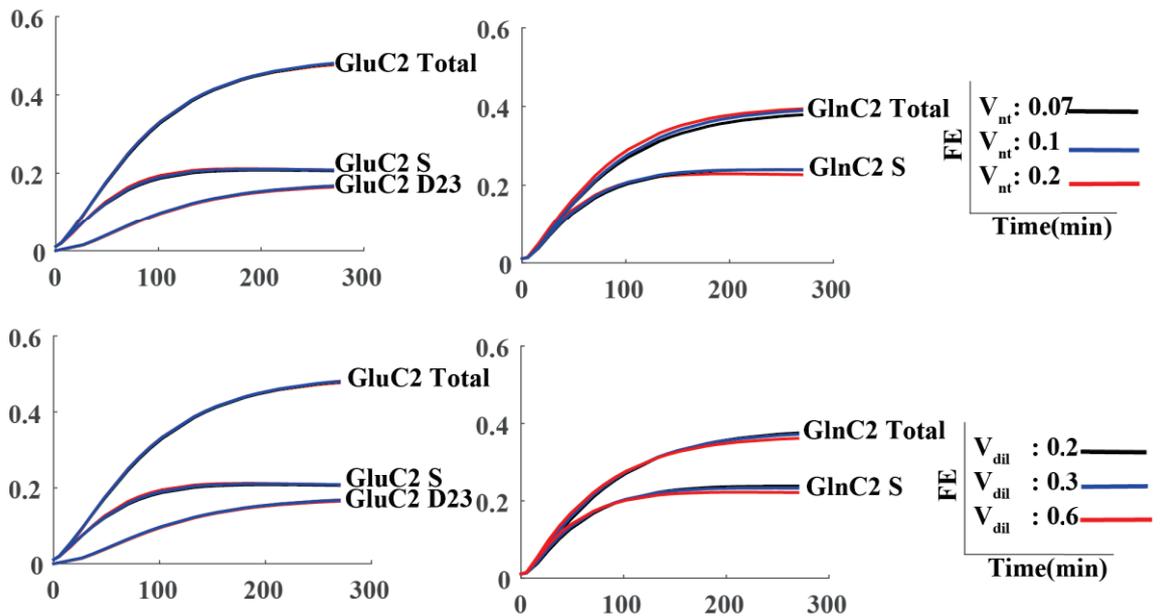(b) Bonded Cumomer model

Fig 2.10 Sensitivity analysis for the fluxes V_{nt} and V_{dil} plotted for the ^{13}C labeling curves of GluC2 and GlnC2 for three different values of V_{nt} (0.07, 0.1 and 0.20 µmol g^{-1}min^{-1}) and three different values of V_{dil} (0.20, 0.30 and 0.60 µmol g^{-1}min^{-1}) using positional model in the top and bonded cumomer model in the bottom.

2.4. Discussion

This study demonstrates that using state of the art dynamic ^{13}C MRS data under ^{13}C-glucose infusion, the recently introduced concept of bonded cumomer metabolic modeling approach provides an extension to the estimation of neuroglia brain metabolic rates, reducing in particular the correlations between most estimated metabolic fluxes in the brain. This kind of approach was applied here for the first time to an extended range of isotopomers and total ^{13}C enrichment curves of Glu and Gln (total of 17 uptake curves), quantified from group-averaged *in vivo* [13]C spectra in rats. The advantages of the bonded cumomer modeling approach and its consistency with previously applied metabolic modeling approaches were evaluated on the experimental data.

2.4.1. Preprocessing approach for reliable and accurate quantification of multiplets

Previous simulation studies suggested that the inclusion of the time courses of individual ^{13}C multiplets from *in vivo* ^{13}C MRS of the brain in the metabolic modeling analysis can result in a significant improvement in the derivation of the metabolic fluxes, determined with better precision (Shestov et al., 2012). Direct ^{13}C NMR detection spectroscopy at 14.1 T used here benefits from higher signal-to-noise ratio and bigger chemical shift dispersion in the NMR signal, potentially allowing higher temporal resolution relative to lower fields (Duarte et al., 2011). The increased chemical shift dispersion of ^{13}C resonances allowed to better separate the GluC3 and GlnC3 resonances (Fig 2.4).

However, the detection and quantification of fine structures of ^{13}C multiplets by *in vivo* NMR spectroscopy are hampered by inherent effects of homonuclear spin-spin J-coupling, which is independent of the applied B_0 magnetic field strength. Therefore, although sensitivity and chemical shift dispersion increase linearly with the applied magnetic field, the spectral separation of the ^{13}C multiplets (in ppm) decreases. However, with the higher sensitivity allowed by surface coils, ^{1}H decoupling and efficient B_0 shimming using FAST(EST)MAP (Gruetter and Tkác, 2000a) method at 14.1 T provided enough homogeneity (less than 10 Hz linewidth) to clearly distinguish the ^{13}C multiplets in the spectral fitting.

The total ^{13}C enrichment of Glc, Glu, Gln and Asp were well determined with CRLB lower than 15% at steady state when using a temporal resolution of 5.3 min and SNR of 9 (spectra not shown). However, to overcome the low signal amplitudes of some of the ^{13}C multiplets, temporal averaging was increased to 10.6 min and spectra were combined from four animals before spectral quantification, which altogether resulted in a threefold elevation of SNR and better defined ^{13}C spectral baseline. This allowed a more robust fitting using LCModel, which in turn resulted in more accurate and reliable quantification of ^{13}C multiplets with CRLB less than 15% at steady state (Fig 2.5).

Due to low enrichment of the singlet and triplet resonance of GluC3 and GlnC3 ,especially in the beginning of [1,6-[13]C$_2$] glucose infusion, it was not possible to resolve these multiplets with enough precision. Therefore, only the sum of singlet and triplet multiplets was considered for the quantification. The precision on the fit of the sum of singlet and triplet in GluC3 and GlnC3 was systematically better than the precision of the fit when using singlet and triplet components separately.

Overall, the increased resolution and sensitivity at 14.1 T provided ^{13}C enrichment turnover curves for GluC4 total, GluC4 S, GluC4 D43, GluC3 total, GluC3 S+T, GluC3 D, GluC2 total, GluC2 S, GluC2 D23, GlnC4 total, GlnC4 S, GlnC4 D43, GlnC3 total, GlnC3 S+T, GlnC3 D, GlnC2 total, GlnC2 S in brain *in vivo*, all of which were quantified with a precision of better than 15% (CRLB) at steady state.

2.4.2.   Positional model

Non-linear regression of the positional model to the total measured ^{13}C enrichment curves for Glu and Gln at position C4, C3 and C2 resulted in seven independently determined brain metabolic fluxes, without a priori constraints (Table 2.1). The estimated fluxes and calculated $CMR_{glc(ox)}$ were overall comparable with previous ^{13}C NMR studies done under α-chloralose anesthesia (Lanz et al., 2014; Ennis et al., 2011; Jeffrey et al., 2013; Duarte et al., 2011; Sibson et al., 1998; Hyder et al., 1996). When quantifying the ^{13}C spectra acquired from brain of four animals using the traditional preprocessing approach as in Duarte et al., 2011, namely spectral quantification for individual animals with time resolution of 5.3 min and averaging over the individually quantified data from four animals, the obtained brain metabolic fluxes using time courses of total ^{13}C enrichment of Glu and Gln for carbon positions C2, C3 and C4 showed a significantly different V_{nt} (p<0.05, corrected for multiple comparison) as the one estimated in this study (data not shown). The SNR of ^{13}C spectra acquired from every individual animal brain with time resolution of 5.3 min (SNR of 9 at steady state) was approximately three times lower than the one obtained by combining the ^{13}C spectra from four animals with temporal average of 10.6 min (SNR of 24 at steady state). Not surprisingly, the lower SNR resulted in ^{13}C multiplets determined with less precision which likely reduced the precision of the averaged times courses of ^{13}C multiplets. These results illustrate the importance of the spectral preprocessing approach and spectral quality on the estimation of brain metabolic fluxes.

In this study, the exchange rate between cytosolic amino acids and mitochondrial TCA cycle intermediates, V_x, was estimated more precisely (with a relative fitting error lower than 5%) than in previous studies (Choi et al., 2002; Henry et al., 2002). The estimated V_x was slightly higher than the pyruvate dehydrogenase rate, V_{pdh}^n and is consistent with malate-aspartate shuttle being the major mechanism for maintaining the cytosolic redox state under normoxic conditions, as reported before (Lanz et al., 2014; Yang et al., 2009; de Graaf et al., 2004; Gruetter et al., 2001).

In the present work, V_{nt} was well determined with a relative SD below 10% using positional modeling under [1,6-^{13}C$_2$] glucose infusion (Table 2.1). The relative error of all fluxes except V_{dil} was lower than 10%, ascribed to the high quality and SNR of the acquired ^{13}C spectra at 14T and the refined preprocessing approach used for spectral quantification. Glial labeling dilution of the acetyl-CoA pool, V_{dil}, had a slightly higher coefficient of variation (19%) and presented strong positive correlation to the apparent rate of neuro transmission, V_{nt}. This correlation was attributed to the observed difference in ^{13}C labeling between Glu C4 and Gln C4. V_{dil} creates a difference between the FEs of Glu and Gln while V_{nt} is responsible for its dissipation by mixing the two pools.

2.4.3. Bonded cumomer model

The addition of dynamic time courses of ^{13}C multiplets of Glu and Gln to the input data for metabolic modeling yielded smaller standard deviations for most fitted metabolic rates compared to the positional modeling (Table 2.1). Probability density functions for brain metabolic fluxes estimated by Monte Carlo simulations (Fig 2.6) indicated narrower distributions compared to the positional model, consistent with a higher precision of the determined flux. One of the largest differences was found in dilution of ^{13}C label at the level of glial acetyl-CoA, V_{dil}, which was more precisely determined in the case of the bonded cumomer model approach.

Using the bonded cumomer model, i.e. the inclusion of the dynamic 13C labeling of Glu and Gln multiplets in the metabolic modeling, reduced the mathematical covariance between most fitted fluxes compared to the positional model (Fig 2.7). The assessment of V_{dil} using the positional model resulted

in a large covariance between V_{dil} and apparent glutamatergic neurotransmission rate, V_{nt}. The significantly reduced covariance between V_{dil} and V_{nt} in the bonded cumomer model is expected to reduce the influence of V_{dil} on V_{nt} and should allow a more precise and independent measurement of V_{dil} and V_{nt}. Therefore the distribution of V_{dil} and V_{nt} determined with bonded cumomer model are significantly different from ones of positional model (p = 0.0001 and 0.01, respectively).

V_{out} and V_{dil} showed remarkably strong correlations in every approach, independently of the addition of the ^{13}C multiplet turnover curves of Glu and Gln which is probably due of the fact that both fluxes are contributing to dilute the ^{13}C enrichment at the level of AcCoA.

Among the potential reasons for the higher precision and independency of brain metabolic fluxes is the simple increased number of ^{13}C time courses and experimental information, arising from dynamic ^{13}C enrichment of the individual multiplets of Glu and Gln, as input in the metabolic model, including partially redundant information. However, a more important part is the sensitivity of given ^{13}C isotopomers labeling to particular fluxes, which are then averaged out when summing all the isotopomers of the considered carbon position, which is evident in Fig 2.8 for GlnC4 sensitivity analysis to V_{nt} and V_{dil}.

2.4.4. Sensitivity analysis of GluC4 and GlnC4 multiplets to the value of V_{nt} and V_{dil}

It is noteworthy that the ^{13}C enrichment time courses of total GlnC4 and total GluC4 ^{13}C enrichments were less sensitive to V_{nt} than the individual ^{13}C multiplets of GluC4 and GlnC4; when increasing V_{nt}, the ^{13}C enrichment of the singlet of GluC4 decreased and the ^{13}C enrichment of the doublet of GluC4 increased, while the total ^{13}C enrichment time course of GluC4 did not change (Fig 2.8). The remaining metabolic fluxes adapt to the constraints fixed on V_{nt} to provide a similar fit quality for total GluC4 in the positional model. This is a manifestation of the higher correlation between V_{nt} and most of the remaining fluxes found with the positional modeling approach (Fig 2.7). For GlnC4 on the other hand, the total ^{13}C enrichment curve is sensitive to V_{nt} resulting in differences in the ^{13}C turnover curve for different constraints on V_{nt}. Nonetheless, the GlnC4 multiplet curves exhibited also a stronger sensitivity to V_{nt}, in particular for GlnC4 S, this already at early time points. As a consequence, including the ^{13}C multiplet curves in the cost function of the regression led to a better defined value of V_{nt} in the bonded cumomer model compared to the positional model as well as a lower correlation between V_{nt} and most other fluxes in the bonded cumomer model as summarized in Fig 2.7. Lower correlation of V_{nt} with other fluxes in the bonded cumomer model is expected to result in a more independent estimation of V_{nt} with less impact from other estimated fluxes.

The above argument was based on the flux V_{nt}, which shows the strongest changes in terms of correlations with other fluxes between the positional model and the bonded cumomer model. However, note that a general reduction of the correlation coefficients between fluxes is observed with the bonded cumomer model (Fig 2.7), leading to more precise flux measurements. It should be mentioned that the obtained correlation was estimated from Montecarlo simulation done using one series data points.

Shestov et al. (2007) also showed lower sensitivity of simulated total ^{13}C enrichment turnover curve of GlnC4 to the value of V_{nt} in the positional model. They concluded that this effect was a consequence of the fast ^{13}C labeling of the smaller glial Gln pool compared to its indirect precursor, the large neuronal Glu pool. Glial Gln ^{13}C labeling therefore is largely influenced by the neuronal Glu pool. However, our results show that changing V_{nt} has an effect on the ^{13}C turnover curves of GlnC4 multiplets in the bonded cumomer model even though the total ^{13}C enrichment of GlnC4 does not change significantly. This can be interpreted in terms of the different precursors of the essentially astrocytic Gln pool: The

Gln pool reflects the ^{13}C enrichment of the small astrocytic Glu pool, which can be labeled either from the glial TCA cycle or from the neuronal TCA cycle via the neuronal Glu pool. However, the ^{13}C labeling patterns in the carbon positions 4 and 3 of Glu generated by the astrocytic or the neuronal TCA cycle are different due to the dilution of the ^{13}C labeling position C3 in the glial TCA cycle through pyruvate carboxylase. This can be seen by lower total ^{13}C enrichment in the C3 of Gln as compared with Glu (see Fig 2.5). The position C4 is also diluted through metabolism of alternative substrates in the astrocytic TCA cycle. Therefore, the probability of generating a doubly labeled C4-C3 Glu molecule from the astrocytic TCA cycle is lower. Increasing the relative value of V_{nt} will generate more Gln molecules with carbon backbones originating from the neuronal TCA cycle, with higher double C4-C3 labeling, increasing the doublet component of GlnC4.

For the same reason, the ^{13}C labeling time courses of multiplets for Glu and Gln in both models showed that the doublet of GlnC4 is not as sensitive as the singlet of GlnC4 to changes in astrocytic V_{dil}, representing the glial oxidative metabolism of alternative, unlabeled substrates. Therefore, changes in the total GlnC4 enrichment reflects the sensitivity of GlnC4 S to the value of V_{dil} while the ^{13}C enrichment curve of GlnC4 D43 does not change significantly.

2.4.5. Limitation of modeling based on ^{13}C labeling time courses of individual multiplets

Removing total ^{13}C enrichment curves from the bonded cumomer model and considering just the ^{13}C labeling of individual multiplets had effect on the estimated brain metabolic fluxes in terms of value, precision and covariance (Fig 2.6 and Fig 2.7). The values found for the brain metabolic rates listed in Table 2.1 were in the range between those found with the positional model and the full bonded cumomer model. One drawback of excluding the total ^{13}C enrichment curves of Glu and Gln in the bonded cumomer model is the reduction of the number of ^{13}C time courses as input to the metabolic model. Simulation and experimental studies verified that a higher number of experimental ^{13}C time courses of Glu and Gln carbon positions increased the precision of estimated brain metabolic fluxes (Shestov et al., 2007; Jeffrey et al., 1999). In addition, the spectral quantification of the ^{13}C multiplet time courses for Glu and Gln has a lower precision due to their lower concentrations as compared to the total ^{13}C enrichment.

Using [1,6-^{13}C$_2$] glucose as a substrate and acquiring ^{13}C spectra at a high field of 14.1T in the present study led to high peak intensities in the ^{13}C multiplet resonances of Glu and Gln at position C2, C3 and C4, which made it more easy to quantify ^{13}C multiplet signals with sufficient sensitivity. However, the ^{13}C multiplets are expected to be much more difficult to detect and quantify at lower magnetic fields, in particular when infusing [1-^{13}C] glucose and limiting the infusion experiment to 60-90 minutes, as typically undertaken in human studies for cost and practical reasons (Rothman et al., 2011). Therefore, the use of [1-^{13}C] glucose remains a limitation for a reliable and accurate quantification of time courses for individual ^{13}C multiplets of metabolites.

Early studies on brain extracts (Taylor et al., 1996) proved that coinfusion of [1,6-^{13}C$_2$] glucose and [1,2-^{13}C$_2$] acetate resulted in different ^{13}C isotopomer patterns that reflect predominantly neuronal and glial metabolism, respectively. The feasibility of measuring dynamic ^{13}C multiplet data in brain arising from simultaneous infusion of [1,6-^{13}C$_2$] glucose and [1,2-^{13}C$_2$] acetate *in vivo* has been reported previously (Deelchand et al., 2009). Simultaneous infusion of labeled glucose and acetate is therefore of more interest in terms of amount of information arising from isotopomer ^{13}C labeling for brain metabolic modeling. (Shestov et al., 2012) showed that the best precision in estimating brain metabolic fluxes by simulated data was obtained in the case of double infusion of [1,6-^{13}C$_2$]glucose and [1,2-

$^{13}C_2$]acetate. Therefore, future *in vivo* studies with simultaneous infusion of labeled glucose and acetate could take better advantage of dynamic multiplet analysis.

2.5. Conclusion

We conclude that incorporating the ^{13}C labeling time courses of multiplets of Glu and Gln measured by ^{13}C MRS at high magnetic field (14.1T) in the neuronal-glial metabolic model brings improvement in the reliability and independency of estimated brain metabolic fluxes. An extended analysis of ^{13}C multiplet time courses of metabolites *in vivo* requires infusion of doubly-labeled Glc as substrate and strong B_0 magnetic field in order to get both enough ^{13}C enrichment and acceptable SNR in ^{13}C multiplets spectra. Therefore this refined modeling approach may be only applicable for preclinical studies on small animals.

2.6. References

1. Choi, I.-Y., Lei, H., Gruetter, R., 2002. Effect of Deep pentobarbital anesthesia on neurotransmitter metabolism *in vivo*: On the correlation of total glucose consumption with glutamatergic action: J. Cereb. Blood Flow Metab. 1343–1351. doi:10.1097/00004647-200211000-00008.

2. Cobelli, C., Foster, D., Toffolo, G., 2000. Tracer kinetics in biomedical research - from data to model. Kluwer Academic Publisher, New York, Boston, Dordrecht, London, Moscow.

3. de Graaf, R.A., Mason, G.F., Patel, A.B., Behar, K.L., Rothman, D.L., 2003. *In vivo* ^{1}H-[^{13}C]-NMR spectroscopy of cerebral metabolism. NMR Biomed. 16, 339–357. doi:10.1002/nbm.847.

4. de Graaf, R.A. de, Mason, G.F., Patel, A.B., Rothman, D.L., Behar, K.L., 2004. Regional glucose metabolism and glutamatergic neurotransmission in rat brain *in vivo*. Proc. Natl. Acad. Sci. U. S. A. 101, 12700–12705. doi:10.1073/pnas.0405065101.

5. Deelchand, D.K., Nelson, C., Shestov, A.A., Uğurbil, K., Henry, P.-G., 2009. Simultaneous measurement of neuronal and glial metabolism in rat brain in vivo using co-infusion of [1,6-^{13}C$_2$]glucose and [1,2-^{13}C$_2$]acetate. J. Magn. Reson. San Diego Calif 1997 196, 157–163. doi:10.1016/j.jmr.2008.11.001.

6. Duarte, J.M.N., Cunha, R.A., Carvalho, R.A., 2007. Different metabolism of glutamatergic and GABAergic compartments in superfused hippocampal slices characterized by nuclear magnetic resonance spectroscopy. Neuroscience 144, 1305–1313.

   doi:10.1016/j.neuroscience.2006.11.027.

7. Duarte, J.M.N., Gruetter, R., 2013. Glutamatergic and GABAergic energy metabolism measured in the rat brain by (^{13}) C NMR spectroscopy at 14.1 T. J. Neurochem. 126, 579–590. doi:10.1111/jnc.12333.

8. Duarte, J.M.N., Lanz, B., Gruetter, R., 2011. Compartmentalized Cerebral Metabolism of [1,6-(13)C]Glucose Determined by *in vivo* (13)C NMR Spectroscopy at 14.1 T. Front. Neuroenergetics 3, 3. doi:10.3389/fnene.2011.00003.

9. Ennis, K., Deelchand, D.K., Tkac, I., Henry, P.-G., Rao, R., 2011. Determination of Oxidative Glucose Metabolism *in vivo* in the Young Rat Brain using Localized Direct-detected ^{13}C NMR Spectroscopy. Neurochem. Res. 36, 1962–1968. doi:10.1007/s11064-011-0519-x.

10. Gruetter, R., 2002. *In vivo* ^{13}C NMR studies of compartmentalized cerebral carbohydrate metabolism. Neurochem. Int. 41, 143–154.

11. Gruetter, R., Adriany, G., Choi, I.-Y., Henry, P.-G., Lei, H., Oz, G., 2003. Localized *in vivo* ^{13}C NMR spectroscopy of the brain. NMR Biomed. 16, 313–338. doi:10.1002/nbm.841.

12. Gruetter, R., Seaquist, E.R., Ugurbil, K., 2001. A mathematical model of compartmentalized neurotransmitter metabolism in the human brain. Am. J. Physiol. Endocrinol. Metab. 281, E100-112.

13. Gruetter, R., Tkác, I., 2000. Field mapping without reference scan using asymmetric echo-planar techniques. Magn. Reson. Med. 43, 319–323.

14. Henry, P.-G., Adriany, G., Deelchand, D., Gruetter, R., Marjanska, M., Oz, G., Seaquist, E.R., Shestov, A., Uğurbil, K., 2006. *In vivo* ^{13}C NMR spectroscopy and metabolic modeling in the brain: a practical perspective. Magn. Reson. Imaging 24, 527–539. doi:10.1016/j.mri.2006.01.003.

15. Henry, P.-G., Oz, G., Provencher, S., Gruetter, R., 2003a. Toward dynamic isotopomer analysis in the rat brain in vivo: automatic quantitation of ^{13}C NMR spectra using LCModel. NMR Biomed. 16, 400–412. doi:10.1002/nbm.840.

16. Henry, P.-G., Tkác, I., Gruetter, R., 2003b. ^{1}H-localized broadband ^{13}C NMR spectroscopy of the rat brain *in vivo* at 9.4 T. Magn. Reson. Med. 50, 684–692. doi:10.1002/mrm.10601.

17. Henry, P.-G., Lebon, V., Vaufrey, F., Brouillet, E., Hantraye, P., Bloch, G., 2002. Decreased TCA cycle rate in the rat brain after acute 3-NP treatment measured by in vivo ^{1}H-[^{13}C] NMR spectroscopy. J. Neurochem. 82, 857–866.

18. Hyder, F., Chase, J.R., Behar, K.L., Mason, G.F., Siddeek, M., Rothman, D.L., Shulman, R.G., 1996. Increased tricarboxylic acid cycle flux in rat brain during forepaw stimulation detected with ^{1}H[^{13}C]NMR. Proc. Natl. Acad. Sci. U. S. A. 93, 7612–7617.

19. Jeffrey, F.M., Marin-Valencia, I., Good, L.B., Shestov, A.A., Henry, P.-G., Pascual, J.M., Malloy, C.R., 2013. Modeling of brain metabolism and pyruvate compartmentation using (13)C NMR *in vivo*: caution required. J. Int. Soc. Cereb. Blood Flow Metab. 33, 1160–1167. doi:10.1038/jcbfm.2013.67.

20. Jeffrey, F.M., Reshetov, A., Storey, C.J., Carvalho, R.A., Sherry, A.D., Malloy, C.R., 1999. Use of a single (13)C NMR resonance of glutamate for measuring oxygen consumption in tissue. Am. J. Physiol. 277, E1111-1121.

21. Jucker, B.M., Schaeffer, T.R., Haimbach, R.E., McIntosh, T.S., Chun, D., Mayer, M., Ohlstein, D.H., Davis, H.M., Smith, S.A., Cobitz, A.R., Sarkar, S.K., 2002. Normalization of skeletal muscle glycogen synthesis and glycolysis in rosiglitazone-treated Zucker fatty rats: an in vivo nuclear magnetic resonance study. Diabetes 51, 2066–2073.

22. Lanz, B., 2012. Mathematical Modeling of Brain Energy Metabolism, Measured with PET and MRS in Rodents. PhD thesis, Ecole polytechnique fédérale de lausanne.

23. Lanz, B., Duarte, J.M.N., Kunz, N., Mlynárik, V., Gruetter, R., Cudalbu, C., 2013. Which prior knowledge? Quantification of *in vivo* brain ^{13}C MR spectra following ^{13}C glucose infusion using AMARES. Magn. Reson. Med. 69, 1512–1522. doi:10.1002/mrm.24406.

24. Lanz, B., Xin, L., Millet, P., Gruetter, R., 2014a. *In vivo* quantification of neuro-glial metabolism and glial glutamate concentration using ^{1}H-[^{13}C] MRS at 14.1T. J. Neurochem. 128, 125–139. doi:10.1111/jnc.12479.

25. Mason, G.F., Gruetter, R., Rothman, D.L., Behar, K.L., Shulman, R.G., Novotny, E.J., 1995. Simultaneous determination of the rates of the TCA cycle, glucose utilization, alpha-ketoglutarate/glutamate exchange, and glutamine synthesis in human brain by NMR. J. Int. Soc. Cereb. Blood Flow Metab. 15, 12–25. doi:10.1038/jcbfm.1995.2.

26. Mason, G.F., Rothman, D.L., 2004. Basic principles of metabolic modeling of NMR (13)C isotopic turnover to determine rates of brain metabolism *in vivo*. Metab. Eng. 6, 75–84.

27. Oz, G., Berkich, D.A., Henry, P.-G., Xu, Y., LaNoue, K., Hutson, S.M., Gruetter, R., 2004. Neuroglial metabolism in the awake rat brain: CO2 fixation increases with brain activity. J. Neurosci. Off. J. Soc. Neurosci. 24, 11273–11279. doi:10.1523/JNEUROSCI.3564-04.2004.

28. Rodrigues, T.B., Valette, J., Bouzier-Sore, A.-K., 2013. (13)C NMR spectroscopy applications to brain energy metabolism. Front. Neuroenergetics 5, 9. doi:10.3389/fnene.2013.00009.

29. Rothman, D.L., Behar, K.L., Hyder, F., Shulman, R.G., 2003. *In vivo* NMR studies of the glutamate neurotransmitter flux and neuroenergetics: implications for brain function. Annu. Rev. Physiol. 65, 401–427.

30. Rothman, D.L., De Feyter, H.M., de Graaf, R.A., Mason, G.F., Behar, K.L., 2011. ^{13}C MRS studies of neuroenergetics and neurotransmitter cycling in humans. NMR Biomed. 24, 943–957. doi:10.1002/nbm.1772.

31. Shen, J., Rothman, D.L., Behar, K.L., Xu, S., 2009. Determination of the glutamate-glutamine cycling flux using two-compartment dynamic metabolic modeling is sensitive to astroglial dilution. J. Int. Soc. Cereb. Blood Flow Metab. 29, 108–118. doi:10.1038/jcbfm.2008.102.

32. Shestov, A.A., Valette, J., Deelchand, D.K., Uğurbil, K., Henry, P.-G., 2012. Metabolic modeling of dynamic brain ^{13}C NMR multiplet data: concepts and simulations with a two-compartment neuronal-glial model. Neurochem. Res. 37, 2388–2401. doi:10.1007/s11064-012-0782-5.

33. Shestov, A.A., Valette, J., Uğurbil, K., Henry, P.-G., 2007. On the reliability of (13)C metabolic modeling with two-compartment neuronal-glial models. J. Neurosci. Res. 85, 3294–3303. doi:10.1002/jnr.21269.

34. Sibson, N.R., Dhankhar, A., Mason, G.F., Rothman, D.L., Behar, K.L., Shulman, R.G., 1998. Stoichiometric coupling of brain glucose metabolism and glutamatergic neuronal activity. Proc. Natl. Acad. Sci. U. S. A. 95, 316–321.

35. Taylor, A., McLean, M., Morris, P., Bachelard, H., 1996. Approaches to studies on neuronal/glial relationships by ^{13}C-MRS analysis. Dev. Neurosci. 18, 434–442.

36. Uffmann, K., Gruetter, R., 2007. Mathematical modeling of (13)C label incorporation of the TCA cycle: the concept of composite precursor function. J. Neurosci. Res. 85, 3304–3317. doi:10.1002/jnr.21392.

37. Wiechert, W., Möllney, M., Isermann, N., Wurzel, M. & de Graaf, A. A. 1999. Bidirectional reaction steps in metabolic networks: Explicit solution and analysis of isotopomer labeling systems. Biotechnol. Bioeng. 66, 69–85.

38. Xin, L., Lanz, B., Lei, H., Gruetter, R., 2015. Assessment of metabolic fluxes in the mouse brain *in vivo* using ^{1}H-[^{13}C] NMR spectroscopy at 14.1 Tesla. J. Int. Soc. Cereb. Blood Flow Metab. 35, 759–765. doi:10.1038/jcbfm.2014.251.

39. Xin, L., Mlynárik, V., Lanz, B., Frenkel, H., Gruetter, R., 2010. ^{1}H-[^{13}C] NMR spectroscopy of the rat brain during infusion of [2-^{13}C] acetate at 14.1 T. Magn. Reson. Med. 64, 334–340. doi:10.1002/mrm.22359.

40.   Yang, J., Xu, S., Shen, J., 2009. Fast isotopic exchange between mitochondria and cytosol in brain revealed by relayed ^{13}C magnetization transfer spectroscopy. J. Int. Soc. Cereb. Blood Flow Metab. 29, 661–669. doi:10.1038/jcbfm.2008.170.

2.7. Appendix

For each multiplet, the index C shows the carbon position in the molecule and the next letter, separated by space, gives the multiplets fine structure (S is for singlet, D for doublet and T for triplet).

In following equations, the indexes b and p specify metabolic pools in brain and plasma, respectively. Metabolic pools in the neuronal compartment are indicated with the index n and in the glial compartment with the index g.

The TCA cycle rate in the neuronal compartment, flux through pyruvate dehydrogenase: V_{pdh}^n

The TCA cycle rate in the glial compartment: $V_{TCA}^g = V_g + V_{pc}$

Flux through neuronal glutaminase : V_{nt}

The anaplerotic flux through pyruvate carboxylase: V_{pc}

Glutamate-alpha–ketoglutarate and oxaloacetate–aspartate exchange rate: V_x

Outflow and inflow of labeling at the level of Lactate: V_{out} and V_{in}

The dilution flux at the level of acetyl-CoA: V_{dil}

A-1. Glucose transport across the blood brain barrier
Brain glucose concentration using a reversible Michaelis-Menten kinetics for glucose transport across the blood brain barrier change according to following expression:

$$\frac{d}{dt}\left[Glc(t)^b\right] = T_{max}\frac{\left[Glc(t)^p\right] - \left[Glc(t)^b\right]/V_d}{K_t + \frac{\left[Glc(t)^b\right]}{V_d} + \left[Glc(t)^p\right]} - CMR_{Glc}$$

T_{max}: The apparent maximal transport rate
K_t : The apparent Michaelis constant for Glucose transport
V_d : The physical volume of distribution for glucose in the brain, 0.77 mL/g

A-2. Mass balance equations of particular interest

With steady-state assumption for the Glu and Gln labeling pools in the case of [1, 6-^{13}C2] Glc infusion, the total concentration of the labeling pools as well as the metabolic fluxes between the pools be assumed to remain same over the duration of the measurement . Thus maintaining the mass balance equations result in following expressions (Henry PG, 2006, Lanz et al., 2013).

$$\frac{d}{dt}\left[Lac^b\right] = V_{in} - V_{out} + 2CMR_{glc} - V_{pdh}^n - V_g - 2V_{pc} = 0$$

$$\frac{d}{dt}\left[OAA^g\right] = V_x + V_{pc} - V_x - V_{syn} + V_{nt} = 0$$

$$\frac{d}{dt}\left[Glu^g\right] = V_{pc} - V_{syn} + V_{nt} = 0$$

$$\frac{d}{dt}\left[Gln^g\right] = V_{syn} - V_{efflux} - V_{nt} = 0$$

The Gln synthesis rate in glial: $V_{syn} = V_{nt} + V_{pc}$

The net Gln efflux: $V_{efflux} = V_{pc}$

The fraction of Glucose metabolized at steady-state in the TCA cycle:

$$CMR_{glc(ox)} = \frac{V_{pdh}^n + V_{TCA}^g + V_{pc}}{2}$$

The cerebral metabolic rate of Glucose consumption: $\text{CMR}_{\text{glc}} = \text{CMR}_{\text{glc(ox)}} + \frac{V_{\text{out}} - V_{\text{in}}}{2}$

A-3. Metabolic equations for labeling isotopomers in bonded cumomer model

$\{i\}$, $\{k\}$ and $\{k\}$ indicating the positions of labeled carbon in metabolite. $\pi_{M\{i\}}$ refers to the sum of isotopomers fractions labeled at least at position $\{i\}$ and interpreted as the probability of labeling metabolite at position i. $\pi_{M\{i,j\}}$ is the probability of metabolite being labeled at adjacent positions i and j. $\pi_{M\{i,j,k\}}$ indicates the probability metabolite being labeled at three adjacent position i, j and k (Shestov et al, 2012) .

Transport of ^{13}C-enriched carbons of Glucose:

$$[Glc(t)^b]\frac{d}{dt}\left(\pi^b_{Glc\{i\}}\right) = T_{max}\frac{[Glc(t)^p]\left(\pi^p_{Glc\{i\}}\right) - [Glc(t)^b]/V_d\left(\pi^b_{Glc\{i\}}\right)}{K_t + \frac{[Glc(t)^b]}{V_d} + [Glc(t)^p]} - CMR_{Glc}\left(\pi^b_{Glc\{i\}}\right)$$

$$[Glc(t)^b]\frac{d}{dt}\left(\pi^b_{Glc\{i,j\}}\right) = T_{max}\frac{[Glc(t)^p]\left(\pi^p_{Glc\{i,j\}}\right) - [Glc(t)^b]/V_d\left(\pi^b_{Glc\{i,j\}}\right)}{K_t + \frac{[Glc(t)^b]}{V_d} + [Glc(t)^p]} - CMR_{Glc}\left(\pi^b_{Glc\{i,j\}}\right)$$

$$[Glc(t)^b]\frac{d}{dt}\left(\pi^b_{Glc\{i,j,k\}}\right) = T_{max}\frac{[Glc(t)^p]\left(\pi^p_{Glc\{i,j,k\}}\right) - [Glc(t)^b]/V_d\left(\pi^b_{Glc\{i,j,k\}}\right)}{K_t + \frac{[Glc(t)^b]}{V_d} + [Glc(t)^p]} - CMR_{Glc}\left(\pi^b_{Glc\{i,j,k\}}\right)$$

Enrichment of neuronal amino acids

$$[Glu^n].\frac{d}{dt}\left(\pi^n_{Glu\{i\}}\right) = V_x\left(\pi^n_{OG\{i\}}\right) + V_{nt}\left(\pi^n_{Gln\{i\}}\right) - (V_x + V_{nt})\left(\pi^n_{Glu\{i\}}\right)$$

$$[Glu^n].\frac{d}{dt}\left(\pi^n_{Glu\{i,j\}}\right) = V_x\left(\pi^n_{OG\{i,j\}}\right) + V_{nt}\left(\pi^n_{Gln\{i,j\}}\right) - (V_x + V_{nt})\left(\pi^n_{Glu\{i,j\}}\right)$$

$$[Glu^n].\frac{d}{dt}\left(\pi^n_{Glu\{i,j,k\}}\right) = V_x\left(\pi^n_{OG\{i,j,k\}}\right) + V_{nt}\left(\pi^n_{Gln\{i,j,k\}}\right) - (V_x + V_{nt})\left(\pi^n_{Glu\{i,j,k\}}\right)$$

$$[Gln^n].\frac{d}{dt}\left(\pi^n_{Gln\{i\}}\right) = V_{nt}\left(\pi^g_{Gln\{i\}}\right) - V_{nt}\left(\pi^n_{Gln\{i\}}\right)$$

$$[Gln^n].\frac{d}{dt}\left(\pi^n_{Gln\{i,j\}}\right) = V_{nt}\left(\pi^g_{Gln\{i,j\}}\right) - V_{nt}\left(\pi^n_{Gln\{i,j\}}\right)$$

$$[Gln^n].\frac{d}{dt}\left(\pi^n_{Gln\{i,j,k\}}\right) = V_{nt}\left(\pi^g_{Gln\{i,j,k\}}\right) - V_{nt}\left(\pi^n_{Gln\{i,j,k\}}\right)$$

$$[Asp^n].\frac{d}{dt}\left(\pi^n_{Asp\{i\}}\right) = V_x\left(\pi^n_{OAA\{i\}}\right) - V_x\left(\pi^n_{Asp\{i\}}\right)$$

$$[Asp^n].\frac{d}{dt}\left(\pi^n_{Asp\{i,j\}}\right) = V_x\left(\pi^n_{OAA\{i,j\}}\right) - V_x\left(\pi^n_{Asp\{i,j\}}\right)$$

$$[Asp^n].\frac{d}{dt}\left(\pi^n_{Asp\{i,j,k\}}\right) = V_x\left(\pi^n_{OAA\{i,j,k\}}\right) - V_x\left(\pi^n_{Asp\{i,j,k\}}\right)$$

Enrichment of glial amino acids

$$[Glu^g].\frac{d}{dt}\left(\pi^g_{Glu\{i\}}\right) = (V_x + V_{pc})\left(\pi^g_{OG\{i\}}\right) + V_{nt}\left(\pi^n_{Glu\{i\}}\right) - (V_x + V_{nt} + V_{pc})\left(\pi^g_{Glu\{i\}}\right)$$

$$[Glu^g].\frac{d}{dt}\left(\pi^g_{Glu\,\{i,j\}}\right) = (V_x + V_{pc})\left(\pi^g_{OG\,\{i,j\}}\right) + V_{nt}\left(\pi^n_{Glu\,\{i,j\}}\right) - (V_x + V_{nt} + V_{pc})\left(\pi^g_{Glu\,\{i,j\}}\right)$$

$$[Glu^g].\frac{d}{dt}\left(\pi^g_{Glu\,\{i,j,k\}}\right) = (V_x + V_{pc})\left(\pi^g_{OG\,\{i,j,k\}}\right) + V_{nt}\left(\pi^n_{Glu\,\{i,j,k\}}\right) - (V_x + V_{nt} + V_{pc})\left(\pi^g_{Glu\,\{i,j,k\}}\right)$$

$$[Gln^g].\frac{d}{dt}\left(\pi^g_{Gln\,\{i\}}\right) = (V_{nt} + V_{pc})\left(\pi^g_{Glu\,\{i\}}\right) - (V_{nt} + V_{pc})\left(\pi^g_{Gln\,\{i\}}\right)$$

$$[Gln^g].\frac{d}{dt}\left(\pi^g_{Gln\,\{i,j\}}\right) = (V_{nt} + V_{pc})\left(\pi^g_{Glu\,\{i,j\}}\right) - (V_{nt} + V_{pc})\left(\pi^g_{Gln\,\{i,j\}}\right)$$

$$[Gln^g].\frac{d}{dt}\left(\pi^g_{Gln\,\{i,j,k\}}\right) = (V_{nt} + V_{pc})\left(\pi^g_{Glu\,\{i,j,k\}}\right) - (V_{nt} + V_{pc})\left(\pi^g_{Gln\,\{i,j,k\}}\right)$$

$$[Asp^g].\frac{d}{dt}\left(\pi^g_{Asp\,\{i\}}\right) = V_x\left(\pi^g_{OAA\,\{i\}}\right) - V_x\left(\pi^g_{Asp\,\{i\}}\right)$$

$$[Asp^g].\frac{d}{dt}\left(\pi^g_{Asp\,\{i,j\}}\right) = V_x\left(\pi^g_{OAA\,\{i,j\}}\right) - V_x\left(\pi^g_{Asp\,\{i,j\}}\right)$$

$$[Asp^g].\frac{d}{dt}\left(\pi^g_{Asp\,\{i,j,k\}}\right) = V_x\left(\pi^g_{OAA\,\{i,j,k\}}\right) - V_x\left(\pi^g_{Asp\,\{i,j,k\}}\right)$$

Enrichment of single brain pyruvate pool by considering its fast equilibrium with lactate

$$[Pyr].\frac{d}{dt}\begin{pmatrix}\pi_{pyr\,\{1\}}\\\pi_{pyr\,\{2\}}\\\pi_{pyr\,\{3\}}\end{pmatrix}$$

$$= CMR_{Glc}\begin{pmatrix}\pi^b_{Glc\{3\}} + \pi^b_{Glc\{4\}}\\\pi^b_{Glc\{2\}} + \pi^b_{Glc\{5\}}\\\pi^b_{Glc\{1\}} + \pi^b_{Glc\{6\}}\end{pmatrix} - \left(V_{out} + 2V_{pc} + Vg + V^n_{pdh}\right)\begin{pmatrix}\pi_{pyr\,\{1\}}\\\pi_{pyr\,\{2\}}\\\pi_{pyr\,\{3\}}\end{pmatrix} + (2V_{pc}$$

$$+ V_g + V^n_{pdh} + V_{out} - 2CMR_{Glc})\begin{pmatrix}\pi^p_{Lac\{1\}}\\\pi^p_{Lac\{2\}}\\\pi^p_{Lac\{3\}}\end{pmatrix}$$

$$[Pyr].\frac{d}{dt}\begin{pmatrix}\pi_{pyr\,\{1,2\}}\\\pi_{pyr\,\{2,3\}}\end{pmatrix}$$

$$= CMR_{Glc}\begin{pmatrix}\pi^b_{Glc\{2,3\}} + \pi^b_{Glc\{4,5\}}\\\pi^b_{Glc\{1,2\}} + \pi^b_{Glc\{5,6\}}\end{pmatrix} - \left(V_{out} + 2V_{pc} + Vg + V^n_{pdh}\right)\begin{pmatrix}\pi_{pyr\,\{1,2\}}\\\pi_{pyr\,\{2,3\}}\end{pmatrix} + (2V_{pc}$$

$$+ V_g + V^n_{pdh} + V_{out} - 2CMR_{Glc})\begin{pmatrix}\pi^p_{Lac\{1,2\}}\\\pi^p_{Lac\{2,3\}}\end{pmatrix}$$

$$[Pyr].\frac{d}{dt}\left(\pi_{pyr\,\{1,2,3\}}\right)$$

$$= CMR_{Glc}\left(\pi^b_{Glc\{1,2,3\}} + \pi^b_{Glc\{4,5,6\}}\right) - \left(V_{out} + 2V_{pc} + Vg + V^n_{pdh}\right)\left(\pi_{pyr\,\{1,2,3\}}\right)$$

$$+ (2V_{pc} + V_g + V^n_{pdh} + V_{out} - 2CMR_{Glc})\left(\pi^p_{Lac\{1,2,3\}}\right)$$

Enrichment of Acetyl-CoA

$$[AcCoA^g].\frac{d}{dt}\begin{pmatrix}\pi^g_{AcCoA\,\{1\}}\\\pi^g_{AcCoA\,\{2\}}\end{pmatrix}$$

$$= V_{dil}\begin{pmatrix}\pi^g_{Ace\,\{1\}}\\\pi^g_{Ace\,\{2\}}\end{pmatrix} + \left(V_g + V_{pc}\right)\begin{pmatrix}\pi^g_{pyr\,\{2\}}\\\pi^g_{pyr\,\{3\}}\end{pmatrix} - \left(V_{dil} + V_g + V_{pc}\right)\begin{pmatrix}\pi^g_{AcCoA\,\{1\}}\\\pi^g_{AcCoA\,\{2\}}\end{pmatrix}$$

$$[AcCoA^g].\frac{d}{dt}\left(\pi_{AcCoA\,\{1,2\}}^{g}\right)$$

$$= V_{dil}\left(\pi_{Ace\,\{1,2\}}^{g}\right) + \left(V_g + V_{pc}\right)\left(\pi_{pyr\,\{2,3\}}^{g}\right) - \left(V_{dil} + V_g + V_{pc}\right)\left(\pi_{AcCoA\,\{1,2\}}^{g}\right)$$

Enrichment of neuronal TCA cycle intermediates

$$[OG^n].\frac{d}{dt}\begin{pmatrix}\pi_{OG\,\{1\}}^{n}\\\pi_{OG\,\{2\}}^{n}\\\pi_{OG\,\{3\}}^{n}\\\pi_{OG\,\{4\}}^{n}\\\pi_{OG\,\{5\}}^{n}\end{pmatrix} = V_{pdh}^{n}\begin{pmatrix}\pi_{OAA\,\{4\}}^{n}\\\pi_{OAA\,\{3\}}^{n}\\\pi_{OAA\,\{2\}}^{n}\\\pi_{pyr\,\{3\}}^{n}\\\pi_{pyr\,\{2\}}^{n}\end{pmatrix} + V_x\begin{pmatrix}\pi_{Glu\,\{1\}}^{n}\\\pi_{Glu\,\{2\}}^{n}\\\pi_{Glu\,\{3\}}^{n}\\\pi_{Glu\,\{4\}}^{n}\\\pi_{Glu\,\{5\}}^{n}\end{pmatrix} - \left(V_{pdh}^{n} + V_x\right)\begin{pmatrix}\pi_{OG\,\{1\}}^{n}\\\pi_{OG\,\{2\}}^{n}\\\pi_{OG\,\{3\}}^{n}\\\pi_{OG\,\{4\}}^{n}\\\pi_{OG\,\{5\}}^{n}\end{pmatrix}$$

$$[OG^n].\frac{d}{dt}\begin{pmatrix}\pi_{OG\,\{1,2\}}^{n}\\\pi_{OG\,\{2,3\}}^{n}\\\pi_{OG\,\{3,4\}}^{n}\\\pi_{OG\,\{4,5\}}^{n}\end{pmatrix} = V_{pdh}^{n}\begin{pmatrix}\pi_{OAA\,\{3,4\}}^{n}\\\pi_{OAA\,\{2,3\}}^{n}\\\pi_{OAA\,\{2\}}^{n}\pi_{pyr\{3\}}^{n}\\\pi_{pyr\,\{2,3\}}^{n}\end{pmatrix} + V_x\begin{pmatrix}\pi_{Glu\,\{1,2\}}^{n}\\\pi_{Glu\,\{2,3\}}^{n}\\\pi_{Glu\,\{3,4\}}^{n}\\\pi_{Glu\,\{4,5\}}^{n}\end{pmatrix} - \left(V_{pdh}^{n} + V_x\right)\begin{pmatrix}\pi_{OG\,\{1,2\}}^{n}\\\pi_{OG\,\{2,3\}}^{n}\\\pi_{OG\,\{3,4\}}^{n}\\\pi_{OG\,\{4,5\}}^{n}\end{pmatrix}$$

$$[OG^n].\frac{d}{dt}\begin{pmatrix}\pi_{OG\,\{1,2,3\}}^{n}\\\pi_{OG\,\{2,3,4\}}^{n}\\\pi_{OG\,\{3,4,5\}}^{n}\end{pmatrix} = V_{pdh}^{n}\begin{pmatrix}\pi_{OAA\,\{2,3,4\}}^{n}\\\pi_{pyr\{3\}}^{n}\pi_{OAA\,\{2,3\}}^{n}\\\pi_{OAA\,\{2\}}^{n}\pi_{pyr\,\{2,3\}}^{n}\end{pmatrix} + V_x\begin{pmatrix}\pi_{Glu\,\{1,2,3\}}^{n}\\\pi_{Glu\,\{2,3,4\}}^{n}\\\pi_{Glu\,\{3,4,5\}}^{n}\end{pmatrix} - \left(V_{pdh}^{n} + V_x\right)\begin{pmatrix}\pi_{OG\,\{1,2,3\}}^{n}\\\pi_{OG\,\{2,3,4\}}^{n}\\\pi_{OG\,\{3,4,5\}}^{n}\end{pmatrix}$$

$$[OAA^n].\frac{d}{dt}\begin{pmatrix}\pi_{OAA\,\{1\}}^{n}\\\pi_{OAA\,\{2\}}^{n}\\\pi_{OAA\,\{3\}}^{n}\\\pi_{OAA\,\{4\}}^{n}\end{pmatrix} = \frac{V_{pdh}^{n}}{2}\begin{pmatrix}\pi_{OG\,\{2\}}^{n}+\pi_{OG\,\{5\}}^{n}\\\pi_{OG\,\{3\}}^{n}+\pi_{OG\,\{4\}}^{n}\\\pi_{OG\,\{3\}}^{n}+\pi_{OG\,\{4\}}^{n}\\\pi_{OG\,\{2\}}^{n}+\pi_{OG\,\{5\}}^{n}\end{pmatrix} + V_x\begin{pmatrix}\pi_{Asp\,\{1\}}^{n}\\\pi_{Asp\,\{2\}}^{n}\\\pi_{Asp\,\{3\}}^{n}\\\pi_{Asp\,\{4\}}^{n}\end{pmatrix} - \left(V_{pdh}^{n} + V_x\right)\begin{pmatrix}\pi_{OAA\,\{1\}}^{n}\\\pi_{OAA\,\{2\}}^{n}\\\pi_{OAA\,\{3\}}^{n}\\\pi_{OAA\,\{4\}}^{n}\end{pmatrix}$$

$$[OAA^n].\frac{d}{dt}\begin{pmatrix}\pi_{OAA\,\{1,2\}}^{n}\\\pi_{OAA\,\{2,3\}}^{n}\\\pi_{OAA\,\{3,4\}}^{n}\end{pmatrix}$$

$$= \frac{V_{pdh}^{n}}{2}\begin{pmatrix}\pi_{OG\,\{2,3\}}^{n}+\pi_{OG\,\{4,5\}}^{n}\\2\pi_{OG\,\{3,4\}}^{n}\\\pi_{OG\,\{2,3\}}^{n}+\pi_{OG\,\{4,5\}}^{n}\end{pmatrix} + V_x\begin{pmatrix}\pi_{Asp\,\{1,2\}}^{n}\\\pi_{Asp\,\{2,3\}}^{n}\\\pi_{Asp\,\{3,4\}}^{n}\end{pmatrix} - \left(V_{pdh}^{n} + V_x\right)\begin{pmatrix}\pi_{OAA\,\{1,2\}}^{n}\\\pi_{OAA\,\{2,3\}}^{n}\\\pi_{OAA\,\{3,4\}}^{n}\end{pmatrix}$$

$$[OAA^n].\frac{d}{dt}\begin{pmatrix}\pi_{OAA\,\{1,2,3\}}^{n}\\\pi_{OAA\,\{2,3,4\}}^{n}\end{pmatrix}$$

$$= \frac{V_{pdh}^{n}}{2}\begin{pmatrix}\pi_{OG\,\{2,3,4\}}^{n}+\pi_{OG\,\{3,4,5\}}^{n}\\\pi_{OG\,\{2,3,4\}}^{n}+\pi_{OG\,\{3,4,5\}}^{n}\end{pmatrix} + V_x\begin{pmatrix}\pi_{Asp\,\{1,2,3\}}^{n}\\\pi_{Asp\,\{2,3,4\}}^{n}\end{pmatrix} - \left(V_{pdh}^{n} + V_x\right)\begin{pmatrix}\pi_{OAA\,\{1,2,3\}}^{n}\\\pi_{OAA\,\{2,3,4\}}^{n}\end{pmatrix}$$

Enrichment of glial TCA cycle intermediates

$$
[OG^g].\frac{d}{dt}\begin{pmatrix}\pi^g_{OG\,\{1\}}\\\pi^g_{OG\,\{2\}}\\\pi^g_{OG\,\{3\}}\\\pi^g_{OG\,\{4\}}\\\pi^g_{OG\,\{5\}}\end{pmatrix}=(V_g+V_{pc})\begin{pmatrix}\pi^g_{OAA\,\{4\}}\\\pi^g_{OAA\,\{3\}}\\\pi^g_{OAA\,\{2\}}\\\pi^g_{AcCoA\,\{2\}}\\\pi^g_{AcCoA\,\{1\}}\end{pmatrix}+V_x\begin{pmatrix}\pi^g_{Glu\,\{1\}}\\\pi^g_{Glu\,\{2\}}\\\pi^g_{Glu\,\{3\}}\\\pi^g_{Glu\,\{4\}}\\\pi^g_{Glu\,\{5\}}\end{pmatrix}-(V_g+V_x+V_{pc})\begin{pmatrix}\pi^g_{OG\,\{1\}}\\\pi^g_{OG\,\{2\}}\\\pi^g_{OG\,\{3\}}\\\pi^g_{OG\,\{4\}}\\\pi^g_{OG\,\{5\}}\end{pmatrix}
$$

$$
[OG^g].\frac{d}{dt}\begin{pmatrix}\pi^g_{OG\,\{1,2\}}\\\pi^g_{OG\,\{2,3\}}\\\pi^g_{OG\,\{3,4\}}\\\pi^g_{OG\,\{4,5\}}\end{pmatrix}
$$

$$
=(V_g+V_{pc})\begin{pmatrix}\pi^g_{OAA\,\{3,4\}}\\\pi^g_{OAA\,\{2,3\}}\\\pi^g_{OAA\,\{2\}}\pi^g_{AcCoA\,\{2\}}\\\pi^g_{AcCoA\,\{1,2\}}\end{pmatrix}+V_x\begin{pmatrix}\pi^g_{Glu\,\{1,2\}}\\\pi^g_{Glu\,\{2,3\}}\\\pi^g_{Glu\,\{3,4\}}\\\pi^g_{Glu\,\{4,5\}}\end{pmatrix}-(V_g+V_x+V_{pc})\begin{pmatrix}\pi^g_{OG\,\{1,2\}}\\\pi^g_{OG\,\{2,3\}}\\\pi^g_{OG\,\{3,4\}}\\\pi^g_{OG\,\{4,5\}}\end{pmatrix}
$$

$$
[OG^g].\frac{d}{dt}\begin{pmatrix}\pi^g_{OG\,\{1,2,3\}}\\\pi^g_{OG\,\{2,3,4\}}\\\pi^g_{OG\,\{3,4,5\}}\end{pmatrix}
$$

$$
=(V_g+V_{pc})\begin{pmatrix}\pi^g_{OAA\,\{2,3,4\}}\\\pi^g_{OAA\,\{2,3\}}\pi^g_{AcCoA\,\{2\}}\\\pi^g_{OAA\,\{2\}}\pi^g_{AcCoA\,\{1,2\}}\end{pmatrix}+V_x\begin{pmatrix}\pi^g_{Glu\,\{1,2,3\}}\\\pi^g_{Glu\,\{2,3,4\}}\\\pi^g_{Glu\,\{3,4,5\}}\end{pmatrix}-(V_g+V_x
$$

$$
+\,V_{pc})\begin{pmatrix}\pi^g_{OG\,\{1,2,3\}}\\\pi^g_{OG\,\{2,3,4\}}\\\pi^g_{OG\,\{3,4,5\}}\end{pmatrix}
$$

$$
[OAA^g].\frac{d}{dt}\begin{pmatrix}\pi^g_{OAA\,\{1\}}\\\pi^g_{OAA\,\{2\}}\\\pi^g_{OAA\,\{3\}}\\\pi^g_{OAA\,\{4\}}\end{pmatrix}=\frac{V_g}{2}\begin{pmatrix}\pi^g_{OG\,\{2\}}+\pi^g_{OG\,\{5\}}\\\pi^g_{OG\,\{3\}}+\pi^g_{OG\,\{4\}}\\\pi^g_{OG\,\{3\}}+\pi^g_{OG\,\{4\}}\\\pi^g_{OG\,\{2\}}+\pi^g_{OG\,\{5\}}\end{pmatrix}+V_x\begin{pmatrix}\pi^g_{Asp\,\{1\}}\\\pi^g_{Asp\,\{2\}}\\\pi^g_{Asp\,\{3\}}\\\pi^g_{Asp\,\{4\}}\end{pmatrix}-(V_g+V_x+V_{pc})\begin{pmatrix}\pi^g_{OAA\,\{1\}}\\\pi^g_{OAA\,\{2\}}\\\pi^g_{OAA\,\{3\}}\\\pi^g_{OAA\,\{4\}}\end{pmatrix}+
$$

$$
V_{pc}\begin{pmatrix}\pi^g_{pyr\,\{1\}}\\\pi^g_{pyr\,\{2\}}\\\pi^g_{pyr\,\{3\}}\\\pi_{CO_2}\end{pmatrix}
$$

$$[OAA^g].\frac{d}{dt}\begin{pmatrix}\pi^g_{OAA\,\{1,2\}}\\\pi^g_{OAA\,\{2,3\}}\\\pi^g_{OAA\,\{3,4\}}\end{pmatrix}=\frac{V_g}{2}\begin{pmatrix}\pi^g_{OG\,\{2,3\}}+\pi^g_{OG\,\{4,5\}}\\2\pi^g_{OG\,\{3,4\}}\\\pi^g_{OG\,\{2,3\}}+\pi^g_{OG\,\{4,5\}}\end{pmatrix}+V_x\begin{pmatrix}\pi^g_{Asp\,\{1,2\}}\\\pi^g_{Asp\,\{2,3\}}\\\pi^g_{Asp\,\{3,4\}}\end{pmatrix}-(V_g+V_x+$$

$$V_{pc})\begin{pmatrix}\pi^g_{OAA\,\{1,2\}}\\\pi^g_{OAA\,\{2,3\}}\\\pi^g_{OAA\,\{3,4\}}\end{pmatrix}+V_{pc}\begin{pmatrix}\pi^g_{pyr\,\{1,2\}}\\\pi^g_{pyr\,\{2,3\}}\\\pi_{CO_2}\pi^g_{pyr\,\{3\}}\end{pmatrix}$$

$$[OAA^g].\frac{d}{dt}\begin{pmatrix}\pi^g_{OAA\,\{1,2,3\}}\\\pi^g_{OAA\,\{2,3,4\}}\end{pmatrix}=\frac{V_g}{2}\begin{pmatrix}\pi^g_{OG\,\{2,3,4\}}+\pi^g_{OG\,\{3,4,5\}}\\\pi^g_{OG\,\{2,3,4\}}+\pi^g_{OG\,\{3,4,5\}}\end{pmatrix}+V_x\begin{pmatrix}\pi^g_{Asp\,\{1,2,3\}}\\\pi^g_{Asp\,\{2,3,4\}}\end{pmatrix}-(V_g+V_x+$$

$$V_{pc})\begin{pmatrix}\pi^g_{OAA\,\{1,2,3\}}\\\pi^g_{OAA\,\{2,3,4\}}\end{pmatrix}+V_{pc}\begin{pmatrix}\pi^g_{pyr\,\{1,2,3\}}\\\pi^g_{pyr\,\{2,3\}}\pi_{CO_2}\end{pmatrix}$$

$$[OAA].\frac{d}{dt}\begin{pmatrix}\pi^g_{OAA\,\{1,2,3\}}\\\pi^g_{OAA\,\{2,3,4\}}\end{pmatrix}$$

$$=\frac{V_g}{2}\begin{pmatrix}\pi^g_{OG\,\{2,3,4\}}+\pi^g_{OG\,\{3,4,5\}}\\\pi^g_{OG\,\{2,3,4\}}+\pi^g_{OG\,\{3,4,5\}}\end{pmatrix}+V_x\begin{pmatrix}\pi^g_{Asp\,\{1,2,3\}}\\\pi^g_{Asp\,\{2,3,4\}}\end{pmatrix}-(V_g+V_x+V_{pc})\begin{pmatrix}\pi^g_{OAA\,\{1,2,3\}}\\\pi^g_{OAA\,\{2,3,4\}}\end{pmatrix}$$

$$+V_{pc}\begin{pmatrix}\pi^g_{pyr\,\{1,2,3\}}\\\pi^g_{pyr\,\{2,3\}}\pi_{Co_2}\end{pmatrix}$$

Chapter 3. Diffusion-weighted MRS of Ace in the rat brain

Acetate (Ace) has been proposed as a specific energy substrate for astrocytes in the brain. Determination of the relative contribution of Ace into the intracellular and extracellular compartment of brain using diffusion-weighted MR spectroscopy can give insight about cellular environment and distribution volume of Ace in the brain. In present study, localized ^{1}H NMR spectroscopy using a diffusion weighted-STEAM sequence at ultra-high magnetic field (14.1T) was used to investigate the diffusivity characteristics of Ace and NAA during prolonged Ace infusion in the rat brain *in vivo*. The presence of Ace resonance in ^{1}H spectra acquired at very large diffusion weighting indicated restricted diffusion of Ace attributed to the intracellular spaces. However, the significant larger diffusion of Ace compared to NAA suggests that a substantial fraction of Ace is located in the extracellular space of brain. Assuming even distribution for Ace in the intracellular and extracellular space as extreme case, diffusion properties of Ace yielded to a smaller volume of distribution for Ace in the rat brain compared to water and glucose.

3.1. Introduction

Acetate (Ace) has been proposed as a specific energy substrate for astrocytes in the brain and used as an attractive alternative precursor to glucose for *in vitro* and *in vivo* NMR studies of brain metabolism (Lanz et al., 2014; Cruz et al., 2005; Waniewski and Martin, 1998; Badar-Goffer et al., 1990; Cerdan et al., 1990; Nicklas and Clarke, 1969). The uptake of Ace as energy substrate for brain metabolism by only a single cell species in the brain, the glial compartment, can simplify the modeling and increase the sensitivity of the measurement of the glutamate-glutamine cycle in the brain compared to glucose which is taken up by both neuronal and glia compartments alike.

To take full advantage of the dynamic information available from *in vivo* ^{13}C NMR spectroscopy and perform dynamic metabolic modeling of the TCA cycle activity and glutamate/glutamine cycling, prior knowledge of the transport and uptake kinetics of infused Ace across the blood brain barrier is required. Quantitative measurement of Ace transport in the brain has been often done by fitting the measured NMR data to the Michaelis-Menten model which requires the distribution volume (V_d) of Ace in the brain (Deelchand et al., 2009 , Patel et al., 2010). However, the distribution volume of Ace in the rat brain during prolonged Ace infusion is not known. To study transport and utilization of Ace in the rat brain, Deelchand et al., 2009 assumed the same distribution volume for Ace as glucose (V_d (Glc) = 0.77 ml/g), while Patel et al., 2010 considered smaller distribution volume for Ace equal to 0.32 ml/g based on the hypothesis that Ace is mainly localized to the glial cells only (while Glc is found in the glial and neuronal cells). The assumed value for V_d impacts the reported parameters for Ace transport kinetics (see Chapter 4). According to our knowledge, the Ace distribution and relative contribution into the

intracellular and extracellular compartment of the brain using noninvasive modalities of NMR technique has not been performed.

Most noninvasive *in vivo* spectroscopy modalities do not discriminate between the intracellular and extracellular contributions in the measured spectra and provide information about the whole tissue properties such as determination of metabolite concentrations in the intact tissue (Lanz et al., 2014b; Henry et al., 2006a; Gruetter et al., 2003; Murphy and Hellerstein, 2000). However, this information is important when looking at the metabolic modeling. In this regard, diffusion-weighted MR spectroscopy (DW-MRS) could help due to its potential for measuring the translational displacement of metabolites in tissue and providing information about the cellular environment (for reviews see Cao and Wu, 2016; Nicolay et al., 2001; Ronen et al., 2015 and references therein). DW-MRS can differentiate between the signal originating from the intracellular and extracellular compartment based on their different diffusion properties (Van Zijl et al., 1991). Therefore, DW-MRS is likely to yield insights into the distribution volume of Ace in the rat brain.

Over the years, proton DW-MRS has remained a very challenging technique from the perspective of the acquisition of robust and reproducible DW-MRS data and their subsequent processing and quantification. The DW-MRS contrast is based on the random displacement of metabolites in the presence of diffusion gradients in an NMR sequence. Therefore any type of bulk motion could result in amplitude or phase fluctuation of the NMR signal. Eddy current impacts on the spectra line shape are not particular to DW-MRS, but the application of diffusion gradients significantly increases the eddy current effect. In diffusion measurements, all NMR gradients operating on the spins during a pulse sequence should be considered in the estimation of the diffusion weighting (*b*-value) in a DW sequence, including the diffusion-weighted gradients and all other gradients generated by the sequence such as slice selection and crusher gradients.

Due to these technical challenges and low sensitivities of the technique, most rodent studies focused on the diffusion properties of highly concentrated metabolites, such as NAA, which are predominantly located in the intracellular compartment (Abe et al., 2000; Assaf and Cohen, 1998; de Graaf et al., 2001; Marchadour et al., 2012; Najac et al., 2014; van der Toorn et al., 1996).

Pfeuffer et al., 2000 performed a DW-MRS study to test the hypothesis about even distribution of infused glucose in the extracellular and intracellular space in the rat brain and characterized the diffusion properties of 14 metabolites. Applying similar strategies, proton DW-MRS of brain under prolonged Ace infusion could also provide information on the intrinsic diffusion properties of Ace in the brain non-invasively and give insight into the cellular constituents that constrain the diffusional displacements.

Overlapping of metabolites resonances in ^{1}H spectra *in vivo* complicates the quantification of each individual metabolite. The challenge in the study of Ace diffusion behavior is the overlap of Ace ^{1}H MRS resonance (1.90 ppm) with a GABA resonance at 1.89, which hinders an accurate estimation of the concentration and diffusivity of Ace. Therefore the purpose of this study was to address the diffusion characteristics of Ace in the rat brain *in vivo* using DW-MRS techniques at steady-state concentration of Ace in brain with a simultaneous minimization of the contribution of the overlapping GABA resonance.

3.2. Methods

3.2.1. Animal preparation

All experimental procedures involving animals were approved by the local veterinary authorities. 11 male Sprague–Dawley rats (200-235g, delivered from Charles River Laboratories, France) were prepared without fasting. Animals were intubated and ventilated with 2% isoflurane during surgery. Both femoral veins were catheterized for the administration of acetate and α-chloralose. Two arteries were cannulated for the continuous monitoring of physiology (blood pressure, heart rate) and periodic blood sampling for blood gas, plasma lactate and glucose concentration measurements. Following surgery, anesthesia was switched to the intravenous α–chloralose administration (bolus of 80mg/kg and continuous infusion rate of 26.7 mg/kg/h). Animals were placed in a home-built holder and the head position was fixed using ear rods and a bite-bar. Body temperature was maintained between 37.0 and 37.5 °C with a temperature-regulated circulating water bath.

3.2.2. Acetate infusion protocol

The sodium Ace infusion protocol was optimized at bench and in the magnet to reach a steady-state concentration of Ace in the rat brain in less than 30 min and keeping animal in physiological limits throughout the study. After adjustment of MRS parameters and shimming, a bolus of 1g/kg of sodium acetate (1.6 M) was administered with an infusion rate decaying exponentially over 10 min. This bolus was followed by a continuous infusion of acetate at a rate of 1.4 g/kg/h.

In order to stay away from metabolic alkalosis in the blood of animals during study (Burnier et al., 1992; Ward et al., 1985), the acetate solution was infused at an acidic pH (of 5.0) as previously used in rats (Deelchand et al., 2009b; Sugimoto et al., 1997).

3.2.3. In vivo and in vitro NMR spectroscopy at 14.1T

Spectra were acquired on a 14.1T MRI system interfaced to a 26-cm horizontal bore magnet (Magnex Scientific, Oxford, UK; Varian, Palo Alto, CA, USA), equipped with 12 cm inner diameter actively shielded gradient reaching 400 mT/m in 120 µs. A home-built quadrature transceiver with two physically decoupled 12 mm-diameter loops was used.

After initial setting, fast spin echo images (TR= 4 s and TE effective = 40 ms; four echoes) were acquired to select a volume of interests (VOI) of 450 µl in the rat brain (Fig 3.1). Magnetic field homogeneity was adjusted using FAST(EST)MAP (Gruetter and Tkác, 2000b). Localized ^{1}H NMR spectra were acquired using the Stimulated Echo Acquisition Mode (STEAM) sequence (Pfeuffer et al., 2000). Acquisition parameters were optimized for Ace detection and are described in the following of this section.

Water suppression was done using seven chemical shift-selective (CHESS) adiabatic RF-pulses followed by crusher gradients. Outer volume suppression was performed using eight adiabatic pulses followed by crusher gradients, which are repeated three times during the CHESS preparation to improve the unwanted signal suppression. To determine the apparent concentration of metabolites, one unsuppressed water signal was acquired from the VOI as reference.
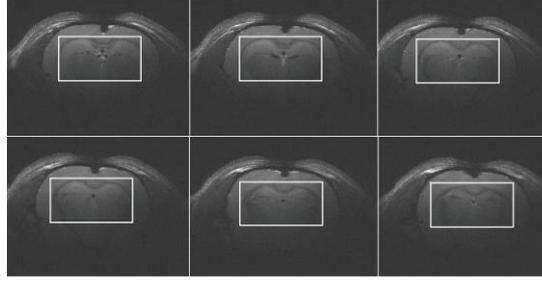
Fig 3.1 Axial image of a rat brain acquired from voxel size of 6×10×4 mm^3 using spin echo (FOV:25×25 mm^2, Ave:4), showing a typical region of interest (ROI) used for acquiring ^{1}H NMR spectra.

3.2.3.1. Accurate detection of Ace in ^{1}H NMR spectra

To distinguish the singlet of Ace ^{1}H MRS resonance (1.90 ppm) from the overlapping GABA resonance at 1.89 ppm, the rational was to minimize GABA signal by playing with J modulation, enabling accurate Ace concentration quantification. Since J modulation is affected by both the echo time (TE) and mixing time (TM) in the STEAM sequence (see Fig 1.19 in Chapter 1), a series of experiments were implemented to establish the optimum acquisition parameters. Experiments were done in a phantom containing GABA (50 mM) and Cho (10 mM) as reference with adjusted pH of 7.2 and temperature of 37°C in order to mimic the *in vivo* conditions and find the optimum parameters for minimizing the GABA resonance at 1.89 ppm. First experiments were acquired with TE ranging from 2.8 ms to 100 ms. With the optimum TE determined by the minimum amplitude of the GABA resonance at 1.89 ppm, a second series of data was acquired with TM ranging from 24 ms to 174 ms. The optimum TM and TE in the STEAM sequence found for minimizing GABA peak in the phantom experiments were evaluated in experiments in the rat brain *in vivo*.

3.2.3.2. Diffusion weighting acquisition parameters

The diffusion weighted-STEAM (DW-STEAM) sequence described by Pfeuffer et al., 2000; Kunz et al., 2010 was used to investigate the metabolite diffusivity characteristics of metabolites *in vivo* in seven adult rat brains. Diffusion gradients are placed during the delay time τ in the STEAM sequence: 90°-τ-90°- TM-90°- τ-ACQ (see Fig 3.2). The signal attenuation of the ^{1}H diffusion is determined by the following acquisition parameters: the diffusion gradients amplitude, G_{diff}, duration of the applied diffusion gradients, δ and separation of the diffusion gradients Δ, which define the diffusion time, $t_{diff} = \Delta - \delta/3$ and give rise to a b–value, $b = \left(\gamma^2 \, G_{diff}^{\;2} \, \delta^2\right)t_{diff}$. In addition to the dedicated diffusion gradients, inherent gradients in the STEAM sequence, such as localization and crusher gradients, also contribute to the diffusion weighting of the MRS signal. Therefore, both diffusion and STEAM gradients were considered in the b-value calculation using a home build Matlab script (MathWorks, Natick, MA, USA). Diffusion gradients were applied in three orthogonal directions simultaneously to be able to reach higher diffusion weighting. To vary the diffusion weighting of the signal in this study, only the diffusion gradient amplitude was changed while the other parameters were kept constant.

In a first set of experiments, *in vivo* data were acquired with G_{diff} = 0, 28, 49, 65 and 91 mT/m which corresponds to the b -values ranging from 0.2 to 5 ms/µm^2. In second set of experiments, three additional diffusion gradients amplitude were used with stronger intensity of 137, 159 and 191 mT/m

to investigate the different diffusion regime resulting in b-values of 10, 13 and 18 ms/µm^2. In all experiments, the signals were acquired with δ =5ms, t_{diff}=73 ms, TR=4s, optimum TM and TE found to minimize GABA resonance at 1.89 ppm in the STEAM sequence (c.f. 3.2.3.1).

To reduce the phase variation between averaged FIDs due to movement, a respiration trigger was applied in the DW-STEAM sequence. In the respiratory-triggered DW-STEAM sequence, spectra are acquired based on the rat breathing patterns and data of each scan were stored separately, which allowed us to do individual phase corrections.

To prevent biasing the attenuated spectra due to minor variability either in physiology, Ace concentration, shimming or spectral quality during experiment, the acquisition over all b-value range (0-18 ms/µm^2) for every animal were split in a series of acquisition sets with interleaved b -values. The number of averages in every set was 16 FIDs for $0 \leq b \leq 7$ ms/µm^2 (1 min5s), 32 FIDs for b -value of 10 (2min10s) and 13 ms/µm^2, and 48 FIDs for b -value of 18 ms/µm^2 (3min15s).

Moreover, extra experiments were performed in a rat without Ace infusion under α-chloralose anesthesia, using same sequence parameters applied in this study for metabolites diffusivity in the rat under Ace infusion. Then the diffusion-attenuated signal of metabolites over b-value range 0 to 18 ms/µm^2 were compared between rats with and without Ace infusion.

Also, two series diffusion experiments were performed in the rat brain *in vivo* (two rats under continuous Ace infusion for every group) at shorter diffusion time (Δ= 45 ms, t_{diff}= 43 ms) and longer diffusion time (Δ= 200ms, t_{diff}= 198 ms) than the one considered in this study (t_{diff}=73 ms), while other acquisition parameters were kept same as ones applied for t_{diff}= 73 ms.
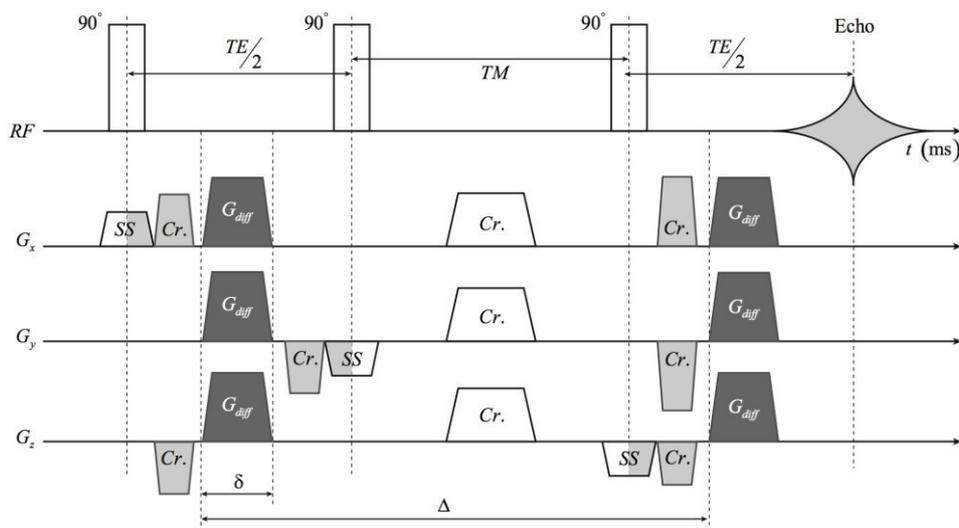

Fig 3.2 Localized diffusion weighed STEAM based spectroscopic pulse sequence (DW-STEAM). The signal localization is performed by application of three slice selection gradients (*SS*) during the 90° RF-pulses. Crushers gradients (*Cr.*) are applied during the mixing time period (TM) as well as during both TE/2 periods. Diffusion gradients G_{diff} are also applied during TE/2 with an application time δ and a diffusion time Δ (Kunz et al., 2010).

3.2.3.3. Processing and quantification of data

To prepare the acquired spectra from individual animals for analysis, some pre-processing steps were performed as following. Firstly, the phase variations were corrected scan by scan by maximizing the N-acetyl aspartate resonance height. Secondly, phased spectra acquired at the same b-value were corrected for B_0 drift and then averaged together.

In vivo ^{1}H NMR summed spectra were processed using LCModel (Stephen Provencher Inc., Oakville, ON, Canada) and the unsuppressed water signal acquired from the same voxel used as reference for eddy current correction and determining the apparent metabolites concentration. No baseline correction, zero-filling or appodization functions were applied to the data prior to the quantification. The Cramera-Rao lower bounds (CRLBs) calculated by the LCModel were used as a measure of the reliability of the metabolites estimate.

The basis sets required by LCModel for spectra quantifications were generated for all metabolites detected in the spectra over the rat brain during continuous intravenous Ace infusion The metabolites signal (except macromolecule) were simulated using NMRSCOPE B plugin in JMRUI (Starčuk Jr et al., 2009) ,with the appropriate chemical-shift and J-coupling pattern as described by Govindaraju et al., 2015 and 2000 and STEAM sequence parameters used in this study. The macromolecules (MM) signals were measured experimentally *in vivo* from a rat brain (see more detail in part 4.3.2).

3.2.4. Diffusion weighting attenuation modeling

To compare with previous *in vivo* diffusion studies of metabolites (Ligneul et al., 2016; Kunz, 2010; Duong et al., 2001; Pfeuffer et al., 2000; van der Toorn et al., 1996), apparent mono-exponential diffusion coefficient (D_{mono}^{App}) were estimated for metabolites quantified precisely over the whole b-value range. Data for metabolites in a b-value interval of 0 to 5 ms/ μm^2 were fitted with a mono exponential diffusion model using the following equation where S and S_0 are the signal intensity with and without diffusion gradients, respectively.

$$\frac{S}{S_0} = \exp\left(-b . D_{mono}^{App}\right)$$
<div align="right">Eq. 3.1</div>

Diffusion-weighted data were then analyzed over the b-values ranging from 0 to 18 ms/μm^2 and all data (except MM) fitted using the following bi-exponential equation where the (D_{fast}^{App}, D_{slow}^{App}) represent apparent diffusion coefficients of the fast and slow decaying signal components of each metabolite and p_{slow}^{App} reflects the relative contribution of the slow component in the metabolite signal (Pfeuffer et al., 2000).

$$\frac{S}{S_0} = p_{slow}^{App} . \exp\left(-b . D_{slow}^{App}\right) + \left(1 - p_{slow}^{App}\right) . \exp\left(-b . D_{fast}^{App}\right)$$
<div align="right">Eq. 3.2</div>

The attenuated signals of MM were fitted mono exponentially using Eq. 3.1 over the whole b-value range of 0 to 18 ms/μm^2. To determine the confidence intervals of the adjusted parameters, Monte Carlo simulations were performed with 500 artificial datasets generated based on the Bootstrapping method (Press, 2007). Bootstrap method relies on random sampling with replacement from measured series spectra for every data point (see part 1.4.1.4.7). In this way, the generated synthetic data sets could be used in Monte Carlo simulation to estimate the distribution of estimated parameters in the model. Curve fitting based on the Levenberg-Marquardt algorithm and further numerical procedures were performed in Matlab (MathWorks, Natick, MA, USA) using home-build scripts. The extracellular fraction of Ace was estimated by the following equation, where k_{intra} was determined by the contribution ratio of the

fast and slow component of known intracellular metabolite like NAA (Pfeuffer et al., 2000), simplified as:

$$k_{intra}(NAA) = \frac{p_{fast}^{App}(NAA)}{p_{slow}^{App}(NAA)} \quad p_{slow}^{App}(NAA) + p_{slow}^{App}(NAA) = 1 \qquad \text{Eq. 3.3}$$

$$k_{intra}(NAA) = \frac{1}{p_{slow}^{App}(NAA)} - 1, \qquad \text{Eq. 3.4}$$

$$p_0^{extra}(Ace) = 1 - p_{slow}^{App}(Ace).(k_{intra}(NAA) + 1) \qquad \text{Eq. 3.5}$$

3.3. Results

The main goal of the present study was to assess the Ace diffusion properties in the brain tissue *in vivo* and compare to a reference intracellular metabolite, NAA. To achieve our objectives, the Ace infusion protocol and DW-STEAM sequence parameters were optimized to ensure a reliable assessment of diffusion behavior at steady state of Ace concentration in the rat brain.

3.3.1. Apparent concentration of Acetate in brain tissue

To minimize spectral signal loss due to the macroscopic motion, respiration cycle triggering was applied during acquisition and each FID signal stored separately. The high quality and SNR of the acquired ^{1}H spectra enabled us to apply the individual spectrum phase correction, which was then followed by the signal averaging. The higher sensitivity given by the surface coil at the high magnetic field (14.1T) and efficient B_0 shimming using FAST (EST) MAP method (Gruetter and Tkac, 2000) provide a typical spectrum with SNR of 14 for 16 averages over a voxel size of 240 µl, based on the NAA resonance. To reduce the signal overlap between the acetate singlet and the GABA resonance at 1.89 ppm, longer TE of 50 ms and a TM of 49 ms in the STEAM sequence were used (see *in vitro* results in Fig 3.3 and *in vivo* in Fig 3.4). This resulted in well-resolved resonances in spatially localized ^{1}H NMR spectra with and without diffusion weighting (Fig 3.5), in particular the Ace resonance at 1.90 ppm. The SNR of the averaged spectra used in this study (0-19.1 G/cm) was ascertained to be higher than 20 (based on the NAA resonance) for all b-values, which was sufficient for a precise quantification of the detected metabolites (CRLB $\leq$ 20).

3.3.2. Diffusion-weighted ^{1}H MRS

To test the performance of DW-STEAM sequence at the acquisition parameters optimized for the *in-vivo* detection of Ace (TE = 50 ms and TM = 49 ms), the attenuation of the signal from a high viscosity phantom containing 1,2-propanediol oil was measured by increasing the b-value up to 18 ms/µm^2, signal attenuation was ascertained to be mono-exponential. The self-diffusion coefficient of 1,2-propanediol oil (Sigma-Aldrich, Buchs SG,Switzerland) at room temperature(around 20°) was about 0.32±0.07 µm^2/ms, close to the published value in a previous study (D'Agostino et al., 2014), demonstrating the reliability of the procedure used in this study. To compare the intrinsic diffusion of Ace and NAA, the free diffusion of Ace and NAA was estimated *in vitro* in a phantom containing NAA and Ace with b-values ranging from 0 to 3.5ms/µm^2 (

Fig 3.6). A mono exponential fitting of acquired DW-signals resulted in a D_{free} of 0.83±0.02 µm²/ms for NAA and 1.27±0.03 µm²/ms for Ace (Table 3.1). To determine the diffusivity of Ace and NAA for 2-3 h during continuous intravenous Ace infusion in rat, diffusion attenuated spectra were acquired using the optimum parameters applied in DW-STEAM sequence (TE=50 ms and TM=49 ms). With increasing the diffusion weighting up to b = 5 ms/µm² (Fig 3.5), the NAA intensity dropped by 35% and Ace by 65 % of their respective initial intensity acquired without applying diffusion gradients. Curve fitting of a mono-exponential decay to the normalized attenuated signal relative to b-value range of 0 to 5 ms/µm² (Fig 3.7) enabled the determination of an apparent diffusion coefficient (ADC) of 0.09µm²/ms for NAA and approximately three times higher ADC for Ace, i.e. 0.24 ms/µm², with a coefficient of variation lower than 5% (Table 3.1). Therefore, when extending the *in vivo* measurement to higher b-values, the normalized diffusion-attenuated signal for NAA and Ace was clearly non-linear, indicating a multi-exponential decay (Fig 3.8). Increasing the diffusion weighting to high b-values up to 18 ms/µm² resulted in the signal attenuation of 63% for NAA and 83% for Ace compared to their initial amplitude. At maximum b-value, the NAA signal was still above noise level on single FID spectrum and the mean CRLB estimated with LCModel for NAA and Ace quantification in summed spectra from single animal was 2% and 10%, respectively. In additions, other metabolites present in brain with high concentration, such as glutamate (Glu), taurine (Tau), creatine(Cr) and phosphocreatine (Pcr) were well quantified with CRLB less than 10%. Furthermore, the diffusivities of other detectable metabolites in acquired ¹H spectra including Glu, Cr+PCr, Gly, Tau and MM were evaluated as well (Fig 3.8). ADC of the metabolites Glu, Cr+PCr, Gly and Tau were estimated with good precision in Table 3.1 using the mono exponential fit to the attenuated signal of metabolites over b value range 0 to 5 ms/µm² (coefficient of variation was less than 10%).
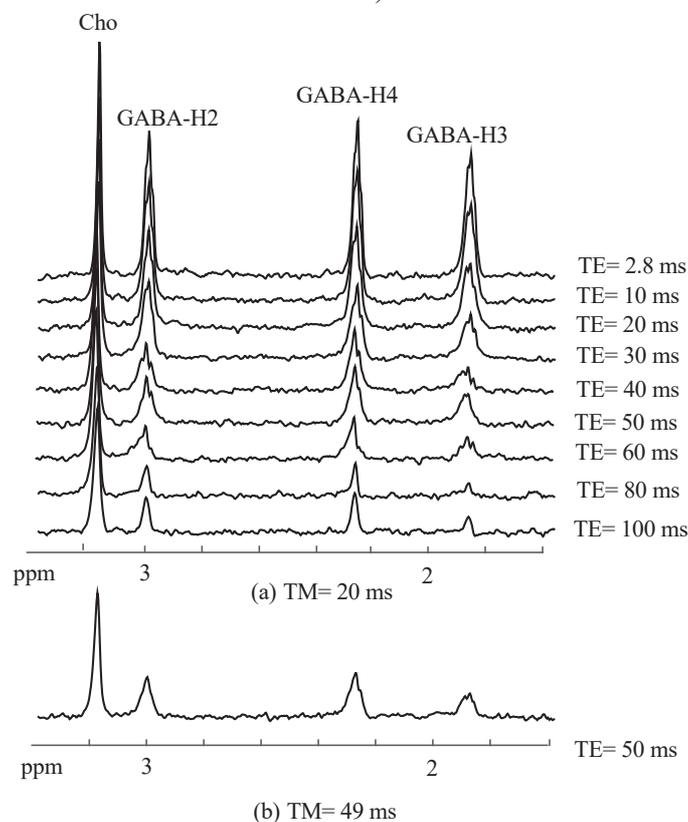

Fig 3.3 *In vitro* spectra of phantom including GABA (50 mM) and Cho(10 mM) as reference were acquired by STEAM sequence at 14.1 T, TR=10 s, (a) different TEs ranging from 2.8 ms to 100 ms,

TM= 20 ms, and (b) TE= 50 ms and TM= 49 ms, the optimum parameters applied in STEAM sequence for minimization of GABA at 1.89 ppm.
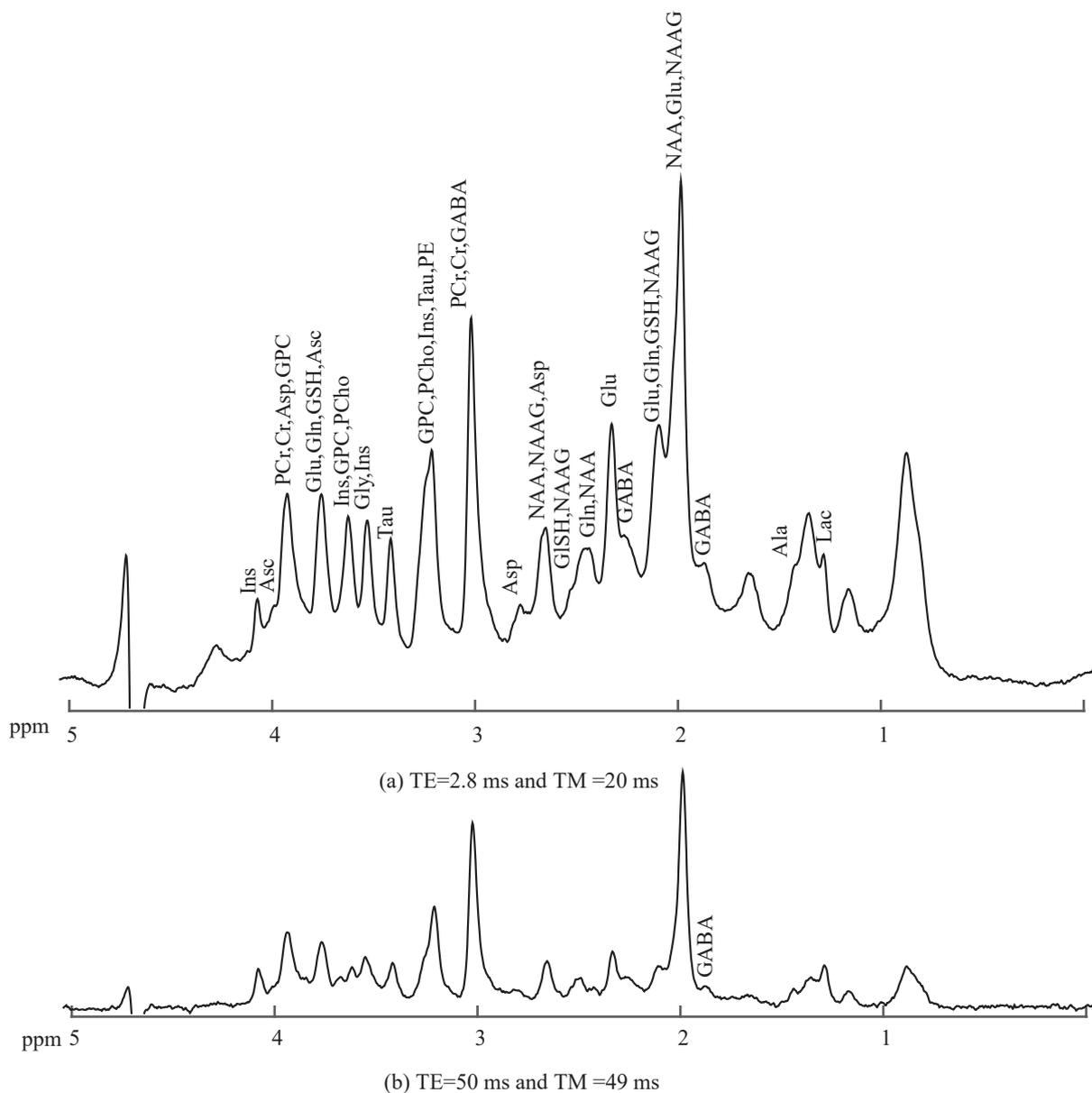

Fig 3.4 Normalized *In vivo* ¹H NMR spectra of the rat brain acquired using STEAM sequence at 14.1T, TR= 4 s using (a) short echo time and mixing time (TE= 8.5 ms and TM= 20 ms), and (b) long echo time and mixing time (TE= 50 ms and TM= 49 ms). The noticeable shoulder corresponding to Gamma-aminobutyric Acid (GABA) at 1.89 ppm was minimized at TE= 50 ms and TM= 49 ms. Different resonances corresponding with presented metabolites in the rat brain are visible in the acquired ¹H proton spectra *in vivo*: N-acetyl aspartate (NAA), N-acetyl aspartate glutamate (NAAG), alanine (Ala), γ-aminobutyric acid (GABA), ascorbic acid (Asc), aspartate (Asp), phosphoryl choline (PCho), glycerolphosphorylcholine (GPC), creatine (Cr), phosphocreatine (PCr), glutamate (Glu), glutamine (Gln), glutathione (GSH), glycerol (Gly), myo-Inosito (Ins), lactate (Lac), taurine (Tau).
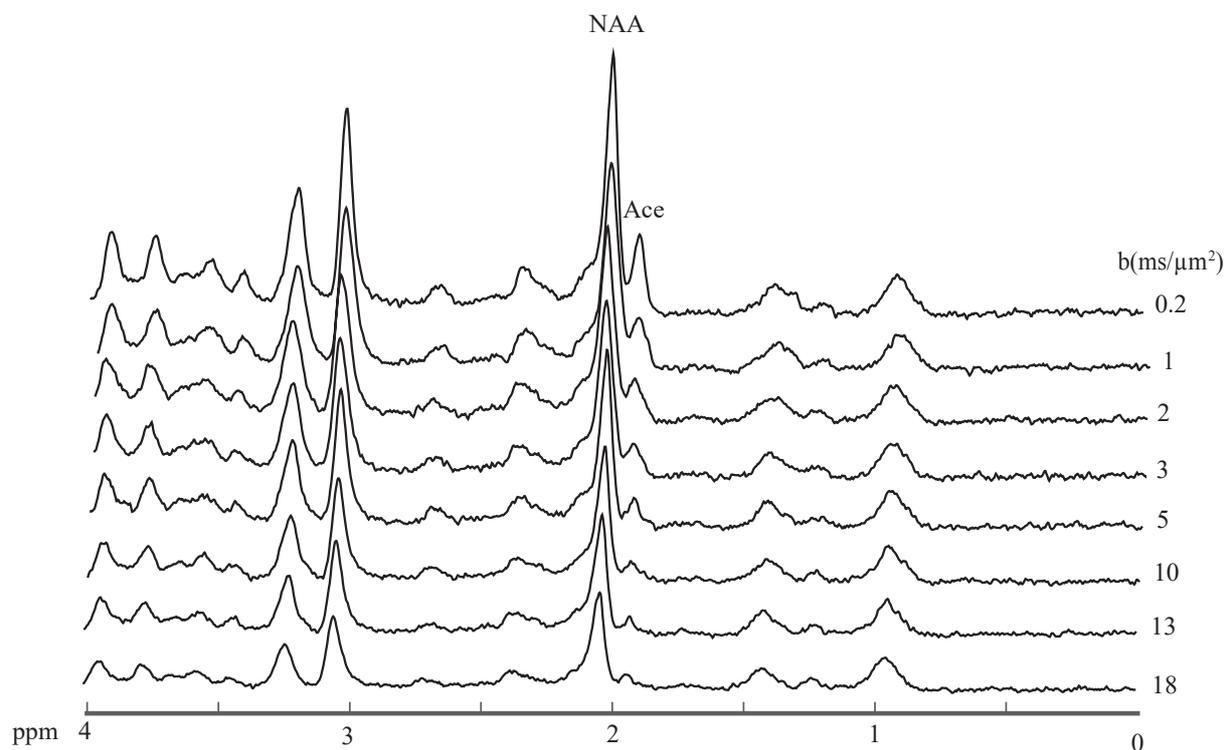
Fig 3.5 Diffusion-attenuated summed ^{1}H NMR spectrum (TR = 4 s, TE = 50 ms, t_{diff} = 73 ms) acquired during the stability of Ace concentration in the single rat brain following continuous intravenous Ace infusion. Every spectrum corresponds to specific b-value, from top to bottom: 0.2, 1, 2, 3, 5, 10, 13 and 18 ms/μm^2.
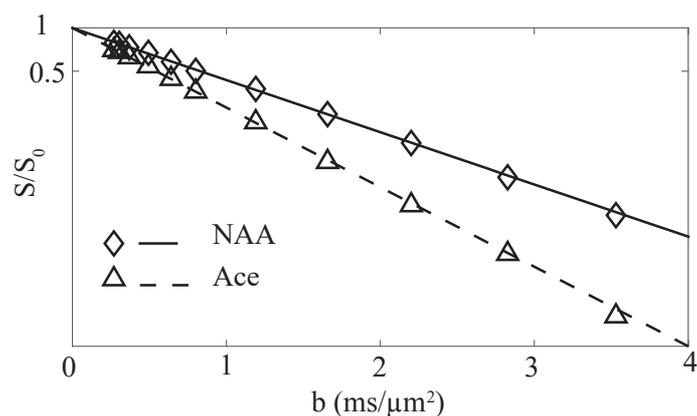

Fig 3.6 The normalized diffusion-attenuated ^{1}H MRS signal intensities of NAA and Ace in the phantom with mono exponential fit in b-value range of 0 to 3.5ms/μm^2. All data acquired at14.1 T using DW-STEAM sequence, TR= 10s, TE= 50 ms, t_{diff}= 73 ms.
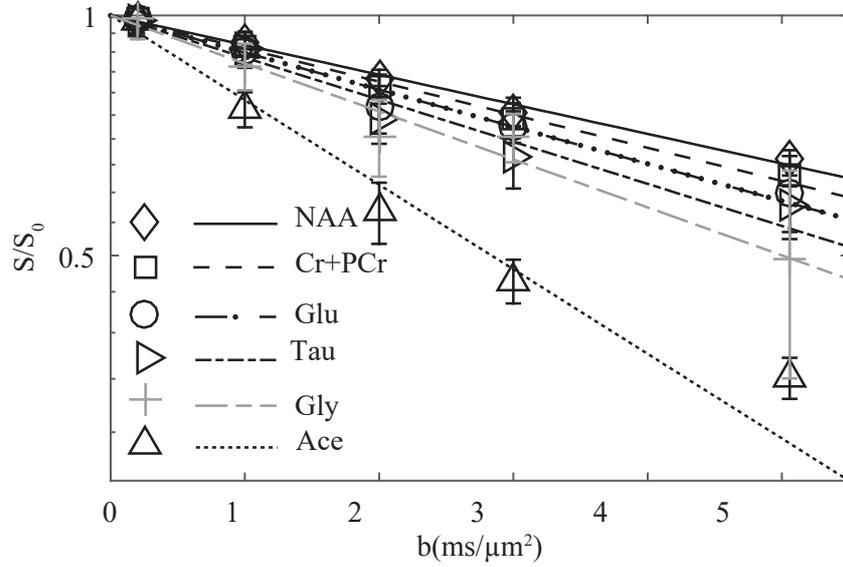
Fig 3.7 The normalized diffusion-attenuated ^{1}H MRS signal intensities of NAA, Ace, Total Cr+PCr, Glu, Tau, Gly, Ace in the rat brain *in vivo* with mono exponential fit over *b*-value range 0 to 5 ms/μm². All data acquired at14.1 T using DW-STEAM sequence, TR= 4s, TE= 50 ms, t_{diff}= 73 ms. The error bars indicate the standard deviation of the data averaged over seven animals.

To characterize the non-monoexponential decay of NAA and Ace, normalized attenuated signal of metabolites were fitted using Eq. 3.2 over all b-value range in Fig 3.8 (0 to 18 ms/μm²). Bi-exponential fitting provided apparent diffusion coefficients for the fast and slow decaying components of NAA and Ace metabolites (Table 3.1). The fast diffusion component of NAA showed an apparent diffusion coefficient (D_{fast}^{App}) of 0.20±0.04 μm²/ms, while the apparent diffusion coefficient D_{fast}^{App} of fast component of Ace was 0.44±0.02 μm²/ms. The slow diffusion component of NAA was characterized by an apparent diffusion (D_{slow}^{App}) of 0.026±0.010 μm²/ms while for Ace D_{slow}^{App} was 0.038±0.003 μm²/ms. The probability distribution of the estimated value for the slow and fast diffusion of NAA and Ace and also the contribution of their slow component in the total attenuated signal (estimated from Monte Carlo simulations, n=500) are shown in Fig 3.9.

Table 3.1 Apparent diffusion coefficient (ADC) of metabolites estimated using mono-exponential fit in the rat brain *in vivo* for 0< *b* <5 ms/ μm² and in phantom (NAA and Ace) for 0< *b* <3.5 ms/ μm², mean ± SD calculated by Monte Carlo (n=500).

	NAA	**Ace**	**Glu**	**Cr+PCr**	**Tau**	**Gly**
D_{mono}^{App}(μm²/ms) *In vivo*	0.086 ±0.002	0.240 ±0.008	0.107 ±0.006	0.096 ±0.003	0.138 ±0.014	0.121 ±0.006
D_{mono}^{App}(μm²/ms) In phantom	0.83 ±0.01	1.27 ±0.01	____	____	____	____
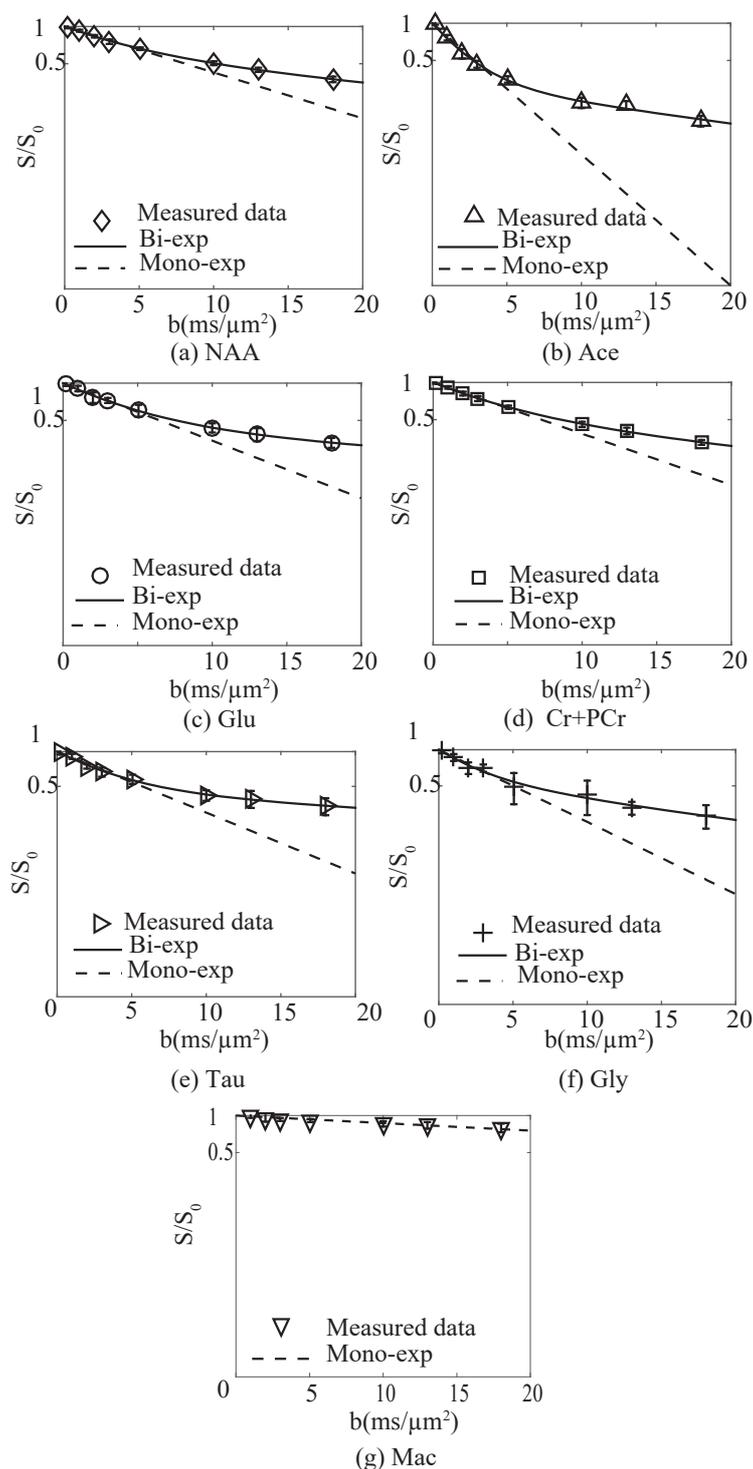
Fig 3.8 The normalized diffusion-attenuated ^{1}H MRS signal intensities of (a) NAA, (b) Ace, (c) Glu, (d) Cr+PCr, (e) Tau and (f) Gly in the rat brain *in vivo* with mono exponential fit in the *b*-value range 0 to 5 ms/µm^2 (dot lines) and bi-exponential fit in the *b*-value range of 0 to 18 ms/µm^2 (solid line) in *logarithmic* plot. (g) The normalized diffusion-attenuated ^{1}H MRS signal intensities of Mac were fitted mono exponentially in the *b*-value range 0 to 18 ms/µm^2 (dot lines). All data acquired at14.1T using DW-STEAM sequence, TR= 4s, TE= 50 ms, t_{diff}= 73 ms. The error bars indicate the standard deviation of data averaged over seven animals.

Table 3.2 Apparent diffusion coefficient of metabolites in the rat brain *in vivo* at 14.1 T, estimated using bi-exponential fit for $0< b <18$ ms/ μm^2, mean $\pm$ SD calculated by Monte Carlo (n=500).

	NAA	Ace	Glu	Cr+PCr	Tau	Gly
$D_{fast}^{App}(\mu m^2/ms)$	0.20 ±0.04	0.44 ±0.02	0.20 ±0.05	0.20 ±0.03	0.26 ±0.04	0.34 ±0.09
$D_{slow}^{App}(\mu m^2/ms)$	0.026 ±0.010	0.038 ±0.003	0.018 ±0.013	0.030 ±0.006	0.017 ±0.010	0.038 ±0.013
P_{slow}^{App}	58% ±10	33% ±2	46% ±12	54% ±7	54% ±7	66% ±13

Contribution of the slow component in the normalized attenuated signal, p_{slow}^{App}, was found to be 58%±10% for NAA and 33%±2% for Ace. The intracellular component ratio, k_{intra} (Eq. 3.1) was estimated from p_{slow}^{App} of NAA (0.72±0.1), and used as reference for the metabolite localized purely to the intracellular compartment. The extracellular fraction, p_0^{extra} for Ace (Eq. 3.5) was estimated 43%±10%. Also, if we consider Cr+PCr as intracellular reference, the estimated p_0^{extra} (39%±8%) is not significantly different from one estimated using NAA.

Diffusion of the fast and slow component of metabolites Cr+PCr, Glu, Tau and Gly in Table 3.2 were in good agreement with the published values (Ligneul et al., 2016; Pfeuffer et al., 2000). The estimated value D_{slow}^{App} for Glu and Tau are more close to the one of NAA, while Cr+PCr and Gly have approximately same D_{slow}^{App} as Ace. However the standard deviation in the estimated value D_{slow}^{App} for these metabolites (Cr+PCr, Glu, Gly and Glu) is a bit high (more than 25%). The contribution of the slow component of these metabolites in diffusion-attenuated signal is in the same range as NAA, around 50%.

Normalized attenuated signal of MM presents linear diffusivity over *b*-value range 0 to 18ms/ μm^2 (Fig 3.8.g) and a mono exponential fit to the normalized attenuated signal yields ADC of 0.014 ±7% μm^2/ms.
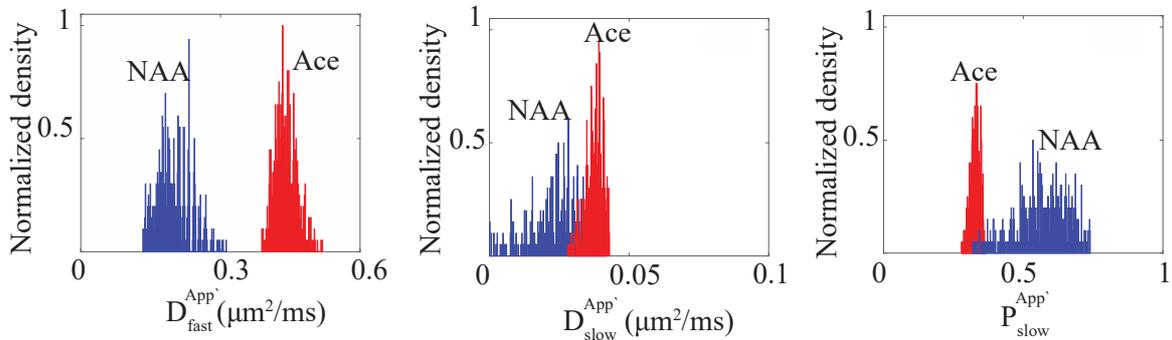
Fig 3.9 Probability distribution of the estimated values for (a) diffusion of fast component, D_{fast}^{App}, (b) diffusion of slow component, D_{slow}^{App}, and (c) the contribution of the slow component, P_{slow}^{App} for the metabolites NAA and Ace in the rat brain *in vivo*, obtained using bi-exponential fit to the noisy data (n=500, generated based on Bootstrapping method in Monte Carlo simulation) over *b*-value range of 0-18 ms/μm^2.
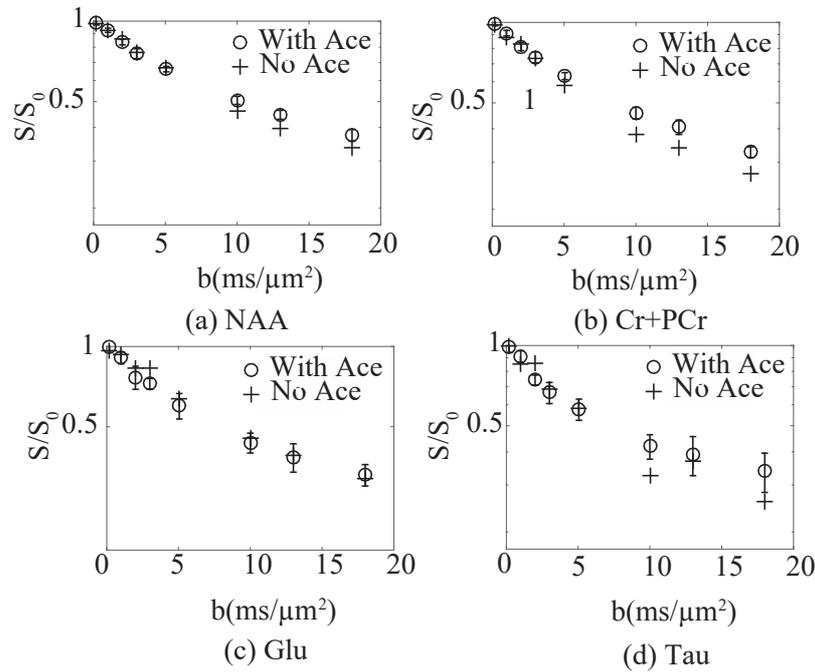
Fig 3.10 The normalized diffusion-attenuated ^{1}H MRS signal intensities of metabolites (a) NAA, (b) Cr+PCr, (c) Glu, and (d) Tau in the rat brain *in vivo* over *b*-value range 0 to 18 ms/µm^2 in *logarithmic* plot. Circles and error bars present the average and standard deviation obtained from seven rat brains under Ace infusion and cross symbols show the data from a normal rat brain without Ace infusion. All data acquired at14.1 T using DW-STEAM sequence, TR= 4 s, TE= 50 ms, t_{diff}= 73 ms.
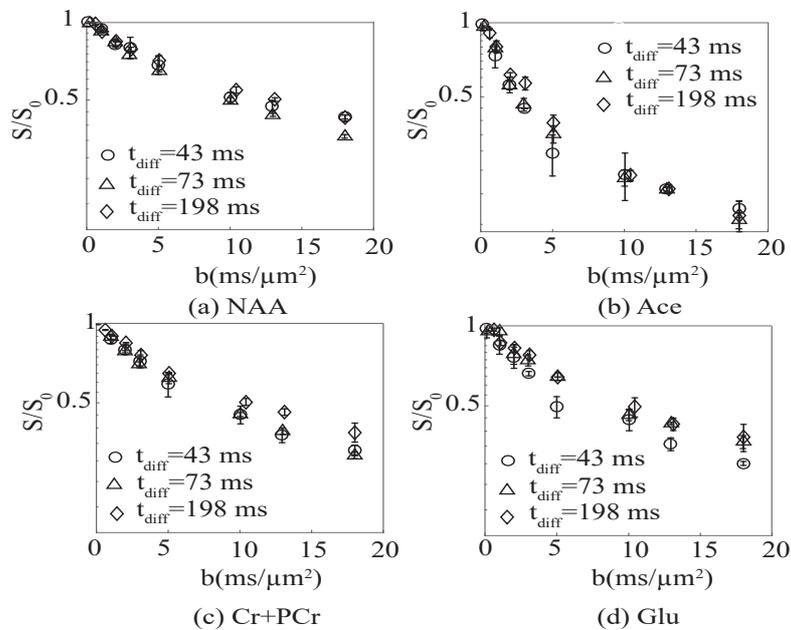
Fig 3.11 The normalized diffusion-attenuated ^{1}H MRS signal intensities of metabolites (a) NAA, (b) Ace, (c) Cr+PCr, and (d) Glu in the rat brain *in vivo* over *b*-value range 0 to 18 ms/µm^2 in *logarithmic* plot. All data acquired at14.1T using DW-STEAM sequence, TR = 4 s, TE = 50 ms and three diffusion times 43, 73 and 198 ms. Error bars present the average and standard deviation obtained from two rats brain at every diffusion time.

To verify the minimum effect of Ace infusion on metabolite diffusivity in the rat brain, the attenuated signal acquired from the rat brain without Ace infusion was evaluated over the b-value range 0 to 18 ms/ μm^2. The data points corresponding to the normalized attenuated signal of metabolites from the rat brain without Ace infusion is not significantly different from the average of attenuated signal of metabolites acquired from seven rats brain under Ace infusion (Fig 3.10).

To validate the diffusion time independency of metabolite diffusivity at given parameters used in this study, the diffusivity of metabolites at $t_{diff} = 73$ ms was compared with ones measured at diffusion times 43 and 198 ms over the b-value range 0 to 18 ms/μm^2 (Fig 3.11) The results showed that there is no significant difference in the diffusivity of the metabolites at different diffusion times t_{diff} 43, 73 and 198 ms, confirming the diffusion time independency of metabolites at $t_{diff} = 73$ ms.

3.4. Discussion

The localized ^{1}H NMR spectroscopy performed using diffusion weighted-STEAM sequence at ultra-high magnetic field (14.1 T) allowed us to investigate the diffusivity characteristics of Ace and NAA metabolites in the rat brain *in vivo*. The diffusion behavior of Ace was compared to the diffusion behavior of NAA, considered as a reference for diffusivity characteristics of an exclusively intracellular metabolite. Observing Ace signal at very high b value implies the restriction of some part of Ace signal in the intracellular space. The most outstanding result of the present work is the observation of significantly higher diffusion for Ace compared to NAA over the studied b-value range. The diffusion characteristic of Ace brought insight about volume distribution of Ace in rat brain.

3.4.1. Precise quantification of Ace in the rat brain *in vivo*

Ace is present at too low concentrations in the normal brain tissue to be consistently detectable by ^{1}H NMR *in vivo*, even at 14.1 T. Studies such as the measurement of Ace transport across the blood-brain barrier or dynamic ^{13}C MRS of labeled acetate has been done in the animal under Ace infusion (Deelchand et al., 2009b; Lanz et al., 2014b). Therefore diffusion characteristic of Ace was studied in the rat under continuous Ace infusion. The infusion protocol was optimized to provide a stable Ace concentration in *vivo* for extended time periods, which reached a steady state level of 3-4 mM.

The challenge to establish the reliable measurement of Ace diffusivity was to minimize the GABA resonance at 1.89 ppm in ^{1}H spectra that might interfere with quantification of the Ace resonance, in particular at high diffusion weighting, as GABA is larger molecule compared with Ace. GABA has six NMR observable protons in three methylene groups, forming an $A_2M_2X_2$ spin system. The triplet resonances for GABA-H4 and H2 appear at 3.01 ppm and 2.28 ppm, while the GABA-H3 quintet is centered at 1.89 ppm that has overlapping with Ace. The Ace resonance in ^{1}H spectra is a singlet peak that does not undergo J coupling evolution, while the GABA resonance could be suppressed using its unique J coupling properties at a specific TE and TM. Therefore, applying optimum parameters found in the DW-STEAM sequence to minimize the GABA peak at 1.89 ppm (TE=50ms and TM=49ms) resulted in reported quantification of Ace with minimal contamination from GABA signal. However, applying long TE during ^{1}H MRS acquisition lead to substantial signal losses from T_2 relaxation decay of the considered metabolites and accordingly required more averaging to achieve sufficient SNR for quantification.

CRLBs obtained from LCModel quantitation were lower than 10% for quantification of NAA and Ace in reference spectra as well as in all diffusion-weighted spectra, at an echo time of 50 ms. The high

precision of the estimated metabolites concentrations was ascribed to the high spectral resolution and SNR of the ^{1}H spectra acquired at 14.1T and the preprocessing approach used for quantification of the metabolites signal; i.e. by the phase and frequency drift correction before averaging spectra.

The use of moderately long echo time and short TR (compare to the T_1 relaxation of Ace, see Chapter 4) implies an impact of T_2 and T_1 and relaxation on quantification, which was taken into consideration by using a correction of the measured signals, based on the measured T_2 and T_1 relaxation of the different metabolites (part 4.4.1) for the measurement of the respective concentrations.

3.4.2. Diffusion characteristics of Ace and NAA

To interpret the diffusivity of Ace independently from assumptions used for diffusion data modeling (see reviews by Cao and Wu, 2016; Nicolay et al., 2001; Ronen et al., 2015), we used the diffusion of NAA for comparison with that of Ace. Since NAA is known as intracellular metabolite that is suggested mostly confined to the neurons (Moffett et al., 1991; Urenjak et al., 1993) it could be used to compare its diffusion properties with that of other metabolites, where the cellular localization may be less established. In addition, NAA presents at high concentration in the rat brain and its main singlet peak is not subject to the J modulation.

When considering a range of b-values of 0-5 ms/µm^2, a mono-exponential decrease was observed, as judged from the linear decay for NAA and Ace *in vivo* signals in a log plot (Fig 3.7). Furthermore, applying the respiration cycle triggering during the ^{1}H spectral acquisition and single-FID phase correction generally avoid the signal loss and related overestimation of the metabolites ADC (Posse et al., 1993). The consistency of the estimated ADC of NAA and also other metabolites such as Cr+PCr and Glu at b-value ranging from 0-5 ms/µm^2 with previous studies performed at longer diffusion time (Ligneul et al., 2016; Kunz, 2010; Pfeuffer et al., 2000) implied that the diffusion time chosen in this study (73ms) was long enough to place the ADC of metabolites in the diffusion time independency regime (Najac et al., 2014). Also the similarity in diffusivity of metabolites at different diffusion times ranging from 43 to 198 ms in our study confirms the diffusion time independency of metabolites at diffusion time of 73 ms.

However, the ADC of NAA was reported with slightly higher values in some studies (Duong et al., 2001; van der Toorn et al., 1996), which could be explained by the shorter diffusion time used in those studies (10-20ms). Shorter diffusion time implies a smaller mean displacement of metabolites which limits the interaction with the environment and increases the apparent diffusion coefficient (Assaf and Cohen, 1998; Helmer et al., 1995). In addition, the lower ADC of metabolites measured here could be ascribed to the higher sensitivity and spectral resolution of the present study performed at higher magnetic field of 14.1 T, as compared to previous reported measurements.

The most striking result of the present study is the observation of an approximately three-fold higher ADC of Ace compared to NAA for *b*-values ranging from 0 to 5 ms/µm^2. While this could be explained to some extent by the smaller molecular size of Ace compared to NAA (as measured in phantom, Table 3.1), but also indicates a substantially different cellular localization. The smaller linear diffusion of Ace vs NAA in the rat brain compared to their free diffusion in phantom in Table 3.1 (ratio of 5 and 10, respectively) indicates that the difference in measured diffusion of acetate *in vivo* is to a large proportion induced by the restrictions encountered by acetate molecules from the cellular boundaries in the rat brain.

The bi-exponential regression of the normalized NAA and Ace signal over the *b*-value range of 0 to 18 ms/µm^2 was characterized by the fast and slow diffusion components of NAA and Ace (D_{fast}^{App}, D_{slow}^{App}).

The diffusion of the fast component of Ace was approximately two-fold higher than for NAA, as observed in the mono-exponential fitting of the Ace and NAA diffusion signal at b-value range of 0-5 ms/µm² (Table 3.1 and Table 3.2).

The D_{slow}^{App} was determined for Ace with higher precision than for NAA (error of 10% for Ace and 40% for NAA). In our study, the rational was to choose a sufficiently large b-value range for studying the diffusion of Ace. Fortunately, the fast diffusion component of Ace showed a fast decay and its contribution at b-value higher than 5 ms/µm² was less than 11% and reached a negligible level of 0.03% at 18 ms/µm². Therefore, acquiring spectra at a b-value range of 0-18 ms/µm² was sufficient to determine both the fast and slow diffusion components of Ace inside the brain for bi-exponential modeling. However, the b-value range of 0 to 18 ms/ µm² might not be sufficiently high for a precise estimation of the slow component of NAA and could thus result in an overestimation of the slow component.

The percentage of Ace signal at b-value of 18 ms/µm² was 16% of total signal, approximately two times less than what was observed for NAA, namely 37%. The faster decay of the fast component of Ace diffsuion compared to NAA and lower contribution of the slow decaying component of Ace at high b-value suggest that a significant part of Ace signal arises from the extracellular compartment.

The diffusion of Ace in the extracellular compartment is reflected mainly in the fast diffusion component and its diffusion in the intracellular compartment likely is attributed to the slow diffusion component. Considering the D_{fast}^{App} of Ace as 0.44 ms/µm², contribution of the extracellular signal to the total signal measured at b-value higher than 5 ms/µm² was less than 10%. Therefore, the observed signal at b-value higher than 5 ms/µm² could be considered mainly as the slow component reflecting the slow diffusing component of the intracellular molecules. The D_{slow}^{App} of NAA and Ace was an order of magnitude lower than their D_{fast}^{App}, as reported for several metabolites in previous studies (Assaf and Cohen, 1998; Pfeuffer et al., 2000). The much smaller values of D_{slow}^{App} compared to D_{fast}^{App} demonstrates that intracellular barrier and restrictions dominate on diffusion of these metabolites at such high b-value and diffusion time.

Both the fast and slow diffusing components of NAA showed a considerable intracellular restriction from which two apparent mean displacements could be deduced using Einstein's equation: $r_{fast/slow}^{App} = \sqrt{2.D_{fast/slow}^{App}.t_D}$ where t_D is diffusion time. The apparent mean displacement of the fast and slow components of NAA were 6–8 µm and 1–2 µm, respectively. These two distinct diffusing distances could reflect the diffusion of NAA in cell body and axonal milieu, proposed by Assaf and Cohen, 1998.

3.4.3. Evidence of Ace localization in glial cells

Acetate has been proposed as the potential glial marker due to its almost exclusive uptake in astrocytes (Lanz et al., 2014a; Patel et al., 2010; Wyss et al., 2011). The estimated D_{slow}^{App} of Ace was slightly higher compared to NAA in Table 3.2. The distribution of estimated D_{slow}^{App} for Ace tended to slightly higher values compared to NAA (Fig 3.9). However at the diffusion time used in this study (73 ms), D_{slow}^{App} of metabolites expected to reflect the cellular dimensions rather than the respective molecule size. Slight differences in the estimated D_{slow}^{App} for Ace and NAA may therefore suggest a different cellular localization such as Ace in the astrocytes, where the different D_{slow}^{App} of Ace from a neuronal marker, NAA, could be attributed to the different structure and shape of glial cytosol compared to

neuronal cells. However, the difference between D_{slow}^{App} of NAA and Ace did not reach statistical significance and further investigations at substantially higher precision would be indicated.

Interestingly, the D_{slow}^{App} for Inositol (0.037±0.003 μm²/ms) reported in the mouse brain recently by (Ligneul et al., 2016) and in the rat brain by (Pfeuffer et al., 2000) is close to the D_{slow}^{App} of Ace. This similarity suggests that Ace and Inositol (Ins) may share a similar intracellular distribution space, which is likely different from that of NAA. It has been proposed in several studies based on different measurements techniques that Ace (Minchin and Beart, 1975; Muir et al., 1986; Waniewski and Martin, 1998; Wyss et al., 2011) and Ins (Brand et al., 1993) are both located mainly in the glial cell.

3.4.4. Distribution volume of Ace in rat brain tissue

In this study, the volume fraction of Ace in the extracellular space of brain (p_0^{extra}) was estimated to be 43% under the experimental conditions of the present study, i.e. continuous intravenous Ace infusion in the rat. Contribution of Ace from ventricles as well as from the blood were assumed to be negligible due of the rapid signal loss at low b-values (self-diffusion of Ace, 1.27±0.01 μm²/ms). The estimated extracellular fraction of the Ace signal, 43%, is two times larger than the reported value for extracellular fraction of Glc 17% (Pfeuffer et al., 1992). Therefore the difference in the extracellular fraction of Ace and Glc implies a distribution of Ace distinctly different from the uniform brain glucose distribution. In other words, the intracellular and extracellular signals have approximately equal contribution in total detected Ace signal. The volume of distribution for Ace in intracellular and extracellular space can be approximated by the same ratio.

Approximately 20% of the whole brain volume is occupied by the extracellular space (Nicholson et al., 2011). Therefore since 43% of the total signal is ascribed to 20% of the whole brain volume, the intracellular fraction of Ace signal (57%) is ascribed to cells, which occupy 27 % of the brain volume. As a consequence, the volume of which acetate has access, i.e. Ace physical distribution volume (V_d), at the brain is estimated to be around 47%. This above calculation is made for an extreme limit of Ace concentration in intracellular space, namely same as Ace concentration in extracellular space. Otherwise, since Ace can be metabolized in intracellular space, the concentration of Ace in intracellular space will be smaller than in extracellular space and so the total V_d might be smaller than 47%.

The lower estimated value of V_d for Ace in the rat brain is comparable with reported V_d values for Ace in ^{13}C-Ace study by Patel et al., 2010 who suggested a smaller V_d for Ace compared to glucose on best fitting for ^{13}C labeling time courses of glutamate and glutamine and time course of Ace concentration in brain in kinetic analysis of Ace transport and utilization across the blood-brain barrier.

To acquire data in this study, the sequence parameters (e.g. TE and b-value) have been optimized for precise quantification and evaluation of diffusivity of Ace in the brain. Therefore, these parameters may not be optimum for assessing diffusion behavior of other metabolites in the brain such as NAA. The D_{fast}^{App} and D_{slow}^{App} of NAA are determined with lower precision compared to Ace (see Fig 3.9) and previous study done by Ligneul et al., 2016 and Pfeuffer et al., 2000. The difference in precision of D_{slow}^{App} and D_{slow}^{App} of NAA could be due to much higher b-value range of 0 to 30 ms/ μm² used by Ligneul et al., 2016 and 0 to 50 ms/ μm² used by Pfeuffer et al. Acquiring spectra with enough SNR at such high b-value, requires more temporal averaging and results in substantial increase in the acquisition time.

The Intracellular-extracellular exchange of metabolites across cell membrane could have an impact on intracellular attenuated diffusion signal, as reported for water diffusion inside the cell (Pfeuffer et al.,

1998). However, the permeability of membrane to Ace is not significant because of its larger molecule size compared to the water molecules. Therefore, the transport of Ace across cell membrane was assumed to have minor impact on intracellular attenuated signal. In respect of the relatively long diffusion time used in this study (73 ms), it was assumed that active transport mechanisms are not significant in exchange of metabolites between intracellular and extracellular media.

3.5. Conclusion

We conclude that the presence of Ace resonance in ^{1}H spectra acquired at very large diffusion weighting indicates restricted diffusion of Ace in intracellular region of brain. However, the significant larger diffusion of Ace compared to NAA demonstrates that a substantial fraction of Ace is located in the extracellular space of brain tissue. The slightly different behavior of the slow diffusion component of Ace in the intracellular space compared to the neuronal marker NAA may suggest different intracellular localization for Ace in brain as compared to NAA, most probably the glial compartment. Finally we conclude that Ace occupies a smaller physical distribution space than water and some other metabolites e.g. glucose.

3.6. Reference

1. Abe, O., Okubo, T., Hayashi, N., Saito, N., Iriguchi, N., Shirouzu, I., Kojima, Y., Masumoto, T., Ohtomo, K., Sasaki, Y., 2000. Temporal changes of the apparent diffusion coefficients of water and metabolites in rats with hemispheric infarction: experimental study of transhemispheric diaschisis in the contralateral hemisphere at 7 tesla. J. Int. Soc. Cereb. Blood Flow Metab. 20, 726–735. doi:10.1097/00004647-200004000-00010.

2. Assaf, Y., Cohen, Y., 1998. *In vivo* and *in vitro* bi-exponential diffusion of N-acetyl aspartate (NAA) in rat brain: a potential structural probe? NMR Biomed. 11, 67–74.

3. Badar-Goffer, R.S., Bachelard, H.S., Morris, P.G., 1990. Cerebral metabolism of acetate and glucose studied by ^{13}C-n.m.r. spectroscopy. A technique for investigating metabolic compartmentation in the brain. Biochem. J. 266, 133–139.

4. Brand, A., Richter-Landsberg, C., Leibfritz, D., 1993. Multinuclear NMR studies on the energy metabolism of glial and neuronal cells. Dev. Neurosci. 15, 289–298.

5. Burnier, P., Tappy, L., Jéquier, E., Schneeberger, D., Chioléro, R., 1992. Metabolic and respiratory effects of infused sodium acetate in healthy human subjects. Am. J. Physiol. 263, R1271-1276.

6. Cao, P., Wu, E.X., 2016. In vivo diffusion MRS investigation of non-water molecules in biological tissues. NMR Biomed. doi:10.1002/nbm.3481.

7. Cerdan, S., Künnecke, B., Seelig, J., 1990. Cerebral metabolism of [1,2-^{13}C$_2$]acetate as detected by *in vivo* and *in vitro* ^{13}C NMR. J. Biol. Chem. 265, 12916–12926.

8. Cruz, N.F., Lasater, A., Zielke, H.R., Dienel, G.A., 2005. Activation of astrocytes in brain of conscious rats during acoustic stimulation: acetate utilization in working brain. J. Neurochem. 92, 934–947. doi:10.1111/j.1471-4159.2004.02935.x.

9. D'Agostino, C., Ryabenkova, Y., Miedziak, P.J., Taylor, S.H., Hutchings, G.J., Gladden, L.F., Mantle, M.D., 2014. Deactivation studies of a carbon supported AuPt nanoparticulate catalyst in the liquid-phase aerobic oxidation of 1,2-propanediol. Catal. Sci. Technol. 4, 1313–1322. doi:10.1039/C4CY00027G.

10. de Graaf, R.A., Braun, K.P., Nicolay, K., 2001. Single-shot diffusion trace (1)H NMR spectroscopy. Magn. Reson. Med. 45, 741–748.

11. Deelchand, D.K., Shestov, A.A., Koski, D.M., Uğurbil, K., Henry, P.-G., 2009. Acetate transport and utilization in the rat brain. J. Neurochem. 109 Suppl 1, 46–54. doi:10.1111/j.1471-4159.2009.05895.x.

12. Duong, T.Q., Sehy, J.V., Yablonskiy, D.A., Snider, B.J., Ackerman, J.J., Neil, J.J., 2001. Extracellular apparent diffusion in rat brain. Magn. Reson. Med. 45, 801–810.

13. Govind, V., Young, K., Maudsley, A.A., 2015. Corrigendum: Proton NMR chemical shifts and coupling constants for brain metabolites. NMR Biomed. 2000; 13: 129–153. NMR Biomed. 28, 923–924. doi:10.1002/nbm.3336.

14. Govind, V., Young, K., Maudsley, A.A., 2000. Proton NMR chemical shifts and coupling constants for brain metabolites. NMR Biomed. 13, 129–153.

15. Gruetter, R., Adriany, G., Choi, I.-Y., Henry, P.-G., Lei, H., Oz, G., 2003. Localized *in vivo* ^{13}C NMR spectroscopy of the brain. NMR Biomed. 16, 313–338. doi:10.1002/nbm.841.

16. Gruetter, R., Tkác, I., 2000. Field mapping without reference scan using asymmetric echo-planar techniques. Magn. Reson. Med. 43, 319–323.

17. Helmer, K.G., Dardzinski, B.J., Sotak, C.H., 1995. The application of porous-media theory to the investigation of time-dependent diffusion in *in vivo* systems. NMR Biomed. 8, 297–306.

18. Henry, P.-G., Adriany, G., Deelchand, D., Gruetter, R., Marjanska, M., Oz, G., Seaquist, E.R., Shestov, A., Uğurbil, K., 2006. *In vivo* ^{13}C NMR spectroscopy and metabolic modeling in the brain: a practical perspective. Magn. Reson. Imaging 24, 527–539. doi:10.1016/j.mri.2006.01.003.

19. Kunz, N., 2010. Biophysical basis of the diffusion weighted magnetic resonance signal in the rat brain. École polytechnique fédérale de Lausanne (EPFL).

20. Kunz, N., Cudalbu, C., Mlynarik, V., Hüppi, P.S., Sizonenko, S.V., Gruetter, R., 2010. Diffusion-weighted spectroscopy: a novel approach to determine macromolecule resonances in short-echo time ^{1}H-MRS. Magn. Reson. Med. 64, 939–946. doi:10.1002/mrm.22490.

21. Lanz, B., Xin, L., Millet, P., Gruetter, R., 2014. *In vivo* quantification of neuro-glial metabolism and glial glutamate concentration using ^{1}H-[^{13}C] MRS at 14.1T. J. Neurochem. 128, 125–139. doi:10.1111/jnc.12479.

22. Ligneul, C., Palombo, M., Valette, J., 2016. Metabolite diffusion up to very high b in the mouse brain *in vivo*: Revisiting the potential correlation between relaxation and diffusion properties. Magn. Reson. Med. doi:10.1002/mrm.26217.

23. Marchadour, C., Brouillet, E., Hantraye, P., Lebon, V., Valette, J., 2012. Anomalous diffusion of brain metabolites evidenced by diffusion-weighted magnetic resonance spectroscopy *in vivo*. J. Cereb. Blood Flow Metab. 32, 2153–2160. doi:10.1038/jcbfm.2012.119.

24. Minchin, M.C.W., Beart, P.M., 1975. Compartmentation of amino acid metabolism in the rat dorsal root ganglion; a metabolic and autoradiographic study. Brain Res. 83, 437–449. doi:10.1016/0006-8993(75)90835-5.

25. Moffett, J.R., Namboodiri, M.A., Cangro, C.B., Neale, J.H., 1991. Immunohistochemical localization of N-acetylaspartate in rat brain. Neuroreport 2, 131–134.

26. Muir, D., Berl, S., Clarke, D.D., 1986. Acetate and fluoroacetate as possible markers for glial metabolism *in vivo*. Brain Res. 380, 336–340.

27. Murphy, E., Hellerstein, M., 2000. Is *in vivo* nuclear magnetic resonance spectroscopy currently a quantitative method for whole-body carbohydrate metabolism? Nutr. Rev. 58, 304–314. doi:10.1111/j.1753-4887.2000.tb01825.x.

28. Najac, C., Marchadour, C., Guillermier, M., Houitte, D., Slavov, V., Brouillet, E., Hantraye, P., Lebon, V., Valette, J., 2014. Intracellular metabolites in the primate brain are primarily localized in long fibers rather than in cell bodies, as shown by diffusion-weighted magnetic resonance spectroscopy. NeuroImage 90, 374–380. doi:10.1016/j.neuroimage.2013.12.045.

29. Nicholson, C., Kamali-Zare, P., Tao, L., 2011. Brain extracellular space as a diffusion barrier. Comput. Vis. Sci. 14, 309–325. doi:10.1007/s00791-012-0185-9.

30. Nicklas, W.J., Clarke, D.D., 1969. Decarboxylation studies of glutamate, glutamine, and aspartate from brain labelled with [1-^{14}C]acetate, L-[U-^{14}C]-aspartate, and L-[U-^{14}C]glutamate. J. Neurochem. 16, 549–558.

31. Nicolay, K., Braun, K.P.J., Graaf, R.A. de, Dijkhuizen, R.M., Kruiskamp, M.J., 2001. Diffusion NMR spectroscopy. NMR Biomed. 14, 94–111. doi:10.1002/nbm.686.

32. Patel, A.B., de Graaf, R.A., Rothman, D.L., Behar, K.L., Mason, G.F., 2010. Evaluation of cerebral acetate transport and metabolic rates in the rat brain *in vivo* using ^{1}H-[^{13}C]-NMR. J. Cereb. J. Int. Soc. Cereb. Blood Flow Metab. 30, 1200–1213. doi:10.1038/jcbfm.2010.2.

33. Pfeuffer, J., Flögel, U., Leibfritz, D., 1998. Monitoring of cell volume and water exchange time in perfused cells by diffusion-weighted ^{1}H NMR spectroscopy. NMR Biomed. 11, 11–18.

34. Pfeuffer, J., Tkác, I., Gruetter, R., 2000. Extracellular-intracellular distribution of glucose and lactate in the rat brain assessed noninvasively by diffusion-weighted ^{1}H nuclear magnetic resonance spectroscopy *in vivo*. J. Int. Soc. Cereb. Blood Flow Metab. 20, 736–746. doi:10.1097/00004647-200004000-00011.

35. Posse, S., Cuenod, C.A., Le Bihan, D., 1993. Human brain: proton diffusion MR spectroscopy. Radiology 188, 719–725. doi:10.1148/radiology.188.3.8351339.

36. Press, W.H., 2007. Numerical Recipes 3rd Edition: The Art of Scientific Computing. Cambridge University Press.

37. Ronen, I., Valette, J., Ronen, I., Valette, J., 2015. Diffusion-weighted magnetic resonance spectroscopy, in: eMagRes. John Wiley & Sons, Ltd, John Wiley & Sons, Ltd.

38. Starčuk Jr, Z., Starčuková, J., Štrbák, O., Graveron-Demilly, D., 2009. Simulation of coupled-spin systems in the steady-state free-precession acquisition mode for fast magnetic resonance (MR) spectroscopic imaging. Meas. Sci. Technol. 20, 104033. doi:10.1088/0957-0233/20/10/104033.

39. Sugimoto, H., Koehler, R.C., Wilson, D.A., Brusilow, S.W., Traystman, R.J., 1997. Methionine sulfoximine, a glutamine synthetase inhibitor, attenuates increased extracellular potassium activity during acute hyperammonemia. J. Cereb. Blood Flow Metab. 17, 44–49. doi:10.1097/00004647-199701000-00006.

40. Urenjak, J., Williams, S. R., Gadian, D. G. & Noble, M., 1993. Proton nuclear magnetic resonance spectroscopy unambiguously identifies different neural cell types. J. Neurosci. 13, 981–989.

41. Van der Toorn, A., Dijkhuizen, R.M., Tulleken, C.A.F., Nicolay, K., 1996. Diffusion of metabolites in normal and ischemic rat brain measured by localized ^{1}H MRS. Magn. Reson. Med. 36, 914–922. doi:10.1002/mrm.1910360614.

42. Van Zijl, P.C., Moonen, C.T., Faustino, P., Pekar, J., Kaplan, O., Cohen, J.S., 1991. Complete separation of intracellular and extracellular information in NMR spectra of perfused cells by diffusion-weighted spectroscopy. Proc. Natl. Acad. Sci. U. S. A. 88, 3228–3232.

43. Waniewski, R.A., Martin, D.L., 1998. Preferential utilization of acetate by astrocytes is attributable to transport. J. Neurosci. Off. J. Soc. Neurosci. 18, 5225–5233.

44. Ward, R.A., Wathen, R.L., Harding, G.B., Thompson, L.C., 1985. Comparative metabolic effects of acetate and dichloroacetate infusion in the anesthetized dog. Metabolism. 34, 680–687.

45. Wyss, M.T., Magistretti, P.J., Buck, A., Weber, B., 2011. Labeled acetate as a marker of astrocytic metabolism. J. Cereb. Blood Flow Metab. 31, 1668–1674. doi:10.1038/jcbfm.2011.84.

Chapter 4. Cerebral acetate transport and utilization in the rat brain in *vivo* using ^{1}H MRS: Consequences of a revised physical distribution volume of acetate

Metabolic modeling of ^{13}C turnover curves of metabolites in the brain with ^{13}C-labeled Ace infused as tracer substrate to probe brain oxidative metabolism requires prior knowledge of the transport and uptake kinetic parameters including the cerebral metabolic rate of Ace (CMR$_{Ace}$) and Ace transport rate constants. To determine the transport and uptake kinetics of Ace, the physical distribution volume of Ace and absolute quantification of apparent Ace concentration is needed. Knowledge of T$_1$ and T$_2$ relaxation times of Ace in the brain *in vivo* is important for an accurate estimation of the apparent Ace concentration in the brain and also provides information on its chemical environment. In this study, the T_1 and T_2 of Ace in the rat brain *in vivo* were measured using Stimulated Echo Acquisition Mode (STEAM) sequence at 14.1 T. We also determined the kinetics of transport and utilization for acetate uptake in the rat brain using a revised physical distribution volume (V_d) of Ace (see Chapter 3). It was found that Ace had significantly longer T_1 relaxation compared with NAA both in the phantom and rat brain under Ace infusion, reflecting the characteristics of small size of the Ace molecule. Ace and NAA had similar T$_2$ values in the phantom but an almost two-fold different T_2 in the measurements *in vivo*, which could reflect the different location of Ace in the brain. The consistency of the estimated Ace consumption rate based on the presented revised V_d of Ace in the brain with reported glial TCA cycle rate in ^{13}C studies is in agreement with the dominant location of Ace in the glial cell. The dependency of the estimated CMR_{Ace} to V_d of Ace in the rat brain highlighted the importance of a refined determination of V_d.

4.1. Introduction

Acetate (Ace), an astrocyte-specific substrate, is proposed as an attractive alternative to glucose (Glc) for isotope labeling studies of glial metabolism. Ace is metabolized mostly in the glial cells (Badar-Goffer et al., 1990; Cerdan et al., 1990; Cruz et al., 2005; Nicklas and Clarke, 1969; Waniewski and Martin, 1998b; Wyss et al., 2011) and gives more insights on the glial-specific processes than Glc. Few

in vivo ^{13}C NMR studies have been performed using ^{13}C labeled Ace as substrate yielding labeling time courses or steady state enrichments of brain metabolites labeled from Ace (Deelchand et al., 2009a; Xin et al., 2010). Brain metabolic analysis using data at isotopic steady state allows determination of relative metabolic rates (Blüml et al., 2002; Lebon et al., 2002; Mason et al., 2006; Patel et al., 2005), while introducing data about the ^{13}C labeling time courses of metabolites in the metabolic modeling process gives rise to the determination of absolute metabolic rates (Deelchand et al., 2009b; Lanz et al., 2012; Patel et al., 2010; Shestov et al., 2012). Kinetic metabolic modeling of ^{13}C turnover curves of metabolites in brain with ^{13}C-labeled Ace infused as tracer substrate requires prior knowledge of its transport across the blood-brain barrier and uptake kinetic parameters including the cerebral metabolic rate of Ace (CMR_{Ace}) and Ace transport constants (e.g. K_T: half-saturation constant; T_{max}: maximum transport rate). To determine the transport and uptake kinetics of Ace, the physical distribution volume of Ace and absolute quantification of apparent concentration of Ace are needed.

Knowledge of the T_1 and T_2 relaxation times of Ace *in vivo* is important for an accurate estimation of the apparent concentration of Ace in the brain and also provides information on its chemical environment. The most common techniques to measure T_1 relaxation times of brain metabolites are inversion recovery, IR (Vold et al., 1968) and progressive saturation techniques, PS (Freeman and Hill, 1971). A drawback of the IR method compared to PS technique is its longer acquisition time and the superposition of spectral lines with opposite signs due to the different T_1 of the metabolites, which may provide a complicated spectral line. Thus we choose the PS technique to measure the T_1 relaxation of metabolites. T_2 relaxation is usually estimated by measuring the signal intensity decay with step increases of echo time. For reliable T_1 and T_2 measurements, correct prior knowledge of the spectral shape is needed to perform the spectra quantification analysis. Therefore the signal changes caused by J modulation should be taken into account by simulating the spectral pattern at each echo time. Ace is a singlet peak and does not undergo J coupling evolution, but additional complications arise from the overlap of resonances from different molecules (e.g. overlapping Ace and a GABA peak at 1.89ppm) and macromolecule (MM) contributions.

In this study, we measured the T_1 and T_2 of Ace in the rat brain at 14.1 T. We also determined the kinetics of transport and utilization for acetate uptake in the rat brain using maximum physical distribution volume (V_d) of Ace that was derived in the present thesis (see Chapter 3). The effects of the V_d considered for Ace in the rat brain on estimated cerebral metabolic rate of Ace (CMR_{Ace}) were investigated in this study.

4.2. Subjects and methods

4.2.1. Animal preparation

All experimental procedures involving animals were approved by the local veterinary authorities. Male Sprague–Dawley rats (200-235g delivered from Charles River Laboratories, France) were prepared without fasting period. Eight rats were intubated and ventilated with 2% isoflurane during surgery. Both femoral veins were catheterized for the administration of Ace and α-chloralose. Two arteries were cannulated for the continuous monitoring of physiology (blood pressure, heart rate) and periodic blood sampling for the blood gas/pH, plasma lactate and glucose concentration measurements as well as high resolution NMR analyzes described below. Following surgery, anesthesia was switched to intravenous α–chloralose administration (bolus of 80mg/kg and continuous infusion rate of 26.7 mg/kg/h). Animals were placed in a home-built holder and the head position was fixed using ear rods and a bite-bar. Body

temperature was maintained between 37.0 and 37.5 °C with a temperature-regulated circulating water bath.

To measure the macromolecule baseline in the rat brain *in vivo,* one extra rat was prepared according to the mentioned protocol just for continuous administration of α-chloralose (one femoral vein and two arteries catheterized).
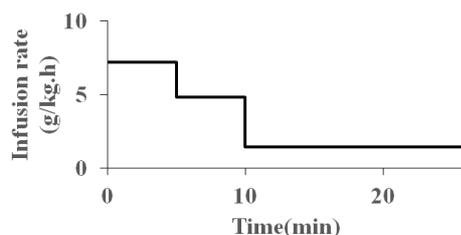

Fig 4.1 Diagram of the Ace infusion protocol.

4.2.2. Ace infusion protocol

The sodium Ace infusion protocol was first optimized with a series of bench experiments and further in the magnet to reach a steady-state concentration of Ace in the rat brain in less than 30 min while keeping the animal within good physiological limits throughout the study. After adjustment of MRS parameters and shimming, a bolus of 1 g/kg bodyweight of sodium acetate (1.6 M) was administered first in a two-step process over 10 min (Fig 4.1). This bolus was followed by a continuous infusion of Ace at a rate of 1.4 g/kg/h. Blood samples were collected before starting Ace infusion, at the end of the Ace bolus and repeated every 15 or 30 minutes. The plasma acetate concentration was measured using high resolution NMR spectroscopy as described below.

In order to stay away from metabolic alkalosis in the blood of the animals under infusion (Burnier et al., 1992; Ward et al., 1985), the Ace solution was infused at an acidic pH (of 5.0) as previously used in rats (Deelchand et al., 2009; Sugimoto et al., 1997).

4.2.3. High resolution NMR spectroscopy

High-resolution ^{1}H NMR spectra were used to determine plasma acetate concentration. Blood samples were prepared for high resolution NMR: 50 µL of plasma and 50 µL of reference containing 5 mM 3-(Trimethylsilyl)-1-propanesulfonic acid sodium salt (DSS, Sigma-Aldrich) dissolved in deuterium oxide were diluted with 500µL deuterium oxide. The pH of the final sample was adjusted to be close to the physiological conditions, 7.20. Measurements were performed at room temperature (20°C) in a 9.4 Tesla, Avance-400 spectrometer equipped with a 5-mm broadband probe (BrukertopSpin, Switzerland) with single Z-axis gradient. In order to remove the broad resonances of MM present in the blood plasma spectra, diffusion NMR methods based on different translational mobility of MM from other metabolites in the blood plasma were utilized (de Graaf and Behar, 2003). Briefly, two ^{1}H spectra were acquired with a STEAM diffusion sequence (TE = 6.8 ms, TR = 10 s, 32 averages); one with a low diffusion factor (0.023 ms/µm^2) and one with a high diffusion factor (2.330 ms/µm^2). The difference between these spectra resulted in a spectrum consisting of metabolites resonances only. Spectral quantification was performed using the Mnova NMR Processing software (2014, Mestrelab Research, S.L).

4.2.4. In vivo and in vitro NMR spectroscopy at 14.1T

[1]H spectra were acquired on a 14.1T MRI system interfaced to a 26-cm horizontal bore magnet (Varian, Palo Alto, CA, USA; Magnex Scientific, Oxford, UK), equipped with 12 cm inner diameter actively shielded gradient set reaching 400 mT/m in 120 µs. A home-built quadrature RF transceiver with two physically decoupled 12mm-diameter loops was used.

After initial settings, fast spin echo images (TR = 4 s and TE effective = 40 ms; four averages) were acquired to select a volume of interests (VOI) of 450 µl in the rat brain (see Fig 3.1). Magnetic field homogeneity was adjusted using FAST(EST)MAP (Gruetter and Tkác, 2000b). Localized ^{1}H NMR spectra were acquired using the Stimulated Echo Acquisition Mode (STEAM) sequence (Tkác et al., 1999). Acquisition parameters were optimized for Ace detection in the *in vivo* [1]H spectra on the rat brain, as described in the following part of this section.

Water suppression was done using seven chemical shift-selective (CHESS) adiabatic RF-pulses followed by crusher gradients. Outer volume suppression was performed using eight adiabatic pulses followed by crusher gradients that are repeated three times during the CHESS preparation to improve the unwanted signal suppression. To determine the apparent concentration of metabolites and eddy current correction, one unsuppressed water signal was acquired from the VOI as reference.

All ^{1}H spectra acquired *in vitro* or *in vivo* (from rat brain during prolonged Ace infusion) at 14.1T are categorized in three groups: measuring T_1 relaxation in group 1, measuring T_2 relaxation in group 2 and measuring the kinetic parameters of acetate transport and uptake in group 3. The acquisition protocol for each part is explained herein.

Group 1:

The T_1 relaxation times were determined using a progressive saturation technique (Freeman and Hill, 1971) in the STEAM sequence by varying TR (TR= 1.4, 2, 4, 8, 10, 14 s). To minimize GABA resonance overlapping with Ace in the *in vivo* spectra (@1.89 ppm), STEAM sequence parameters were set to specific value (TM = 49 ms and TE = 50 s) for the ^{1}H-MRS data acquisition (see section 3.2.3.1). First of all, the T_1 of Ace was investigated in a phantom containing Ace (50mM) and NAA (50mM) as reference. In a second step, for the *in vivo* T_1 measurements in the rat brain under Ace infusion, the mentioned procedures were followed using two adult rats. One ^{1}H spectrum (TE = 50 ms and TR = 4 s, TM = 49 ms) was acquired as reference to check for the stability of the cerebral Ace concentration over the different time points of each experiment. Because of incomplete recovery of the longitudinal magnetization at short TR, more averages were required at short TR to provide enough SNR for accurate quantification. The number of scans over the TR range was160 averages for TR = 1.4 and 2 s, and 80 averages for TR = 4, 8, 10 and 14 s.

Group 2

^{1}H-MRS data for the T_2 measurement were acquired using the STEAM sequence (TM = 49 ms and TR = 4 s) and specific TEs (2.8,50,110,150,170 and 300 ms) to minimize GABA resonance overlapping with Ace in the *in vivo* [1]H spectra (@1.89 ppm). The T_2 of Ace was investigated in a phantom containing Ace (50 mM) and NAA (50 mM) as reference. Furthermore, the *in vivo* T_2 measurements were performed in the brain of two rats under Ace infusion using the same procedures. To check or correct the Ace concentration level in different time intervals of the experiments, one ^{1}H spectrum (TE = 50 ms and TR = 4s, TM =49 ms) was acquired to use as reference. To provide enough SNR over all TE range, higher number of scans was considered for [1]H *in vivo* data as TE increased. (For TE =2.8 and

50 ms, 64 averages; TE = 110 ms , 160 averages; TE = 150 ms, 240 averages; TE = 170 ms, 320 averages; TE = 300 ms, 480 averages).

Group 3

Brain ^{1}H-MRS data were acquired using the STEAM sequence with optimized parameters (TM = 49 ms, TR = 4 s and TE = 50 ms) to minimize the GABA resonance overlapping with Ace in *in vivo* [1]H spectra (@1.89 ppm). ^{1}H MRS data were acquired from the brain of four rats following Ace infusion in two series with a time resolution of 1.2 min. The data set was acquired not only during the bolus, but also during the non-steady state part of the brain Ace time course. The number of scans for every acquired time point was 16. The physical distribution volume of Ace in the rat brain of this group is estimated using the diffusion characteristics of brain Ace under Ace infusion (see Chapter 3).

4.2.5. Data analysis and quantification

Phase variation and frequency drift of ^{1}H spectra *in vivo* were corrected on the basis of the NAA signal at 2.01 ppm before spectral summation. In group 1 and 2, [1]H *in vivo* data acquired at specific TR and TE were summed over the individual animals. The averaged spectra in group 1 and 2 belonged to interval times where acetate concentration was approximately at steady state (time > 20 min). In case of group 3, the ^{1}H spectra acquired at each time point were summed over the individual animals. Summed *in vivo* ^{1}H NMR spectra were processed using LCModel (Stephen Provencher Inc., Oakville, ON, Canada). The criteria for selecting reliable metabolite concentrations were based on the Cramér–Rao lower bounds (CRLBs), which are estimates of the percentage SD of the fit for each metabolite (Provencher, 1993). In group 1 and 2, ^{1}H NMR data acquired at specific TE and TR were corrected for minor changes in Ace concentration level based on the reference spectra for each individual animal.

The required TE-specific basis-sets for LCModel were generated for all metabolites excluding the macromolecule baseline (measured *in vivo*) using the NMRScopeB plugin to JMRUI (Starčuk Jr et al., 2009). Each metabolite was simulated with the appropriate chemical-shift and J-coupling pattern as described by (Govindaraju et al., 2015 and 2000) and the particular STEAM sequence parameters applied in this study. J-modulation characteristics of the simulated spectra were evaluated using *in vitro* spectra acquired at 14.1 T on a phantom containing Glu (50 mM) and Cr (25 mM) at approximately 37°. Phantom spectra were acquired using the STEAM sequence (TM = 20 ms and TR= 10 s) for a wide range of TEs, from 2.8 to 100 ms with maximum steps of 10 ms.

The *in vivo* measurement of the MM spectrum was done by the inversion recovery (IR) method combined with the diffusion-weighted (DW) module in the STEAM sequence as developed by Kunz et al., 2010. IR was performed using a nonselective full-passage hyperbolic secant RF pulse with inversion time (TI) of 1 s. The maximum achievable gradient strength for an application time of 6 ms was 300 mT/m, which were applied simultaneously along the three orthogonal directions to reach high enough b-value (41 ms/μm2) to minimize most metabolites signals in the spectrum. The MM baseline was acquired with TM = 49 ms, TR = 1 s and TE = 12 ms for the quantification of the measured data at short TE (e.g. T_2 relaxation study) and TE = 50 ms for the quantification of the measured data at long TE.

4.2.6. Data modeling

The T_1 relaxation of brain metabolites (group 1 rats) was estimated by performing a mono exponential fit to the mean normalized apparent concentrations (ratio of measured signal at each TR to the maximum-recovered signal, S/S_0) as a function of TR.

$$\frac{S(TR)}{S_0} = (1 - \exp^{-\frac{TR}{T_1}}) \qquad\qquad \text{Eq. 4.1}$$

The T_2 relaxation of brain metabolites (group 2 rats) was calculated by performing a mono-exponential fit to the mean normalized apparent concentrations of each metabolite (ratio of measured signal at each TE to the maximum intensity signal (which has not undergone T_2 relaxation), S/S_0) as a function of TE.

$$\frac{S(TE)}{S_0} = \exp^{-\frac{TE}{T_2}} \qquad\qquad \text{Eq. 4.2}$$

To derive the statistical significance of the estimated T_1 and T_2, Monte Carlo simulation was performed with 500 trials. Artificial datasets were generated by adding random Gaussian noise with a variance based on the difference between the best fit and experimental data. T_1 and T_2 values of Ace and NAA in the phantom were calculated with the same method.

The apparent concentration of the cerebral Ace in rats under Ace infusion belonging to group 3 was determined at different time points of brain Ace time course, corrected for T_1 and T_2 relaxation of Ace obtained from group 1 and 2, respectively. Ace time course in brain and plasma for the rats in group 3 were used to model the kinetic transport and uptake of Ace through the blood-brain barrier (BBB). The transport through the BBB was considered as a bi-directional process. Thus reversible non-steady state Michaelis-Menten model was applied to estimate the kinetic parameters for Ace transport and uptake.

$$S_{plasma} + E \leftrightarrow ES \leftrightarrow E + S_{brain} \xrightarrow{CMR_{Ace}} \qquad\qquad \text{Eq. 4.3}$$

The S_{plasma} and S_{brain} are Ace concentration in the plasma and brain, respectively. ES is the Ace transporter complex (the transporter being the monocarboxylase transporter) and CMR_{Ace} is the cerebral metabolic rate of Ace. The Michaelis-Menten constants for transport and uptake of Ace were mathematically estimated by adjusting the corresponding parameters ($V_{max}^t, V_{max}^{util}, K_M^t, K_M^{util}$) in the following equation to get the best fit of the experimental Ace time courses in the plasma and brain.

$$\frac{d[S_{brain}]}{dt} = \frac{V_{max}^t[S_{plasma}] - V_{max}^t[S_{brain}]/V_d}{K_M^t + [S_{plasma}] + [S_{brain}]/V_d} - \frac{V_{max}^{util}[S_{brain}]}{K_M^{util}.V_d + [S_{brain}]} \qquad\qquad \text{Eq. 4.4}$$

Where K_M^t is the Michaelis-Menten constant for Ace transport through the BBB and V_{max}^t the maximal transport rate of Ace. CMR_{Ace} is defined as follows:

$$CMR_{Ace} = \frac{V_{max}^{util}[S_{brain}]}{K_M^{util}.V_d + [S_{brain}]} \qquad\qquad \text{Eq. 4.5}$$

The K_M^{util} and V_{max}^{util} represent the apparent Michaelis-Menten constant for Ace utilization and the maximal utilization rate for acetate transport through the mitochondrial inner membrane and acetyl-CoA synthesis from Ace. The V_d represents the distribution volume of Ace, i.e. the volume brain tissue that Ace can access. To investigate the effect on the other parameters of the assumed V_d for Ace in the rat brain, the kinetic parameters were first estimated with V_d = 0.48 ml/g (estimated based on the diffusion characteristics of Ace in Chapter 3) and in a second step by assuming a V_d of 0.77ml/g (same physical distribution volume as Glc in the rat brain, as applied in previous studies (Pfeuffer et al., 2000; Silver and Erecińska, 1994).

4.3. Results

4.3.1. Apparent concentration of Ace in plasma and brain tissue

Ace concentrations in plasma and brain increased rapidly after the start of the Ace infusion (Fig 4.2), as brain Ace concentration reached a steady state with a delay compared to the plasma Ace. At steady state, Ace in plasma (19 ± 2 mM) was substantially higher than in the brain (3 ± 1 mM, corrected for T_1 and T_2). *In vivo* ^{1}H NMR spectra were acquired during the steady state period of Ace concentration in the rat brain (group 1 and 2) for the study of T_1 and T_2 relaxations. Minor changes in Ace concentration level during steady state were corrected based on the acquired reference spectra. While in group 3, the ^{1}H spectra were acquired directly after the start of the Ace infusion to provide information about the rising Ace time course introduced in the kinetic modeling of transport and uptake of Ace (Fig 4.3).
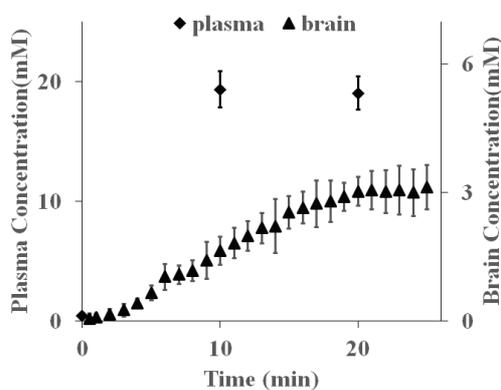

Fig 4.2 Time course of Ace concentration in the plasma and brain following continuous intravenous Ace infusion in the rat. Each time point and respective error bars represent the average and standard deviation over four animals.

4.3.2. LCModel basis sets

To enable an accurate quantification of brain metabolites, LCModel was used for the analysis of the measured spectra with appropriate synthetic metabolite signals. In this regards, the required basis sets for LCModel were generated using metabolite spectra simulated in the JMRUI software and measured *in vivo* MM baseline. MM signal was shown for two different echo times of 12 ms and 50 ms in Fig 4.4. MM resonance signals decayed with increasing TE, resulting in a flatter baseline at an echo time of 50 ms. The simulations were validated using *in vitro* spectra of the glutamate and creatine for wide range of echo times, from 2.8 ms to 100 ms in steps of 10 ms. The J-modulation of the coupled resonance signals, simulated in NMRScopeB within JMRUI, fairly described the shape of *in vitro* spectra of glutamate and creatine at all echo times (Fig 4.5). Six different basis sets were generated for the different acquisition parameters used in this study, TM = 49 ms and TE = 2.8, 50, 110,150, 170 and 300 ms.

In vivo water-suppressed ^{1}H MR spectra and their corresponding LCModel fits showed excellent correspondence at all TE s (
Fig 4.6) as are visible from the flat residual between the measured and fitted spectra.
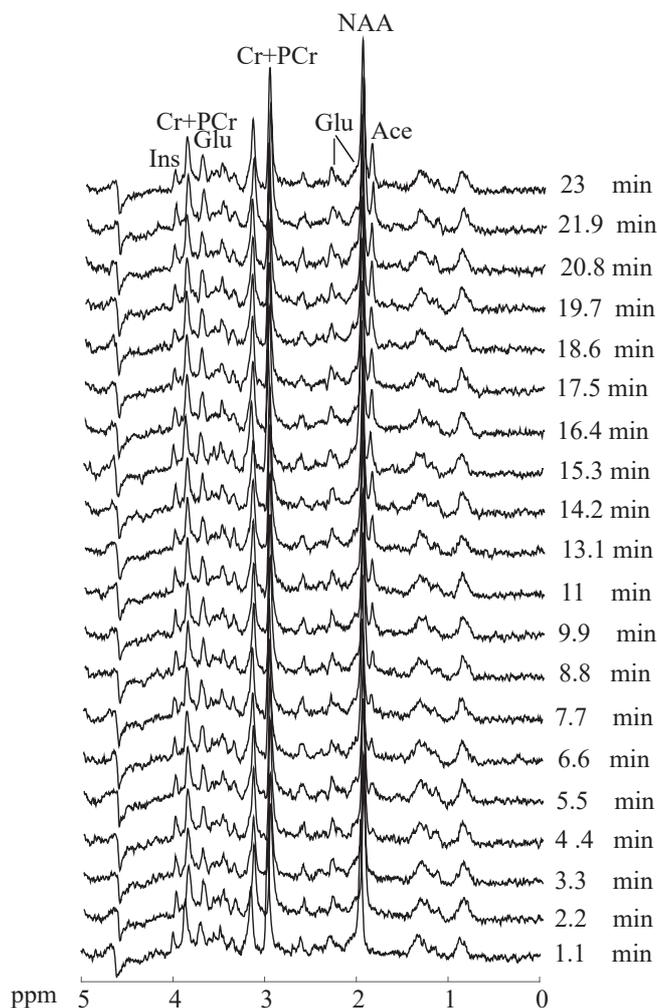
Fig 4.3 ^{1}H NMR spectra acquired on a rat brain following Ace infusion at 14.1 T using the STEAM sequence (VOI= $4\times6\times10$ mm^3, TR = 4 s, TE = 50 ms, TM = 49 ms, appodization= 10 Hz). Raising the Ace resonance at 1.90 ppm, next to the methyl peak of NAA, can be seen as time increases after bolus and continuous Ace infusion. The amplitude of the Ace peak reached a stable level after ~ 15 min.
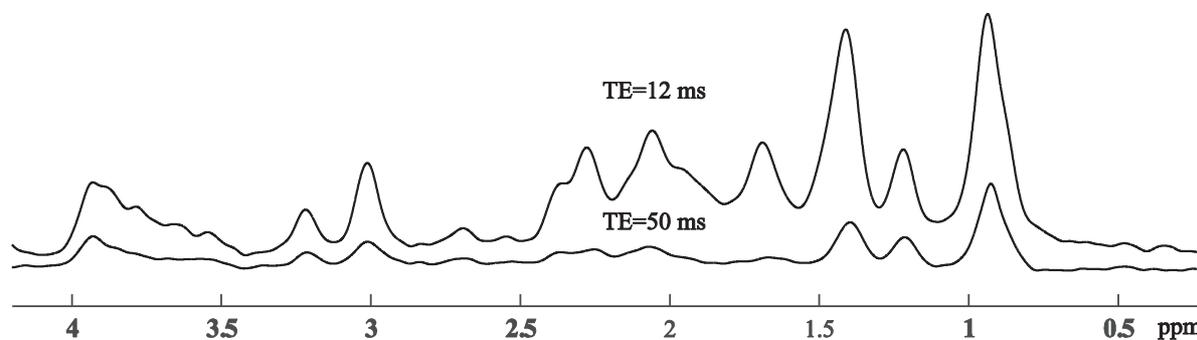

Fig 4.4 *In vivo* [1]H macromolecule signal acquired from the rat brain using an inversion recovery method combined with the diffusion spectroscopy in the STEAM sequence for two different echo times of 12 ms and 50 ms (VOI=$4\times6\times10$ mm^3, TM =49 ms, TR =1s).
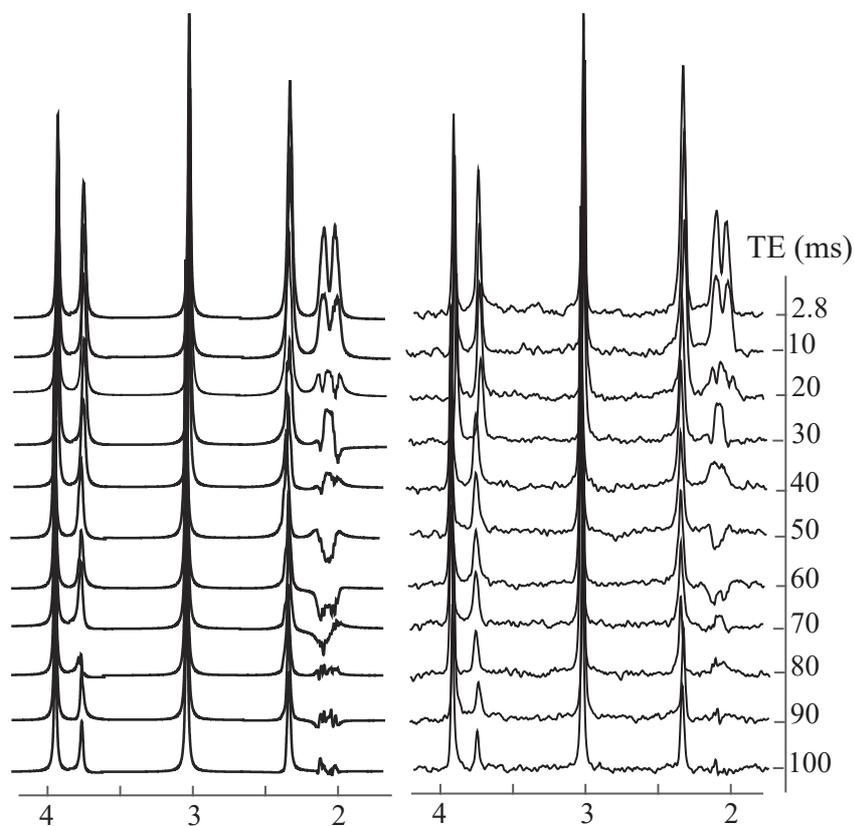
Fig 4.5 Right: *In vitro* ^{1}H NMR spectra of glutamate and creatine (CH$_3$) measured at 14.1 T using the STEAM sequence with TM = 20 ms and TE ranging from 2.8 to 100 ms (VOI= 2.5×2.5×2.5 mm^3, TR = 10 s, appodization= 10 Hz). Left: Simulated spectra at the same TM and TEs. Signal intensities are scaled using the *in vitro* methyl signal of creatine as a reference.

4.3.3. T$_2$ relaxation of Ace

To measure the T_2 relaxation, specific TE s (TE = 2.8, 50, 110, 150, 170 and 300 ms) and TM = 49 ms were chosen to minimize the GABA contribution under the Ace peak. The SNR of the averaged ^{1}H spectra for the entire range of analyzed TE values was more than 15, based on the NAA peak. Data analysis of the CRLB obtained from LCModel was performed over the whole TE range for the metabolites detected in the spectra. Ace, NAA (CH$_3$), Cr+PCr (CH$_3$, CH$_2$) and Ins were quantified with CRLB lower than 15% over the whole TE range. Metabolites with singlet peaks such as Ace or NAA (CH$_3$) do not undergo J-coupling modulation. As TE increased (
Fig 4.6), signal intensity decreased but no changes in spectral line shape of Ace or NAA (CH$_3$) were observed. In case of J-coupled metabolites resonances such as Ins, the spectral line shape changed at 3.61 ppm as TE increased. The signal intensity of metabolites reduced mono-exponentially with TE, giving rise to a decrease in their apparent concentrations (Fig 4.7).

In the rat brain under Ace infusion, the T_2 value of Ace and NAA (CH$_3$) were estimated by a mono exponential fit to the normalized concentration of every metabolite (R^2>99.5%). The Ace signal decayed faster with increasing TE (Fig 4.7) compared to NAA (CH$_3$). Consequently the T_2 value of Ace, 84±4 ms, was significantly shorter than NAA (CH$_3$), 146±3 ms. T$_2$ of other metabolites Cr+PCr(CH$_3$), Cr+PCr(CH$_2$) and Ins were also estimated (Table 4.1) and were all lower than the T$_2$ of

NAA(CH$_3$). In the case of Cr+PCr(CH$_3$), the data were poorly fitted with the mono exponential model ($R^2 \approx 91\%$).

As TE was increased, the intensity of Ace and NAA(CH$_3$) resonances dropped roughly with the same rate in phantom (Fig 4.8). Mono exponential fit to the measured data for Ace and NAA(CH$_3$) in phantom resulted in an estimation of approximately similar T_2 for these two metabolites. *In vitro* measured T_2 of Ace and NAA (CH$_3$) in phantom were 440 ± 24 ms and 468 ± 25 ms, respectively.

Table 4.1 T_2 relaxation times (mean $\pm$ SD) of metabolites in the brain of rat under Ace infusion at 14.1 T, averaged over two rats and corresponding standard deviation obtained from Monte Carlo simulation (n=500) in the mono exponential regression.

	Ace	NAA(CH$_3$)	Cr+PCr(CH$_3$)	Cr+PCr(CH$_2$)	Ins
T_2 (ms)	84$\pm$3	146$\pm$3	88$\pm$18	94$\pm$9	90$\pm$7
R^2	0.996	0.998	0.913	0.975	0.990

(a) *In vivo* spectra   (b) LCmodel fit   (c) Residual

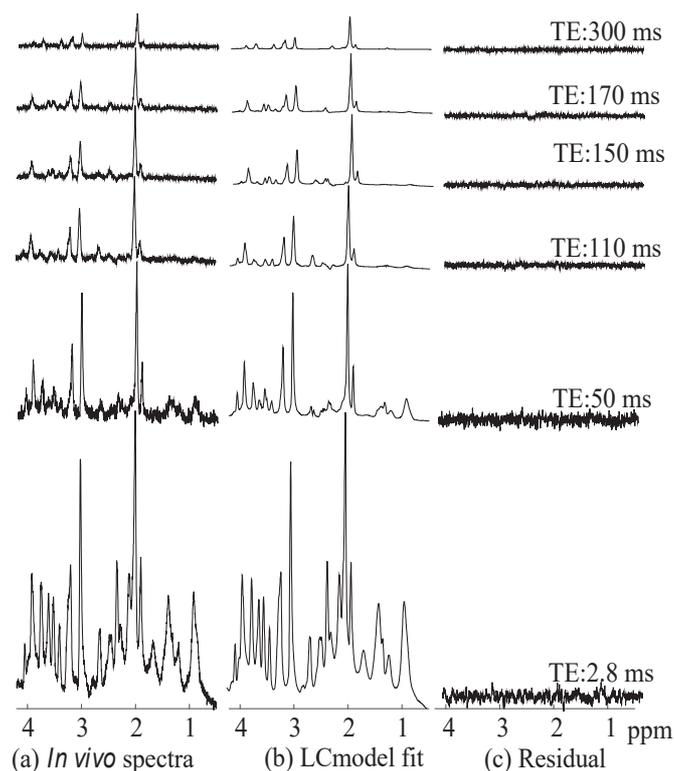Fig 4.6 (a) Series of normalized *in vivo* spectra acquired at 14.1 T from a voxel ($4 \times 6 \times 10$ mm^3) placed in the brain of single rat under Ace infusion, using the STEAM sequence with TR = 4 s, TM = 49 ms and specific TEs (shown on the right side of each spectrum) adjusted to minimize the GABA resonance at 1.89 ppm. (b) The corresponding LCModel fits and (c) the fitting residuals for different TEs.
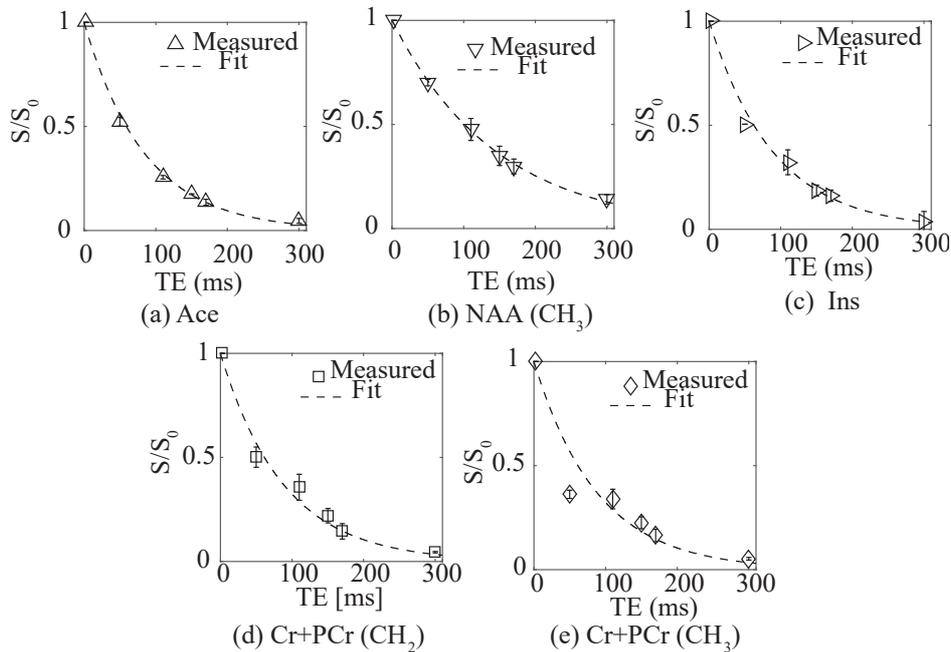
Fig 4.7 Plots of the normalized apparent concentration as a function of echo time (TE) for acetate (Ace), (b) N-acetyl-aspartate singlet (NAA(CH3)), (c) myo-inositol (Ins), (d) and (e) creatine plus phosphocreatine (Cr+ PCr) CH_2 and CH_3. Every data point and its error bar represent the average and standard deviation over two rats. Solid lines show the mono-exponential fit of the T_2 relaxation.
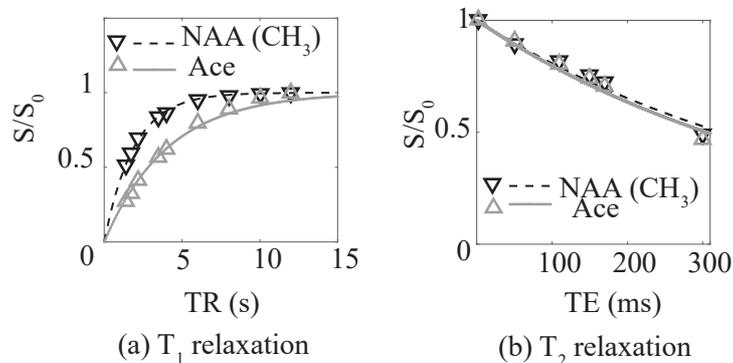
Fig 4.8 (a) Plots of the normalized apparent concentration of Ace and NAA(CH3) in phantom as a function of (a) repetition time (TR), and (b) echo time (TE). Lines show the mono exponential fit using the formula (a) $S/S_0=(1-\exp(-TR/T_1))$, $R^2>99\%$ and (b) $S/S_0=\exp(-TE/T_2)$, $R^2>97\%$ adjusted to the measured *in vitro* data.

4.3.4. T_1 relaxation of Ace

To determine the T_1 of metabolites in brain of rat under Ace infusion, spectra acquired using the PS technique at different TR, ranging from 1.4 s to 14 s. All measured spectra exhibited excellent SNR (all averaged spectra had SNR larger than 30, based on the NAA resonance). The chosen parameters for the acquisition of ^1H MRS data (TM = 49 ms and TE = 50 ms) resulted in a minimization of the overlapping GABA peak at 1.89 ppm and a more precise quantification of Ace. Metabolites such as Ace,

NAA(CH_3), Cr+PCr(CH_3,CH_2) and Ins were quantified with CRLB lower than 10% over the entire TR range. As TR extended to the higher value, the amplitude of the metabolites was recovered, increasing their apparent concentration (Fig 4.9).
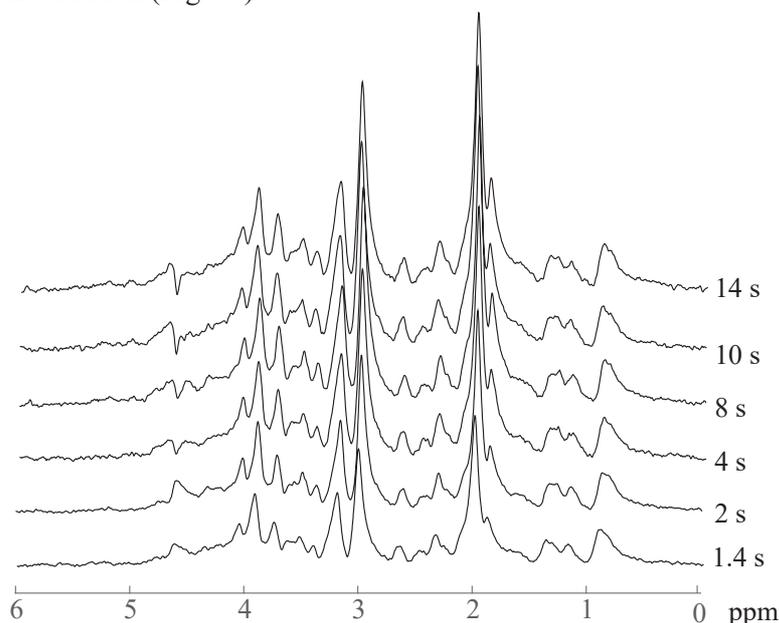
Fig 4.9 Typical series of *in vivo* spectra acquired at 14.1 T from a voxel ($4\times6\times10$ mm^3) placed in the brain of rat under Ace infusion using the STEAM sequence with TE = 50 ms, TM = 49 ms and different TRs (shown on the right side of each spectrum). A gaussian apodization of 10 Hz was applied and signal intensities were normalized to the number of scans in each spectrum.

When comparing the signal recovery of Ace with that of NAA(CH_3) in the rat brain, a distinct difference was noted and the concomitant fits indicated a nearby two-fold slower T_1 relaxation for Ace (T_1 = 3.55 $\pm$ 0.18 s) compared to NAA (CH_3) (T_1 = 1.78 $\pm$ 0.07 s) (Fig 4.10). T_1 relaxation times of other metabolites Cr+PCr(CH_3), Cr+PCr(CH_2) and Ins estimated from the mono exponential regression were close to the one of NAA(CH_3) (Table 4.2).

 In vitro T_1 measurements also demonstrated that Ace had a two times longer T_1 (4.07 $\pm$ 0.14 s), compared with NAA (CH_3) (1.90 $\pm$ 0.02 s).

Table 4.2 T_1 relaxation times (mean $\pm$ SD) of brain metabolites in the rat under Ace infusion at 14.1 T, averaged over two rats and corresponding standard deviation obtained from Monte Carlo simulation (n=500) in the mono exponential regression.

	Ace	NAA(CH_3)	Cr+PCr(CH_3)	Cr+PCr(CH_2)	Ins
T_1 (s)	3.5±0.18	1.78±0.07	1.63±0.07	1.16±0.03	1.14±0.10
R^2	0.987	0.980	0.975	0.991	0.892

Fig 4.10 Plots of the normalized apparent concentration as a function of the repetition time (TR) for acetate (Ace), (b) N-acetyl-aspartate singlet (NAA(CH₃)), (c) myo-inositol (Ins), (d) and (e) creatine plus phosphocreatine (Cr+ PCr) CH2 and CH3. Every data point and its error bar represent the average and standard deviation over two rats. Solid lines show the mono-exponential fit of the T_1 relaxation.
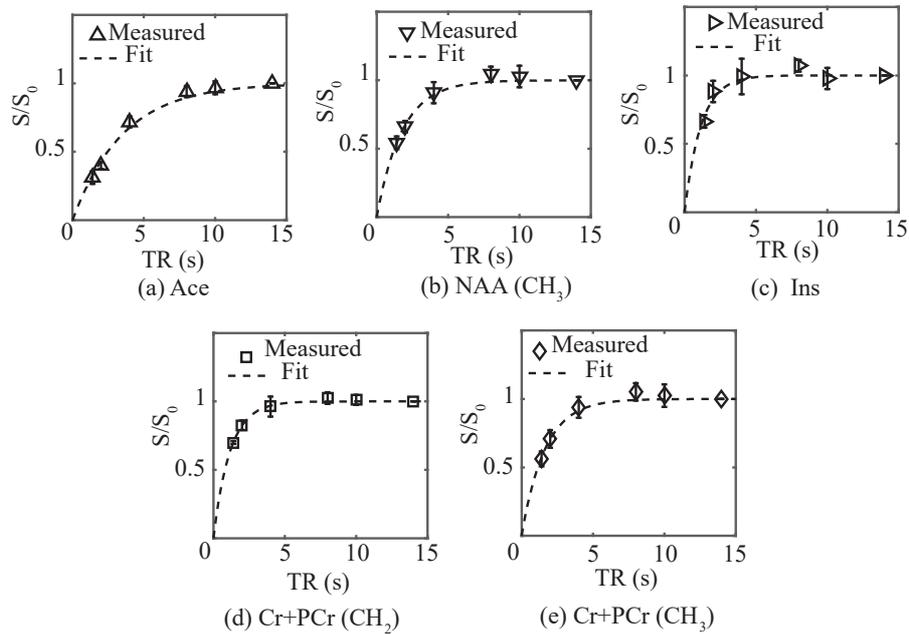
4.3.5. Kinetics of Ace transport and utilization

To determine precisely the time course of Ace concentration in ^{1}H spectra acquired from the rat brain under Ace infusion, the optimum parameters in the STEAM sequence (TM = 49 ms and TE = 50 ms) were chosen to minimize the overlap of the GABA peak with Ace at 1.89 ppm. The averaged ^{1}H spectra with time resolution of 1.1 min presented a high SNR for every time point (more than 15, based on NAA resonance). The value of K_M^t, V_{max}^t, K_M^{util} and V_{max}^{util} were determined by simultaneous regression of the solution of equation Eq. 4.4 to the time course of [S$_{brain}$] and [S$_{plasma}$] acquired from the brain of rats in group 3.

Table 4.3 Kinetic parameters of Ace transport and utilization in the rat brain under Ace infusion for two different fixed values for physical distribution volume (V_d) of Ace in brain (mean ± SD; n=4).

$V_d \left(\frac{ml}{g}\right)$	0.48	0.77
$V_{max}^t(\frac{\mu mol}{g.min})$	0.89±0.14	1.12±0.16
$K_M^t(\frac{mmol}{L})$	5.59±2.86	2.92±1.25
$V_{max}^{util}(\frac{\mu mol}{g.min})$	0.31±0.02	0.54±0.05
$K_M^{util}(\frac{mmol}{L})$	0.12±0.11	0.83±0.04

The revised physical distribution volume of Ace (V_d) in the rat brain of this group has been estimated to 0.48 ml/g (based on the diffusion characteristics of Ace in Chapter 3). An example of the fit obtained in one animal (using the revised V_d) is presented in Fig 4.11 .a. Following Ace infusion in rats, CMR_{Ace} increased and reached a steady state value in less than 10 min The average fitted values for Michaelis-Menten constant for transport and uptake of Ace in Table 4.3 were: $V_{max}^t = 0.89 \pm 0.14 \frac{\mu mol}{g.min}$, $V_{max}^{util} = 0.31 \pm 0.02 \frac{\mu mol}{g.min}$, $K_M^t = 5.59 \pm 2.86 \frac{mmol}{L}$, $K_M^{util} = 0.12 \pm 0.11 \frac{mmol}{L}$ and $CMR_{Ace} = 0.30 \pm 0.02 \frac{\mu mol}{g.min}$ (mean $\pm$ SD; n=4).

In a second step, considering a V_d for Ace of 0.77 ml/g (same as V_d of Glc in brain), kinetic transport and uptake parameters of Ace were estimated again by fitting the time course of Ace in the brain and plasma, shown in Table 4.3. The kinetic transport parameters V_{max}^t and K_M^t calculated using $V_d = 0.77$ ml/g were not significantly different from the ones estimated using $V_d = 0.48$ ml/g and the difference were in the dispersion range of the estimated values. However, the estimated values for the uptake parameters V_{max}^{util} and K_M^{util} using $V_d = 0.77$ ml/g yielded a higher value for the consumption rate of Ace, $CMR_{Ace} = 0.59 \pm 0.06 \frac{\mu mol}{g.min}$ compared with the one estimated using $V_d = 0.48$ ml/g.
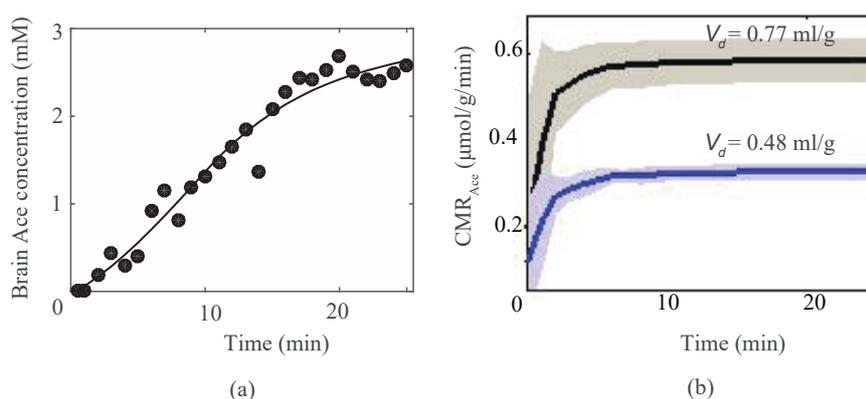

Fig 4.11 (a) Result of the regression of the non-steady-state Michaelis-Menten model to the time course of brain Ace concentration, shown for one animal with $V_d = 0.48$ ml/g. Circles show the measured data points and the black line represents the best model fit. (b) Estimated time courses of Ace metabolic rates for two different physical distribution volume values considered for Ace in brain, 0.48 ml/g and 0.77 ml/g. Line and shadow represent the average and SD of the estimated temporal evolution of the CMR_Ace over four animals.

4.4. Discussion

4.4.1. T₁ and T₂ relaxations of Ace in the rat brain

This study reports for the first time T_1 and T_2 relaxation values for Ace in the rat brain *in vivo* at 14.1 T under an Ace infusion protocol. In normal conditions, Ace in the rat brain is very low and hard to detect reliably. To determine the T_1 relaxation of Ace, optimum parameters in the STEAM sequence (TE=50 ms and TM=49ms) were chosen to minimize the GABA resonance at 1.89 ppm in the acquired spectra at different TRs. Similarly, for the T_2 relaxation study, we picked specific TEs (2.8 , 50, 110, 150, 170, 300 ms) where the overlapping GABA peak has minimum contribution in the Ace signal.

The accuracy of the estimated relaxation times depends clearly on the accuracy of the quantification of the spectral line. Although the quantification of singlet is comparatively straightforward, Ace singlet suffers from this strong overlap with one strongly coupled spin resonance of GABA. Thus, signal modulation of the GABA peak caused by J-coupling should be taken carefully into account for the quantification of spectra at different TEs. In this study, this was performed using LCModel to fit coupled spin resonances at different TEs. LCModel enables a robust data analysis based on prior knowledge provided through simulated or measured spectra, called basis sets. Metabolite spectra at specific TEs were simulated using NMRScopeB in JMRUI software and MM baseline was measured *in vivo* in the rat brain for short TE (12 ms) and long TE (50 ms). Simulated spectral patterns were validated by comparison with *in vitro* measurement and the spectral appearance of simulated spectra closely matched that observed from phantom over all TEs up to 100 ms.

The high spectral resolution and sensitivity at 14.1 T allowed the estimation of T_1 and T_2 of Ace using the specific parameters applied in the STEAM sequence for the precise quantification of Ace.

The T_1 and T_2 relaxation of NAA(CH_3), Cr+PCr(CH_3), Cr+PCr(CH_2) and Ins were in excellent agreement with the published values at 14.1 T (Cudalbu et al., 2009; Xin et al., 2013). To the best of our knowledge, there is no reported information about biological effects of continuous Ace infusion in rat on T_1 and T_2 relaxations of metabolites in brain. However the consistency between the T_1 and T_2 relaxation of metabolites in this study with published value for normal rat brain conditions at 14.1T (Cudalbu et al., 2009; Xin et al., 2013) can be taken as a validation of minor effects of continuous Ace infusion on T_1 and T_2 relaxation of metabolites.

Ace showed approximately a two times slower T_1 relaxation compared with other metabolites such as NAA(CH_3) both in phantom and *in vivo* measurements. The significant larger value of T_1 for Ace compared to NAA(CH_3) may reflect the smaller size of Ace molecules. Considering the typical repetition time used in the *in vivo* measurement (4 s), around 87% and 66% of NAA and Ace signal are recovered, respectively. To obtain a same recovered signal as NAA in every acquisition, the repetition time needs to be increased at least two times (8 s) during data acquisition. However it should be kept in mind that available time for the whole NMR data acquisition depends on the animal physiology conditions and usually is limited to about 3 hours.

NAA (CH_3) and Ace metabolites had approximately similar T_2 relaxation in phantom measurements, while showed different T_2 relaxation in *in vivo* measurements. The different value for *in vivo* T_2 relaxation of NAA(CH_3) and Ace (ratio of 145/84) points to the fact that spin-spin relaxation of metabolites is likely to be sensitive to the surrounding microenvironment. From the diffusion studies of Ace in rat brain in Chapter 3, we found that a significant part of Ace lies in extracellular space. Therefore, part of the Ace signal in the extracellular space has a different environment from the intracellular part. On another hand, NAA is known as a mostly neuronal marker and Ace was proposed as potential glial marker. It might be appropriate to assign the smaller T_2 relaxation of Ace compared with NAA (CH_3) to their different environment. Indeed, investigating the T_2 of other intracellular metabolites claimed to be a glial marker, e.g. myoinositol (Ins), showed that Ins also presented a smaller T_2 relaxation compared with NAA(CH_3).

4.4.2. Importance of V_d for Ace in brain metabolic studies

In this study, we investigated the kinetic parameters of Ace transport and utilization in the rat brain under Ace infusion based on a revised value for V_d of Ace in brain. The revised V_d value was estimated to 0.48 ml/g from diffusion characteristics of Ace in brain (see Chapter 3). The smaller value of V_d for Ace compared with Glc (ratio of 0.48/0.77) is in line with the proposed hypothesis of Ace mainly

localized in glial cells and Glc in both neuronal and glial cells. The kinetic parameters of Ace transport and utilization in the rat brain was estimated non-invasively using localized ^{1}H NMR spectroscopy performed with the STEAM sequence at ultra-high magnetic field (14.1 T). Maximum transport rate was higher for the blood-brain barrier ($V_{max}^t = 0.89 \pm 0.14 \frac{\mu mol}{g.min}$) than for Ace utilization after entry of Ace in the brain ($V_{max}^{util} = 0.31 \pm 0.02 \frac{\mu mol}{g.min}$). This is consistent with the fact that the limitation of CMR_{Ace} is not due to transport through the blood brain barrier but to the limitation of Ace utilization after entry of Ace in the brain (Deelchand et al., 2009b). The estimated CMR_{Ace} increased and reached a steady-state value (Fig 4.11.b) in about 10 min following Ace infusion, which reflects non-saturated Ace utilization under normal physiological conditions. The estimated CMR_{Ace} ,0.30±0.02, using V_d = 0.48 ml/g was in better agreement with reported glial TCA cycle rates (0.36±0.03 $\frac{\mu mol}{g.min}$ by Lanz et al., 2014 and 0.30±0.02 $\frac{\mu mol}{g.min}$ by Duarte et al., 2011). In addition, it is consistent with the fact that most acetyl-CoA entering the glial TCA cycle is synthesized from exogenous Ace transported to the rat brain (Lanz et al., 2012; Wyss et al., 2011).

Increasing V_d to the value of water and glucose in the rat brain as previously applied (Deelchand et al., 2009b), 0.77ml/g, resulted in a doubled value for CMR_{Ace} , while the same saturation behavior as in case of V_d = 0.48 ml/g was observed in Fig 4.11.b. The value of the estimated CMR_{Ace} ,0.59±0.06 $\frac{\mu mol}{g.min}$, is close to the reported value in the previous study reported by Deelchand et al., 2009b with same assumption (CMR_{Ace}=0.49±0.0.8 $\frac{\mu mol}{g.min}$, V_d = 0.77 ml/g). The dependency of the estimated CMR_{Ace} to the physical distribution volume of Ace in the rat brain highlights the importance of a refined determination of V_d for Ace in the brain metabolic studies.

4.5. Conclusion

From the presented results, we can conclude that cerebral Ace has a significantly slower T_1 relaxation compared with other metabolites in brain (a ratio of T_1s around 2). Therefore, increasing the repetition time in Ace studies could be an advisable strategy to obtain higher signal intensity in every acquisition at the cost of an increased acquisition time. The shorter T_2 of Ace compared to NAA, a mostly neuronal marker, could be the sign of a different location of Ace in brain cellular compartments, most probably in glial cells and extracellular space. The consistency of the estimated Ace consumption rate based on the revised V_d of Ace in brain with the previously reported glial TCA cycle rates could be another evidence of the main location of Ace in the glial cells. The dependency of the estimated CMR_{Ace} to V_d of Ace in the rat brain highlights the importance of a properly in situ determined value of V_d for Ace in brain metabolic studies.

4.6.   References

1. Badar-Goffer, R.S., Bachelard, H.S., Morris, P.G., 1990. Cerebral metabolism of acetate and glucose studied by 13C-n.m.r. spectroscopy. A technique for investigating metabolic compartmentation in the brain. Biochem. J. 266, 133–139.

2. Blüml, S., Moreno-Torres, A., Shic, F., Nguy, C.-H., Ross, B.D., 2002. Tricarboxylic acid cycle of glia in the *in vivo* human brain. NMR Biomed. 15, 1–5.

3. Burnier, P., Tappy, L., Jéquier, E., Schneeberger, D., Chioléro, R., 1992. Metabolic and respiratory effects of infused sodium acetate in healthy human subjects. Am. J. Physiol. 263, R1271-1276.

4. Cerdan, S., Künnecke, B., Seelig, J., 1990. Cerebral metabolism of [1,2-^{13}C2]acetate as detected by *in vivo* and *in vitro* ^{13}C NMR. J. Biol. Chem. 265, 12916–12926.

5. Cruz, N.F., Lasater, A., Zielke, H.R., Dienel, G.A., 2005. Activation of astrocytes in brain of conscious rats during acoustic stimulation: acetate utilization in working brain. J. Neurochem. 92, 934–947. doi:10.1111/j.1471-4159.2004.02935.x.

6. Cudalbu, C., Mlynárik, V., Xin, L., Gruetter, R., 2009. Comparison of T_1 relaxation times of the neurochemical profile in rat brain at 9.4 tesla and 14.1 tesla. Magn. Reson. Med. 62, 862–867. doi:10.1002/mrm.22022.

7. de Graaf, R.A., Behar, K.L., 2003. Quantitative ^{1}H NMR Spectroscopy of Blood Plasma Metabolites. Anal. Chem. 75, 2100–2104. doi:10.1021/ac020782.

8. Deelchand, D.K., Nelson, C., Shestov, A.A., Uğurbil, K., Henry, P.-G., 2009a. Simultaneous measurement of neuronal and glial metabolism in rat brain *in vivo* using co-infusion of [1,6-^{13}C2]glucose and [1,2-^{13}C2]acetate. J. Magn. Reson. San Diego Calif 1997 196, 157–163. doi:10.1016/j.jmr.2008.11.001.

9. Deelchand, D.K., Shestov, A.A., Koski, D.M., Uğurbil, K., Henry, P.-G., 2009b. Acetate transport and utilization in the rat brain. J. Neurochem. 109 Suppl 1, 46–54. doi:10.1111/j.1471-4159.2009.05895.x.

10. Duarte, J.M.N., Lanz, B., Gruetter, R., 2011. Compartmentalized Cerebral Metabolism of [1,6-(13)C]Glucose Determined by in vivo (13)C NMR Spectroscopy at 14.1 T. Front. Neuroenergetics 3, 3. doi:10.3389/fnene.2011.00003.

11. Freeman, R., Hill, H.D.W., 1971. Fourier Transform Study of NMR Spin–Lattice Relaxation by "Progressive Saturation." J. Chem. Phys. 54, 3367–3377. doi:10.1063/1.1675352.

12. Govind, V., Young, K., Maudsley, A.A., 2015. Corrigendum: Proton NMR chemical shifts and coupling constants for brain metabolites. Govindaraju V, Young K, Maudsley AA, NMR Biomed. 2000; 13: 129–153. NMR Biomed. 28, 923–924. doi:10.1002/nbm.3336.

13. Govind, V., Young, K., Maudsley, A.A., 2000. Proton NMR chemical shifts and coupling constants for brain metabolites. NMR Biomed. 13, 129–153.

14. Gruetter, R., Tkác, I., 2000. Field mapping without reference scan using asymmetric echo-planar techniques. Magn. Reson. Med. 43, 319–323.

15. Kunz, N., Cudalbu, C., Mlynarik, V., Hüppi, P.S., Sizonenko, S.V., Gruetter, R., 2010. Diffusion-weighted spectroscopy: a novel approach to determine macromolecule resonances in short-echo time ^{1}H-MRS. Magn. Reson. Med. 64, 939–946. doi:10.1002/mrm.22490.

16. Lanz, B., Uffmann, K., T Wyss, M., Weber, B., Buck, A., Gruetter, R., 2012. A two-compartment mathematical model of neuroglial metabolism using [1-(11)C] acetate. J. Int. Soc. Cereb. Blood Flow Metab. 32, 548–559. doi:10.1038/jcbfm.2011.162.

17. Lanz, B., Xin, L., Millet, P., Gruetter, R., 2014. *In vivo* quantification of neuro-glial metabolism and glial glutamate concentration using ^{1}H-[^{13}C] MRS at 14.1T. J. Neurochem. 128, 125–139. doi:10.1111/jnc.12479.

18. Lebon, V., Petersen, K.F., Cline, G.W., Shen, J., Mason, G.F., Dufour, S., Behar, K.L., Shulman, G.I., Rothman, D.L., 2002. Astroglial contribution to brain energy metabolism in humans revealed by ^{13}C nuclear magnetic resonance spectroscopy: elucidation of the dominant pathway for neurotransmitter glutamate repletion and measurement of astrocytic oxidative metabolism. J. Neurosci. Off. J. Soc. Neurosci. 22, 1523–1531.

19. Mason, G.F., Petersen, K.F., Lebon, V., Rothman, D.L., Shulman, G.I., 2006. Increased brain monocarboxylic acid transport and utilization in type 1 diabetes. Diabetes 55, 929–934.

20. Nicklas, W.J., Clarke, D.D., 1969. Decarboxylation studies of glutamate, glutamine, and aspartate from brain labelled with [1-^{14}C]acetate, L-[U-^{14}C]-aspartate, and L-[U-14C]glutamate. J. Neurochem. 16, 549–558.

21. Patel, A.B., de Graaf, R.A., Mason, G.F., Rothman, D.L., Shulman, R.G., Behar, K.L., 2005. The contribution of GABA to glutamate/glutamine cycling and energy metabolism in the rat cortex in vivo. Proc. Natl. Acad. Sci. U. S. A. 102, 5588–5593. doi:10.1073/pnas.0501703102.

22. Patel, A.B., de Graaf, R.A., Rothman, D.L., Behar, K.L., Mason, G.F., 2010. Evaluation of cerebral acetate transport and metabolic rates in the rat brain in vivo using ^{1}H-[^{13}C]-NMR. J. Int. Soc. Cereb. Blood Flow Metab. 30, 1200–1213. doi:10.1038/jcbfm.2010.2.

23. Pfeuffer, J., Tkác, I., Gruetter, R., 2000. Extracellular-intracellular distribution of glucose and lactate in the rat brain assessed noninvasively by diffusion-weighted ^{1}H nuclear magnetic resonance spectroscopy in vivo. J. Int. Soc. Cereb. Blood Flow Metab. 20, 736–746. doi:10.1097/00004647-200004000-00011.

24. Provencher, S.W., 1993. Estimation of metabolite concentrations from localized *in vivo* proton NMR spectra. Magn. Reson. Med. 30, 672–679. doi:10.1002/mrm.1910300604.

25. Shestov, A.A., Valette, J., Deelchand, D.K., Uğurbil, K., Henry, P.-G., 2012. Metabolic modeling of dynamic brain ^{13}C NMR multiplet data: concepts and simulations with a two-compartment neuronal-glial model. Neurochem. Res. 37, 2388–2401. doi:10.1007/s11064-012-0782-5.

26. Silver, I.A., Erecińska, M., 1994. Extracellular glucose concentration in mammalian brain: continuous monitoring of changes during increased neuronal activity and upon limitation in oxygen supply in normo-, hypo-, and hyperglycemic animals. J. Soc. Neurosci. 14, 5068–5076.

27. Starčuk Jr, Z., Starčuková, J., Štrbák, O., Graveron-Demilly, D., 2009. Simulation of coupled-spin systems in the steady-state free-precession acquisition mode for fast magnetic resonance

(MR) spectroscopic imaging. Meas. Sci. Technol. 20, 104033. doi:10.1088/0957-0233/20/10/104033.

28. Sugimoto, H., Koehler, R.C., Wilson, D.A., Brusilow, S.W., Traystman, R.J., 1997. Methionine Sulfoximine, a Glutamine Synthetase Inhibitor, Attenuates Increased Extracellular Potassium Activity During Acute Hyperammonemia. J. Cereb. Blood Flow Metab. 17, 44–49. doi:10.1097/00004647-199701000-00006.

29. Tkác, I., Starcuk, Z., Choi, I.Y., Gruetter, R., 1999. *In vivo* ^{1}H NMR spectroscopy of rat brain at 1 ms echo time. Magn. Reson. Med. 41, 649–656.

30. Vold, R.L., Waugh, J.S., Klein, M.P., Phelps, D.E., 1968. Measurement of Spin Relaxation in Complex Systems. J. Chem. Phys. 48, 3831–3832. doi:10.1063/1.1669699.

31. Waniewski, R.A., Martin, D.L., 1998. Preferential utilization of acetate by astrocytes is attributable to transport. J. Soc. Neurosci. 18, 5225–5233.

32. Ward, R.A., Wathen, R.L., Harding, G.B., Thompson, L.C., 1985. Comparative metabolic effects of acetate and dichloroacetate infusion in the anesthetized dog. Metabolism. 34, 680–687.

33. Wyss, M.T., Magistretti, P.J., Buck, A., Weber, B., 2011. Labeled acetate as a marker of astrocytic metabolism. J. Cereb. Blood Flow Metab. 31, 1668–1674. doi:10.1038/jcbfm.2011.84.

34. Xin, L., Gambarota, G., Cudalbu, C., Mlynárik, V., Gruetter, R., 2013. Single spin-echo T2 relaxation times of cerebral metabolites at 14.1 T in the *in vivo* rat brain. Magma N. Y. N 26, 549–554. doi:10.1007/s10334-013-0378-3.

35. Xin, L., Mlynárik, V., Lanz, B., Frenkel, H., Gruetter, R., 2010. ^{1}H-[^{13}C] NMR spectroscopy of the rat brain during infusion of [2-^{13}C] acetate at 14.1 T. Magn. Reson. Med. 64, 334–340. doi:10.1002/mrm.22359.

Chapter 5. Design and performance of transmit-birdcage coil and receive-quadrature pair surface coil at 14.1 T

Characteristics of the radio frequency (RF) coil used as transmit and receive probes play the main role in the quality of acquired NMR data. Surface coils offer a considerable gain in the signal to noise ratio over a targeted volume but fall short in their ability to generate a homogeneous RF field. The angle of excitation is influenced by the experienced magnetic field B_1 by spins. Therefore non-homogeneous magnetic field can lead to degradations in the desired flip angle and signal intensity, especially in spin echo sequences. A birdcage coil generates homogeneous excitation over a large region of interest but with lower receive sensitivity than a surface coil. The aim of this research was to design a separate transmit-birdcage coil and receive-quadrature pair surface coil, to provide homogeneous excitation and high receive sensitivity for NMR applications at the ultra-high field of 14.1 T. Introducing varactor diodes in the surface coil give the possibility of remote tuning and matching the coil for different loading by changing the applied DC voltage on diodes. The optimum decoupling configuration was found for both coils to reduce the coupling between the coils during transmission and reception. The birdcage coil is detuned by activating PIN diodes through DC current and surface coil is detuned by the PIN diode controlled trap and varactor diodes. The performance of the transmit-birdcage coil and receive-quadrature pair surface coil was compared with one of birdcage coil in the transmit and receive mode. The preliminary results of this study are described and further steps suggested.

5.1. Introduction

Characteristics of the radio frequency (RF) coil used for transmission and reception play a major role in the quality of acquired NMR data. RF coils may be classified as either surface or volume coils. Surface coils offer higher transmit efficiency and receive sensitivity than volume coils, but over a smaller sample volume. The higher sensitivity of the surface coil can be extended over a larger volume of interest (VOI) by using a set of RF coils in phased array coil (e.g. Keil et al., 2011; Mogatadakala et al., 2008, and etc.). Adjacent loops in an array coil are usually overlapped to minimize the mutual inductance between the coils. Coupling between the non-adjacent elements can be eliminated by using an impedance- mismatched preamplifier (Roemer et al., 1990). The implementation of phased array RF coil at the ultra-high field for animal applications has received less attention compared with the low

field used for clinical application. The number of phased array coils for clinical applications has been raised up to 128 channels (Hardy et al., 2008), while there are few reports about designing phased array coil operating at the ultra-high field (e.g. transmit-receive two channel phased array coil operating at 16.7T by Gareis et al., 2006; four transmit/receive saddle geometry volume coil operating at 14.1 by Zhang and Webb, 2004, eight channel receive volume coil combined with transmit volume coil operating at 9.4 T by Lanz et al., 2010). Because of the small size of coils used for rodents at the ultra-high field, there is strong coupling between different elements of phase array coil. Usually, the traditional approach of impedance-mismatched preamplifiers has been used for decoupling neighbor and non-neighbor elements in phased array coils. To preserve the high sensitivity (SNR) of the phased array coils, decoupling circuit of impedance-mismatched preamplifiers should be placed close to the coil. But the small size of the bore at the ultra-high field used for rodent studies puts limitations in placing preamplifiers close to the coil. Besides, the further problem concerns the reliance on impedance-mismatched preamplifier such as direct coupling between preamplifiers, protection switches, and other RF component outside of the coil. Also, the antenna effect can be present on the board used for impedance-mismatched preamplifiers due to the short wavelength at high magnetic field.

Surface coils offer the considerable gain in the signal to noise ratio over a targeted volume but fall short in their ability to generate a homogenous RF field. For imaging and spectroscopy sequences, such as spin echoes, it is important to generate uniform excitation across the sample. To have the high sensitivity and improved spatial coverage from a homogeneously excited region, the transmit volume coil can be used with receive array surface coil for NMR data acquisition (Barberi et al., 2000; Beck and Blackband, 2001; Vaughan et al., 2002). One of the most popular resonators for producing uniform, circularly polarized and transverse radiofrequency magnetic fields in cylindrical magnetic resonance systems is the birdcage coil (Hayes, 2009; Hayes et al., 1985; Qian et al., 2012; Watkins and Fukushima, 1988).

Although the use of separate transmit and receive coils permits uniform excitation with better local SNR, interactions between the coils often cause problems. If the receive coil is not decoupled during the transmit pulse, its resonance dominates and destroys the homogeneity of the transmit field. With a linear transmit coil, the coils may be adequately decoupled by orienting the surface coil so that its B_1 is orthogonal to that of the transmit coil. Another approach that often works well (when there is adequate space) is the self-shielded surface coil, also called a gradiometer or quadrupolar coil (Suits et al., 1998), consisting of two loops, one above the other with oppositely directed currents. Such a coil also has a reduced depth of field, which is often a disadvantage, but it can have higher SNR because of reduced far-field losses when used on large samples. A conventional scheme is to use diodes in a passive or active switched configuration for decoupling transmit and receive coils (Boskamp, 1985; Edelstein et al., 1986). Passive diodes show high impedance (open circuit) in present of low voltage and low impedance (short circuit) in present of high voltage. In passive decoupling scheme, no external source is added to bias the diode. During transmit, diodes are biased to a high RF voltage and present low impedance and during receive diodes present a high impedance due of small induced voltage (lower than the cut-off voltage). Passively switched diodes have a problem at high frequencies application specifically during signal reception. The junction capacitance of typical diodes is substantial (typically ~1 pF per diode) so the sum of the capacitance of pair diodes (~2pF) is comparable with small capacitors used for impedance matching of the coil at high frequency. In addition, the junction capacitance of passive diode corresponds to a low reactance (only ~-j133 Ω at 600 MHz), and a significant amount of induced current may couple noise into the receive coil during signal reception. So actively switched

diodes are recommended for high-frequency operation. Sufficient isolating transmit and receive coil through active PIN diodes has been reported at the ultra-high magnetic field (Zhang and Webb, 2005). Developing separate transmit and receive coils at the ultra-high field for rodent applications is hampered by the small size of the bore which limits the available space for placing separate RF coils for reception and transmission together. The small size of coils and their closer proximity cause strong coupling between the transmit coil and receive coils. Since ultra-high field have been used mostly for animal studies, enough space should be considered in the design of the coil for accommodating the animal and all necessary equipment such as lines for anesthesia delivery to the animal or controlling the animal physiology during an experiment. There are limited numbers of studies which reported application of separate transmit and receive coils at ultra-high field (e.g. volume transmit coil combined with eight volume receive array coil operating at 9.4T by Lanz et al., 2010, and transmit patch antenna combined with three channel receive coil operating at 16.4T by Shajan et al., 2012).

In this work, we present a design for a transmit birdcage coil combined with quadrature pair surface coil for ^{1}H application at 14.1T (600MHz). The receive coil is remotely tuned and matched using varactor diodes, eliminating the need for variable capacitors and so saving considerable space in the probe design. The optimum configuration for decoupling the birdcage coil and surface coil was found and tested at the bench and in the scanner. The birdcage coil is detuned using PIN diodes while the surface coil is detuned using a combination of PIN diode controlled trap and varactor diodes. The performance of transmit-birdcage coil and receive- quadrature pair surface coil was compared with transmit-receive birdcage coil. The preliminary results and further steps of this study were addressed in the following section.

5.2. Subjects and methods

5.2.1. Varactor and pin diodes

Two different types of diodes are used in this chapter to control the behavior of RF coils: PIN diodes and varactor diodes.

PIN diodes act as current-controlled resistors at radio frequencies. In the simple case, PIN diodes can be treated as a switch. When PIN diodes are sufficiently forward biased (~100 mA) to ensure low resistance (~ 0.1Ω) to the RF that needs to be passed, the diode acts as a closed switch. When a reverse bias voltage is applied, the diodes resistance reaches several kilohms and acts as an open switch. Chokes and capacitors are usually used to separate the respective DC and RF current paths through circuits incorporating the diodes.

PIN diodes may be used to detune RF coils during transmission or reception. A forward biased PIN diode can be used to bypass the capacitor that it is placed parallel with, and therefore shift the resonance frequency of the circuit. This detuning configuration was used in the birdcage coil, where a PIN diode was placed in parallel with each capacitor on one end ring of the coil. A PIN diode switch can also be used to connect an inductor in parallel with a coil capacitor to form an LC trap, which blocks current and detunes the coil. Such an LC trap, called PIN diode controlled trap, was integrated into the surface coil used in this study.

Varactor diodes have a capacitance controlled by a DC drive voltage, which can be used to tune and match RF coils to samples with widely varying dielectric and resistive loads (Fig 5.1). If the capacitance range of the diode is large enough then it can also be used to shift the coil resonant frequency during transmission to provide detuning. Another advantage, particularly for small coils, is that the current drawn by the reverse-biased varactor diodes (<0.1μA) is considerably lower than for PIN diodes,

reducing any current-induced magnetic field distortions in the images. Varactor diodes are typically not used on transmit coils because of their low breakdown voltage. In this study, varactor diodes are integrated into the surface coil circuit for tuning and matching of the coil for different loadings.
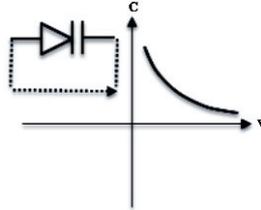

Fig 5.1 Voltage/capacitance characteristic of a varactor diode biased by an external DC voltage.

5.2.2. Birdcage coil

The transmit coil is a 16-rung high pass birdcage (50 mm diameter, 30 mm long) made on PCB (12 μm Cu on 0.1 mm FR4), and driven in quadrature (Magill et al., 2012). The birdcage coil is surrounded by a slotted shield (100mm diameter, 90mm long) to prevent eddy currents generated by gradient switching. A circuit diagram of the birdcage coil is shown in Fig 5.2.a. Five variable capacitors were used (2×tuning, 2×matching, balance, 1-9pF, all type NMKJ10HVE, Voltronics); fixed capacitors are type 100B (American Technical Ceramics). Bazooka baluns were fitted to the coaxial cables approximately 40 mm from the probe, (9 mm diameter × 50 mm long PTFE tubes coated with 35 μm copper tape (3M), tuned using three 1.2 pF capacitors (100B, ATC)).
PIN diodes (MA4P1450 SMQ, M/A-COM, Inc.) were added between every rung on one end ring to detune the resonator during the reception. The resonator is active under reversed bias voltage. When a forward current is applied (100 mA per diode), each PIN diode makes a short circuit across the end ring capacitors. RF chokes (150 nH, 1206CS Series, Coilcraft Inc.) were placed between the diodes and driving voltage source to block RF current while passing DC current.
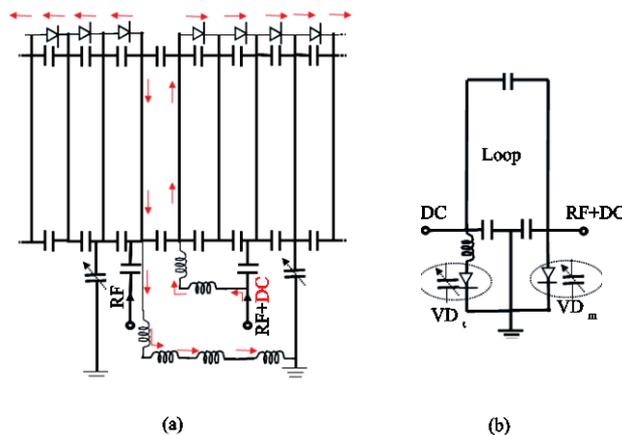

Fig 5.2. (a) Schematic showing the circuit used for the birdcage coil. PIN diodes were placed between every rung, parallel to the capacitors in top ring of the coil. One port of coil is used for applying RF and DC simultaneously to detune the coil during the reception and the other port is driven just with RF. Chokes , are shown as inductor, were placed in the path of DC current to stop the RF and pass the DC during receive (red arrow). (b) Schematic of the circuit used for the prototype single surface coil; two varactor diodes were introduced in the surface coil for tuning (VD_t) and matching coil (VD_m) during the reception and detuning the coil during the transmission.

The coil was characterized using a network analyzer (E5071C, Agilent), while loaded with a saline phantom. Imaging tests were performed in a 14.1T MR system with a 26 cm horizontal bore (Agilent, Oxford, UK). To test the homogeneity of the transmit coil, the RF field across a central slice of the phantom was mapped using the double angle method (Cunningham et al., 2006). Two images (matrix: 64×64, FOV: 25 ×25 mm^2, slice thickness: 2 mm, TE=1.9 ms, TR = 5 s, average=1) were acquired using the gradient echo magnetization sequence (GEMS), at flip angles of 30° and 60°, respectively. The performance of the birdcage coil as transmitter and receiver was also evaluated using the fast spin echo multi slices (FSEMS) sequence (slice thickness = 2 mm, FOV=25×25 mm^2, Data matrix= 64×64, Effective TE=52 ms, TR=10 s, average=4).

5.2.3. Single loop surface coil

To find the best design for the surface coil as receive and its optimum decoupling from the birdcage coil during transmission, a single prototype surface coil was first built (Fig 5.2.b). The surface coil, also made from PCB (10mm×15mm, 1mm track width), includes the varactor diodes (GC1513, Microsemi) for tuning and matching. The fixed capacitors are type 100B (ATC). The capacitance of varactor diodes are controlled by the applied DC voltage and the capacitance can be changed from 5 pF to 22 pF in the voltage range of 0-30 V. A voltage control board was developed to generate signals for driving the varactor diodes on the surface coil. The single loop surface coil, loaded with saline phantom, was characterized at the bench using a network analyzer. Decoupling between the surface coil and birdcage coil was measured at the bench using the network analyzer. Decoupling was measured for different positions of the surface coil inside the birdcage coil. To test the homogeneity of the field generated by the birdcage coil in presence of the detuned surface coil (by downshifting the resonance frequency of the surface coil using varactor diodes), the RF field on a slice of the phantom was mapped using the double angle method. Two images at flip angles 30° and 60° (matrix: 64×64, FOV: 25 ×25 mm^2, slice thickness= 2 mm, TE=1.9 ms, TR = 20 s, average=1) were acquired using the gradient echo magnetization sequence when birdcage coil was used in transmit/receive mode with the detuned surface coil present inside the birdcage coil.

Furthermore, a PIN diode controlled trap, made from an inductor and PIN diode placed in parallel with a loop capacitor, was added to the surface coil. The above bench measurement and B_1 homogeneity tests were repeated with the modified surface coil inside the birdcage coil, detuned using PIN diode controlled trap and varactor diode. The performance of the detuning circuit of the surface coil during transmit was compared between two cases, with and without the PIN diode controlled trap in the circuit of surface coil.

5.2.4. Quadrature pair surface coil

Two-array surface coil consists of two loops made of silver wire and decoupled by overlapping method (Roemer et al., 1990). In the initial version of the coil, we used silver as conductor (not printed PCB) due to simplification in changing the distance between two loops. In every loop, two varactor diodes (BB181, NXP semiconductors, and capacitance 1-13 pF at a reverse voltage range 0-30 V) were added for matching and tuning of the surface coil to 600 MHz for different loading. Circuit diagram of the single loop is shown in Fig 5.3. A PIN diode controlled trap made of inductor and PIN diode was added in parallel to the capacitance placed in top of every circuit. During transmit, varactor diodes were detuned and DC current was supplied to activate the PIN diode controlled trap on the top of the circuit.

During receive the PIN diode in detuning traps was deactivated by a reverse voltage and the voltage was supplied for tuning and matching of the coil by varactor diodes.
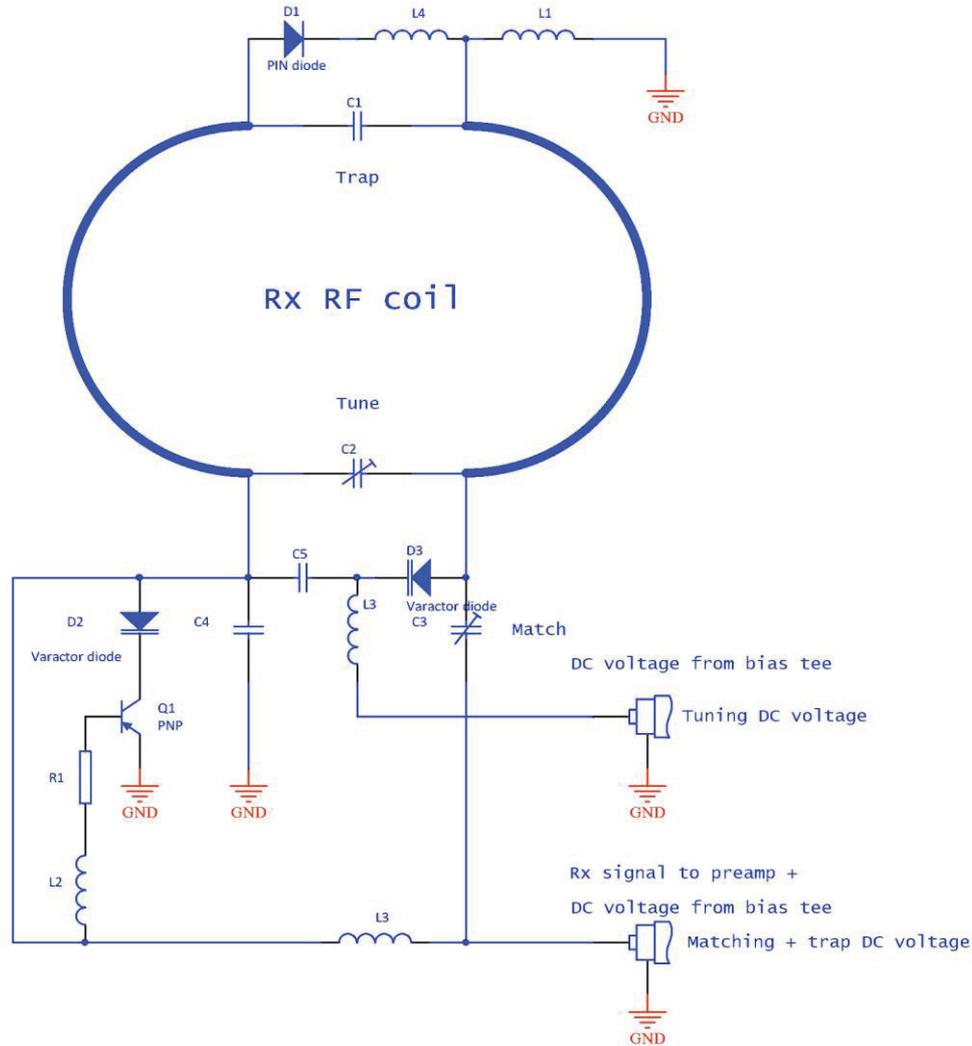

Fig 5.3 Schematic diagram showing the final circuit used for each loop in the quadrature pair surface coil. The PIN diode controlled trap circuit can be switched on and off by the PIN diode. When a positive DC voltage is applied to the RF cable, the PIN diode conducts, creating a high impedance resonant circuit (L4, C1) in the middle of the loop. Q1 acts as an open switch and the varactor is floating. The two diodes cannot be controlled without a transistor, because the current through parallel diodes is unpredictable and the varactor current is limited to 20 mA. When a negative DC voltage is applied to the RF cable, below -0.7V, the transistor Q1 acts as a short-circuit, the varactor is reverse biased and its capacitance varies with the voltage; this permits adjustment of the tuning and matching of the coil, while the PIN diode is non-conducting. L1, L2, L3 are chokes with a value of 470 nH to ensure the DC path. The bias voltage is applied through a bias tee, not represented here, made with a capacitor and a choke. The injected current/voltage must be limited to the maximum current of the PIN diode and the voltage must comply with the maximum range of the varactor voltage; it should be able to cover the range from -25V to +2V with 100 mA current limitations. The negative voltage depends on the varactor specifications.

A new voltage control board was designed to supply the voltage required by the varactor diodes (0-24V) during reception and current for activating the PIN diode controlled trap during transmission. The resonance frequency of the coil can be shifted over a certain range, limited by the capacitance range of the varactor diodes. Therefore two trimmer capacitors were added in each loop in the initial version of the coil to avoid changing the fixed capacitance frequently and easily shift the resonance frequency of the coil to 600MHz. These trimmer capacitors will be removed in the final version of the coil.

The quadrature pair surface coil was characterized at the bench using a network analyzer. It was loaded with a saline phantom and placed inside the birdcage coil. Decoupling between the detuned surface coil and tuned birdcage coil, and tuned surface coil and detuned birdcage coil were both measured.

The performance of the transmit-birdcage coil/receive-quadrature surface coil was then tested with a saline phantom in the scanner. A homemade PIN diode driver (Pilloud and Gruetter, 2013) was used to generate the necessary signals for driving the PIN diodes on the birdcage coil during the reception (+100mA/-10V) and switching between the transmit and receive coil.

To test the homogeneity of the B_1 field generated by the birdcage coil, in the presence of the detuned quadrature pair surface coil, the double-angle method was used. The birdcage coil was used as transmit and receive and quadrature pair surface coil was detuned inside the birdcage coil by PIN diode controlled trap and varactor diodes. Two images (matrix: 64×64, FOV: 25 ×25 mm^2, slice thickness: 2 mm, TE=1.9ms, TR = 20s, average=1) were acquired using the GEM sequence, at flip angles of 30° and 60°, respectively. The performance of the coil was also evaluated on axial images of the phantom acquired using the FSEM sequence (FOV=25×25 mm^2, data matrix= 64×64, Effective TE=52 ms, TR=10 s, average=6). An SNR map was generated over the same axial slice of the phantom for both cases using the GEM imaging data (matrix: 64×64, FOV: 25 ×25 mm^2, slice thickness= 2 mm, TE=1.9 ms, TR = 20 s, average=1) at flip angles of 30° (signal) and 0° (noise).

The SNR of images acquired using the transmit-birdcage coil/receive-quadrature pair surface coil was compared with the one obtained from the transmit/receive birdcage coil.

5.3. Results

5.3.1. Birdcage coil in transmit and receive mode

To fabricate the birdcage coil according to the design shown in Fig 5.2.a, fixed capacitors were spread over two rings placed in top and bottom of the coil, forming a high-pass birdcage coil. Trimmer capacitors were used for tuning, matching and balancing the symmetry of the coil (Fig 5.4). To detune the birdcage coil during the reception, PIN diodes were placed between every rung of the coil, parallel to the capacitors in the top ring. To activate PIN diodes during reception, a DC current is applied to one of the input port of the coil (Fig 5.5.b).

To characterize all resonant modes of the birdcage coil, a network analyzer was used at bench experiment. As the coil uses a high pass design, the imaging mode at 600 MHz appears at the high limit of the frequency range of the coil (Fig 5.5.a). The two degenerate imaging modes of the birdcage coil loaded with a saline phantom could be matched better than -25 dB while the coupling between the two modes was less than -20 dB. The quality factors (Q) of the unloaded to loaded coil (with saline phantom) for the two degenerate imaging modes at 600 MHz were 213/127 and 202/120, respectively (span 30 MHz and notch -7 dB applied in the network analyzer).

To test the birdcage coil at scanner in the transmit/receive mode, it was loaded with a saline phantom. An axial slice of the phantom acquired using the FSEM sequence is shown in Fig 5.6. As expected,

most of the acquired slice has approximately the same brightness, indicating nearly same sensitivity over all regions. A B1 map (processed using Matlab) is shown in Fig 5.7.

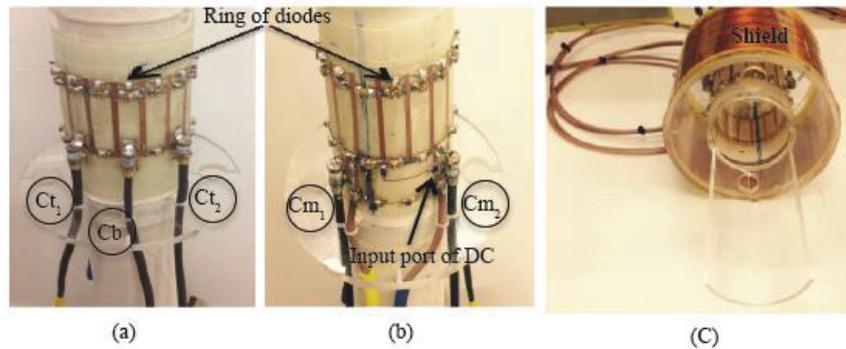(a)   (b)   (C)

Fig 5.4 Final birdcage coil design. PIN diodes were distributed on a ring parallel to the top ring of the coil and, during reception, are activated by an DC current applied in one of the input port of the coil: (a) image from front side of coil shows the tuning capacitors ($Ct_{1,2}$) for the two modes of the coil and balance capacitor (Cb) for adjusting the symmetry of the coil, (b) image from back side of the coil shows matching capacitors ($Cm_{1,2}$) for matching the two modes of coil to 50 Ω, and (c) the whole coil is placed inside the homemade faraday shield.

(a) Resonances of tuned birdcage coil over span of 1 GHz

(b) Resonances of detuned birdcage coil over span of 1 GHz

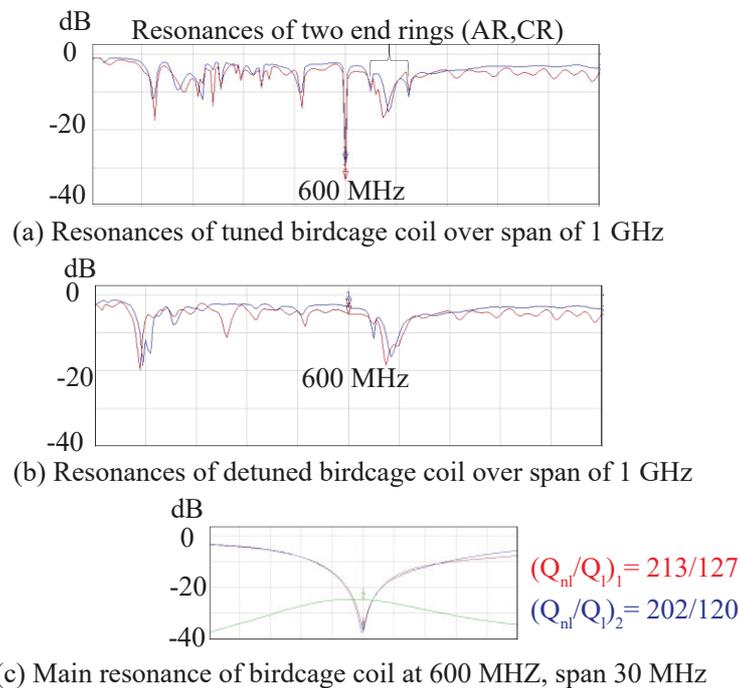(c) Main resonance of birdcage coil at 600 MHZ, span 30 MHz

Fig 5.5. Resonant modes of (a) the tuned birdcage coil and (b) the detuned birdcage coil with activated PIN diodes, obtained using a network analyzer over a span of 1 GHz. The Co-rotational mode (CR) corresponds to the Helmoltz resonance of the two coupled rings in which current in the rings is in phase. Anti-rotational mode (AR) corresponds to Maxewell resonant mode in which the end ring currents are out of phase. (c) Both modes of the birdcage coil can be tuned and matched well (~ -35 dB) to the interest mode 600 MHz. Coupling between the two modes is less than -20 dB and the ratio of Q factors (unloaded to loaded) of each mode is around 1.7.
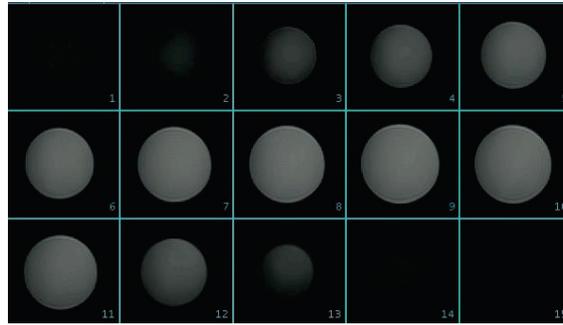
Fig 5.6 Axial slices of a saline phantom were acquired at 14.T using the birdcage coil in the transmit/receive mode. Images were acquired using the fast spin echo magnetization (FSEM) sequence, thickness of slices= 2 mm, FOV=30×30 mm^2, Data matrix= 64×64, Effective TE=52 ms, TR=10 s, average=6.

Fig 5.7 (a) The gradient echo magnetization (GEMS) images were acquired using the birdcage coil in the transmit/receive mode for flip angles=30° (right) and 60° (left) and TR=20 s, TE=1.9 ms, average=1, data matrix=64×64, FOV=30×30 mm^2, thickness=2 mm. (b) B$_1$ map was generated from the GEMS images at two flip angles of 30° and 60°.

5.3.2. Prototype receive surface coil

To design the single surface coil according to the design shown in Fig 5.2.b, varactor diodes were introduced into the circuit for tuning and matching the coil to the resonance frequency of 600 MHz during reception and also for detuning the surface coil during transmission (Fig 5.8.a)

To test the performance of the single surface coil at the bench, it was loaded with a saline phantom and characterized using a network analyzer. The coil could be matched very well (-40 dB) to the resonance frequency 600 MHz (Fig 5.8.b) and tuned over a frequency range 10 MHz using the varactor diodes. The ratio Q factors, unloaded to loaded, was 126/86. To measure the decoupling between the birdcage coil and surface coil, the loaded surface coil was placed inside of the birdcage coil. Decoupling between the detuned surface coil (detuned using varactor diodes) and tuned birdcage coil, and also between the tuned surface coil and detuned birdcage coil (activated PIN diodes), were better than -15 dB.

The resonance frequency of the birdcage coil was slightly shifted when the detuned surface coil was placed inside it. To explore the impact of the shifting frequency on the coil performance in the scanner, the birdcage coil was tested in the transmit/receive mode when the surface coil, detuned by the varactor diodes, was present. A black hole was evident in the axial GEMS images (Fig 5.9.a). Furthermore, B$_1$ maps (Fig 5.9.c) showed that the black hole in the GEMS images originated from a disturbance of the B$_1$ homogeneity, caused by the detuned surface coil. When the surface coil was detuned using the

varactor diodes and a PIN diode, the residual coupling between the birdcage coil and detuned surface coil no longer shifted the resonance frequency of the birdcage coil, and the black hole disappeared from the GEMS image (see Fig 5.9.b). Efficient decoupling of the birdcage coil and surface coil was further confirmed by B_1 maps (Fig 5.9.d), where homogeneity of the B_1 field was seen to be preserved in the presence of the surface coil detuned by the PIN diode controlled trap and varactor diodes.
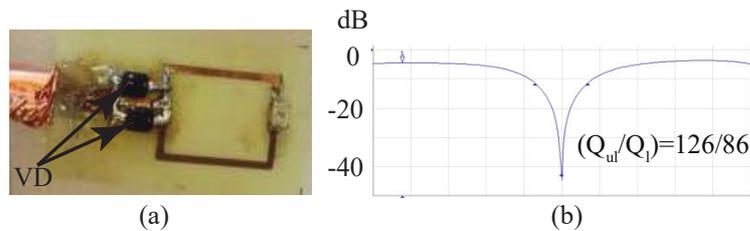

Fig 5.8 (a) Single surface coil: varactor diodes (VD) were used in the circuit of the surface coil for tuning and matching during the reception and detuning during transmission, and (b) the resonance frequency of the surface coil tuned and matched using the varactor diodes to 600 MHz. The ratio of Q factors, unloaded to loaded, was 1.46.

5.3.3. Transmit-birdcage coil and receive-quadrature pair surface coil

To build the quadrature pair surface coil, the optimum design found from the single surface coil was used in the configuration of two overlapped loops (Fig 5.10).

To characterize the coil at the bench, the surface coil was loaded with the saline phantom and measurement done using the network analyzer. The two modes of the surface coil were decoupled very well through the overlapping of two loops (better than -20 dB). Both modes of the surface coil could be matched and tuned using varactor didoes to 600 MHz, better than -35 dB. The coil could be tuned over a frequency range of 5 MHz using varactor diodes. Both loops of the surface coil could be detuned during transmission by the PIN diode controlled trap and varactor diodes. The ratio Q factors of the unloaded to the loaded coil is approximately 1.4 for both modes of the surface coil. Decoupling between the birdcage coil and quadrature surface coil for either the detuned surface coil/tuned birdcage coil or the detuned birdcage coil/tuned surface coil was better than -20 dB (Fig 5.11).

To evaluate the homogeneity of B_1 generated by the birdcage coil in the presence of detuned quadrature pair surface coil, B_1 map was measured in the scanner (Fig 5.12). Also the coverage of the transmit birdcage coil/receive quadrature pair surface coil is illustrated in the axial images acquired using the FSEMS sequence (Fig 5.13). The periphery region of phantom appears brighter and the signal intensity drops with increasing distance from the receive coil (Fig 5.13).

To compare the performance of two different configurations, the transmit/receive birdcage coil and the transmit birdcage coil/receive quadrature pair surface coil, SNR map was estimated over an axial slice of the phantom acquired using GEMS sequence at each configuration (Fig 5.14). Images acquired with the transmit/receive birdcage coil had almost the same SNR over the entire axial slice of the phantom, while there is a gradient in SNR in the image acquired with the transmit birdcage coil/receive quadrature pair surface coil. Comparison between the transmit birdcage coil/receive quadrature pair surface coil and the transmit/receive birdcage coil showed an SNR increase of 2 fold at the phantom periphery and similar SNR at the depth of 5mm (Fig 5.15).

(a) GEMS image, no detuning trap   (b) GEMSimage, with detuning trap

(c) B_1 map, no detuning trap   (d) B_1 map, with detuning trap
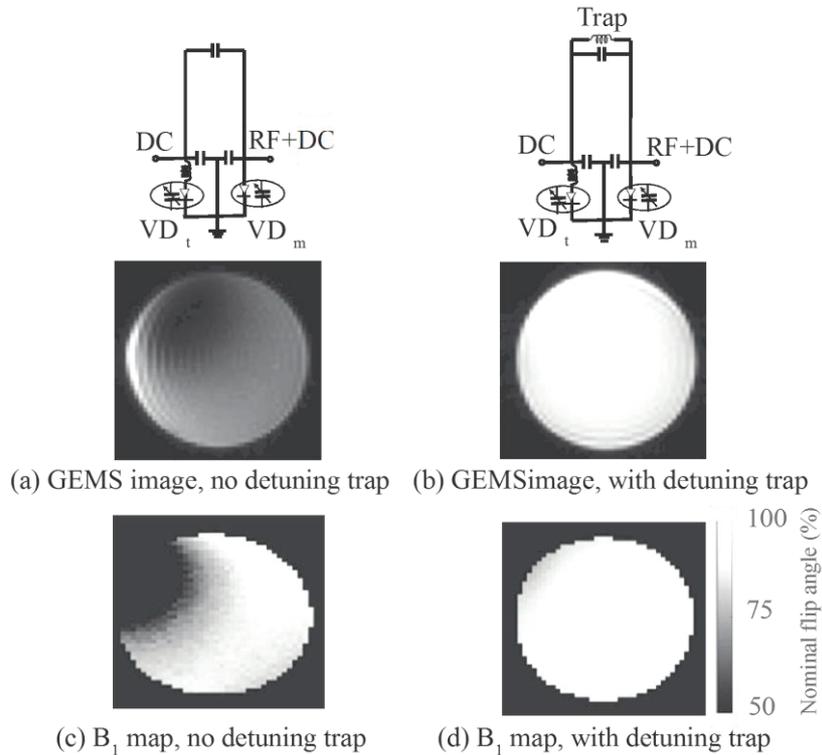
Fig 5.9 An axial slice of the saline phantom acquired using the transmit/receive birdcage coil at the presence of the surface coil detuned by (a) the varactor diodes, and (b) the PIN diode controlled trap and varactor diodes. Images were acquired using the gradient echo multi slices (GEMS) sequence, TR = 20 s, TE = 1.9 ms, flip angle = 30°, average = 1, data matrix = 64×64, FOV = 25×25 mm², thickness = 2 mm. (c) and (d) B_1 map generated from GEMS images acquired at flip angles of 30° and 60° in case of a and b, respectively.
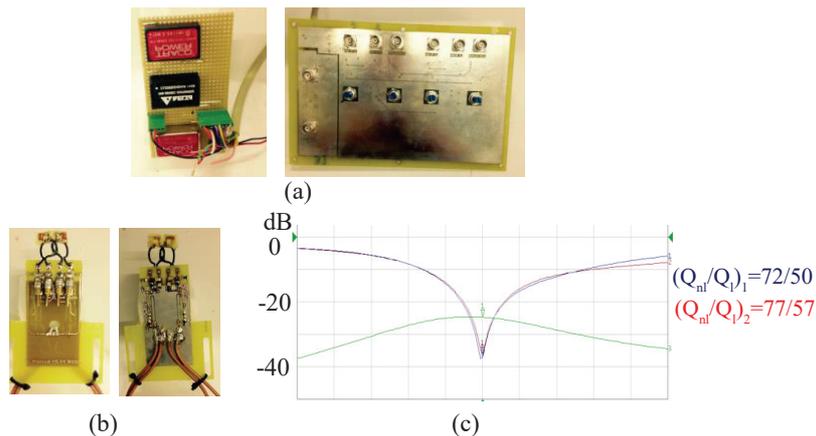
Fig 5.10 (a) Designed voltage control board for supplying different voltages to the varactor diodes and PIN diodes during transmit and reception, and (b) the quadrature pair surface coil. (c) The resonance frequency of both modes of the quadrature pair surface coil is matched well to 600 MHz (a span of 30 MHz). The green line shows the coupling between two modes of the coil. The Q factor of both modes (measured by the network analyzer, span 30MHz and notch=-7dB) is ~1.4.

(a) Tuned birdcage coil (Vol 1, 2),
detuned surface coil (Surf 1,2)

(b) Detuned birdcage coil (Vol 1, 2),
tuned surface coil (Surf 1,2)

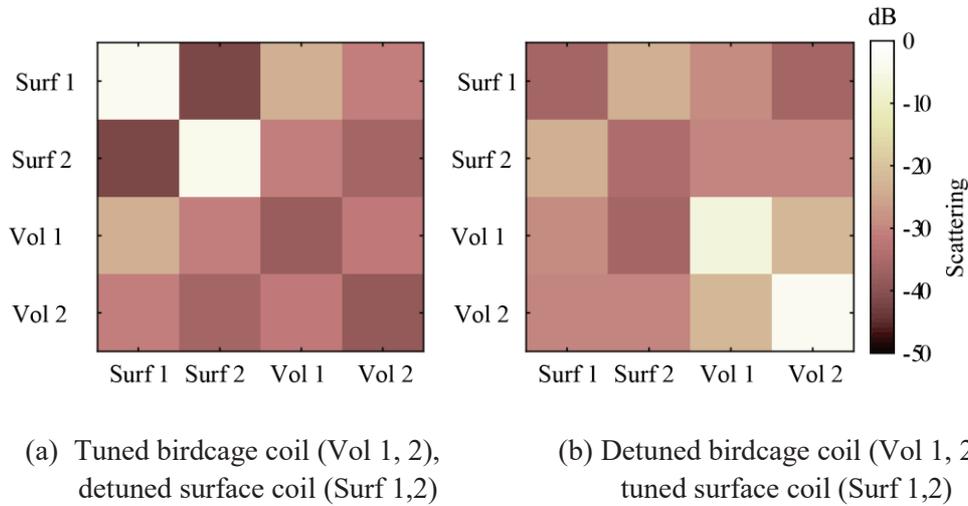Fig 5.11 Coupling between the two modes of the birdcage coil (Vol 1,2) and two modes of the loaded quadrature pair surface coil (Surf 1,2) were measured at the bench using a network analyzer for (a) the tuned birdcage coil and detuned surface coils, and (b) the detuned birdcage coil and tuned surface coils.
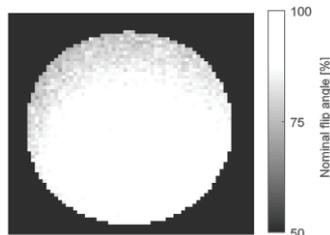
Fig 5.12 B_1 map of the axial slice of the saline phantom, acquired using the transmit/receive birdcage coil in presence of the detuned quadrature pair surface coil. Two images were acquired using the gradient echo multi slices (GEMS) sequence with different flip angles = 30° and 60° and TR = 20 s, TE = 1.9 ms, average = 1, data matrix = 64×64, FOV = 25×25 mm², thickness = 2mm.

Fig 5.13 Axial slices of a saline phantom acquired using the transmit birdcage coil/receive quadrature pair surface coil. Images were acquired using fast spin echo multi slices (FSEMS) sequence, Thickness of slices = 2 mm, FOV = 30×30 mm², data matrix = 64×64, Effective TE = 52 ms, TR = 10 s, average = 6.

(a) Tx, Rx: birdcage coil

(b) Tx: birdcage coil ,
Rx: quadrature pair surface coil

Fig 5.14 Map of the signal to noise ratio (SNR) obtained from an axial slice of the phantom. Imaging was performed using (a) the transmit/receive birdcage coil (birdcage coil: Tx-Rx), and (b) the transmit birdcage coil (Tx) /receive quadrature pair surface coil (Rx). Images data were acquired using the gradient echo multi slices (GEMS) sequence, FOV = 30×30 mm^2, data matrix = 64×64, TE = 1.9 ms, flip angle = 30°, TR = 20s, average = 1.

Tx, Rx: Birdcage coil

Tx: Birdcage coil,
Rx: Quadrature pair surface coil

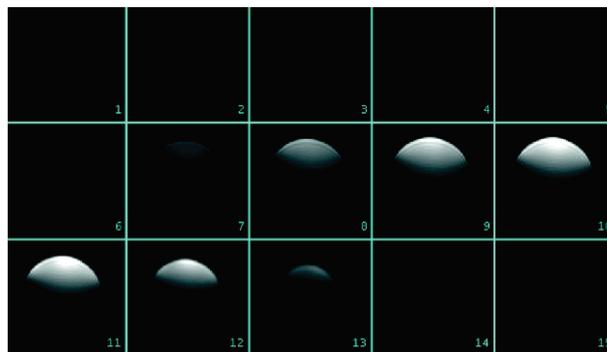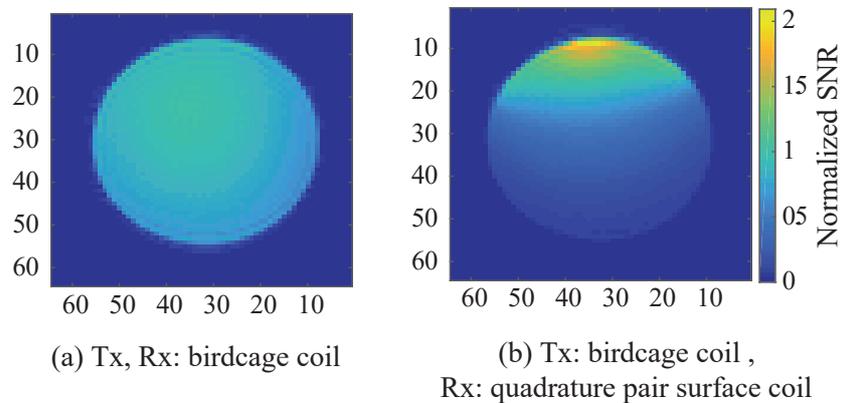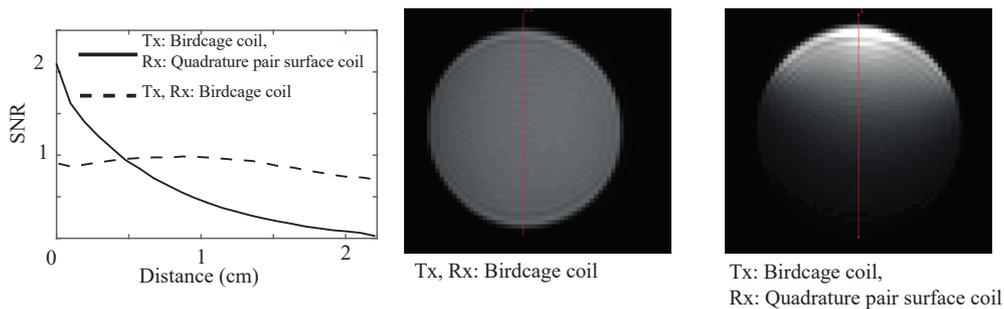Fig 5.15 Comparison of SNR along one diameter of an axial slice of the saline phantom acquired using the transmit/receive birdcage coil (shown by solid line) and the transmit birdcage coil/ receive quadrature pair surface coil (shown by a dot line). Images were acquired using the fast spin echo multi slices (FSEMS) sequence, FOV = 30×30 mm^2, data matrix = 64×64, Effective TE = 52 ms, TR = 10s, average = 6.

5.4. Discussion

5.4.1. Decoupling coils during transmit and receive

Using a separate coil for transmission and reception gives the opportunity to profit from the specific characteristics of different types of the coil, specifically homogenous excitation with high sensitivity reception. Therefore in this study, we considered a birdcage coil for transmission and surface coil for reception. Birdcage coils offer homogenous excitation and surface coil benefits from high sensitivity, especially in the region close to the coil. Besides their small size, coupling between the two coils during transmission and reception is a big challenge in designing animal coils at 14.1 T.

In this project, the birdcage coil could be detuned efficiently (decoupling better than 30 dB) using PIN diodes placed between every rung, parallel to the capacitors in the top ring.

In the prototype version of the surface coil, varactor diodes were introduced into the single loop to be used as tuning and matching capacitors during reception. Varactor diodes offer remote tuning and matching for the coil at different loading by varying the voltage in a control board. However, it should be mentioned that the most varactor diodes suffer from low Q factor and also are broken if a high power is applied. Therefore the varactor diodes are not recommended for the coil design used in transmission mode. Varactor diodes with high Q factor are an advantage for the coil design used in reception mode. The dual roles of the varactor diodes in the circuit of the coil, namely remote tuning and matching the coil during the reception and shifting the resonance frequency of the coil during transmission, provide gain in space that is a big challenge in the design of a small animal coil. Bench experiments showed that detuning single surface coil by varactor diodes increases the decoupling between the birdcage coil and surface coil to the range of 12 - 30 dB, depending on the position of the surface coil inside the birdcage coil. However, results of NMR tests at the scanner demonstrated that detuning the surface coil by the varactor diodes was not sufficient to decouple the surface coil during transmission, resulting in the appearance of a black shadow in all images acquired using the GEMS sequence (which is sensitive to B_1 inhomogeneities), as shown in Fig 5.9. The B_1 map in Fig 5.9 demonstrates that the black shadow in the image is due to the B_1 field distortion caused by coupling between the surface coil and birdcage coil during transmission. We found that adding a PIN diode controlled trap to the circuit of the surface coil could efficiently decouple the surface coil from the birdcage coil during the transmission and preserve the homogeneity of the B_1 field. Comparison the B_1 maps obtained using the transmit/receive birdcage coil with and without the presence of the detuned surface coil (Fig 5.9 and Fig 5.7, respectively) demonstrated that the surface coil, detuned using PIN diode controlled trap and varactor diodes, does not disturb significantly the homogeneity of the B_1 field during the transmission. Therefore an optimum configuration for decoupling the surface coil from the birdcage coil during the transmission was chosen as the combination of changing the voltage on the varactor diodes and activating the PIN diode controlled trap.

The optimum detuning configuration found for the birdcage coil and quadrature pair surface coil results in efficient decoupling of the transmit and receive coil (better than 20 dB at the bench). The ratio of Q factors of the unloaded to the loaded quadrature pair surface coil with the saline phantom is a bit low (around 1.4). The low Q factor of the quadrature surface coil could be due to low Q factor of used varactor diodes and/or the present of PIN diode controlled trap in the top of the circuit that introduces resistance to the coil. Therefore modification of the surface coil circuit toward decreasing the resistance and increasing the Q factor of the coil will be the next step for this project.

5.4.2. Transmit/receive birdcage coil versus transmit-birdcage coil and receive-quadrature pair surface coil

Birdcage coils are the standard resonator for producing uniform, circularly polarized, transverse radiofrequency magnetic field in cylindrical magnetic resonance system. As it is evident in the B_1 map in Fig 5.7, the birdcage coil produces homogenous B_1 field. When a birdcage coil is used for transmission and reception, it offers approximately the same sensitivity over the whole field of view, as is visible in Fig 5.15. The uniform sensitivity of the transmit/receive birdcage coil results in approximately same brightness over the entire region of interest (Fig 5.6). Since the birdcage coil is large in size, it covers a large region of the sample but with low sensitivity, compared the surface coil, in the region close to the surface coil.

Use of a birdcage coil in transmission mode and quadrature pair surface coil in reception mode is an optimum design to have homogenous excitation and high receive sensitivity over the region of interest. The designed quadrature pair surface coil covers a larger area than the single surface coil, and its two loops could be decoupled by the known simple method of overlapping. As expected, the sensitivity of the coil drops with distance from the surface coil resulting in more brightness in the periphery of phantom, regions close to the coil (Fig 5.13). The transmit birdcage coil/receive quadrature pair surface coil offers higher sensitivity than the transmit/receive birdcage coil up to the distance of 5 mm from the surface coil (ratio of 2 at the periphery of the phantom, see Fig 5.15). However, at distance more than 5mm, the SNR of the transmit birdcage coil/receive quadrature pair surface coil drops below that of the transmit/ receive birdcage coil.

5.4.3.   Future work

Homogenous excitation and high detection sensitivity over a targeted volume are the desired objectives in the design of separate coil for transmission and reception in this study. So there is always room for more modifications in the circuits of the coil to improve its performance. Few potential modifications are briefly explained in the following.

The designed quadrature pair surface coil in this project has a rather low Q factor, which affects the sensitivity of the coil during the NMR data acquisition. Therefore modification of the surface coil toward increasing its Q factor has been considered as future work. A source of resistance can be the PIN diode controlled trap introduced in the circuit of surface coil. So finding the best configuration for placing the PIN diode controlled trap in the circuit of the coil may decrease the resistance and increase the sensitivity of the coil. Also, the varactor diodes used in the circuit of quadrature pair surface coil can bring down the Q factor of the coil. In the present quadrature pair surface coil, varactor diodes model BB181 were used because of their low price and also availability in our RF lab. Therefore replacing the current varactor diodes by ones with higher Q factor can help to increase the sensitivity of the coil. In the final version of the coil, the trimmer capacitances used temporarily in the circuit will be removed as well. Another point which should be addressed is about the configuration used for connecting the receive coil to the preamplifier during the data acquisition at 14.1T. In our setup, the two ports of the surface coil were connected through long cables to the preamplifier placed in the magnet leg. Placing the preamplifier close to the probe can minimize the signal loss in the cable used for connecting the probe to the preamplifier. At the end, the final designed coil should be tested on a rat and/or mice at 14.1T as well. Therefore the suitable holder should be designed for fixing animal inside of the coil with the required equipment for controlling the animal physiology during the study.

To increase the coverage of the surface coil and benefit from high SNR in the voxel placed far from the coil, one can increase the number of loops in the surface coil. In this regards, a three array coil is proposed as a continuation of this project. The advantage of this design is that three loops could be decoupled by the overlapping method and there is no need for more complicated decoupling methods such as preamplifier decoupling.

An array coil with more than three loops is more challenging at the ultra-high magnetic field for rodents because of the small size of the coil. Also, the decoupling between the non-neighbor coils should be considered in the coil design. The typical decoupling method for the non-neighbor coil is the preamplifier method. Tuning and matching a coil with the presence of preamplifier is usually done with sniffer loop, which is not feasible at NMR scanner. Array coil designed for a clinical scanner (lower field) usually is tuned and matched once at the bench by sniffer loop connected to the network analyzer. Moreover, loadings for the clinical array coil are approximately in the same range, while the loading in

the preclinical application at the ultra-high field is varied from one study to the other and the coil need to be tuned and matched frequently.

5.5. Conclusion

The transmit birdcage coil and receive quadrature pair surface coil presented in this chapter provide homogenous excitation during transmission and high sensitivity during the reception for NMR application at the ultra-high field of 14.1T (600MHz for ^{1}H). Using the varactor diodes for tuning and matching gives the possibility of remote tuning and matching the coil for different loads. The optimum decoupling configurations found for the birdcage and surface coil was sufficient to reduce the coupling between the coils during transmission and reception, resulting in preservation homogeneity of the B_1 field generated by the birdcage coil and profiting from high sensitivity of the quadrature pair surface receive coil. These preliminary results are promising for further development of this configuration toward its application for animal study at 14.1 T.

5.6. References

1. Barberi, E.A., Gati, J.S., Rutt, B.K., Menon, R.S., 2000. A transmit-only/receive-only (TORO) RF system for high-field MRI/MRS applications. Magn. Reson. Med. 43, 284–289.

2. Beck, B.L., Blackband, S.J., 2001. Phased array imaging on a 4.7T/33cm animal research system. Rev. Sci. Instrum. 72, 4292–4294. doi:10.1063/1.1406916.

3. Boskamp, E.B., 1985. Improved surface coil imaging in MR: decoupling of the excitation and receiver coils. Radiology 157, 449–452. doi:10.1148/radiology.157.2.4048454

4. Cunningham, C.H., Pauly, J.M., Nayak, K.S., 2006. Saturated double-angle method for rapid B1+ mapping. Magn. Reson. Med. 55, 1326–1333. doi:10.1002/mrm.20896.

5. Edelstein, W.A., Hardy, C.J., Mueller, O.M., 1986. Electronic decoupling of surface-coil receivers for NMR imaging and spectroscopy. J. Magn. Reson. 67, 156–161. doi:10.1016/0022-2364(86)90421-X.

6. Gareis, D., Neuberger, T., Behr, V.C., Jakob, P.M., Faber, C., Griswold, M.A., 2006. Transmit-receive coil-arrays at 17.6T, configurations for 1H, 23Na, and 31P MRI. Concepts Magn. Reson. Part B Magn. Reson. Eng. 29B, 20–27. doi:10.1002/cmr.b.20055.

7. Hardy, C.J., Giaquinto, R.O., Piel, J.E., Rohling, K.W., Marinelli, L., Blezek, D.J., Fiveland, E.W., Darrow, R.D., Foo, T.K.F., 2008. 128-channel body MRI with a flexible high-density receiver-coil array. J. Magn. Reson. Imaging JMRI 28, 1219–1225. doi:10.1002/jmri.21463.

8. Hayes, C.E., 2009. The development of the birdcage resonator: a historical perspective. NMR Biomed. 22, 908–918. doi:10.1002/nbm.1431.

9. Hayes, C.E., Edelstein, W.A., Schenck, J.F., Mueller, O.M., Eash, M., 1985. An efficient, highly homogeneous radiofrequency coil for whole-body NMR imaging at 1.5 T. J. Magn. Reson. 63, 622–628. doi:10.1016/0022-2364(85)90257-4.

10. Keil, B., Wiggins, G.C., Triantafyllou, C., Wald, L.L., Meise, F.M., Schreiber, L.M., Klose, K.J., Heverhagen, J.T., 2011. A 20-Channel Receive-Only Mouse Array Coil for a 3T Clinical MRI System. Med. Soc. Magn. Reson. Med. 66, 582. doi:10.1002/mrm.22791.

11. Lanz, T., Müller, M., Barnes, H., Neubauer, S., Schneider, J.E., 2010. A high-throughput eight-channel probe head for murine MRI at 9.4 T. Magn. Reson. Med. 64, 80–87. doi:10.1002/mrm.22414.

12. Magill, A., Lei, H., Gruetter, R., 2012. A high-pass birdcage coil for small animal imaging at 600MHz/14.1T. Presented at the 20th Scientific Meeting of the International Society for Magnetic Resonance in Medicine, International Society for Magnetic Resonance in Medicine.

13. Mogatadakala, K.V., Bankson, J.A., Narayana, P.A., 2008. Three Element Phased Array Coil for Imaging of Rat Spinal Cord at 7T. Med. Soc. Magn. Reson. Med. 60, 1498. doi:10.1002/mrm.21777.

14. Pilloud, Y., Gruetter, R., 2013. Quad channel Pin diode driver, in: ESMRMB. Presented at the European Society for Magnetic Resonance in Medicine and Biology, Toulouse, France.

15. Qian, C., Masad, I.S., Rosenberg, J.T., Elumalai, M., Brey, W.W., Grant, S.C., Gor'kov, P.L., 2012. A volume birdcage coil with an adjustable sliding tuner ring for neuroimaging in high field vertical magnets: Ex and in vivo applications at 21.1 T. J. Magn. Reson. 221, 110–116. doi:10.1016/j.jmr.2012.05.016.

16. Roemer, P.B., Edelstein, W.A., Hayes, C.E., Souza, S.P., Mueller, O.M., 1990. The NMR phased array. Magn. Reson. Med. 16, 192–225.

17. Shajan, G., Hoffmann, J., Balla, D.Z., Deelchand, D.K., Scheffler, K., Pohmann, R., 2012. Rat brain MRI at 16.4T using a capacitively tunable patch antenna in combination with a receive array. NMR Biomed. 25, 1170–1176. doi:10.1002/nbm.2786.

18. Suits, B.H., Garroway, A.N., Miller, J.B., 1998. Surface and gradiometer coils near a conducting body: the lift-off effect. J. Magn. Reson. San Diego Calif 1997 135, 373–379. doi:10.1006/jmre.1998.1608.

19. Vaughan, J.T., Adriany, G., Garwood, M., Yacoub, E., Duong, T., DelaBarre, L., Andersen, P., Ugurbil, K., 2002. Detunable transverse electromagnetic (TEM) volume coil for high-field NMR. Magn. Reson. Med. 47, 990–1000. doi:10.1002/mrm.10141.

20. Watkins, J.C., Fukushima, E., 1988. High‐pass bird‐cage coil for nuclear‐magnetic resonance. Rev. Sci. Instrum. 59, 926‐929. doi:10.1063/1.1139751.

21. Zhang, X., Webb, A., 2005. Design of a four-coil surface array for in vivo magnetic resonance microscopy at 600 MHz. Concepts Magn. Reson. Part B Magn. Reson. Eng. 24B, 6–14. doi:10.1002/cmr.b.20022.

22. Zhang, X., Webb, A., 2004. Design of a capacitively decoupled transmit/receive NMR phased array for high field microscopy at 14.1 T. J. Magn. Reson. 170, 149–155. doi:10.1016/j.jmr.2004.05.004.

Chapter 6. Concluding remarks and perspectives

The present thesis first focused on a refined metabolic modeling approach in the adult rat brain that incorporated information on the ^{13}C labeling time courses of multiplets of glutamate and glutamine (total number of 17) that ultimately improved the reliability of the estimated cerebral metabolic fluxes. One might now ask: (1) how might the young and aging brain influence the dynamic brain ^{13}C NMR multiplet data? And, (2) can the dynamics of ^{13}C isotopomers extend to other pairs of amino acids or metabolites, other than glutamate and glutamine?

Two future studies are proposed as a continuation of this thesis on brain energy metabolism, *in vivo*, for the estimation of metabolic fluxes: (1) comparing single infusion protocols of [1,6-^{13}C$_2$] glucose and [1,2-^{13}C$_2$] acetate, as opposed to a combined infusion of [1,6-^{13}C$_2$] glucose and [1,2-^{13}C$_2$] acetate, and incorporating the approach of dynamic enrichment of multiplets in the mathematical model; and (2) adapting such protocols in the smaller brain from healthy and genetically modified mice, with the aim to better estimate cerebral metabolic fluxes.

We then focused on the diffusion characteristics of acetate in the adult rat brain under prolonged unlabeled acetate infusion using DW-^{1}H-MRS techniques. We found out the presence of Ace resonance in ^{1}H spectra acquired at very large diffusion weighting indicates restricted diffusion of Ace in intracellular region of brain. However, the significant larger diffusion of Ace compared to intracellular metabolites such as NAA demonstrates that substantial fraction of Ace located in extracellular space of brain tissue. Assuming even distribution for Ace in intracellular and extracellular space, diffusion properties of Ace yielded to a smaller physical distribution volume (V_d) for Ace in the rat brain compared to water and glucose. We noticed a slightly different behavior of the slow diffusion component of acetate in the intracellular compartment, compared to that of the neuronal marker NAA, suggesting a different chemical environment of acetate. Further interpretations about the dependency of the slow diffusion component of metabolites on the subcellular distribution space would need to be established in future experiments using, for example, potential glial cell markers, such as glutamine and myo-inositol.

To quantify the apparent concentration of Ace in rat brain under prolonged Ace infusion, the T_1 and T_2 relaxation times of acetate was measured. Acetate has a significantly larger T_1 and smaller T_2 relaxation compared with other metabolites, e.g. NAA, in the brain. Therefore, increasing the repetition time in the acetate study may offer higher signal intensity per acquisition, but at the cost of increasing the acquisition time. The shorter T_2 of Ace compared to NAA, as mainly neuronal marker, could be sign of different localization of Ace in the brain.

Furthermore, we also determined the kinetic parameters of transport and utilization for acetate uptake in the rat brain using revised V_d of Ace. The estimated Ace consumption rate in brain was in the same range as reported glial TCA cycle rate, which is in consistency with proposed hypothesis about main localization of Ace in the glial cells. The effects of V_d considered for Ace in the rat brain on estimated cerebral metabolic rate of Ace (CMR_{Ace}) were investigated in details. The dependency of estimated CMR_{Ace} to V_d of Ace in the rat brain highlights the importance about a refined determination of V_d for Ace in brain metabolic studies. If measuring localized kinetic parameters of acetate transport and utilization in the brain becomes feasible, this opens the door to valuable insights about regional brain metabolism.

The concluding thesis chapter focused on the design, construction and evaluation of a combined transmit-birdcage coil and receive-quadrature pair surface coil, and its promising use for NMR studies at 14.1T. Introducing varactor diodes in the circuit of the receive-quadrature pair surface coil provided the practical possibility of remote tuning and matching of the coil for different loadings. The optimum decoupling configurations found for the birdcage coil and surface coil resulted in preserving the homogeneity of B_1 field generated by the birdcage coil and simultaneously profiting from high sensitivity of the surface coil. Improving coil design to maximize sensitivity will be the next step. Additionally, by increasing the number of loops in the receive coil to three loops should increase the coverage of the receive coil sensitivity. The advantage of a three-loop configuration enables decoupling all loops sufficiently by the overlapping method. The use of this coil for the acquisition of NMR data from small animals, *in vivo*, will be facilitated by the design of an appropriate physical support for fixing the animal inside of the coil, and still enabling the introduction and placement of other materials to maintain the animal under anesthesia and to register animal physiology.

Acknowledgements

Preparing the PhD thesis for me was similar to ascending a very high, steep and unexplored mountain. Any mountain possesses many routes, each starting from a different place and each having a different character and set of challenges to deal with. One must also have the faith that the summit actually exists; it may not be visible at all at the beginning of the climb. Clearly, no one can follow all routes, but one must choose a way to reach to the top. In this expedition the most important thing is the efforts and memories that bring satisfaction. I would like to express my sincere gratitude to the leader and the teammates who supported and helped me in all steps of this amazing route.

Firstly, I would like to thank my supervisor, Prof. Rolf Gruetter, who gave me this opportunity to do my PhD in Centre d'Imagerie BioMédicale (CIBM), one of the most unique research centers in the field of NMR. I really appreciate all his continuous support, immense knowledge and patience whilst allowing me to work through my own way. It was a particular honor to have a leader like him during the entire research and enlighten the route to summit by his advice and encouragement.

I gratefully acknowledge Prof. Steve Williams, Prof. Vincenzo Savona, Dr. Julien Valette, and MER Dr. Giovanni Boero for accepting to be the members of my thesis committee.

I would like to give special thanks to Bernard Lanz. His constant encouragement and enthusiasm have helped me to develop my knowledge in NMR spectroscopy and brain energy metabolism. I am extremely thankful and indebted to him for sharing expertise, sincere and valuable guidance extended to me. He has been always available to answer my questions and clear any doubt I had, even after he moved to UK for postdoc. Thanks for all time he spent on reviewing the manuscripts and my thesis.

I would like to express my deep gratitude to Nicolas Kunz, whose expertise in the field of diffusion spectroscopy, preprocessing data and modeling and his continuous advice and support added considerably to my graduate experience. This thesis and outcome manuscripts were enriched significantly through his useful comments and revisions.

I would like to express my sincere thanks Arthur W. Magill who taught me the basics of RF coil design during the first year of my PhD. His vast knowledge and guidance into the world of building RF coil and reviewing RF part of thesis have been a valuable input for this thesis.

I would like to thank Pilloud Yves for his great support in the technical part of RF coil and our great collaboration in design of the electronic part of the RF coil.

I would like to thank Joao Das Neves Duarte who provided the ^{13}C data for modeling of brain energy metabolism and organized all group meeting for presenting and sharing our results and experiences.

I would like to thank Pascal Mieville from chemistry lab, who developed the diffusion sequence in high resolution for analyzing plasma sample and his entire patience in answering my questions with regards to running the experiments in high-resolution scanner.

I gratefully acknowledge the contribution of Poitry-Yamate Carole who has profound knowledge in neuroscience and patiently revised my thesis. I am always impressed about her beautiful writing and enjoyed after reading the corrected version of my thesis.

I would like to express my gratitude to Hongxia Lei for all his great supports and help in the acquisition of NMR data at 14.1 T and his useful comments during entire preparation of the thesis. I have great memories working with her and also from all dinners organized in the Chinese restaurants.

I would like to thank Cristina Cudalbu and Lijing Xin for their help and productive comments about the process and analysis of NMR data and also Ozlem Ipek for her helpful comments and feedback about RF coil.

I also thank all people in vet support team, especially Jaquelina Romero, Mario Lepore, and Corina Berset for the time they spent preparing animals and addressing the different physiological issues I faced through my experiments.

I would also like to thank Tanja Egener-Kuhn and Lillian Vernacchio for taking care of all the administrative matters.

During my PhD, I have been blessed with very friendly and cheerful people in CIBM. They were fundamental in supporting me during the very challenging moments. I would never forget all the chats and beautiful moments I shared with them especially Elise Vinckenbosch and Veronika Račkayová at the university, during the vacations and hiking. I am always proud of having a kind, smart and talented friend, Guillaume Donati, from Valley, area surrounded with beautiful mountains. I appreciate all our scientific discussion about design of RF coil and his constructive comments that push me forward in the RF coil project, and also his help about translating the abstract of my thesis in French. I am very grateful to all other colleagues and friends I have met along the way and have supported me spiritually and contributed to the development of my research. Thanks all for the pleasant time we spent together in the nice environment of CIBM.

I would like to thank all my dear Iranian friends for their invaluable friendship especially Mostafa, Mohammad, Maryam, Elham, Mina and Sina. All your supports and memorable moments shared together has made my graduate life in Lausanne so wonderful.

My deep and sincere gratitude goes to my family for providing me with the opportunities and experiences that have made me who I am. They selflessly encouraged me to explore new directions in life and seek my own destiny. I would like to thank my partner, for his unconditional love, continuous support and encouragement throughout this entire journey.

Publications

Masoumeh Dehghani M., Bernard Lanz, João M. N. Duarte, Nicolas Kunz, and Rolf Gruetter. *"Refined Analysis of Brain Energy Metabolism Using In Vivo Dynamic Enrichment of 13C Multiplets".* ASN neuro ,Vol. 8, Num. 2, p. 1-18 (2016).

Masoumeh Dehghani M., Nicolas Kunz, Bernard Lanz, and Rolf Gruetter. **"***Diffusion-weighted MRS of acetate in the rat brain* ". NMR in Biomed (2016, under revision).

Masoumeh Dehghani M., Bernard Lanz, Nicolas Kunz, and Rolf Gruetter. **"***Cerebral acetate transport and utilization in the rat brain in vivo using ^{1}H MRS: consequences of a revised physical distribution volume of acetate* ". Manuscript is under revision by coauthors.

Masoumeh Dehghani M., Arthur Magill W. , Yves Pilloud, Nicolas Kunz, and Rolf Gruetter. **"**Transmit-*birdcage coil and receiver-two array surface coil for operating at ultra high magnetic field.* Manuscript is under preparation.

Masoumeh Dehghani M., Hongxia Lei, Nicolas Kunz, Rolf Gruetter. "*Diffusion characteristic of metabolites in the brain of shunt and healthy mice in vivo* ". Manuscript is under preparation.

Koroush Arbabi , Gholamreza Raisali , **Masoumeh Dehghani M.** , Mostafa Ghafoori , Arjang Shahvar , Saied Hamidi, *"Fabrication of Free Air Well Type Ionization Chamber and Calculational Assessment and Measurement of Its Operational Characteristics".* Iranian Journal of Medical Physics, ISSN 2252-0309 (2008).

Masoumeh Dehghani M., *"Design and Construction of Free Well-Type Ion Chamber for Measurement of Brachy Therapy Sources strengths"*, Master thesis**.** Arak National University (2006**).**

Conference Proceeding

Y. Pilloud, **Masoumeh. Dehghani M.**, Rolf Gruetter. *"One wire matching and detuning 14T receive coil".* European Society for Magnetic Resonance in Medicine and Biology, Vienna, Austria (2016).

Masoumeh Dehghani M., Hongxia Lei, Nicolas Kunz, Rolf Gruetter. "*Diffusion of Gln and NAA in the mouse brain in vivo* at 14.1T*".* European Society for Magnetic Resonance in Medicine and Biology, Vienna, Austria (2016).

Masoumeh Dehghani M., Hongxia Lei, Nicolas Kunz, Rolf Gruetter. "*Non-mono-exponential diffusion signal attenuation of metabolites in the mouse brain in vivo at 14.1T".* Brain Mind Symposia, Lausanne, Switzerland (2016).

Masoumeh Dehghani M., Bernard Lanz, Nicolas Kunz, Pascal Mieville, Rolf Gruetter. *"Cerebral*

Acetate Transport and Utilization in the Rat Brain in vivo using ^1H MRS: Consequences of a revised acetate volume of distribution value". International Society for Magnetic Resonance in Medicine, Singapore (2016).

Masoumeh Dehghani M., Nicolas Kunz, Bernard Lanz, and Rolf Gruetter**.** *"Revised distribution volume of acetate based on its in vivo diffusion characteristic in rat brain"*, International School on Magnetic Resonance and Brain Function, Erice, Italy (2016).

Yves. Pilloud, **Masoumeh Dehghani M.,** Rolf. Gruetter. *"Four coils varactor diodes controller for tuning and matching.* European Society for Magnetic Resonance in Medicine and Biology, Scotland, UK (2015).

Masoumeh Dehghani M., Nicolas Kunz, Bernard Lanz, and Rolf Gruetter**.** *"Multi-exponential characteristics of acetate diffusion-weighted MRS signal in the in vivo rat brain at 14.1T"*.International Society for Magnetic Resonance in Medicine, Canada (2015).

Masoumeh Dehghani M. Arthur Magill W., Yves Pilloud, Nicolas Kunz, and Rolf Gruetter**.** *"Transmit volume coil-receive surface coil for proton operating at 14 Tesla"*. International Society for Magnetic Resonance in Medicine, Toronto, Canada (2015).

Masoumeh Dehghani M., Nicolas Kunz, and Rolf Gruetter. *"T_1 and T_2 relaxation times of infused Acetate in rat brain at 14.1 Tesla"*. European Society for Magnetic Resonance in Medicine and Biology. Scotland, UK (2015).

Masoumeh Dehghani M., Nicolas Kunz, Bernard Lanz, and Rolf Gruetter**.** *"Diffusion characteristic of infused acetate in the rat brain in vivo"*. International Society for Magnetic Resonance in Medicine & European Society for Magnetic Resonance in Medicine and Biology. Milan, Italy (2014).

Masoumeh Dehghani M., Bernard Lanz, João M. N. Duarte, Nicolas Kunz, Cristina R. Cudalbu and Rolf Gruetter**.** *"Brain energy metabolism studied in vivo by 13C MRS: refined analysis using multiplet time courses"*.European Society for Magnetic Resonance in Medicine and Biology. Toulouse, France (2013).

Masoumeh Dehghani M., Gholamreza Raisali *"Design and Construction Collimator for Measurement of Linear Attenuation Coefficient of Material"*. The 15th Iranian conference of Nuclear, Mashhad,Iran (2009).

Masoumeh Dehghani M., Gholamreza Raisali, Koroush Arbabi, Saied Hamidi. *"Optimization of response unsealed well-type ionization chamber at range of ^{103}Pd source's energy "*. The 8th Iranian conference of Nuclear, Tehran, Iran (2007).

Masoumeh Dehghani M., Gholamreza Raisali, Koroush Arbabi, Saied Hamidi. *"Investigation on the effect of chamber wall aluminum alloy on the response of free-air well-type ionizationc for ^{137}Cs, ^{57}Co and ^{241}Am Gamma Rays"*. The 7th Iranian conference of Nuclear, Boshehr, Iran (2006).

Curriculum Vita

Name: Masoumeh Dehghani Moghadam
Date of birth: September 21, 1981
Place of birth: Bojnord, Iran
Nationality: Iranian

Education

	Doctor of philosophy (PhD) in Physics
2011-2016	Ecole Polytechnique Fédérale de Lausanne (EPFL), Switzerland
	Phd thesis : *Proton Diffusion Spectroscopy and Modeling of Brain Metabolism at 14.1 T,* done at Laboratoire d'Imagerie Fonctionnelle et Métabolique (LIFMET), EPFL
	Master of Science (MSc) in Physics
2003 –2006	National university of Arak, Iran Master thesis: *Design and construction of free well-type ion chamber for measurement of brachy therapy sources strengths*, done at Agricultural, Medical and Industrial Research School, Atomic energy organization of Iran (AEOI), Karaj-Iran
1999-2003	**Bachelor (BSc) in Physics**
	Basic science department, National university of Birjand, Iran

Work experience

	Teaching assistant
2011-2016	École Polytechnique Fédérale de lausanne (EPFL), Switzerland
	Research assistant
2007 –2011	Medical physics group, Nuclear technology center, Atomic energy organization of Iran (AEOI), Tehran-Iran
	Internship in medical physics
2006-2007	Department of nuclear medical science and applications, Agricultural, Medical and Industrial Research School (AMIRS), Atomic energy organization of Iran (AEOI), Karaj-Iran
	Teaching assistant
	University of Takestan, Gazvin, Iran